DOMINIC LAGROIS

UN REGARD SUR L'ÉVOLUTION DYNAMIQUE DES RÉGIONS H II GÉANTES

INTERPRÉTATION DES MOUVEMENTS DU GAZ IONISÉ

Thèse présentée
à la Faculté des études supérieures de l'Université Laval
dans le cadre du programme de doctorat en Physique
pour l'obtention du grade de Philosophiæ Doctor (Ph.D.)

DÉPARTEMENT DE PHYSIQUE, DE GÉNIE PHYSIQUE ET D'OPTIQUE
FACULTÉ DES SCIENCES ET DE GÉNIE
UNIVERSITÉ LAVAL
QUÉBEC

2009

For those who ever walked that lonely road of faith.

"A life is not important except in the impact it has on
other lives."
- Jackie Robinson, *Brooklyn Dodgers (1919-1972)*

Résumé

L'interférométrie de Fabry-Pérot nous permet de quantifier les mouvements systémiques du matériel ionisé confiné à l'intérieur de deux nébuleuses géantes : la région H II galactique W4 et la région H II géante extragalactique NGC 595.

La région H II W4 fut autrefois qualifiée de sérieuse candidate de cheminée dynamique. La cinématique Hα du gaz ionisé, obtenue à l'Observatoire du mont Mégantic, révèle que la nébuleuse est séparée en deux portions distinctes, définies par leurs étendues en latitude. W4-sud ($0° \leqslant b \leqslant 3°$) est largement régie par une série d'écoulements Champagne à petite échelle résultant de la photoérosion d'agrégats moléculaires associés à la nébuleuse. Une importante partie de W4-sud, par contre, semble renfermer une composante ionisée reliée à la photoionisation de la coquille H I enveloppant l'imposante région H II. Si W4-sud nous apparaît comme le dernier stade dans la vie d'un complexe moléculaire géant, W4-nord ($3° < b \leqslant 7°$) confirme la formation d'une cheminée dynamique dans la nébuleuse. Des instabilités au niveau de la portion nord de la coquille se sont vraissemblablement développées, entraînant la rupture de cette dernière. Un scénario de raréfaction domine W4-nord menant à un gradient de vitesse sud-nord à grande échelle au fur et à mesure que le matériel ionisé est éjecté. Le comportement cinématique de la composante H^+ indique que l'amas stellaire IC 1805 contribue à l'ionisation du matériel interstellaire au-dessus du plan galactique. Nous proposons que les objets astronomiques similaires à W4 correspondent au chaînon manquant entre les régions H II galactiques de petite taille et les régions H II géantes extragalactiques.

La région H II géante extragalactique NGC 595 se classe au second rang des nébuleuses les plus imposantes de M33, une galaxie spirale membre du Groupe Local. L'objet fut cartographié en Hα et [S II] suite à diverses missions d'observations à l'Observatoire du mont Mégantic. Les données [O III] furent, pour leur part, obtenues au Télescope Canada-France-Hawaii par le directeur de thèse. Les observations spectro-interférométriques du gaz ionisé sont utilisées en combinaison avec des observations radio de la raie à 21 cm. Les largeurs de raie indiquent des mouvements supersoniques, un comportement régulièrement observé dans les objets extragalactiques. Ce comportement est potentiellement expliqué par le fait qu'écoulements Champagne et une forte turbulence isotrope dominent l'intérieur de la nébuleuse géante. En première approximation, il semblerait que composantes H^+, O^{++} et S^+ ne coexistent pas spatialement. Une région au voisinage de l'amas stellaire montre un dédoublement de raies en Hα et [O III]. Nous proposons que cette particularité spectrale résulte de bulles de vents stellaires en expansion confinées à l'intérieur d'objet. L'étude de NGC 595 nous permet de présenter la première carte bidimensionnelle en densités électroniques associée à une région H II géante extragalactique.

Abstract

Fabry-Perot interferometry allows us to quantify the systemic motions of the ionized material embedded in two giant nebulae : the W4 Galactic H II region and the giant extragalactic H II region NGC 595.

The W4 H II region has been previously qualified as an interesting candidate of dynamic chimney. The Hα gas' kinematics, obtained at the Observatoire du mont Mégantic, reveals that the nebula can be separated in two distinct parts, defined by their extent in latitudes. W4-south ($0° \leqslant b \leqslant 3°$) is mostly regulated by a series of small-scale Champagne flows resulting from the photoerosion of molecular clumps associated to the nebula. A large fraction of W4-south, however, seems to enclose ionized material related to the photoionization of the ovoid H I shell circumscribing the large H II region. If W4-south appears as the last stage in the life of a giant molecular complex, W4-north ($3° < b \leqslant 7°$) confirms the formation of a dynamic chimney in the nebula. Shell instabilities have likely developed along the northernmost portion of the H I supershell and led to fracture. A rarefaction scenario dominates W4-north leading to a large-scale south-north velocity gradient as the ionized material is vented outward. The kinematic behavior of the H^+ component indicates that the IC 1805 star cluster contributes to ionize the interstellar material above the Galactic mid-plane. We propose that W4-like objects are the missing link between small-size Galactic H II regions and giant extragalactic H II regions.

The giant extragalactic H II region NGC 595 is ranked second on the list of the most imposing nebulae of M33, a spiral galaxy located in the Local Group. The object has been investigated in Hα and [S II] following a series of observing runs at the Observatoire du mont Mégantic. The [O III] data were obtained at the Canada-France-Hawaii Telescope by the thesis adviser. The spectro-interferometric observations of the ionized gas were used in conjunction with high-resolution radio observations of the 21 cm line. The non-thermal line widths reveal supersonic motions, a behavior typically observed in extragalactic objects. The behavior likely results from the fact that a large amount of Champagne flows and violent turbulent motions potentially dominate the interior of the nebula. Our first results indicate that the H^+, O^{++}, and S^+ components do not spatially coexist. A localized area in the vicinity of the star cluster shows evidence for line splitting in Hα and [O III]. We confirm that this spectral characteristic results from expanding wind-blown bubbles confined inside the nebula. Our study of NGC 595 allows to publicize the first bidimensional electron density map of a giant extragalactic H II region.

Avant-propos

Ce manuscrit constitue une thèse de doctorat en astrophysique avec insertion d'articles. Les chapitres 5 et 6 présentent deux articles (Lagrois & Joncas 2009a,b) préalablement soumis, arbitrés et publiés par *The Astrophysical Journal*. Le chapitre 7 présente un article (Lagrois & Joncas 2009c) récemment accepté pour publication par *The Astrophysical Journal*. Dans tous les cas, l'étudiant sous évaluation, Dominic Lagrois, en est l'auteur principal. Le directeur de recherche, Gilles Joncas, en est le coauteur. Les trois articles scientifiques sont repris textuellement dans cette thèse sans aucune modification.

Une importante fraction des données interférométriques optiques présentées aux chapitre 5 à 7 furent obtenues au télescope de l'Observatoire du mont Mégantic par l'étudiant. La majeure partie de la réduction lui est également attribuable. L'essentiel des trois publications fut rédigé, de façon originale, par l'étudiant. Notons, par contre, un apport scientifique non-négligeable attribué au coauteur lors de la révision des différents travaux. En particulier, l'auteur aimerait remercier Gilles Joncas (turbulence et simulations) et Laurent Drissen (rapports de flux et densités électroniques) pour leur apport majeur au chapitre 7.

Cette thèse fut entièrement rédigée à l'aide de LaTeX 2_ε.

Mes remerciements personnels sont dirigés vers un groupe de jeunes chercheurs et chercheuses dynamiques. Mes salutations très sincères à deux étudiants pour qui LaTeX et IDL n'ont plus de secrets; Véronique Petit et Simon Cantin, merci pour votre patience et votre génie. À l'équipe SpIOmM, menée par Anne-Pier Bernier, qui nous aura enseigné que persévérance et succès vont de pair. Longue vie à un instrument fabuleux ! À tous ces étudiants et étudiantes qui auront appris à composer avec mon tempérament, disons-le, particulier. À de jeunes gens brillants ; Léo Barriault, Élaine Brière, Simon Richard, Vanessa Juneau et Jean-François Robitaille. Aux grands esprits qui nous ont quittés ; Chris Brook, Matthew Pieri, Mario Lelièvre, André Khalil, Anne Pellerin, François Cazzolato, Jean-François Rochon, Cédric Grenon, Steeve Pinsonneault et Maxime Charlebois. Et à tous ceux et celles qui seront appelés à les remplacer ; Benoît Côté, Pierre Couture, Jean-Michel Mugnes, Laurie Rousseau-Nepton et Kevin Roy. Je lève mon verre au preux chevalier, Monseigneur, « son excellence », Yvan Ladouceur avec qui j'aurai appris que Wayne Gretzky ne sera jamais au vin ce qu'il fut jadis au hockey.

Un merci particulier à Sylvie Beaulieu, ma voisine de Campanile, qui aura eu à faire face à moult « Codes 18 » au cours de mon passage. Ouvrez les yeux dans les allées d'outils au *Canadian Tire* ; vous la trouverez sûrement. Au corps professoral du groupe de recherche en astrophysique de l'Université Laval, je présente mes salutations distinguées. Merci à Hugo Martel dont le génie et le talent aux cartes sont aux antipodes. Salut à Laurent Drissen, un scientifique enjoué, dynamique, optimiste et vulgarisateur hors pair. À Serge Pineault qui m'aura beaucoup manqué pendant son long voyage dans la jungle argentine. ¡Hola, amigo devoto ! Finalement, un merci très spécial à mon directeur de thèse, Gilles Joncas, un père, un ami et un confident qui m'aura, en tout temps, traité d'égal à égal. Sous la tutelle de ce grand scientifique, je serai devenu un meilleur physicien.

À ces amis uniques qui ne sont que trop peu nombreux dans une vie, d'où leur importance ; Marco Pilon et Christian Morin, deux modèles à suivre dans leur domaine respectif. Finalement, merci aux deux femmes de ma vie. À Geneviève, ma muse et ma compagne de tous les jours, pour sa patience et sa compréhension (et sa cuisine !). À ma mère, Carolle, qui aura rapidement compris que déposer des livres éducatifs dans les mains de jeunes enfants peut mener à de grandes réalisations.

May all your cards be live and your pots be monsters ! Ce manuscrit est dédié à ceux et celles, scientifiques de ce monde, qui persévèrent sur le chemin de la foi.

Table des matières

I. Introduction

II. Publications scientifiques

III. Conclusion

IV. Annexe

Liste des figures

Liste des tableaux

Première partie

I. Introduction

> **“Limit poker is a science, but no-limit is an art.**
> **In limit, you are shooting at a target.**
> **In no-limit, the target comes alive and shoots back at you.”**
> - Crandall « Dandy » Addington, *Founder of the World Series of Poker*

Chapitre 1

Mise en situation, problématique et objectifs

Les régions H II géantes (> 100 pc), de par leur taille imposante, leur amas stellaires massifs et leur âge relativement avancé, représentent des structures idéales afin de quantifier l'interaction dynamique entre de gigantesques volumes de matériel interstellaire et les effets combinés de puissants vents stellaires et d'importantes quantités de photons ionisants, tous deux induits par plusieurs dizaines (voir plusieurs centaines) d'étoiles chaudes ($T_{eff} \geqslant 30\,000$ K) et massives ($M \geqslant 10$ $M_\odot$). Les progrès récents en matière de détecteurs optiques hautement performants permettent maintenant d'estimer avec précision la cinématique du gaz interne ionisé et d'interpréter de façon adéquate les mouvements observés.

Les régions H II dites « normales », caractérisées par des tailles faible à intermédiaire (2 - 30 pc) et un nombre d'étoiles massives relativement restreint, renferment un plasma ionisé dont la cinématique est généralement bien comprise de nos jours. Des modèles hydrodynamiques, bien que simples, montrent, en temps normal, un accord saisissant entre théorie et données observationnelles. D'un autre côté, les régions H II évoluées, vieilles de plusieurs millions d'années, sont à l'origine d'une structure cinématique plus complexe, difficilement interprétable. Ce type d'objet montre, bien souvent, des propriétés physiques s'apparentant à :

1. une quantité appréciable de matériel moléculaire et/ou des indices d'un ancien complexe moléculaire géant,
2. d'imposantes associations OB susceptibles de déposer de grandes quantités d'énergie au niveau du milieu interstellaire ambiant par l'entremise de fronts d'ionisation, de violents vents stellaires et, finalement, de supernovae,

3. et une succession de générations d'amas stellaires indiquant potentiellement différentes phases de formation stellaire déclenchée.

Qui plus est, les régions H II géantes montreront, dans plusieurs cas, une morphologie ovoïde, signe que le milieu neutre, dans lequel elles évoluent, devient fortement anisotrope compte tenu des dimensions importantes en jeu. L'aspect allongé aura poussé la communauté scientifique à considérer ce type d'objets comme candidats primordiaux permettant d'établir une connexion en masse et en énergie entre le plan et la couronne d'une galaxie. Bien qu'un tel modèle de « cheminée dynamique » fut proposé théoriquement il y a plus de 35 ans, les indices observationnels susceptibles de corroborer l'existence de telles structures demeurent bien peu nombreux à ce jour.

L'essentiel de cette thèse repose sur la cartographie cinématique du gaz optique ionisé retrouvé à l'intérieur de deux nébuleuses évoluées et de grandes dimensions. Les régions H II W4 (Voie lactée) et NGC 595 (M33) possèdent toutes deux des caractéristiques similaires à celles mentionnées au début de ce chapitre.

La cinématique du gaz ionisé associé à chacune des deux nébuleuses examinées est obtenue via interférométrie Fabry-Pérot. L'acquisition des données est rendue possible grâce à l'utilisation d'une caméra à comptage de photons, ultra-sensible et parfaitement adaptée à l'étude dynamique des objets astronomiques diffus.

La région H II galactique W4, candidate de cheminée dynamique et située au coeur du bras de Persée à une distance héliocentrique de 2.35 kpc (Massey *et al.* 1995), fut choisie, au même titre que ses voisines plus petites W3 et W5, comme cible pour établir le protocole d'observations du *Canadian Galactic Plane Survey* (CGPS). Plus d'une quarantaine d'étoiles massives forment l'amas stellaire IC 1805 (Shi & Hu 1999) associé à l'immense bulle de vents stellaires couvrant grossièrement 20 deg^2 sur le plan du ciel. Les observations à 21 cm montrent une imposante cavité dépouillée d'émission H I pointant en direction de la couronne galactique (Normandeau *et al.* 1997). Épousant les parois atomiques de la cavité, une coquille ionisée, ovoïde (Dennison *et al.* 1997), demeure visible sur pratiquement tout l'intervalle en latitude couvert par la bulle ($0° \leqslant b \leqslant 6°$). La calotte polaire semble culminer à environ 245 pc au-dessus du plan galactique (Normandeau 2000; West *et al.* 2007). Notre échantillonnage Hα se caractérise par une résolution spatiale de 0.02 pc pixel^{-1} à la distance de W4 permettant ainsi une analyse très fine des mouvements à courte et moyenne échelle. Un total de 27 champs, ne couvrant par contre qu'une faible proportion de l'étendue ionisée de la nébuleuse, sont obtenus permettant de quantifier partiellement la cinématique de la composante H^+ interne. Notre étude permet de faire les comparaisons appropriées entre le gaz ionisé et les observations en gaz atomique et moléculaire. La taille imposante de l'objet (165×245 pc^2) demande que les résultats de l'étude cinématique soient présentés dans deux papiers séquentiels.

La région H II géante extragalactique NGC 595 est située à relativement faible distance du centre galactique de la galaxie spirale M33 (Comte & Monnet 1974). Une distance héliocentrique de 847 kpc fut considérée (Galleti *et al.* 2004) fixant ainsi la résolution spatiale des observations optiques à 6.61 pc pixel^{-1}. D'imposantes extensions sous forme de filaments ionisés (Courtès *et al.* 1987) y sont détectées donnant à l'objet un aspect allongé, en accord avec la théorie des cheminées dynamiques, et un diamètre approximatif (selon l'axe majeur) de plus de 400 pc (Kennicutt 1984). L'amas stellaire central est gigantesque, renfermant près d'une centaine d'étoiles O (Malumuth *et al.* 1996) et un nombre appréciable d'étoiles Wolf-Rayet (Drissen *et al.* 2008). La nébuleuse s'étendant sur à peine $2'$ sur le plan du ciel (permettant d'obtenir l'information nécessaire à partir d'une seule pose), une étude multi-ionique du gaz ionisé interne devenait envisageable. Cette thèse présente une cartographie cinématique en Hα, [O III] et [S II] de NGC 595. La cinématique de la composante ionisée est comparée à de récentes observations de M33 à 21 cm ainsi qu'à l'émission en ^{12}CO (1-0) associée à NGC 595, courtoisies respectives du Dr. David A. Thilker (Université Johns Hopkins) et de la Pr. Christine Wilson (Université McMaster).

Nous présentons, au **chapitre 2**, un bref résumé des aspects théoriques liés au milieu interstellaire et à ses différentes composantes. Le **chapitre 3** sera spécifiquement consacré à l'étude des régions H II. Le modèle théorique des cheminées dynamiques y sera, entre autres, plus amplement détaillé. Le **chapitre 4**, plus technique, abordera les concepts d'instrumentation et de réduction de données qui nous auront été utiles afin de conduire efficacement nos recherches.

Le **chapitre 5** présente le premier de deux articles associés à la région H II galactique W4. L'étendue en latitude s'échelonne de $b = 0°$ à $b = 3°$. Cette portion de W4 (nommée, pour la cause, W4-sud) renferme l'amas stellaire IC 1805 ainsi que tout le matériel moléculaire résiduel présent dans la nébuleuse. Il n'est donc pas surprenant d'y retrouver une luminosité Hα relativement élevée. À partir de notre relevé, nous espérons quantifier et interpréter, sur une échelle de quelques parsecs sur le plan du ciel, les mouvements du gaz ionisé confiné dans une région H II évoluée. Spécifiquement, les buts visés seront de (1) déterminer si des écoulement à grande échelle sont présents, (2) quantifier le rôle des vents stellaires et du flux ionisant sur la photoévaporation des structures neutres et (3) vérifier si la phase Champagne a une incidence majeure sur la cinématique observée.

Le **chapitre 6** présente le second article associé à la région H II galactique W4. Nous y présentons un relevé Hα de la portion nord de la nébuleuse (W4-nord) entre $b = 3°$ et $b = 7°$. Cette portion de la nébuleuse renferme une composante ionisée excessivement diffuse, demandant ainsi l'élaboration d'un protocole d'observations bien particulier. Les objectifs associés à l'investigation de W4-nord seront de (1) déterminer si des écoulement à grande échelle sont présents, (2) caractériser [ou non] W4 comme cheminée dynamique en interaction avec la couche de Reynolds, (3) déterminer l'impact cinématique des parois atomiques sur le processus d'évacuation du gaz ionisé et (4) estimer les conséquences d'une succession d'amas stellaires sur l'évolution de la nébuleuse.

Le **chapitre 7** révèle les résultats de notre étude multi-ionique de la nébuleuse NGC 595. Le gaz ionisé y est détecté jusqu'à une distance appréciable de l'amas d'étoiles massives nous permettant ainsi d'examiner sa cinématique sur une fraction importante de l'objet. Le fait que données H I et CO soient mises à notre disposition pour cette étude renforce grandement la valeur du travail. En effet, une connaissance accrue de la cinématique du gaz neutre (i.e., donnant les vitesses de référence) est cruciale afin d'interpréter correctement les mouvements du gaz ionisé. À notre connaissance, ce chapitre représente une des études cinématiques les plus complètes d'une région H II extragalactique. Pour NGC 595, nous nous proposons de (1) obtenir une image cinématique fiable à grande échelle des composantes neutres et ionisées, (2) interpréter les mouvements du gaz observé, (3) estimer la contribution des différents mécanismes dynamiques favorisant l'élargissement des raies d'émission, (4) quantifier l'implication des bulles de vents stellaires en expansion sur l'aspect des différents profils en vitesse et (5) vérifier si la nébuleuse, selon sa morphologie H I, peut se classifier comme candidate de cheminée dynamique. Qui plus est, notre étude de NGC 595 nous permettra d'obtenir la première cartographie bidimensionnelle en densités électroniques associée à une région H II extragalactique.

Le **chapitre 8** présente une revue des principales conclusions obtenues suite à l'investigation des nébuleuses W4 et NGC 595. De plus, une sous-section soulignera les différences et les similitudes que l'on peut tirer d'une comparaison entre les deux objets. Le **chapitre 9** ouvre une fenêtre sur l'avenir, discutant en particulier des interrogations qui subsistent à notre étude et des possibilités/travaux supplémentaires pouvant être exploités à partir de notre riche banque de données. Finalement, une annexe est présentée au **chapitre 10** permettant de faciliter la lecture du chapitre 5. Les diagrammes complémentaires, qui y sont présentés, renforcent certaines conclusions déduites de notre étude de W4-sud.

Chapitre 2

Le milieu interstellaire

Sommaire

2.1 Avant-propos

"The Interstellar Skie... hath... so much Affinity with the Starre, that there is a Rotation of that, as well as of the Starre."

C'est à Francis Bacon, éminent philosophe et scientifique réputé de la Renaissance, que l'on doit la première mention du milieu interstellaire (MIS) dans la littérature populaire. À l'intérieur d'une galaxie, le MIS peut être représenté par tout ce qui se trouve entre les étoiles individuelles ; molécules, atomes, ions, poussières... Il est d'une complexité impressionnante. C'est dans le MIS que naissent les étoiles, au coeur de denses et froids agrégats de gaz moléculaire. Ces étoiles évoluent et se déplacent dans le MIS, « imprégnant » ce dernier de mouvements résultant de leurs violentes réactions nucléaires. Si dans certains cas la cinématique est relativement simple à interpréter, le MIS peut devenir en proie à d'importants mouvements turbulents, dont la modélisation reste difficile. Près de 400 ans après Francis Bacon, un homme sage à qui l'on demanda si le MIS était vide s'exclama : « Heureusement que non ! ». La mort des étoiles massives, souvent cataclysmique, permet de l'enrichir en métaux lourds. Métaux qui, plus tard, auront servi à fabriquer les pages de ce manuscrit ainsi que les molécules qui forment le corps du lecteur qui les parcourt.

La simple description du MIS reste une tâche hasardeuse puisque les matériaux qui le composent émettent ou absorbent la lumière sur une importante fraction du spectre électromagnétique.

2.2 Modèle à deux phases

Field *et al.* (1969) proposent le premier modèle descriptif du MIS. Leurs arguments indiquent que deux phases gazeuses stables et distinctes coexistent en équilibre de pression. La composante tiède (10^4 K) et diffuse (< 0.1 cm^{-3}) occupe une majeure partie de l'espace disponible, enveloppant les fragments froids (< 300 K) et denses (> 100 cm^{-3}). L'ionisation partielle du plasma tiède est soutenue par des rayons cosmiques de faibles énergies produits au coeur de supernovae avoisinantes. Considérant la contribution des champs magnétiques induits par la dynamo de la galaxie, les auteurs proposent que cette distribution en équilibre du MIS est maintenue jusqu'à une altitude d'environ 150 pc au-dessus du plan galactique. Cette valeur correspond bien en première approximation à la demie-épaisseur du disque neutre de la Voie lactée.

Toutefois, certaines failles apparaissent rapidement dans les hypothèses proposées par Field *et al.* (1969). En particulier, Yentis *et al.* (1972) obtiennent un flux anormalement élevé de rayons-X mous à haute latitude, laissant croire à une composante du MIS à haute température ($\sim 10^6$ K) au niveau de la couronne[1] galactique (Spitzer 1956). Chevalier & Gardner (1974) élucidèrent en partie la question par une série de simulations hydrodynamiques de restes de supernova en expansion dans une atmosphère galactique stratifiée (Dickey & Lockmann 1990; Heiles 1991). Les résultats démontrent que, pour une explosion suffisamment puissante (ou une série d'explosions successives à l'intérieur d'un objet unique), l'énergie spécifique du MIS externe ne peut contenir la pression thermique interne engendrée par le gaz brûlant. Ceci permet à la coquille en expansion d'atteindre des altitudes impressionnantes de l'ordre du kiloparsec au-delà du plan galactique. Les auteurs estiment que plusieurs centaines à plusieurs milliers de masses solaires de cette composante chaude et très diffuse peuvent potentiellement être déversées, par une seule superbulle, au niveau de la couronne galactique, en accord avec les observations à hautes latitudes galactiques.

---

[1] Par « couronne », ce manuscrit réfère au gaz coronal détecté à haute altitude de part et d'autre du plan d'une galaxie.

2.3 Modèle à trois phases

La présence de la composante chaude implique une réorganisation du modèle du MIS. McKee & Ostriker (1977) établissent les fondements du modèle à trois phases qui prédomine toujours de nos jours[2]. Les auteurs mentionnent, entre autres, que le modèle à deux phases ne peut survivre au fait que les restes de supernova, réservoirs de la composante chaude, devront nécessairement s'imbriquer les uns dans les autres avant même de se dissiper. La composante chaude doit obligatoirement jouer un rôle non-négligeable dans l'équilibre thermique du MIS. Le nouveau modèle implique désormais trois composantes ; chaude, tiède et froide, de la plus diffuse à la plus dense. Encastrés dans la composante chaude, une panoplie de nuages froids sont dispersés au niveau du plan galactique. La composante tiède est confinée en périphérie de ces nuages, partiellement ionisée par le flux ultra-violet des étoiles chaudes environnantes mais constamment maintenue à 10 000 K par le continuum en rayons-X et par effet photoélectrique sur les grains de poussière.

Les auteurs établissent une distribution exponentielle en latitude de chacune des composantes du modèle. L'atmosphère galactique est décrite en fonction de l'échelle de hauteur de chaque composante. Pour une composante donnée, l'échelle de hauteur indique l'altitude à laquelle la densité (et la pression) de cette dernière aura décliné jusqu'à un facteur e^{-1} de la valeur estimée au niveau du plan. L'échelle de hauteur typique pour la composante froide est estimée entre 90 et 225 pc. Les composantes tiède et chaude s'étendent sur une plus grande distance avec des échelles de hauteur de 1 000 et 3 000 pc respectivement. La fraction de la composante tiède située au-dessus du disque neutre est communément appelée « couche de Reynolds » (Reynolds 1989a) et s'étend jusqu'aux portes de la couronne galactique. La composante chaude à haute altitude forme cette dernière.

Les étoiles présentes dans la couronne galactique sont relativement froides avec peu ou pas d'incidence cinématique et/ou thermique sur leur environnement. Certes, un mécanisme énergétique externe, permettant de maintenir l'ionisation de la couronne, doit être envisagé. Les restes de supernova, modélisés par Chevalier & Gardner (1974), représentent sans doute une solution possible. Puisque la quantité totale d'énergie mécanique, intégrée sur toute la durée de vie d'une étoile massive, déversée dans le MIS par ses vents stellaires équivaut sensiblement au souffle de la phase

---

[2] Notez par contre que le modèle à trois phases ne tient pas compte de la composante moléculaire et des régions H II.

supernova (Dyson & Williams 1980, Chapitre 7), cette thèse se penchera plutôt sur les régions H II comme sources d'énergie visant à établir une connexion entre le plan et la couronne d'une galaxie.

Chapitre 3

Les régions H II

Sommaire

3.1 Formation et rayonnement

Au coeur des agrégats les plus denses de gaz moléculaire naissent les étoiles massives. Ces étoiles ont comme caractéristique d'émettre un flux de photons suffisamment énergétique ($\lambda < 912$ Å) pour photoioniser l'hydrogène moléculaire ambiant. C'est ce qui donne lieu à la formation d'une région H II. Dans le modèle classique, l'étendue de la nébuleuse ionisée est limitée par le fait qu'un atome photoionisé devra nécessairement se recombiner tôt ou tard en atome neutre. La recombinaison force un photon ionisant à ré-ioniser l'atome recombiné plutôt qu'à poursuivre l'étendue en gaz H^+. Pour le cas statique où le taux d'ionisation induit par l'étoile excitatrice est parfaitement équilibré par le taux de recombinaison dans le plasma ionisé, le degré d'ionisation de la région H II est estimé à 99.99%. Le gaz d'une région excitée est pour ainsi dire entièrement ionisé (Dyson & Williams 1980, Chapitre 5). Par contre, la condition d'équilibre indique qu'une étoile ne peut ioniser une quantité infinie de matériel neutre. Le rayon R_S de Strömgren (Strömgren 1939), donnant la dimension de la sphère ionisable, est donné par :

$$R_S = \left[\frac{3}{4\pi} \cdot \frac{S_*(\lambda < 912)}{n^2 \beta_2} \right]^{\frac{1}{3}} \tag{3.1}$$

où $S_*(\lambda < 912)$ est le flux du continu Lyman de l'étoile, n est la densité du milieu excité et β_2 est le coefficient de recombinaison dépendant de la température électronique. Pour des valeurs typiques d'une étoile O6.5V et d'un milieu ambiant de gaz moléculaire de densité intermédiaire, l'équation (3.1) donne un rayon de l'ordre de quelques parsecs, représentatif d'une grande quantité de régions H II galactiques (Sharpless 1959). D'autre part, la sphère de Strömgren d'amas stellaires pouvant renfermer une dizaine à plus d'une centaine d'étoiles massives ne représente bien souvent qu'une fraction des dimensions associées aux objets géants et supergéants répertoriés (Rosa 1983; Kennicutt 1984; Shields 1990). La frontière (à la position de R_S pour le cas statique) séparant le matérial ionisé de la composante neutre se nomme le front d'ionisation. Au-delà du front d'ionisation, une coquille non-choquée de matériel atomique résulte de la photodissociation du gaz moléculaire (Roger & Dewdney 1992). Supposant que le front d'ionisation soit transparent à la radiation stellaire sub-Lyman, certains photons ultra-violets[1] permettront l'excitation du gaz H_2 sans toutefois parvenir à l'ioniser. Suivant la désexcitation au niveau fondamental, un certain nombre de molécules auront acquis suffisamment d'énergie vibrationnelle pour mener à la dissociation. Le front de dissociation sépare le matériel H I du nuage moléculaire.

Puisque les observations révèlent bien souvent des étendues spatiales ionisées supérieures en dimensions à la sphère de Strömgren associée (voir ci-haut), il est évident que le modèle statique ne peut expliquer l'évolution des régions H II. Dynamisant le modèle, le milieu ionisé présente généralement une température environ deux ordres de magnitude supérieure au milieu neutre ambiant. Le gaz chaud, sous pression, ne peut être contenu par le nuage et le front d'ionisation entrera en expansion. Considérant la dilution géométrique du flux stellaire et qu'un certain nombre de photons ionisants doivent servir à pallier aux recombinaisons intérieures, la position $R(t)$ du front d'ionisation est donnée par :

$$\frac{R(t)}{R_S} = \left[1 + \frac{7}{4} \frac{c_0 t}{R_S} \right]^{\frac{4}{7}} \tag{3.2}$$

---

[1] La photodissociation du gaz moléculaire est attribuable aux photons Lyman-Werner (912 Å $< \lambda \leqslant$ 1120 Å).

où c_0 est la vitesse du son dans la région excitée et t, le temps écoulé depuis l'apparition de l'étoile excitatrice (Dyson & Williams 1980, Chapitre 7). La zone photodissociée croîtra également avec le temps, régie par le taux de destruction du H_2 par désexcitation vibrationnelle et sa reformation sur les grains de poussière (Roger & Dewdney 1992). Éventuellement, la zone de gaz atomique sera ionisée, devenant partie intégrante de la région H II, lorsqu'englobée par le front d'ionisation. Dérivant l'équation (3.2), nous obtenons $dR(t)/dt \propto t^{-\frac{3}{7}}$, ce qui signifie que la vitesse du front d'ionisation décroîtra avec le temps. La région H II se dissipe lorsque la vitesse d'expansion devient subsonique par rapport au milieu neutre. Dans bien des cas, le temps requis pour atteindre un tel régime dépasse la durée de vie approximative d'une étoile massive ; pour une étoile isolée, il s'agit donc de la mort de cette dernière qui sonne le glas de la région H II.

Bien que les nébuleuses ionisées émettent dans plusieurs bandes du spectre électromagnétique (e.g., l'émission bremsstrahlung en continu radio), leurs constituants prédominants demeurent observables en émission optique. La série de Balmer de l'hydrogène reste le traceur de régions H II le plus employé[2]. Ce manuscrit traite en grande partie de la dynamique entourant la composante ionisée des régions H II observée par l'entremise de la raie Hα par laquelle l'électron se recombine au niveau d'excitation trois de l'atome d'hydrogène pour cascader au niveau deux. La perte d'énergie, engendrée par la désexcitation radiative, est compensée par l'émission d'un photon à 6562.8 Å dans le référentiel de l'atome recombiné. La nébuleuse est relativement transparente à l'émission Hα qui devient alors aisément observable (en supposant que la région excitée n'est plus confinée à son nuage moléculaire ; voir section 3.2).

Le processus de photoionisation, induit par la présence de l'étoile excitatrice, provoque un ajout continuel d'énergie dans le gaz ambiant. Les processus de refroidissement régularisent la température de la région excitée qui autrement augmenterait indéfiniment (Dyson & Williams 1980, Chapitre 5). Les raies de transitions interdites sont parmi les mécanismes de refroidissement les plus efficaces. L'expression « interdites » est attribuée au fait que ces transitions sont strictement défendues selon les règles de sélection associées à la mécanique quantique. À l'inverse des raies de la série de Balmer, les transitions interdites ne résultent pas d'un phénomène de recombinaison à l'intérieur du plasma ionisé mais plutôt d'une excitation collisionnelle entre un ion et un électron libre. L'excitation de l'ion se fait au détriment de

---

[2] Notez que le modèle considère la nébuleuse opaque à tout photon Lyman résultant d'une recombinaison dans la région excitée.

l'énergie cinétique de l'électron ce qui résulte en un refroidissement du plasma. Dans un milieu de faible densité, typique des nébuleuses ionisées, la désexcitation collisionnelle est peu probable et la désexcitation radiative de l'ion à un niveau inférieur engendre la production d'un photon pouvant habituellement quitter la région H II au même titre que l'émission Hα.

Cette thèse se penchera sur deux transitions interdites spécifiques : la raie de [O III] à 5006.9 Å et le doublet [S II] à 6716.4 et 6730.8 Å. Le potentiel d'ionisation de l'ion O^+ est de 35.1 eV comparativement à 13.6 eV pour l'atome d'hydrogène. Seule une fraction relativement faible du continu Lyman est en mesure de fournir un flux si énergétique. Le nombre d'atomes O^+ pouvant être ionisés par l'étoile excitatrice est alors bien inférieur à celui d'atomes d'hydrogène : l'étendue de la composante O^{++} est alors limitée au voisinage de l'étoile uniquement. Le potentiel d'ionisation du soufre neutre est de 10.4 eV. La spère de matériel S^+ est normalement aussi (sinon plus) étendue que la composante H^+ mais largement plus diffuse en raison de la faible abondance du soufre par rapport à l'hydrogène. Qualitativement, la Figure 3.1 montre l'étendue spatiale relative, au voisinage d'une étoile massive, des différents atomes/ions traités dans ce manuscrit. D'un point de vue quantitatif, le lecteur est invité à se référer aux travaux de Rubin (1983) et Osterbrock (1989, Chapitre 2) montrant la fraction d'ionisation d'un élément donné en fonction de la distance à l'étoile. Les modèles sont particulièrement dépendants de l'opacité des métaux et de la température effective de l'étoile excitatrice.

3.2 Phase Champagne

La région H II demeure optiquement invisible tant et aussi longtemps qu'elle demeure confinée à l'intérieur de son nuage moléculaire. La nébuleuse devient observable lorsque le front d'ionisation atteint la paroi du nuage dense pour croître dans le milieu inter-nuages. Tenorio-Tagle (1979) modélise brillamment la dynamique anticipée d'un tel scénario. L'important gradient de densité qui existe entre le nuage dense et le milieu inter-nuages diffus force l'expansion supersonique de la composante fraîchement ionisée. Le gaz H^+ est accéléré uniformément en un gradient de vitesse linéaire. Supposant une vitesse du son c_0 d'environ 10 km s^{-1} dans la région excitée, les modélisations bidimensionnelles de l'écoulement Champagne (Bodenheimer *et al.* 1979) indiquent qu'une vitesse de 30 km s^{-1}, par rapport au gaz moléculaire, peut être atteinte par la composante ionisée dans le cas de contrastes en densité

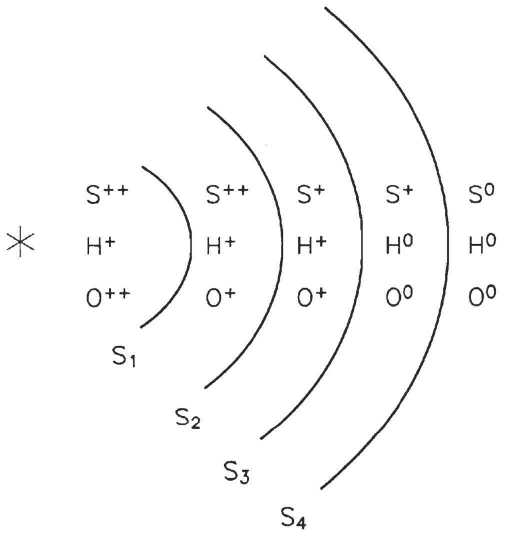

Figure 3.1: Stratification qualitative du matériel ionisé confiné à une nébuleuse.

Afin d'identifier les différents états d'ionisation pour chaque atome, nous considérons une étoile massive de température effective intermédiaire (e.g., O9-B1). De cette façon, le spectre de radiation ionisante favorise un grand nombre de photons au voisinage de 13.6 eV alors que les photons plus énergétiques sont beaucoup plus rares. Les différentes surfaces S_i *indiquent l'étendue parcourue par les différents photons ionisants du continu Lyman. Les photons très énergétiques (> 35.1 eV), moins nombreux, sont rapidement absorbés et sont donc limités, en étendue, au voisinage immédiat de l'étoile par* S_1*. Ces photons peuvent ioniser l'hydrogène de même que le matériel* O^+ *et* S^+*. La surface* S_2 *indique la zone comportant des photons d'énergies inférieures à 35.1 eV mais supérieures à 23.3 eV. L'hydrogène et la composante* S^+ *y sont toujours ionisés. L'oxygène ne peut être ionisé qu'une seule fois. Entre 23.3 eV et 13.6 eV en* S_3*, le soufre est également ionisé à une reprise. Le potentiel d'ionisation de l'oxygène neutre étant pratiquement identique à celui de l'hydrogène, les deux atomes se retrouvent à l'état neutre en* S_4*, dominée par les photons Lyman-Werner (voir section 3.1) d'énergies comprises entre 10.4 et 13.6 eV. Pour ce cas spécifique, seul le soufre demeure ionisé. Théoriquement, la zone de photodissociation du gaz* H_2 *apparaît entre* S_3 *et* S_4 *et peut s'étendre bien au-delà de cette dernière. Inspirée de Dyson & Williams (1980, Chapitre 5), cette figure est l'oeuvre de l'auteur de ces pages.*

importants ($n_{\text{nuage}}/n_{\text{inter-nuages}} > 1\,000$). Tant et aussi longtemps que la composante gazeuse dense n'est pas entièrement érodée et dispersée, l'écoulement Champagne est maintenu et le gradient de vitesse demeure mesurable.

La phase Champagne indique qu'un gradient de densité entraînant la dilution de la composante ionisée est spatialement corrélé au gradient de vitesse gardant ainsi le débit de matériel par unité de surface constant dans l'écoulement. Cyganowski *et al.* (2003) mentionnent une tendance vers l'élargissement des raies d'émission au fur et à mesure que le gaz accéléré s'éloigne de la composante moléculaire. Ceci est intimement lié au dédoublement de raies prédit par un écoulement Champagne conique dont les « parois » divergent avec la distance au nuage dense (Yorke *et al.* 1984). Tel que confirmé par diverses études (e.g., Joncas & Roy 1984; Miville-Deschênes *et al.* 1995; Godbout *et al.* 1997; Barriault & Joncas 2007), la phase Champagne montre un accord saisissant avec les observations cinématiques de régions H II de tailles faible à intermédiaire (2 - 30 pc).

Aux chapitres 5 et 7, un nombre appréciable d'écoulements en gaz ionisé seront examinés afin de confirmer [ou non] leur nature Champagne. Nous proposons une série de conditions, devant être respectées, afin de caractériser un écoulement comme étant de ce type :

1. L'écoulement doit être initié en périphérie d'une structure, habituellement neutre, en apparence beaucoup plus dense que le MIS ambiant.
2. Dans une direction s'éloignant de cette structure, le matériel photoérodé et accéléré doit montrer un comportement linéaire, sur le plan du ciel, en vitesses radiales.
3. Le gradient de vitesse doit, en principe, être dirigé vers la source ionisante. Cette dernière condition n'est pas obligatoire à priori puisque la géométrie de la structure photoionisée peut jouer un rôle déterminant dans la direction de l'écoulement.
4. Le matériel érodé, toujours en contact avec la structure dense, doit montrer un certain accord en vitesses avec la cinématique du gaz neutre. Il s'agit ici de l'ordonnée à l'origine du gradient de vitesse.
5. Spatialement coïncidant avec le gradient de vitesse, un gradient montrant l'élargissement monotonique des raies d'émission doit être observé.
6. L'ordonnée à l'origine du gradient en largeur de raie doit être généralement subsonique. Ceci découle du fait que le matériel ionisé en contact avec la struc-

ture neutre doit montrer des caractéristiques cinématiques relativement en accord avec cette dernière, autant en vitesses radiales (voir point 4) qu'en largeurs de raie étroites (particulièrement typique du gaz moléculaire). Par contre, la géométrie de la structure neutre de même que la disposition spatiale des étoiles massives l'entourant peuvent potentiellement mener à des mesures de dispersion supersoniques à l'origine.

7. Lorsque disponible, la densité électronique à l'intérieur de l'écoulement doit décroître avec la distance à la structure dense. Ceci n'est vrai que si l'écoulement est parfaitement isolé du reste de la nébuleuse (aucun autre écoulement « contaminant » le long de la ligne de visée).

Qu'un certain nombre de ces conditions ne soient pas respectées n'est pas suffisant, en première approximation, pour discréditer automatiquement un écoulement Champagne hypothétique. En particulier, la géométrie et les caractéristiques physiques de l'objet étudié doivent être connues avec grande précision puisque celles-ci jouent un rôle déterminant dans la cinématique observée.

3.3 Vents stellaires et bulles en expansion

Les régions H II géantes et supergéantes, avec des dimensions pouvant varier de 100 à 1 000 pc, possèdent des amas stellaires renfermant plusieurs dizaines à plus d'une centaine d'étoiles massives. La présence d'amas massifs est souvent associée à une quantité phénoménale de matériel moléculaire, ce qui laisse croire que même les plus grandes structures nébulaires sont régies par l'écoulement Champagne. Or, la coquille de gaz neutre bordant une grande fraction des régions H II limitée par l'ionisation indique possiblement une onde de choc compressive et isotrope émanant de l'amas stellaire. Puisque la phase Champagne est étroitement liée à la distribution spatiale des étoiles individuelles et des agrégats moléculaires, il est peu probable qu'un écoulement parfaitement isotrope, radial et grossièrement circulaire à grande échelle en résulte. D'un autre côté, les vents stellaires d'une étoile ponctuelle répondent à cette condition et sont à l'origine des bulles de vents en expansion. Les coquilles asymétriques ou partiellement incomplètes découlent habituellement d'un MIS ambiant inhomogène.

Les étoiles massives sont caractérisées par l'expulsion violente de leurs couches superficielles dans le MIS environnant. Le taux de perte de masse sous forme de vents stellaires dépend, entre autres, de la métallicité, du type spectral de l'étoile et de son stade d'évolution. Un éventail de valeurs entre $10^{-6.5}$ et $10^{-4.5}$ $M_{\odot}$ an^{-1} est régulièrement proposé (e.g., Chiosi & Maeder 1986; Kudritzki & Puls 2000). La vitesse terminale[3] des vents est estimée entre 1 000 et plus de 3 000 km s^{-1}. L'importance des vents stellaires dans notre compréhension des régions H II est motivée par le fait que 20%[4] de l'énergie cinétique contenue dans les vents peut être transférée au MIS (Dyson & Williams 1980, Chapitre 7). Par comparaison, l'expansion du front d'ionisation tel que décrit à la section 3.1 indique que seulement 1% de l'énergie émise par le flux du continu Lyman de l'étoile peut être convertie en énergie cinétique dans le gaz environnant (Dyson & Williams 1980, Chapitre 7).

Castor *et al.* (1975) présentent un article-culte décrivant l'interaction entre les vents stellaires d'une étoile massive isolée et son milieu environnant. Les auteurs y décrivent quatres zones particulières associées à une bulle de vents stellaires en expansion. Le lecteur est invité à se référer à la Figure 3.2, inspirée de Lozinskaya (1992, Section 13). L'étoile (ou l'amas d'étoiles) est positionnée au centre du diagramme en forme d'arcs de cercle concentriques. Le MIS non-perturbé se trouve en zone (d). La zone (a) correspond à l'expansion libre des vents stellaires. La vitesse terminale des vents y est mesurée. Ce matériel, hautement supersonique, se heurte au MIS ambiant et une onde de choc adiabatique (C_2) s'y développe immédiatement. Au fur et à mesure que C_2 s'étend à haute vitesse, la quantité de matériel interstellaire choqué augmente rapidement. Bientôt, l'impulsion des vents de faible densité ne suffit plus à faire progresser la coquille et cette dernière ralentit (Henny *et al.* 1999, Chapitre 12). Ceci implique le développement d'un second choc (C_1) se déplaçant vers l'étoile. Ce choc convertit l'énergie cinétique des vents libres en énergie thermique. Les vents choqués, ralentis, et présentant une température de l'ordre de 10^7 K se retrouvent dans la zone (b). Selon la fonction de refroidissement du MIS choqué (Dyson & Williams 1980, Chapitre 6), cette zone aura tendance à se refroidir difficilement et sera donc spatiallement étendue plutôt que compressée. La zone brûlante, sous haute pression, force l'expansion de la discontinuité R_d séparant les particules de vents ionisées et le matériel interstellaire compressé par C_2

---

[3] La vitesse terminale correspond à la vitesse des particules situées suffisamment loin de l'étoile pour que l'accélération attribuée à la force motrice des vents ne se fasse plus sentir. D'autre part, la vitesse terminale est mesurée en un point où la décélération encourue par l'interaction avec le MIS ambiant ne s'est pas encore produite.

[4] Notez que le 80% additionnel est, en grande majorité, converti en énergie thermique ; voir, ci-dessous, l'interprétation de la Figure 3.2.

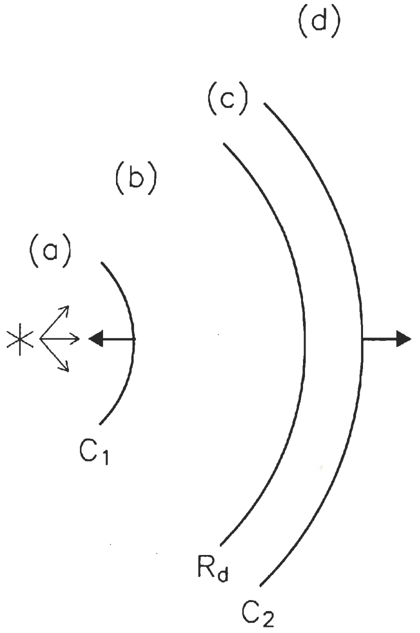

Figure 3.2: Modèle de bulle de vents stellaires en expansion.

Quatre zones sont identifiées : (a), la zone d'expansion libre des vents ; (b), la zone de vents choqués portés à haute température ; (c), la coquille de MIS choqué ; et (d), le MIS non-perturbé. La discontinuité R_d *marque la séparation entre les vents chauds à* 10^7 *K et la coquille semi-neutre, semi-ionisée de la bulle. Les deux chocs associés à une bulle en expansion sont indiqués par* C_1 *et* C_2*. Les flèches grasses indiquent leur direction de propagation respective. Les flèches minces indiquent la propagation isotrope des vents stellaires émanant de l'étoile. Inspirée de Lozinskaya (1992, Section 13), cette figure est l'oeuvre de l'auteur de ces pages.*

en zone (c). Le matériel neutre rencontrant C_2 est rapidement ionisé et conduit à une température de 10^6 K. Le refroidissement par radiation (transitions interdites) est alors très efficace et le gaz est maintenu à une température de 10^4 K par le flux ionisant de l'étoile excitatrice. Le refroidissement rapide augmente la compression derrière C_2 signifiant que la zone (c) sera habituellement très mince. Par dilution géométrique, le nombre de photons incidents sur la coquille compressée diminuent avec l'expansion (Weaver *et al.* 1977). Une fraction importante de la zone (c) peut alors se recombiner et demeurer neutre avec une température avoisinant 100 K.

Le temps requis pour qu'une bulle de vents stellaires atteigne cette configuration est d'environ 1 000 ans, une fraction infime dans la durée de vie de l'étoile. On peut donc supposer qu'une bulle de vents observée devrait déjà posséder cette configuration, dite « snowplow ». Ce terme réfère au fait qu'une coquille froide de matériel compressé est poussée par l'arrière. L'expansion de la bulle de vents est régie sur une longue période (pouvant parfois équivaloir à la durée de vie de l'étoile) par l'énergie thermique présente dans la zone (b). Cette sous-étape de la phase snowplow est appelée « Expansion par conservation de l'énergie ». La dernière sous-étape dans l'expansion d'une bulle de vents, dite « Expansion par conservation de l'impulsion », ne survient que très tardivement lorsque la zone de vents stellaires choqués aura eu le temps de refroidir radiativement. Le refoidissement entraînera la compression de la zone (b) jusqu'à devenir une mince couche en périphérie de R_d. À ce stade, la zone (a), dite d'expansion libre, atteint l'extrémité de la bulle : les vents libres eux-mêmes assureront l'expansion de la coquille de matériel interstellaire compressé en zone (c).

Or, l'étude des modèles théoriques (Vishniac 1994; García-Segura *et al.* 1996; Capriotti & Kozminski 2001) indique en particulier que la discontinuité R_d sera thermiquement conductive. Le développement d'instabilités dans la mince zone (c) permet l'apport en matériel de haute densité et de faible température dans le plasma de vents stellaires choqués de faible densité et de haute température. Un mélange efficace entre les deux composantes mène à un équilibre thermique à une température suffisamment basse pour initier le refoidissement radiatif de la zone (b). Ainsi, le passage à la phase « Expansion par conservation de l'impulsion » peut se faire légèrement plus rapidement que prévu. Bien que cette notion se révèle importante du point de vue de l'évolution d'une bulle de vents, ce manuscrit se penchera essentiellement sur l'impact qu'aura la conduction thermique entre les zones (b) et (c) sur le contenu en gaz ionisé présent à l'intérieur de la bulle.

Puisque l'onde de choc C_2 est compressive et que l'épaisseur de la coquille en zone (c) est négligeable, l'on peut s'attendre à ce que très peu de matériel, laissé derrière C_2, forme le contenu gazeux de la bulle. La composante très chaude de vents stellaires choqués occupe une grande fraction de l'espace disponible et est essentiellement observée par un continu libre-libre en rayons-X et par une foison de raies d'émission et d'absorption de métaux lourds fortement ionisés dans l'ultraviolet et en rayons-X mous (Lequeux 2005, Chapitre 5). Bien qu'une partie du rayonnement interne Hα observé puisse être reliée à l'érosion [par le flux et les vents stellaires] de la composante moléculaire captive de la région excitée, l'investigation du contenu émissif d'une bulle de vents demande de considérer nuages, filaments et globules atomiques comme zones importantes de photoionisation. À un stade d'évolution avancé, une bulle de vents stellaires, propulsée par un amas stellaire massif, aura vraissemblablement atteint une dimension bien supérieure à l'étendue de son nuage moléculaire. La majorité du matériel interstellaire compressé par C_2 devrait pouvoir être associée à la composante H I diffuse[5] environnante à la région H II (d'où la référence bien commune aux coquilles H I). Ce gaz atomique, recombiné derrière l'onde de choc, érodé par l'amas stellaire, et « déversé » dans la bulle dû à la conduction thermique (voir ci-dessus), participe à l'émission optique du gaz ionisé interne et devrait influencer sur sa cinématique.

3.4 Cheminées dynamiques et interaction plan vs couronne galactique

Certaines régions H II/bulles de vents, possédant des caractéristiques bien spécifiques, deviennent des candidates de premier ordre pouvant former des structures similaires aux restes de supernova modélisés par Chevalier & Gardner (1974). Naissant à proximité du plan galactique, ces structures présentent des quantités impressionnantes de matériel moléculaire, une succession d'amas stellaires massifs par formation stellaire déclenchée et d'imposantes associations OB (voir chapitre 1). Croissant vers la couronne galactique selon la direction de moindre résistance, ces superbulles reçoivent la connotation de « cheminées dynamiques » puisqu'il s'agit

---

[5] Advenant qu'une portion de l'onde de choc se trouve toujours au voisinage du nuage moléculaire, freinée dans sa propagation par le gaz dense ambiant, une importante fraction du matériel interstellaire compressé par C_2 est susceptibe de provenir de la zone H I de photodissociation pouvant englober la région H II (voir section 3.1).

d'objets allongés, ovoïdes, au coeur desquels les photons ionisants peuvent aisément voyager, se butant à un minimum de matériel neutre (Norman & Ikeuchi 1989). Ce manuscrit fera référence aux cheminées galactiques comme des cheminées dynamiques associées à la Voie lactée.

La théorie des bulles de vents stellaires indique que la vitesse d'expansion de la coquille H I décroîtra avec le temps. Comme pour l'expansion dynamique du front d'ionisation, la bulle se dissipe lorsque cette vitesse atteint un régime subsonique par rapport au MIS ambiant. Or, l'expansion dans une atmosphère galactique exponentielle (voir section 2.3) mène à une constante diminution de la pression externe exercée par le MIS non-perturbé sur la coquille de matériel compressé. Advenant que la coquille puisse croître suffisamment dans le gradient de densité et outrepasser le disque neutre de sa galaxie, une ré-accélération de l'expansion peut survenir en raison du MIS externe excessivement diffus. Les modélisations indiquent que cette phase « d'éclatement de la bulle » [hors du plan H I] survient lorsque la calotte polaire de cette dernière atteint une altitude estimée entre deux et trois fois[6] le facteur d'échelle du disque atomique (Mac Low *et al.* 1989). Dove *et al.* (2000) mentionnent que la soudaine ré-accélération favorise le développement d'instabilités pouvant mener à la rupture de la coquille H I. En supposant que la quantité de matériel neutre présent dans la bulle est limitée (afin d'éviter une absorption drastique des photons ionisants), une fraction non-négligeable du continu Lyman de l'amas peut évacuer la région H II et participer à l'ionisation de la couche de Reynolds et de la couronne galactique. Norman & Ikeuchi (1989) mentionnent qu'environ 1 000 de ces structures pourraient suffir à expliquer la composante chaude et diluée détectée dans la couronne de la Voie lactée.

Les régions H II géantes partiellement limitées par la densité ne requièrent pas obligatoirement la rupture de leur coquille afin d'interagir avec la couronne galactique. Or, l'identification de telles structures peut être parfois hasardeuse, reposant bien souvent sur une investigation qualitative de l'émission radio. D'un autre côté, la rupture de la coquille neutre et la formation d'une faille de dimension

---

[6] Il est important de préciser que cet intervalle en altitude est normalement bien en deçà du niveau proposé pour la couronne galactique (voir section 2.3). Pour une cheminée dynamique se formant à relativement basse altitude, l'interaction avec la couronne se fera par l'entremise de photons ionisants uniquement. Le déversement de matériel chaud et ionisé se fera à des latitudes intermédiaires favorisant la formation de fontaines galactiques (Shapiro & Field 1976). Ce type de structures pourrait être à l'origine des nuages H I à hautes vitesses (HVC, de l'anglais *High-velocity clouds*) (Wakker 2001) et de l'enrichissement chimique du plan de la galaxie (Spitoni *et al.* 2008; Bekki *et al.* 2009).

appréciable devrait entraîner une signature cinématique particulière et mesurable sur la composante ionisée située à l'intérieur de la bulle. L'interaction énergétique plan/couronne devient fortement probable si cette signature indique un alignement favorable amas → faille → couronne.

Chapitre 4

Instrumentation et traitement des données

Sommaire

4.1 Interférométrie de Fabry-Pérot

L'interféromètre de Fabry-Pérot représente une option particulièrement intéressante pour l'observateur désireux de privilégier la résolution spectrale à l'étendue en longueur d'onde balayée par les observations. Pour l'étude cinématique d'une raie d'émission donnée, l'interféromètre de Fabry-Pérot peut se limiter au voisinage spectral de cette dernière et permettre d'extraire l'information en émission sur une série de petits espacements en longueur d'onde. Ceci permet, entre autres, de résoudre spectralement les largeurs de raie associées aux profils de vitesse observés ainsi que de détecter des variations en vitesse radiale de l'ordre du km s^{-1} à l'intérieur de la nébuleuse visée (voir section 4.3). L'interféromètre de Fabry-Pérot, de par sa polyvalence et sa facilité d'opération, possède une variété d'applications dans une fraction non-négligeable du spectre électromagnétique allant de l'ultra-violet à l'infra-rouge.

4.1.1 Étalon de Fabry-Pérot

Contrairement à son proche parent, l'interféromètre de Michelson, le Fabry-Pérot est composé de deux lames semi-réfléchissantes constamment maintenues parallèles tel qu'indiqué à la Figure 4.1. Ces lames sont d'épaisseur négligeable. La distance h entre les deux lames peut être fixe (étalon de Fabry-Pérot) ou variable (interféromètre de Fabry-Pérot à balayage), contrôlée par l'actionneur piézoélectrique situé sous la lame inférieure. Attardons-nous au cas statique de l'étalon de Fabry-Pérot (EFP) avec h constant. Le milieu inter-lames est d'indice de réfraction $n \gtrapprox 1$. Un faisceau lumineux, monochromatique de longueur d'onde λ_0 et d'amplitude arbitraire A, est incident sur la lame supérieure à un angle θ par rapport à la normale. La nature semi-réfléchissante, semi-tranparente des lames permet à l'EFP d'agir comme cavité résonante d'où émaneront une série de faisceaux transmis (d'amplitudes $a_i < A$) et réfléchis (d'amplitudes $b_i < A$). Nous nous attarderons uniquement aux faisceaux transmis puisque le détecteur (voir section 4.2) se situera sous la lame inférieure. Les différents faisceaux a_i sont recombinés à la sortie de l'EFP par une

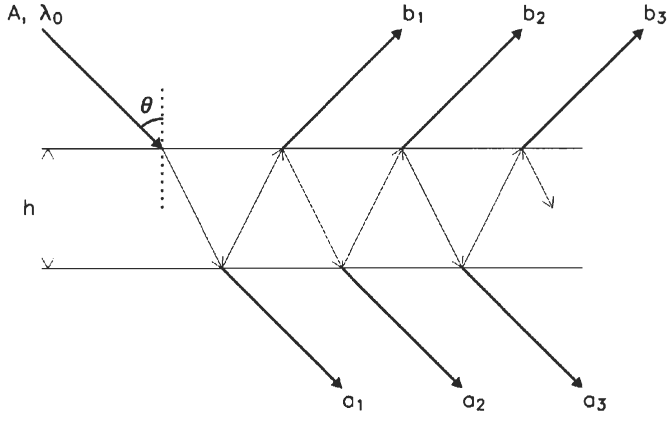

Figure 4.1: Trajet optique encouru dans un étalon de Fabry-Pérot.

Le Fabry-Pérot est composé de deux lames semi-réfléchissantes, semi-tranparentes. L'espacement entre les lames est donné par h. Un faisceau monochromatique d'amplitude A est incident à angle θ sur la lame supérieure. Dans le cas d'un EFP idéal, la cavité résonante permet qu'une fraction du signal d'entrée soit transmise (a_i) alors que l'autre fraction est réféchie (b_i). Inspirée de Yariv (1997, Chapitre 4), cette figure est l'oeuvre de l'auteur de ces pages.

lentille focalisante, partie intégrante du réducteur focal. Le déphasage angulaire δ entre deux a_i consécutifs est calculé selon le « retard » pris par le plus tardif (ayant le parcours optique le plus long à l'intérieur de l'EFP) et est donné par :

$$\delta = \frac{4\pi}{\lambda_0} nh \cos\theta. \tag{4.1}$$

La recombinaison des faisceaux mènera à une interférence constructive uniquement si ces derniers sont en phase angulaire. Cela signifie qu'un maximum de transmission n'est observé que si le déphasage angulaire δ, donné par l'équation (4.1), est un rapport entier de 2π :

$$m = \frac{\delta}{2\pi} = \frac{2}{\lambda_0} nh \cos\theta, \tag{4.2}$$

où m est appelé l'ordre d'interférence de l'EFP. L'interférence des faisceaux recombinés sera destructive (minimum de transmission) si m a une valeur demi-entière.

Ceci étant dit, nous ignorons le comportement en intensité transmise entre les phases constructives et destructives (pour une valeur de m ni entière, ni demi-entière). L'amplitude totale A_t des faisceaux transmis à la Figure 4.1 revient à faire la somme de tous les a_i :

$$A_t = AT[1 + R{\cdot}e^{-i\delta} + (R{\cdot}e^{-i\delta})^2 + (R{\cdot}e^{-i\delta})^3 + ...] = \frac{AT}{1 - R{\cdot}e^{-i\delta}}, \tag{4.3}$$

où R et T sont respectivement la réflectivité et la transmittivité de l'EFP. Les coefficients en $R{\cdot}e^{-i\delta}$ indiquent que les faisceaux transmis ont rebondi un certain nombre de fois (donné par l'exposant) à l'intérieur de l'EFP avant de quitter le résonateur. Portant l'équation (4.3) au carré, nous obtenons l'intensité relative transmise par la lentille focalisante en fonction du déphasage :

$$\frac{I_t}{I} = \frac{A_t{\cdot}A_t^*}{A{\cdot}A^*} = \frac{(1-R)^2}{(1-R)^2 + 4R\sin^2\left(\frac{\delta}{2}\right)}, \tag{4.4}$$

où $T \equiv 1 - R$ et A^* et A_t^* sont respectivement les complexes conjugués de l'amplitude incidente A (voir Figure 4.1) et de l'amplitude totale tranmise A_t donnée par l'équation (4.3). La Figure 4.2 montre le comportement de l'intensité relative transmise (traits pleins) pour différents EFP (réflectivité/transmittivité variables). Le patron d'intensité résultant du phénomène d'interférence prend la forme d'une fonction d'Airy. Toute l'intensité du faisceau incident à l'EFP est transmise en phase constructive. En phase destructive, l'intensité relative transmise décroît avec la transmittivité. Or, il advient qu'un EFP sera bien souvent caractérisé par des pertes en transmission au niveau du milieu inter-lames. Le maximum d'intensité relative transmise sera alors moindre que l'unité ($< 100\%$). Posant $(1 - P)$, la fraction d'amplitude perdue pour chaque aller-retour dans le milieu inter-lames (e.g., entre a_1 et a_2), un réarrangement de l'équation (4.4) pour un EFP non-idéal (Yariv 1997, Chapitre 4) est donné par :

$$\frac{I_t}{I} = \frac{(1-R)^2 P}{(1-RP)^2 + 4RP\sin^2\left(\frac{\delta}{2}\right)}. \tag{4.5}$$

L'équation (4.5) est présentée à la Figure 4.2 en trait pointillé pour $R = 0.7$ et $P = 0.95$. Pour cet exemple, les pertes encourues par l'EFP non-parfait mènent à une transmission relative maximale de l'ordre de 75%.

Considérant la symétrie radiale de l'EFP par rapport à son axe optique, le pic d'intensité maximale d'ordre m à la Figure 4.2 devrait, une fois focalisé (par la lentille du même nom) au niveau du détecteur, correspondre à un anneau concentrique de rayon r_m. Or, il advient qu'une série d'anneaux concentriques sont habituellement observés émanant de l'EFP, chacun possédant un rayon différent. Un exemple de patron d'interférence est montré à la Figure 4.3 pour une lampe au sodium masquée d'un filtre interférentiel étroit.

Puisque la source est monochromatique, chacune des franges brillantes doit nécessairement correspondre à la transmission de la longueur d'onde λ_0. La solution vient du fait que la source est incidente à l'EFP sur toute une gamme d'angles θ. Le centre géométrique des anneaux d'interférence constructive correspond à une incidence normale ($\theta = 0°$). L'angle d'incidence augmente jusqu'en périphérie du déctecteur (voir section 4.3.2). Certains angles favoriseront donc la transmission de λ_0 selon les différentes valeurs prises par l'ordre d'interférence. De ce fait, :

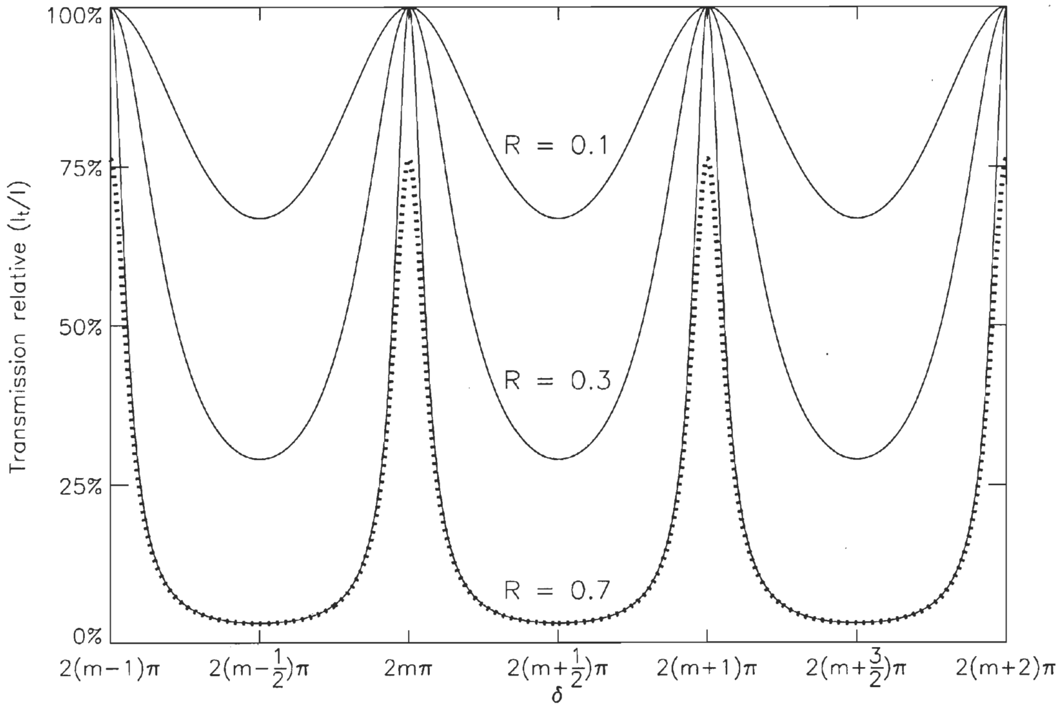

Figure 4.2: Intensité relative transmise par un EFP en fonction du déphasage.

L'intensité relative transmise est maximale pour des faisceaux a_i *en phase constructive (où* δ *est un multiple entier de* 2π*). La variable* R *indique la réflectivité de l'EFP. La largeur des pics de transmission et le plancher en transmission minimale décroissent avec la transmittivité* T *(*$\equiv 1 - R$*) de l'EFP. Pour un EFP non-idéal, les pertes en transmission dans le milieu inter-lames réduisent l'intensité relative maximale pouvant être transmise (trait pointillé).*

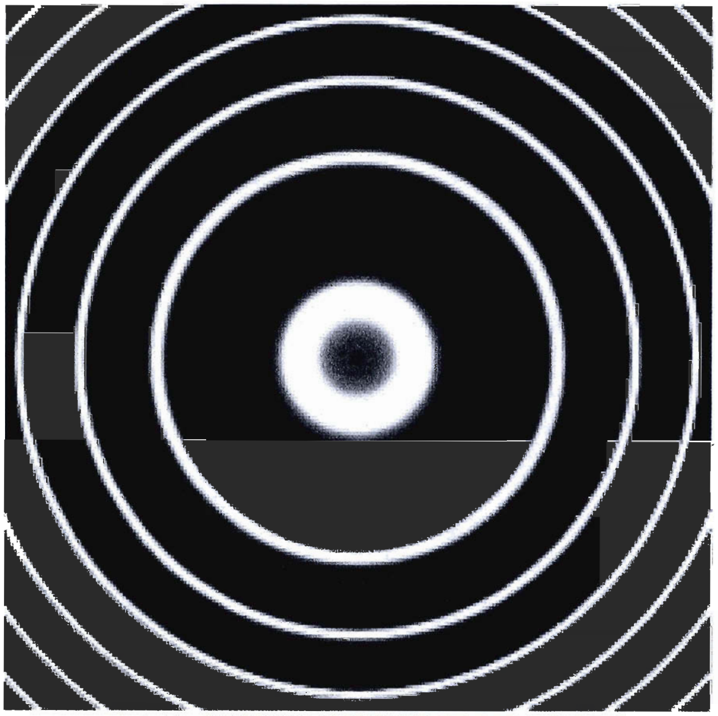

Figure 4.3: Patron d'interférence émanant d'un EFP.
La raie d'émission à λ5890.1 Å provenant d'une lampe au sodium est utilisée comme source monochromatique. Les différents anneaux correspondent à différents ordres d'interférence satisfaisant à l'équation (4.2). Tirée de History of science at Science Online 2009 (http ://skullsinthestars.com/2008/10/15/history-of-science-at-scienceonline-09/).

$$
\begin{aligned}
r_{m+1} &\longrightarrow (m+1)\,\lambda_0 = 2\,nh\,\cos\theta_{m+1}, && (4.6a)\\
r_{m+2} &\longrightarrow (m+2)\,\lambda_0 = 2\,nh\,\cos\theta_{m+2}, && (4.6b)\\
r_{m+3} &\longrightarrow (m+3)\,\lambda_0 = 2\,nh\,\cos\theta_{m+3}, && (4.6c)\\
&\qquad\qquad \ldots\\
&\qquad\qquad \ldots\\
&\qquad\qquad \ldots
\end{aligned}
$$

où r_{m+1}, r_{m+2} et r_{m+3} sont les rayons des anneaux d'interférence observés au détecteur. Chaque anneau respecte la condition de transmission maximale donnée par l'équation (4.2). Chacun possède son ordre d'interférence propre et correspond à un angle d'incidence distinct à l'EFP. La diminution centre-bord de $\cos\theta$ est compensée par un ordre d'interférence plus petit afin de satisfaire à l'équation de transmission maximale. De ce fait, les ordres les plus élevés seront situés près du centre alors que les ordres plus petits se retrouveront en périphérie du détecteur ($r_{m+1} > r_{m+2} > r_{m+3}$ etc...). Le contraste entre les anneaux brillants et les zones inter-anneaux sera plus ou moins important dépendant des caractéristiques en réflectivité et transmittivité de l'EFP utilisé. Puisque les pics de transmission correspondant à chaque anneau ne sont pas infiniment étroits (voir Figure 4.2), nous utiliserons plutôt l'expression « bandes de transmission ».

4.1.2 Interféromètre de Fabry-Pérot à balayage

La théorie statique de l'EFP indique, par l'équation (4.2), que pour une source à incidence θ fixe, le passage d'un ordre d'interférence à un autre n'est possible que par un changement en longueur d'onde de la source émissive. L'intervalle en longueur d'onde entre deux ordres adjacents définit l'intervalle spectral libre (ISL) du Fabry-Pérot. Considérant m fonction de λ_0 et $m-1$ fonction de $\lambda_0 + \Delta\lambda$, l'équation (4.2) montre que :

$$\Delta\lambda = \frac{\lambda_0^2}{2nh\cos\theta - \lambda_0} \approx \frac{\lambda_0^2}{2nh\cos\theta}. \tag{4.7}$$

où $\Delta\lambda$ corespond, par définition, à l'ISL. La notion d'ISL devient critique lorsque le Fabry-Pérot est utilisé en mode balayage, avec un espacement h variable entre les lames. Nous parlerons alors d'interféromètre de Fabry-Pérot (IFP) plutôt que d'étalon. L'équation (4.2), pour un ordre m entier fixe, indique qu'une variation de h modifiera la longueur d'onde λ_0 transmise avec un maximum d'efficacité. Spécifiquement, l'équation (4.2) se réduit, pour une bande de transmission d'ordre m, à :

$$h \sim m\frac{\lambda_0}{2}, \tag{4.8}$$

supposant $n\cos\theta \sim 1$. Ainsi, une variation de h de l'ordre de $\frac{\lambda_0}{2}$ permet d'atteindre le mode voisin $m-1$ et de balayer l'ISL de l'IFP. Le balayage se fait en une série de N déplacements (pas) δh de telle sorte que :

$$N\delta h \sim \frac{\lambda_0}{2}. \tag{4.9}$$

À chaque pas i (variant de 0 à N), l'exposition [pendant un certain temps] au détecteur permet d'obtenir l'émission transmise par l'IFP à une longueur d'onde :

$$\lambda_i = \lambda_0 + i\delta\lambda, \tag{4.10}$$

où $\delta\lambda = \frac{\Delta\lambda}{N}$ est le « saut » de pas. Au détecteur, le balayage de l'ISL se caractérisera, pour un anneau donné, par une série d'incréments en rayon δr de telle sorte que :

$$r_i = r_0 + i\delta r, \tag{4.11}$$

où r_0 est le rayon initial de l'anneau et r_i, le rayon de l'anneau au pas i. De ce fait, le balayage de l'ISL est complété à r_N, le rayon initial r_0 du mode adjacent externe $m-1$.

Le nombre de pas N nécessaire au balayage de l'ISL est une valeur critique obtenue au télescope directement. Ce nombre dépend principalement des propriétés des anneaux d'interférence au détecteur. Si nous pouvions dynamiser la Figure 4.2 au fur et à mesure que le balayage s'effectue, chaque pas i verrait la bande de transmission située à $2m\pi$ se déplacer légèrement vers la gauche jusqu'à atteindre la position à $2(m-1)\pi$. Le nombre de pas est donc intimement lié à la largeur des bandes de transmission. Pour $R = 0.1$, un nombre N trop important causera un recouvrement partiel de la bande entre deux incréments δh adjacents. Ce cas correspond au scénario de sur-échantillonnage, pas dramatique à priori mais coûteux en temps d'exposition (le recouvrement fait en sorte que la même information astronomique est observée deux fois plutôt qu'une). D'un autre côté, pour $R = 0.7$ par exemple, un nombre N sous-estimé aura comme conséquence l'apparition d'un « trou spectral », l'intervalle en longeur d'onde balayé étant inférieur à l'ISL dû à l'étroitesse de la bande de transmission. Le sous-échantillonnage doit être absolument évité puisqu'une fraction de l'ISL ne présentera aucune information spectrale utilisable. La finesse réflective $\mathcal{F}_r$ de l'IFP quantifie, en quelque sorte, la largeur des bandes de transmission :

$$\mathcal{F}_r = \frac{\Delta\lambda}{FWHM_\lambda} = \frac{\pi}{2\,\mathrm{arcsin}\left(\frac{1}{\sqrt{F}}\right)}, \tag{4.12}$$

où $FWHM_\lambda$ est la pleine largeur à mi-hauteur d'une bande quelconque et F est le coefficient de finesse donné en simplifiant le facteur $(1 - R)^2$ au numérateur et au dénominateur de l'équation (4.4). Le coefficient de finesse correspond au terme résultant associé à la fonction sinus carré :

$$F = \frac{4R}{(1-R)^2}. \tag{4.13}$$

L'on remarque ainsi que pour une réflectivité élevée, la finesse réflective de l'IFP sera importante et les bandes de transmission (voir Figure 4.2) seront excessivement étroites. L'avantage d'un tel scénario est un « saut » de pas très restreint ; la valeur de $\delta\lambda$ donnée à l'équation (4.10) sera petite permettant d'acquérir l'information astronomique sur une multitude de longueurs d'onde au voisinage de λ_0. Ceci est particulièrement utile dans le cas d'un objet montrant des variations de l'ordre du km s^{-1} en vitesse radiale (voir section 4.3). D'un autre côté, une finesse réflective élevée et l'étroitesse des bandes de transmission résultante demanderont un grand nombre de pas N afin de couvrir l'ISL. Ceci se traduira par un important prolongement des temps d'exposition. Généralement, les pertes diffractives survenant dans un IFP limitent la valeur maximale pouvant être atteinte par R et, par le fait même, $\mathcal{F}_r$.

La finesse effective (ou totale) de l'IFP dépend également des défauts de parallélisme entre les lames de l'interféromètre ($\mathcal{F}_d$) ainsi que de la discrétisation du détecteur attribuée à son nombre fini de pixels ($\mathcal{F}_i$). Amram (1991) indique que la finesse effective $\mathcal{F}_e$ de l'IFP est donnée par :

$$\frac{1}{\mathcal{F}_e^2} = \frac{1}{\mathcal{F}_r^2} + \frac{1}{\mathcal{F}_d^2} + \frac{1}{\mathcal{F}_i^2}. \tag{4.14}$$

Habituellement, la finesse de défaut $\mathcal{F}_d$ peut être négligée advenant que le parallélisme de l'IFP puisse être atteint avec une précision de l'ordre de $\frac{\lambda_0}{100}$. Afin d'éviter le sous-échantillonnage, le critère de Nyquist demande que le nombre de pas N excède en tout temps le double de la finesse effective :

$$N = \frac{\Delta\lambda}{\delta\lambda} \geqslant 2\,\mathcal{F}_e. \tag{4.15}$$

Les expériences démontrent qu'il est prudent d'augmenter ce critère d'environ 10% (Atherton *et al.* 1982). Les chapitres 5 à 7 présentent des données interférométriques optiques en Hα et [S II][1] dont l'acquisition s'est étalée sur plus de cinq ans entre 2003 et 2008. De légères fluctuations de la finesse effective de l'IFP employé furent enregistrées pendant cette période. Nous avons fait preuve d'une certaine forme de « tolérance » (voir section 4.3.1), par rapport au critère de Nyquist, permettant un facteur de proportionnalité N vs $\mathcal{F}_e$ pouvant varier entre 2.2 et 2.5. Ce faisant, les observations furent conduites utilisant, le plus souvent possible, un nombre de pas N identique d'une mission d'observations à l'autre. Les comparaisons cinématiques ou, dans certain cas, la juxtaposition (sous forme de mosaïques) des données obtenues lors de différentes missions furent grandement facilitées.

4.2 Caméra à comptage de photons

Deux écoles de pensée prévalent toujours en astronomie instrumentale concernant le choix du détecteur approprié pour l'étude en question. Les détecteurs CCD (de l'anglais *Charge-Coupled Device*) ont comme avantage d'avoir une haute efficacité quantique (> 80%) signifiant que une forte majorité des photons incidents à la surface photoréactive du détecteur seront normalement comptabilisés. La caméra à comptage de photons ou IPCS (de l'anglais *Image Photon Counting System*) possède une efficacité quantique rarement plus élevée que 30%. D'un autre côté, l'amplification du signal incident à la photocathode aura comme conséquence un bruit de lecture pratiquement nul pour ce type de caméra (voir ci-dessous). De plus, le pro-

---

[1] Notez que les observations [O III], présentées au chapitre 7, n'ont pas été effectuées par l'auteur de ces lignes (voir section 7.5). Les « manipulations » du critère de Nyquist, telles que discutées ici, ne se sont donc pas appliquées aux données [O III] de NGC 595.

blème de distorsion d'image, typique des caméras CCD grand format, ne s'applique pas à l'IPCS, améliorant ainsi la qualité des images obtenues.

Pour la présente étude, une forte majorité des données spectro-interférométriques optiques furent obtenues à l'aide du système FaNTOmM (Fabry-Pérot de Nouvelle Technologie pour l'Observatoire du mont Mégantic) composé du réducteur focal PANOMARIX (Godbout *et al.* 1998), d'un IFP à balayage (voir section 4.1.2) et d'une caméra IPCS (Hernandez *et al.* 2003).

La caméra IPCS se compose de trois sections distinctes : (1) un tube amplificateur (augmentant, de façon drastique, l'intensité du signal reçu), (2) lié par fibre optique (3) à un détecteur CCD standard de 1 024 pixels^2. Tout photon incident à la photocathode est amplifié d'un facteur 10^6 à 10^7 permettant ainsi de complètement négliger le bruit de lecture du CCD utilisé. Une des qualités de FaNTOmM, par opposition aux autres caméras IPCS conventionnelles, est son système d'acquisition des patrons d'interférence fait en temps réel grâce au logiciel ADHOCw[2] (Laval *et al.* 1987). Cette caractéristique particulière permet de diminuer, d'un facteur appréciable, le temps de lecture à chaque pas nécessaire au balayage de l'ISL. De ce fait, l'ISL peut être couvert à plusieurs reprises au cours d'une nuit d'observations. Chaque balayage de l'ISL correspond à un « cycle » d'observations. L'accumulation de cycles permet, entre autres, de contôler le rapport signal-sur-bruit des raies d'émission détectées et, par le fait même, d'assurer la qualité des observations spectro-interférométriques. Les faibles temps de lecture permettent également de couvrir l'ISL en un temps inférieur aux variations photométriques typiques du ciel nocturne. FaNTOmM montre un temps de lecture de 25 milli-secondes par image. Pour un temps d'exposition d'une heure, ceci se traduit typiquement par un temps de lecture total d'approximativement 10 secondes.

La philosophie d'acquisition du signal est passablement différente entre caméras CCD et IPCS. Si la première est conçue pour accumuler un flux sur un pixel donné, l'IPCS compte plutôt les « événements », un à un, tombant sur ce même pixel. Ainsi, la caméra IPCS, au contraire du détecteur CCD, est moins affectée par les rayons cosmiques puiqu'un événement revient à compter un photon unique.

La Figure 4.4, reproduite de Hernandez *et al.* (2003), montre une étude comparative entre FaNTOmM (formé d'une cathode photoréactive en composite Gallium-Arsenic) et deux caméras CCD conventionnelles de différentes efficacités quantiques.

---

[2] http ://www-obs.cnrs-mrs.fr/adhoc/adhoc.html

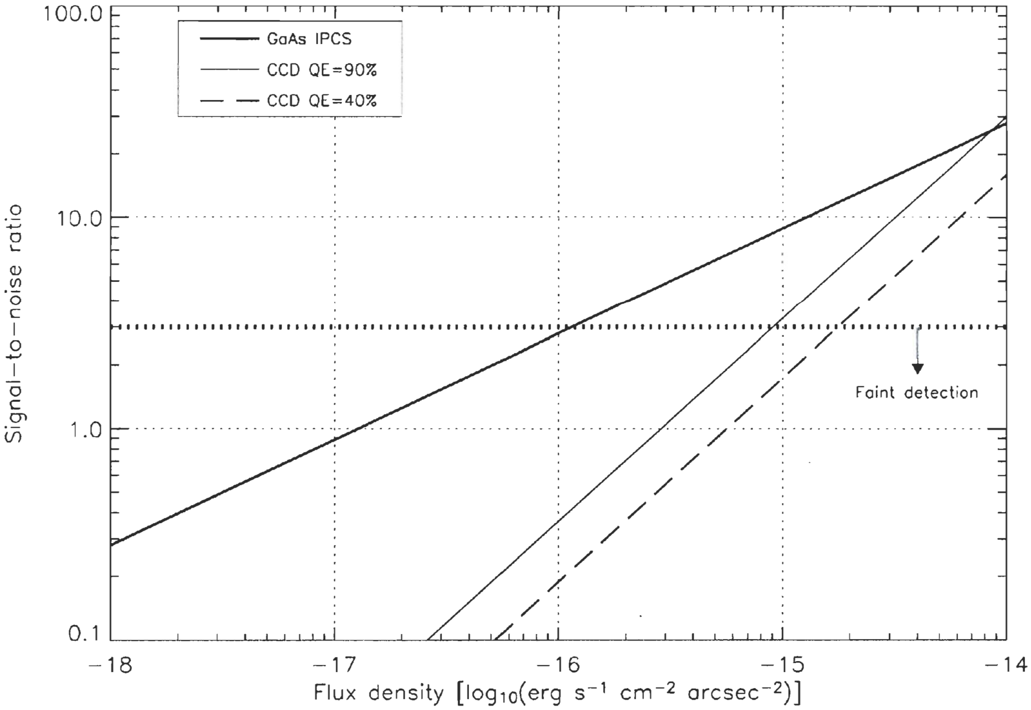

Figure 4.4: Comparaison de l'efficacité entre caméras CCD et IPCS.

Le diagramme propose une étude comparative entre divers détecteurs, CCD et IPCS. Dans tous les cas, le temps d'intégration sur le ciel, au télescope de 8m, était de 60 minutes pour des conditions photométriques relativement similaires. Pour FaN-TOmM (trait gras), ceci correspond à une accumulation de 10 cycles sur le ciel (chacun comportant 48 pas et tous caractérisés par un temps d'exposition de 7.5 secondes). Les deux CCD examinés montrent des efficacités quantiques de 90% (trait régulier) et 40% (trait en tiret). Le trait pointillé horizontal, marquant un rapport signal-sur-bruit de trois, indique la limite en-dessous de laquelle une détection ne peut être jugée comme fiable (voir section 4.3.2). Inspirée de Hernandez et al. (2003), cette figure est l'oeuvre de l'auteur de ces pages.

À faible flux, il apparaît que l'absence de bruit de lecture de l'IPCS prévaut sur sa faible efficacité quantique et permet d'obtenir un signal jugé beaucoup plus fiable. D'autre part, ce même signal (à faible flux) se « noie » rapidement dans le bruit de lecture du détecteur CCD. La haute efficacité du CCD permet à ce dernier de surpasser l'IPCS uniquement pour des objets relativement brillants ($> 10^{-14}$ erg s^{-1} cm^{-2} arcsec^{-2}). Pour les objets astronomiques de faible intensité nous concernant (voir chapitre 1), l'IPCS apparaît comme un choix optimal. À titre d'exemple, Malumuth *et al.* (1996) mentionne un flux Hα de $\sim 5 \times 10^{-15}$ erg s^{-1} cm^{-2} arcsec^{-2} pour la portion la plus émissive de NGC 595.

Finalement, le lecteur pourra noter qu'une nouvelle génération de détecteurs alliant à la fois la sensibilité et le faible bruit de lecture des caméras IPCS et l'efficacité quantique élevée des détecteurs CCD voit actuellement le jour à l'Université de Montréal (Daigle *et al.* 2008).

4.3 Réduction et dépouillement des données

4.3.1 Calibration et correction de phase

À la section 4.1.2, nous avons démontré les possibiliés intéressantes engendrées par l'utilisation d'un IFP dans le but de conduire des observations optiques à haute résolution spectrale. La première étape du protocole d'observations revient à obtenir une série de N interférogrammes formant le cube d'étalonnage d'une source monochromatique de longueur d'onde connue située à même le montage expérimental du télescope. La calibration astronomique est essentielle afin de (1) estimer la finesse effective de l'IFP, (2) convertir les unités internes de l'IFP en unités astronomiques physiques et analysables et (3) quantifier la réponse intrumentale du détecteur.

Tout d'abord, les raies d'émission fines, stables et intenses des lampes d'étalonnage sont utilisées afin de quantifier [approximativement] la finesse effective de l'IFP employé. Selon l'équation (4.15), la largeur du profil de calibration dicte le nombre de pas N devant être couvert en mode observation afin de satisfaire au critère de Nyquist et d'échantillonner adéquatement l'ISL. Notez que la finesse effective, obtenue par l'entremise du cube d'étalonnage, est une valeur moyennée sur la surface du détecteur et ne tient donc pas compte du gradient centre-bord engendré par la dispersion angulaire (voir section 4.3.2). Ceci justifie donc le choix d'une constante de proportionnalité plus ou moins constante entre N et $\mathcal{F}_e$ à l'équation (4.15).

De plus, la calibration est essentielle puisqu'elle permet d'associer à chaque pas i, des interférogrammes d'observations, une longueur d'onde spécifique. Ceci découle de l'obtention de la carte de phase à partir du cube d'étalonnage (Atherton *et al.* 1982; Bland & Tully 1989). De l'équation (4.2), l'on remarque que, pour un pixel donné sur le détecteur, une variation de δh dans l'espacement des lames provoque une variation de phase $\delta \rightarrow \delta + d\delta$. De ce fait, chaque pixel, selon sa position radiale, correspondra nécessairement à un maximum de transmission au cours d'un des N pas nécessaires au balayage de l'ISL. Le « mouvement » d'une frange brillante, d'un pas à l'autre, revient à tracer une surface d'isophase à l'intérieur du cube de calibration. Cette surface (ou carte de phase), exprimée en fonction de l'espacement entre les lames de l'IFP, est indépendante de la longueur d'onde de la source d'étalonnage et peut donc être appliquée à une série d'observations obtenues à l'aide du même montage, indépendamment de la longueur d'onde observée. Spécifiquement, l'application de la carte de phase permet de déplacer chaque profil d'émission des interférogrammes d'observations du nombre de pas nécessaire afin de générer une série de N images monochromatiques de l'objet visé. L'espacement en longueur d'onde entre chaque carte bidimensionnelle correspond au « saut » de pas $\delta\lambda$. Leur combinaison permet l'obtention du cube d'observations formé de deux dimensions spatiales (α, δ) et d'une dimension spectrale (λ).

Le logiciel ADHOCw (Laval *et al.* 1987), utilisé lors de l'acquisition au télescope (voir section 4.2), permet également d'effectuer toutes les étapes de la réduction de données jusqu'à l'obtention du cube d'observations (voir section 7.5). Une procédure IDL (de l'anglais *Interactive Data Language*), possédant des caractéristiques similaires[3] à ADHOCw, aura de plus été mise à notre disposition (Daigle *et al.* 2006, voir sections 5.5 et 6.5). Il semblerait, par contre, que la procédure montréalaise montre des déficiences majeures lorsque les données brutes renferment deux (ou plusieurs) raies d'émission présentes dans différents ordres d'interférence (e.g., le doublet du soufre en [S II] ; voir section 7.5). Au moment d'écrire ces lignes, cette problématique demeurait toujours à être éclaircie. Pour des observations spectro-interférométriques dites plus « simples » (e.g., Hα), les deux outils de dépouillement sont parfaitement équivalents. Mention honorable, en particulier, à la la procédure IDL qui permet un réalignement spatial automatisé des étoiles du champ de vue d'un cycle à l'autre.

---

[3] Notez que cette procédure permet uniquement d'effectuer la réduction de données, et non l'acquisition au télescope.

L'auteur de ce manuscrit encourage fortement son utilisation lorsqu'une seule raie est observée à la fois.

4.3.2 Ajustement de gaussiennes

L'élargissement naturel et collisionnel d'une raie spectrale mène à une distribution lorentzienne en intensité alors que l'élargissement thermique produit une distribution gaussienne (Gill 1965, Chapitre 10). La convolution de ces deux distributions mène à une fonction de Voigt (Rees 1989, Chapitre 5). Le profil de Voigt montre des tendances gaussiennes depuis la hauteur maximale du pic jusqu'à environ 3σ où σ est la dispersion de la raie observée (Thorne 1974, Chapitre 7). Pour cette raison, la totalité des raies d'émission, optiques et radios, présentées dans cette thèse auront été ajustées exclusivement par une distribution de forme gaussienne. L'avantage principal de la procédure d'ajustement IDL, utilisée à cet égard, réside dans l'option « multi-composantes ». Plusieurs composantes gaussiennes peuvent alors être ajustées pour un profil de vitesse donné. Ceci est particulièrement utile dans le cas de raies d'émission dédoublées et pour les observations Hα où certaines raies contaminantes de l'atmosphère terrestre se retrouvent à l'intérieur de l'intervalle en longueur d'onde balayé par l'IFP. Ces raies, dont les longueurs d'onde (et donc les valeurs de pas correspondants) sont connues, doivent nécessairement être ajustées individuellement afin d'éviter les distorsions spectrales de la raie nébulaire observée. La procédure IDL renvoie l'amplitude (en unité de comptes), la position du centroïde de vitesse (en unité de pas) et la dispersion (en unité de pas) de chaque composante ajustée. Notez que ce manuscrit considère qu'une composante ajustée est jugée comme fiable si et seulement si son rapport signal-sur-bruit est supérieur à trois. Les diverses composantes, d'un profil de vitesse donné, montrant des rapports signal-sur-bruit inférieurs sont automatiquement rejetées de l'analyse cinématique.

Les vitesses radiales sont estimées par décalage Doppler, utilisant la valeur du pas correspondant au centroïde de vitesse convertie en longueur d'onde d'émission. Les vitesses sont extraites utilisant la convention optique de calcul des vitesses malgré que données optiques et radio soient fréquemment comparées cinématiquement. Les équations (4.16a) et (4.16b) nous indiquent que la différence cinématique entre les deux conventions, optique et radio, est directement proportionnelle à la différence entre longueurs d'onde d'observation et théorique :

$$\text{Convention optique} \longrightarrow \frac{\lambda_{\text{obs}} - \lambda_{\text{rest}}}{\lambda_{\text{rest}}} = \frac{v_{opt}}{c}, \tag{4.16a}$$

$$\text{Convention radio} \longrightarrow \frac{\lambda_{\text{obs}} - \lambda_{\text{rest}}}{\lambda_{\text{obs}}} = \frac{v_{rad}}{c}, \tag{4.16b}$$

où λ_{obs} et λ_{rest} sont respectivement les longueurs d'onde d'observation et celle de la raie au repos (théorique) et v_{opt} et v_{rad} sont les vitesses géocentriques de l'objet en mouvement calculées par décalage Doppler et obtenues respectivement par convention optique et radio. La vitesse de la lumière est donnée par c. Pour des objets relativement « locaux » comme ceux présentés aux chapitres 5 à 7, la différence entre λ_{obs} et λ_{rest} est de l'ordre de quelques angströms tout au plus. La conversion en vitesse radiale nous montre que v_{opt} et v_{rad} diffèrent, pour les cas les plus extrêmes, par environ 0.1 km s^{-1}, bien en deçà des incertitudes cinématiques typiquement observées (e.g., voir Tableau 5.3).

Les vitesses radiales géocentriques sont corrigées afin d'être exprimées dans le référentiel cinématique local standard (LSR, de l'anglais *Local Standard of Rest*). Ce référentiel tient compte de la rotation de la Terre sur elle-même, de la révolution de cette dernière autour du Soleil et du mouvement de ce dernier autour du centre galactique. Le mouvement solaire standard est estimé à 19.5 km s^{-1} dirigé vers $\alpha_{1900} = 18^h00^m00^s$ et $\delta_{1900} = 30°00'00''$. La correction LSR est dépendante de la position (α, δ) de l'objet observé.

Les largeurs (dispersions) de raie observées (σ_{obs}) sont traitées en supposant une contribution quadratique de chaque mécanisme pouvant participer à l'élargissement. Ainsi, :

$$\sigma^2_{non-th} = \sigma^2_{\nabla} + \sigma^2_{turb} = \sigma^2_{obs} - \sigma^2_{th} - \sigma^2_{instr} - \sigma^2_{nat}, \tag{4.17}$$

où σ_{non-th} est la largeur de raie non-thermique, corrigée pour l'élargissement thermique (σ_{th}), la réponse instrumentale (σ_{instr}) et l'élargissement naturel (σ_{nat}) selon le cas. L'élargissement thermique quantifie les mouvements maxwelliens des ions à l'intérieur de la nébuleuse et dépend, entre autres, de la température électronique du plasma ionisé. La réponse instrumentale du détecteur employé est estimée par la dispersion de la raie d'étalonnage (voir section 4.3.1). Or, la dispersion angulaire de l'IFP augmente avec l'angle d'incidence. Ceci se traduit par un rétrécissement des anneaux d'interférence en périphérie du détecteur (voir Figure 4.3). Le champ de vue utilisable est, de ce fait, limité par la dispersion angulaire ; pour tout montage, il existera un angle d'incidence θ_{max} au-delà duquel les franges brillantes, au niveau du détecteur, deviennent si fines que la variation en longueur d'onde enregistrée à l'intérieur d'un pixel de dimension finie excèdera la résolution spectrale de l'instrument. Cette variation centre-bord de la finesse effective sur la surface du détecteur demande alors une estimation pixel-à-pixel du profil instrumental plutôt qu'une valeur moyennée sur le champ de vue. Pour notre étude, l'élargissement naturel est associé exclusivement à la raie Hα, ne s'appliquant pas à l'état métastable des atomes excités à l'origine des transitions interdites (Dyson & Meaburn 1971). Les largeurs de raie non-thermiques (ou corrigées) indiquent les contributions cinématiques associées aux mouvements le long de la ligne de visée ; le terme σ_{∇} est associé aux gradients de vitesse radiale et σ_{turb}, à la turbulence isotrope dans la nébuleuse. Il est possible d'estimer approximativement les contributions relatives de ces deux termes à partir d'une connaissance accrue de l'objet étudié.

Deuxième partie

II. Publications scientifiques

"Science without religion is lame.
Religion without science is blind."
- Albert Einstein, *Physicist and Genius*

Chapitre 5

Cinématique du gaz ionisé associé à W4 $(0^\circ \leqslant b \leqslant 3^\circ)$

Sommaire

Référence : Lagrois, D., & Joncas, G. 2009a, *ApJ*, 691, 1109

Titre original : *On the Dynamical Evolution of H*II *Regions : an Investigation of the Ionized Component of W4, a Galactic Chimney Candidate. I. Kinematics and Dynamics in the Latitude Range* $0^\circ \leqslant b \leqslant 3^\circ$.

Cet article traite de la portion sud de W4 dans l'intervalle en latitude de $b = 0°$ à $b = 3°$. L'article fut soumis le 20 décembre 2007 et accepté pour publication le 2 octobre 2008. Le manuscrit, tel que présenté au chapitre 5, parut dans l'édition du $1^{\underline{\text{er}}}$ février 2009 de *The Astrophysical Journal.*

5.1 Résumé

L'interférométrie Fabry-Pérot fut utilisée afin d'obtenir un relevé Hα de la portion la plus émissive de W4, une superbulle/région H II géante située dans le bras de Persée. Présentée par Normandeau et collaborateurs comme une cavité H I pointant en direction opposée au plan galactique, cette pénurie de gaz atomique fut morphologiquement interprétée comme une candidate de cheminée dynamique en interaction avec la couronne galactique. Nous présentons les résultats cinématiques d'environ cinq millions de spectres d'émission Hα obtenus dans la portion sud de la nébuleuse ($0° \leqslant b \leqslant 3°$). Plusieurs gradients de vitesse radiale à petite échelle sont détectés dans la composante ionisée interne et sont attribués à la photoionisation de denses fragments, habituellement moléculaires, présents à l'intérieur ou en périphérie de la supercoquille en expansion. La vitesse moyenne LSR associée à notre relevé Hα est de -42.565 ± 5.204 (1σ) km s^{-1}, décalée vers le rouge d'environ 5 km s^{-1} par rapport au matériel moléculaire détecté dans le voisinage de la superbulle. L'investigation des largeurs de raie Hα montre que W4-sud correspond à un cas intermédiaire entre les régions H II galactiques de petite taille caractérisées par des valeurs relativement faibles de dispersion et les largeurs de raie supersoniques associées aux structures extragalactiques supergéantes. Caractérisée par plus d'une dizaine d'écoulements gazeux indépendants s'entrecroisant dans la nébuleuse, la cinématique globale de W4-sud est en accord avec la phase Champagne décrivant l'évolution dynamique des régions H II. Pour la première fois, un écoulement Champagne est observé se terminant à même la nébuleuse, se mélangeant avec le gaz ionisé environnant. La nature (moléculaire vs atomique) de la composante neutre, susceptible d'être érodée, est une caractéristique critique puisqu'elle mène à des interprétations cinématiques bien différentes. W4-sud nous apparaît comme un exemple idéal montrant les derniers stades évolutifs d'un complexe moléculaire géant.

5.2 Abstract

Fabry-Perot interferometry was used to obtain an Hα survey of the most emissive part of W4, a giant superbubble/H II region located in the Perseus arm. Presented by Normandeau and colleagues as an H I cavity aiming away from the Galactic plane, the void has been morphologically interpreted as a Galactic chimney candidate in interaction with the Galactic corona. We present the kinematical results of nearly five million Hα spectra obtained in the southern portion of the nebula ($0° \leqslant b \leqslant 3°$). Many small-scale radial velocity gradients are detected in the embedded ionized component and are attributed to the photoionization of dense, mostly molecular, fragments found either in or at the periphery of the expanding supershell. The mean LSR radial velocity associated with our Hα survey is found at -42.565 ± 5.204 (1σ) km s^{-1}, redshifted by roughly 5 km s^{-1} from the molecular material found in the vicinity of the large superbubble. Investigation of the Hα line-width measurements has shown W4-south to fall in a transient regime between low velocity dispersions characteristic of small-size Galactic H II regions and supersonic line widths associated with supergiant extragalactic structures. The overall kinematics of W4-south is best explained with the Champagne model for the dynamical evolution of H II regions where at least 10 independent gas flows crisscross the nebula. For the first time, a Champagne flow is seen coming to an end within a nebula, mingling with the surrounding ionized gas. The nature (molecular vs. atomic) of the neutral material, prone to erosion, is critical as it leads to much different kinematical interpretations. W4-south appears as a text book example of the last stage in the life of a giant molecular cloud complex.

5.3 Introduction

Most spiral galaxies are known to be embedded into a hot and ionized gaseous component forming galactic coronae. Introduced by Spitzer (1956) and later confirmed by high-latitude observations (Yentis *et al.* 1972), this tenuous hot ionized medium (HIM) was also found in a sizeable proportion near the Galactic mid-plane (Jenkins & Meloy 1974) making the old two-phase interstellar medium (ISM) model proposed by Field *et al.* (1969) inadequate. Considering the low-latitude X-ray emission, McKee & Ostriker (1977) proposed the now accepted three-phase ISM model in which the HIM component takes a significant role in the pressure equilibrium.

Highly energetic mechanisms, such as strong stellar winds from massive star clusters and supernova (SN) blast waves, are held responsible for the detection of such a hot plasma at the Galactic plane level. However, the low-latitude constraint associated with these mechanisms forced the scientific community to investigate on different possibilities in order to explain the high-latitude observations. In fact, typical cold corona stars do not have a significant impact, either kinematical or thermal, on the ISM material in their vicinity. Therefore, nonlocal mechanisms were priorized in order to provide energetic feeding able to sustain the ionization of the Galactic corona.

Chevalier & Gardner (1974) presented numerical modelizations of SN remnants in expansion through a stratified Galactic atmosphere where both the particle density and the pressure of the upstream ISM material were meant to exponentially decrease with latitude (Heiles 1991; Dickey & Lockmann 1990). It was found that powerful SNe, located slightly above or under the Galactic mid-plane, can generate ovoid shells likely to be accelerated through the ISM density gradient. The largest features were seen having their hot embedded material discharged at the corona level. Norman & Ikeuchi (1989) used the expression "Galactic chimneys" to refer to these collimated and highly elongated structures in which energetic photons can easily travel. The authors estimated the number of Galactic chimneys throughout the Milky Way required to explain the high-latitude observations to be a thousand. Unfortunately, Galactic plane surveys (Normandeau *et al.* 1997; McClure-Griffiths *et al.* 2001) have not shown the anticipated number of supershells. Even though promising candidates (Müller *et al.* 1987; Callaway *et al.* 2000; McClure-Griffiths *et al.* 2000, 2006) have already been identified in the radio regime, a high resolution kinematical investigation of the ionized interior of a Galactic chimney candidate yet remains to be accomplished.

Being born mainly in the Galactic plane, H II regions showing large amounts of molecular material, successive generations of massive star clusters through triggering and OB associations are also prime candidates for investigation. Under such conditions, large ovoid H II regions should show ionized gas velocity and density gradients pointing toward the Galactic corona. If such gradients remain undetected, the so-called Champagne phase (Tenorio-Tagle 1979) presents an interesting alternative in order to explain and quantify the dynamical evolution of large H II regions. This model is based on the pressure difference between the freshly photoionized material (at the periphery of dense neutral features exposed to the UV flux of nearby hot stars) and the ambient ISM. Numerical simulations (Bodenheimer *et al.* 1979; Tenorio-Tagle & Bedjin 1981; Tenorio-Tagle *et al.* 1982; Franco *et al.* 1990) predict well-defined linear velocity gradients as the ionized material is carried away from the pressure discontinuity. Each gradient peaks at an end velocity dependent on the pressure discontinuity (Bodenheimer *et al.* 1979). For large pressure contrasts ($n_{\rm cloud}/n_{\rm inter\text{-}clouds} > 1000$), the end velocity is estimated slightly above 30 km s^{-1} with respect to the eroded feature (this is obtained assuming a speed of sound of roughly 10 km s^{-1} in the ambient ISM). The maximal velocity gradient of the Champagne phase is estimated at 3-5 km s^{-1} pc^{-1} (Bodenheimer *et al.* 1979). Modelizations have shown larger line widths down the Champagne flow as the ionized material is accelerated away (Cyganowski *et al.* 2003). This tendency toward line broadening could be partially related to line splitting observed in theoretical Champagne flows (Yorke *et al.* 1984). Interferometric observations of small-size (2-30 pc) Galactic H II regions (Joncas & Roy 1984; Miville-Deschênes *et al.* 1995; Godbout *et al.* 1997; Barriault & Joncas 2007) have shown complicated radial velocity fields in agreement with the Champagne phase. Alternately, the blister model (Hester *et al.* 1996), mainly governed by the photoionization of photoevaporative flows, was also proposed to explain the evolution of H II regions. The model predicts ionized flows characterized by nonlinear velocity gradients and surprisingly small H II regions that remain relatively close to the boundaries of the associated molecular cloud (Henney *et al.* 2005). This is explained from the blister model being nonhydrodynamic. For a relatively old H II region showing an ionized extension many times larger than the dimensions covered by the molecular material, the blister model is apparently inadequate (Barriault & Joncas 2007).

We chose to study the kinematical behavior of the giant superbubble/H II region W4, one of the few identified Galactic chimney candidates. Our aims are to (1) determine whether large gas flows are present, (2) quantify the role of stellar winds and UV photons in the photoevaporation of the neutral material, (3) verify if the Champagne phase plays a sizeable role on observed kinematics, (4) investigate if the chimney walls have any kinematical impact, and (5) determine how successive stellar generations have impacted the evolution of the chimney. Our findings suggest that we address this investigation in two sequential papers.

In Section 5.4, previous work associated with the H II region W4 is presented. Our description mainly focuses on the southern portion of W4 ($0° \leqslant b \leqslant 3°$, hereafter W4-south) while the second paper to follow (Lagrois & Joncas 2009b, hereafter Paper II) will investigate the kinematics of the ionized material found at northern latitudes ($3° < b \leqslant 7°$, hereafter W4-north). After a brief description of the data acquisition and reduction techniques in Section 5.5, in Section 5.6, we provide the results of our Fabry-Perot Hα survey. Particular areas of the large W4-south region were priorized in order to favor an investigation of the molecular clumps found embedded or at the periphery of the expanding supershell. In Section 5.7, the time-dynamical evolution of W4-south is discussed through kinematical analysis and interpretation associated with nearly five million Hα spectra. From our kinematical investigation, a spatial scenario of W4-south is proposed in Section 5.8 while summarized results are presented in Section 5.9.

5.4 The W4 superbubble

Introduced by Westerhout (1958) as an irregular nebula of medium brightness, the H II region W4 is often referred to as the Heart nebula due to the heart-shaped morphology of its southern hemisphere ($0° \leqslant b \leqslant 1°$). It is suggested that outflows from the OB association IC 1805 ($l = 134\overset{\circ}{.}8$, $b = 0\overset{\circ}{.}9$) are responsible for the actual superbubble's expansion (Basu *et al.* 1999). Proper motion investigation has allowed the identification of 126 stars intrinsic to the star cluster (Shi & Hu 1999). The authors confirmed, through spectroscopic observations, the presence of numerous massive stars ; about 40 from spectral types O4 to B2 (including 10 O-type stars) have been identified with a high probability of membership. An important proportion of these massive stars is still found on the main-sequence branch indicating a very young cluster age evaluated at 2.5 Myr (Llorente de Andrés *et al.* 1982).

UBV photometry, properly corrected for absorption, puts IC 1805 at a heliocentric distance of 2.35 kpc (Massey *et al.* 1995). Using 8.5 kpc as the distance between the Galactic center and the Sun, we obtained a galactocentric distance of 10.29 kpc for the star cluster. The CGPS obtained spectroscopic 21 cm line observations across the W3/W4/W5 complex in order to quantify both the emission and the kinematics of the atomic hydrogen (Normandeau *et al.* 1997). The CGPS-mosaicked data cube covers almost 40 deg^2 on the plane of the sky in the longitude and latitude ranges from 131° to 139° and from $-1°$ to 5°, respectively. The W4 region takes the form of an impressive, elongated H I cavity aiming at the Galactic corona. The void is centered on a LSR radial velocity range between -38.46 and -45.05 km s^{-1} (West *et al.* 2007). The large H I supershell was presented as being slightly tilted toward the observer (Normandeau *et al.* 1996).

Low-latitude ($b \leqslant 1.^{\circ}5$) far-infrared and radio observations have shown tenuous ionized material beyond the shell boundary that was interpreted as evidences for the percolation of UV photons (Terebey *et al.* 2003). The authors proposed the southern hemisphere of W4 to lie in a transitional state where particular density-bounded segments can be found on the shell path while the densest emissive clumps seem to energetically confine the H II region.

Dennison *et al.* (1997) obtained, through narrow-band Hα imaging, a 10° diameter view of the W4 superbubble. The photoionization of the neutral ISM material, compressed by the outer shock wave, induces an emissive Hα counterpart observed on the inner side of the H I supershell. We will, therefore, refer to the W4 supershell as being semineutral, semi-ionized. Considering the apparent dimensions of the superbubble, the authors proposed a timescale formation of roughly 6-10 Myr (about three times the estimated age of the star cluster) and assumed a succession of many star generations in order to have formed the W4 superbubble. Very few Hα features seem to be observed trapped inside the supershell, the ionized mixture being mostly diffuse. Since the compressive outer shock wave is meant to leave very little material behind it (Henny *et al.* 1999, Chapter 12), we assume the inner diffuse component to be mostly formed of stellar winds and eroded shell/molecular cloud material.

Observations at the James Clerk Maxwell Telescope (JCMT) of the CO (2-1) transition have revealed two elongated cometary clouds, still found embedded in the W4 superbubble, whose remarkable alignment, pointing toward the star cluster IC 1805, provided clues that the UV flux and the mechanical action of stellar winds portrayed the actual shape of the molecular features (Taylor *et al.* 1999). Based on well-detected radial velocity gradients, the authors proposed spatial scenarios where, in the first case, the southern fragment G134.9+1.4 is located behind the star cluster moving away toward the rear side of the superbubble. Dennison *et al.* (1997) particularly noticed a bright Hα filament roughly $0.^{\circ}5$ above the star cluster and extending from the western side of G134.9+1.4. The authors interpreted the filament as the anticipated ionized component resulting from the interaction between the cloud fragment and the UV flux of the star cluster. Secondly, the overall kinematics of G134.9+1.4 and the northern cloud fragment, G134.6+1.9, are said to be roughly similar if, inversely, the latter one is located in front of the star cluster. The reader is referred to Figure 5.1, presenting a schematic view of W4-south, in order to visualize the location of the different structures. The smaller H II region W3 and the SN remnant HB3 were added to the W4 superbubble, as shown in Figure 5.1. Aside from the two cometary clouds, observations of the CO (1-0) transition have also

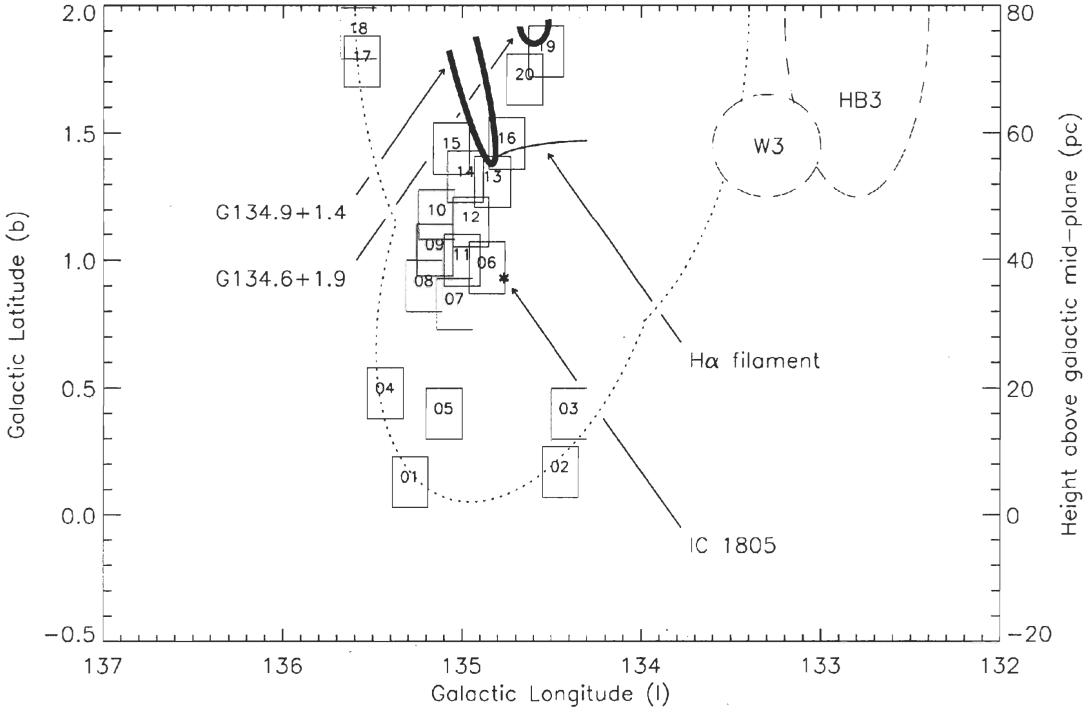

Figure 5.1: Schematic diagram of W4-south.

*The numbers coincide with the optical centers of the 20 gathered Hα fields. Boxes enclosed the area covered by each field. The dotted line is related to the semineutral, semi-ionized W4 supershell while thick solid lines and the regular bold line are associated, respectively, with the CO (2-1) transition emission of the two embedded (large) molecular fragments and the thin Hα filament. Also included are the H*II *region W3 and the SN remnant HB3 (long-dashed lines).*

provided evidences of numerous molecular fragments still found in the W3/W4/W5 star-forming complex (Heyer *et al.* 1998). A contour plot extracted from the Five College Radio Astronomy Observatory (FCRAO) CO (1-0) survey of the second Galactic quadrant is added to the large-scale view of the Hα emission in W4-south, as shown in Figure 5.2. Compressed clumps of molecular material can be seen at the periphery of the expanding southern supershell. Thin fragments, confined inside the shell, are also detected east of the star cluster. The contours are traced out between 5 and 40 K km s^{-1} with a spacing of 5 K km s^{-1}.

In order to estimate the kinematical impact attributed to the photoionization of these neutral structures and their role played on the dynamical evolution of the H II region, an Hα survey via Fabry-Perot interferometry was carried out on the embedded ionized component found in W4-south.

5.5 Observations and data reduction

Hα observations were performed between 2003 and 2007 using the Ritchey-Chrétien 1.6 m telescope of the Observatoire du mont Mégantic (OmM). The data were gathered using the Fabry-Perot of New Technology for the Observatoire du mont Mégantic (FaNTOmM) device system composed of a f/2 focal reducer, a Fabry-Perot Interferometer (FPI), and an Image Photon Counting System (IPCS). Both the parallelism and the spacing between the plates of the FPI were monitored using a servo-control system. The finesse varied slightly between observing runs giving spectral resolutions between 0.15 and 0.21 Å channel^{-1}. The central interference order of the FPI was fixed at $m_0 = 765$ for a free spectral range of 8.56 Å centered on the Hα rest frequency. The spectral scanning covers seven interference orders (labeled m_0, $m_{\pm1}$, $m_{\pm2}$, $m_{\pm3}$) for a total range of 60 Å (roughly seven times the free spectral range). Calibration interferograms were obtained using the λ6598.95 Å Ne-line. To isolate the Hα emission from other ionic lines, narrow-band ($\Delta\lambda_{FWHM} = 10$ Å) interference filters, slightly redshifted from λ6562.78 Å in order to compensate for blueshifting effects caused by cold ambient temperatures, were used. Emission attributed to the peripheral scanned orders ($m_{\pm2}$, $m_{\pm3}$) is, therefore, flattened out by the narrow transmissive bands.

The use of the PANORAMIX f/2 focal reducer (Godbout *et al.* 1998) allowed a $12\rlap{.}'3 \times 12\rlap{.}'3$ field of view (FOV) for a spatial resolution of $1\rlap{.}''45$ pixel^{-1}. The IPCS

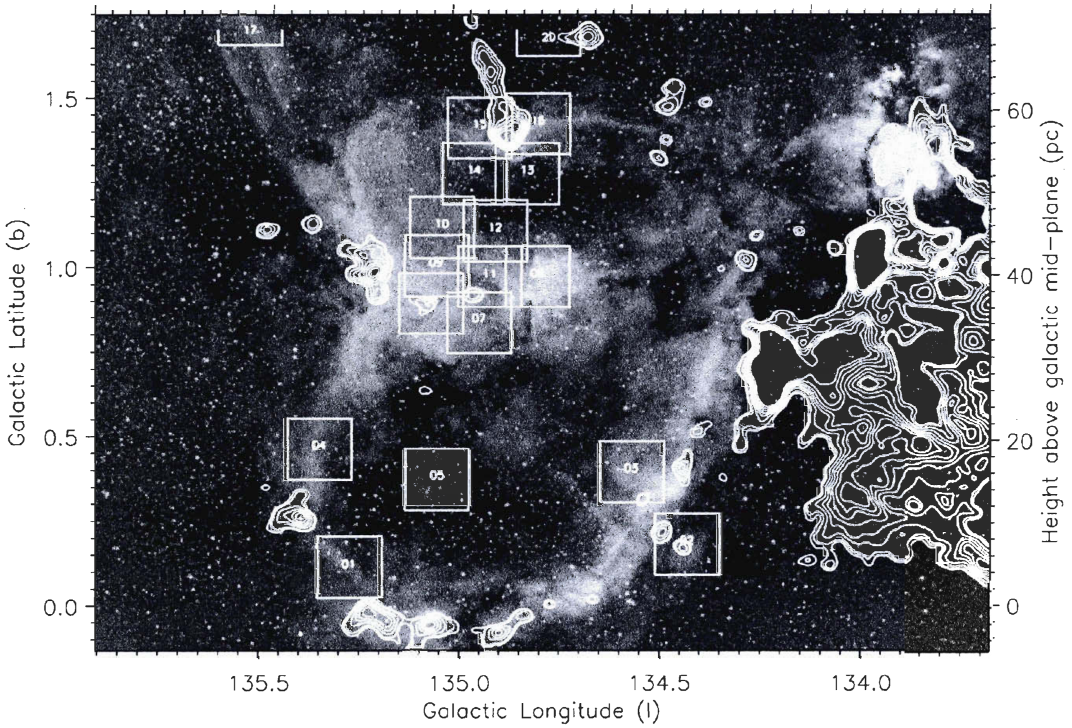

Figure 5.2: Narrow-band imaging of the Hα emission across W4-south. *Courtesy of astro-imager Richard Crisp, the image was taken on 2004 August 27-28, from Castro Valley, CA, USA. A custom 50 mm narrow-band emission line filter was used centered on λ6563.0 Å. The filter had a 30 Å FWHM transmissive band. A 2 hr exposure time was required. A contour plot of the CO (1-0) transition emission in the vicinity of W4-south is added to the Hα image. An integrated intensity map of the molecular emission was extracted from the FCRAO CO (1-0) observations. The spectral collapse of the data cube was made for LSR radial velocities between -22.90 and -63.30 km s^{-1}. Eight contour levels are drawn between 5 and 40 K km s^{-1}. As in Figure 5.1, numbers coincide approximately with the location of the Fabry-Perot observations.*

camera (Hernandez *et al.* 2003) is composed of a Gallium-Arsenide (GaAs) photocathode, a high-voltage intensifier tube, and a regular 1024×1024 CCD. Instead of using the 1024×1024 40 frames per second mode of the CCD, we used the hard binned mode of 512×512 at 80 frames per second. This type of camera differs from other IPCS systems due to the centering work of events done in real time using the ADHOCw[1] software as opposed to a usual hardwiring system. This method allows for very small readout times. Therefore, each channel can be observed numerous times and summed at the end of the acquisition in order to increase the signal-to-noise ratio (S/N) (Gach *et al.* 2002). Combined with the no-readout noise characteristic of IPCS cameras, the FaNTOmM system represents an ideal device to study particularly faint astronomical objects. Exposure times varied according to the particular Hα emission of individual fields. The bright emission associated with targeted regions in the direct vicinity of the star cluster IC 1805 allowed us to obtain reliable kinematical information in approximately 120 minutes. However, farther fields undergoing emission attenuation through flux dilution or due to a simple lack of ionized material required a more important number of cycles in order to obtain acceptable S/Ns. Roughly, 4-5 hr were needed for the faintest fields of our Hα survey of W4-south.

Data reduction was carried out using IDL routines (Daigle *et al.* 2006), specially tailored to reproduce the method used for the TAURUS FP spectrometer (Atherton *et al.* 1982). For each field, computation of the phase map and its application to the observed interferograms allowed us to obtain a three-dimensional (l, b, λ) raw data cube. Sky subtraction has been found to be highly complicated since the dimensions of the superbubble are much larger than those of a single FOV ; night-sky emission was, therefore, not available near the fields' edges, a method typically used for extragalactic observations. In order to subtract from Hα profiles contaminant night-sky lines found in the scanned wavelength interval (Osterbrock *et al.* 1996), a multicomponent Gaussian fit giving the amplitude, spectral position (or radial velocity), and observed line width of each component was applied to each emission spectrum. The minimal S/N allowed for a fitted line was fixed at 3. All radial velocities were measured with respect to the LSR using the optical convention. For close objects like W4, the two conventions, radio or optical, show a difference in radial velocities of the order of a fraction of km s^{-1}, below the typical uncertainty of our velocity measurements (see Section 5.6).

---

[1] http ://www-obs.cnrs-mrs.fr/adhoc/adhoc.html

In order to extract purely kinematical information from Hα line widths, we supposed each contribution to the observed broadening to be approximated by independent Gaussian profiles. Individual widths related to the instrumental and thermal profiles, and the Hα-fine structure, were therefore quadratically subtracted from each observed line width. The latter is discussed by Dyson & Meaburn (1971) with a contribution of 1.37 km s^{-1}. Thermal broadening was obtained for an electronic temperature of 7400 K using the galactocentric electronic temperature gradient for known H II regions (Paladini *et al.* 2004). Finally, the instrumental contribution was taken as the width of the Ne-line calibration profile, also properly corrected for thermal broadening intrinsic to excited neon plasmas (Sáinz *et al.* 2005). The corrected Hα line widths provide the kinematical broadening attributed to turbulence and radial velocity gradients along the line of sight (LOS).

5.6 Kinematical results

Bounded boxes, in Figures 5.1 and 5.2, indicate the location of the FPI observations and the area covered by each field. A total of 20 fields were obtained in order to estimate the kinematical impact of neutral structures (H I walls, molecular clouds embedded inside the supershell or found partially compressed near the outer shock wave) on the ionized gas' overall behavior. The northern boundary of the Hα image used in Figure 5.2 is fixed at $b = 1^{\circ}\!.75$ and, therefore, does not allow to indicate the location of Fields 17-19 (see Section 5.6.2). Due to particularly faint Hα emission found for Fields 05, 19, and 20, we performed a 2×2 spatial binning of each data cube. The remaining fields were kept at their original spatial resolution. A Gaussian kernel with FWHM = 2 pixels has been used as a spatial smoothing filter in order to emphasize structures in the velocity maps.

For each field, Tables 5.1 and 5.2, respectively, present the main results obtained from individual radial velocity and corrected line-width distributions ; mean values ($\langle v_{i,LSR} \rangle$ and $\langle \beta_{i,corr} \rangle$) are presented in Column 3 while standard deviations ($\sigma_{v_{i,LSR}}$ and $\sigma_{\beta_{i,corr}}$) for each distribution are shown in Column 4. Skewness and kurtosis excess are also, respectively, given in Columns 5 and 6. A brief comment related to the location of each field is proposed in Column 7. From now on, the label "i" will be referred to the field's number (e.g., $\langle v_{01,LSR} \rangle$ corresponds to the mean radial velocity observed in Field 01). In Tables 5.1 and 5.2, uncertainties on mean values and one standard deviations correspond to statistical uncertainties (inversely proportional

Table 5.1: **LSR radial velocity investigation in W4-south.**

Field	Optical center (l,b)	$\langle v_{i,LSR} \rangle$ (km s^{-1})	$\sigma_{v_{i,LSR}}$ (km s^{-1})	Skewness	Kurtosis excess	Location
01	(135°.29, 0°.10)	-45.340 ± 0.008	4.017 ± 0.006	0.17	1.06	Southern hemisphere
02	(134°.45, 0°.17)	-43.290 ± 0.009	4.274 ± 0.006	0.63	2.05	Southern hemisphere
03	(134°.62, 0°.40)	-42.895 ± 0.008	4.144 ± 0.006	-0.07	2.21	Southern hemisphere
04	(135°.45, 0°.48)	-42.480 ± 0.009	4.317 ± 0.006	-0.19	3.23	Southern hemisphere
05	(135°.10, 0°.40)	-40.790 ± 0.022	5.529 ± 0.016	-0.55	1.05	Southern hemisphere
06	(134°.81, 0°.95)	-40.781 ± 0.012	5.986 ± 0.008	-0.08	0.32	IC 1805 vicinity
07	(134°.97, 0°.83)	-46.111 ± 0.011	5.343 ± 0.007	0.19	0.69	IC 1805 vicinity
08	(135°.13, 0°.90)	-40.307 ± 0.009	4.798 ± 0.007	0.34	0.49	IC 1805 vicinity
09	(135°.10, 1°.04)	-46.607 ± 0.007	3.754 ± 0.005	0.67	1.31	IC 1805 vicinity
10	(135°.08, 1°.13)	-44.436 ± 0.007	3.589 ± 0.005	0.25	0.70	IC 1805 vicinity
11	(134°.96, 0°.95)	-41.075 ± 0.008	4.029 ± 0.006	-0.08	3.33	IC 1805 vicinity
12	(134°.93, 1°.11)	-40.004 ± 0.009	4.596 ± 0.006	0.26	0.72	IC 1805 vicinity
13	(134°.82, 1°.26)	-45.144 ± 0.009	4.669 ± 0.007	0.48	1.21	G134.9+1.4 fragment
14	(134°.98, 1°.30)	-42.955 ± 0.009	4.403 ± 0.006	-0.09	0.15	G134.9+1.4 fragment
15	(134°.96, 1°.36)	-39.251 ± 0.011	4.094 ± 0.008	0.29	0.57	G134.9+1.4 fragment
16	(134°.80, 1°.40)	-40.789 ± 0.008	4.046 ± 0.006	0.70	1.26	G134.9+1.4 fragment
17	(135°.52, 1°.78)	-40.888 ± 0.009	4.661 ± 0.007	0.17	0.88	W4 eastern wall
18	(135°.65, 1°.89)	-44.751 ± 0.009	4.407 ± 0.006	0.35	0.50	W4 eastern wall
19	(134°.53, 1°.82)	-36.699 ± 0.017	4.185 ± 0.012	0.17	1.24	G134.6+1.9 fragment
20	(134°.72, 1°.69)	-37.202 ± 0.025	6.379 ± 0.018	0.33	0.74	G134.6+1.9 fragment

Table 5.2: Line-width investigation in W4-south.

Field	Optical center (l,b)	$\langle\beta_{i,corr}\rangle$ (km s^{-1})	$\sigma_{\beta_{i,corr}}$ (km s^{-1})	Skewness	Kurtosis excess	Location
01	(135°.29, 0°.10)	8.338 ± 0.007	3.728 ± 0.005	0.03	-0.35	Southern hemisphere
02	(134°.45, 0°.17)	9.062 ± 0.011	5.339 ± 0.007	1.49	2.50	Southern hemisphere
03	(134°.62, 0°.40)	9.761 ± 0.006	2.978 ± 0.004	0.26	2.39	Southern hemisphere
04	(135°.45, 0°.48)	10.933 ± 0.007	3.741 ± 0.005	0.78	1.27	Southern hemisphere
05	(135°.10, 0°.40)	10.972 ± 0.022	5.564 ± 0.016	0.37	-0.35	Southern hemisphere
06	(134°.81, 0°.95)	10.233 ± 0.006	3.032 ± 0.004	0.54	0.92	IC 1805 vicinity
07	(134°.97, 0°.83)	9.493 ± 0.008	3.978 ± 0.006	0.38	-0.35	IC 1805 vicinity
08	(135°.13, 0°.90)	9.535 ± 0.006	2.958 ± 0.004	0.19	0.28	IC 1805 vicinity
09	(135°.10, 1°.04)	7.412 ± 0.004	1.918 ± 0.003	-0.28	0.42	IC 1805 vicinity
10	(135°.08, 1°.13)	8.080 ± 0.003	1.688 ± 0.002	0.01	0.54	IC 1805 vicinity
11	(134°.96, 0°.95)	5.795 ± 0.004	2.224 ± 0.003	-0.03	-0.06	IC 1805 vicinity
12	(134°.93, 1°.11)	8.925 ± 0.004	2.317 ± 0.003	0.10	0.07	IC 1805 vicinity
13	(134°.82, 1°.26)	11.473 ± 0.007	3.420 ± 0.005	0.20	0.28	G134.9+1.4 fragment
14	(134°.98, 1°.30)	10.803 ± 0.005	2.744 ± 0.004	-0.22	0.20	G134.9+1.4 fragment
15	(134°.96, 1°.36)	9.792 ± 0.008	4.047 ± 0.006	0.08	-0.05	G134.9+1.4 fragment
16	(134°.80, 1°.40)	9.328 ± 0.007	3.727 ± 0.005	0.64	1.07	G134.9+1.4 fragment
17	(135°.52, 1°.78)	5.620 ± 0.005	2.323 ± 0.003	0.45	0.95	W4 eastern wall
18	(135°.65, 1°.89)	5.918 ± 0.006	2.991 ± 0.004	0.47	0.34	W4 eastern wall
19	(134°.53, 1°.82)	10.622 ± 0.018	4.449 ± 0.012	0.41	0.42	G134.6+1.9 fragment
20	(134°.72, 1°.69)	12.245 ± 0.017	4.251 ± 0.012	0.02	-0.12	G134.6+1.9 fragment

to $\sqrt{N}$, where N is the number of events in each distribution). Kinematical uncertainties, for each radial velocity and corrected line-width point, were also calculated with the method proposed by Lenz & Ayres (1992). For each field, histograms of the kinematical uncertainties have mainly shown Poissonian characteristics. Table 5.3 presents the mean uncertainties, for radial velocities and line-width measurements respectively in Columns 2 and 3, extracted from the different distributions.

The FPI observations were carried out to investigate five different portions of W4-south : the southern hemisphere (Fields 01-05), the star cluster vicinity (Fields 06-12), the molecular cloud fragment G134.9+1.4 (Fields 12-16), the W4 eastern wall at intermediate latitudes (Fields 17 and 18), and the molecular cloud fragment G134.6+1.9 (Fields 19 and 20). Sections 5.6 and 5.7 will be divided into four subsections : (1) a general overview using the kinematical information obtained from our Hα survey taken as a whole followed by localized investigations of the ionized gas' kinematical behavior in the vicinity of (2) molecular and (3) atomic material. A last subsection will be added to discuss the (4) interflow medium of W4-south.

5.6.1 General overview

Nearly five million Hα spectra were obtained for Fields 01-20. Combined together, distributions for the LSR radial velocities and corrected Hα line widths are, respectively, presented in Figures 5.3 and 5.4. The mean LSR radial velocity is found at $\langle v_{\mathrm{survey},LSR}\rangle = -42.565 \pm 0.002$ km s^{-1}, in agreement with the LSR radial velocity range revealing the H I cavity in the radio regime (see Section 5.4). The standard deviation of the radial velocity distribution is found at $\sigma_v = 5.204 \pm 0.002$ km s^{-1}. The asymmetry coefficient is found at 0.29, an indication for an overabundance of radial velocity points above -35 km s^{-1}. This contributes for a mean radial velocity slightly redshifted from the most probable value of the distribution near -44 km s^{-1}. The distribution has a kurtosis excess of 0.87. Since a perfect Gaussian would show a value of 0, the distribution has extended tails indicating the presence of "extreme" radial velocities in both the red and blue parts.

Figure 5.4 presents the histogram obtained from the investigation of the corrected Hα line widths. A mean dispersion of $\langle \beta_{\mathrm{survey},corr}\rangle = 9.213 \pm 0.002$ km s^{-1} is found, slightly below the sonic regime. This value seems to coincide with an intermediate case scenario between subsonic Hα line widths usually found for Galactic objects and

Table 5.3: Mean kinematical uncertainties in W4-south.

Field	$\langle e_{i,\lambda} \rangle$ (km s^{-1})	$\langle e_{i,\beta} \rangle$ (km s^{-1})
01	0.498 ± 0.001	1.512 ± 0.088
02	0.644 ± 0.001	1.993 ± 0.154
03	0.669 ± 0.002	1.640 ± 0.239
04	0.599 ± 0.001	0.898 ± 0.004
05	0.855 ± 0.003	2.254 ± 0.054
06	0.470 ± 0.001	0.616 ± 0.079
07	0.574 ± 0.002	0.997 ± 0.040
08	0.468 ± 0.001	0.701 ± 0.071
09	0.376 ± 0.001	0.598 ± 0.050
10	0.399 ± 0.001	0.524 ± 0.003
11	0.388 ± 0.001	1.018 ± 0.066
12	0.517 ± 0.002	0.609 ± 0.003
13	0.497 ± 0.001	0.718 ± 0.004
14	0.545 ± 0.001	0.852 ± 0.015
15	0.530 ± 0.001	0.727 ± 0.004
16	0.602 ± 0.001	0.933 ± 0.045
17	0.571 ± 0.002	1.310 ± 0.004
18	0.566 ± 0.001	2.916 ± 0.106
19	1.220 ± 0.003	2.897 ± 0.085
20	0.690 ± 0.002	1.361 ± 0.007

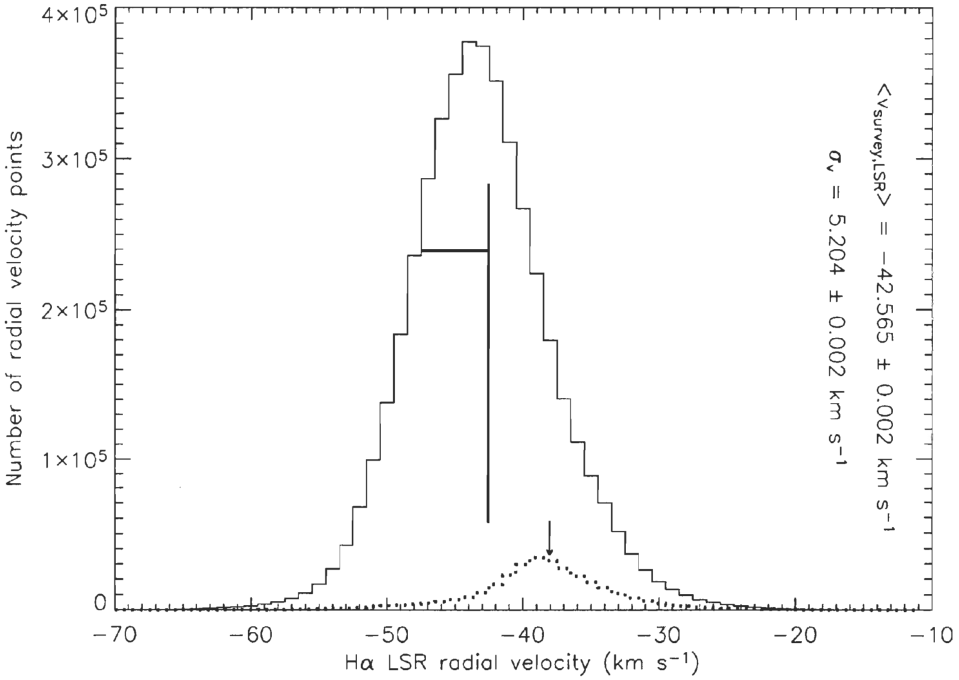

Figure 5.3: Hα LSR radial velocity distribution of W4-south.

Both the mean LSR radial velocity and the statistical standard deviation, found respectively at -42.565 ± 0.002 km s^{-1} *and 5.204 ± 0.002 km* s^{-1}*, are schematically represented by the vertical and horizontal thick solid lines. A slight asymmetry is found with a skewness being estimated at 0.29. The kurtosis excess is found at 0.87. A normal distribution would give a skewness and a kurtosis excess of 0. The dotted histogram corresponds to the LSR radial velocity distribution of the interflow medium of W4-south. The mean of the distribution, estimated at -38.04 ± 0.01 km* s^{-1}*, is indicated by the solid arrow.*

larger, supersonic dispersion values associated with giant extragalactic H II regions (O'Dell & Townsley 1988). The standard deviation of the line-width distribution is found at $\sigma_\beta = 3.889 \pm 0.001$ km s^{-1}. An asymmetry coefficient of 0.66 is obtained, mainly due to a long right tail of dispersion points well above 20 km s^{-1}. However, the left tail stops its progression before reaching 0 count (as would be expected). Actually, about 3% of our Hα spectra (a fraction roughly equivalent to the missing portion of the distribution's left tail) have failed to provide reliable line-width information as the quadratic subtraction method (see Section 5.5) gave $\beta^2_{i,corr} < 0$ km s^{-1}, which is numerically inadequate. These spectra were rejected from both the

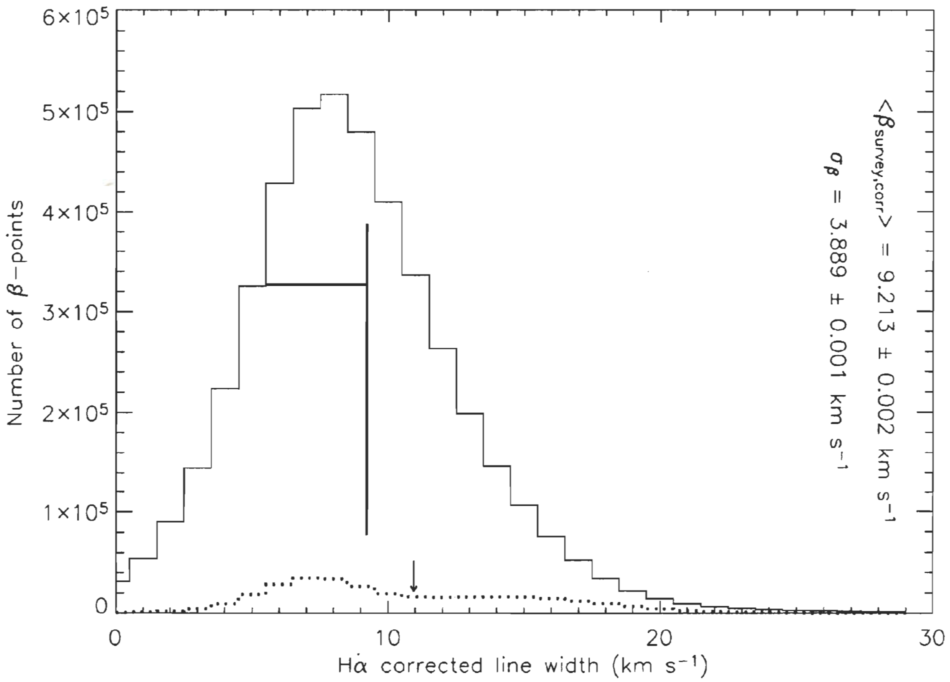

Figure 5.4: Corrected Hα line-width distribution of W4-south.

Both the mean dispersion value and the statistical standard deviation, found respectively at 9.213± 0.002 km s^{-1} *and 3.889± 0.001 km* s^{-1}*, are schematically represented by the vertical and horizontal thick solid lines. The asymmetry coefficient is estimated at 0.65 and the kurtosis excess is found at 1.23. A normal distribution would give a skewness and a kurtosis excess of 0. The dotted histogram corresponds to the corrected H*α *line-width distribution of the interflow medium of W4-south. The mean of the distribution, estimated at 10.95± 0.01 km* s^{-1}*, is indicated by the solid arrow.*

Hα line-width and LSR radial velocity analysis. The two "fat tails" contribute to a kurtosis excess of 1.23.

In the two following subsections, kinematical evidences for numerous radial velocity and line-width linear gradients will be provided. Each flow is labeled from A to X in Column 2 of Table 5.4. The range on which each flow remains well defined (i.e., the distance on the plane of the sky over which the slopes of the radial velocity and line-width gradients remain roughly constant) is presented in Column 4. In the text, end radial velocities and line widths will refer to the radial velocities and line widths observed at the end of these ranges. These values are not presented

Table 5.4: Kinematical investigation of localized ionized flows.

Field	Flow	Figure	Range	LSR radial velocities			Hα line widths		
			(pc)	∇_v (km s^{-1} pc^{-1})	$v_{k,\mathrm{initial}}$ (km s^{-1})	Correlation	∇_β (km s^{-1} pc^{-1})	$\beta_{k,\mathrm{initial}}$ (km s^{-1})	Correlation
01	A	5.5*a*	7.39	-0.31 ± 0.06	-45.13 ± 0.08	-0.92	0.16 ± 0.04	9.30 ± 0.09	0.88
02	B	5.5*b*	2.43	-1.43 ± 0.14	-43.98 ± 0.20	-0.81	0.83 ± 0.12	6.79 ± 0.17	0.75
03	C	5.5*c*	4.74	-0.58 ± 0.04	-44.06 ± 0.10	-0.90	0.56 ± 0.04	9.21 ± 0.12	0.85
04	D	5.5*d*	3.25	1.56 ± 0.19	-44.95 ± 0.49	0.83	2.14 ± 0.05	9.43 ± 0.09	0.93
06	E	5.6	3.25	1.29 ± 0.08	-40.54 ± 0.16	0.92	1.21 ± 0.05	8.36 ± 0.10	0.97
06-07	F	5.6	4.91	-0.85 ± 0.07	-46.39 ± 0.21	-0.87	-1.69 ± 0.05	15.17 ± 0.16	-0.97
11	G	5.6	1.60	1.53 ± 0.27	-43.97 ± 0.25	0.79	-0.87 ± 0.19	8.67 ± 0.18	-0.71
08-09-11	H	5.6	1.27	0.76 ± 0.24	-44.45 ± 0.18	0.66	-0.64 ± 0.21	6.52 ± 0.16	-0.57
09-10	I	5.6	4.91	0.53 ± 0.03	-49.14 ± 0.09	0.92	-0.07 ± 0.05	8.75 ± 0.13	-0.06
09-10	J	5.6	2.43	1.29 ± 0.08	-48.18 ± 0.11	0.95	0.09 ± 0.08	8.03 ± 0.12	0.36
10-14	K	5.6	1.60	2.43 ± 0.23	-47.18 ± 0.21	0.93	0.05 ± 0.17	6.73 ± 0.16	0.05
13	L	5.6	0.69	-2.60 ± 0.27	-45.43 ± 0.11	-0.96	3.62 ± 0.45	12.28 ± 0.19	0.95
13-14-15	M	5.6	1.35	-2.29 ± 0.26	-41.37 ± 0.21	-0.91	1.02 ± 0.06	6.97 ± 0.05	0.97
13	N	5.6	0.78	-2.43 ± 0.17	-45.52 ± 0.08	-0.98	3.16 ± 0.28	11.51 ± 0.13	0.98
13-16	O	5.6	1.35	-1.33 ± 0.09	-43.95 ± 0.07	-0.97	1.57 ± 0.09	8.96 ± 0.07	0.98
16	P	5.6	3.25	-0.09 ± 0.06	-41.96 ± 0.11	-0.30	0.07 ± 0.07	10.20 ± 0.14	0.06
13-14-15	Q	5.6	0.94	-0.57 ± 0.10	-41.81 ± 0.06	-0.88	1.97 ± 0.24	7.12 ± 0.14	0.94
13-14-15	R	5.6	1.11	-1.88 ± 0.30	-42.21 ± 0.20	-0.87	1.46 ± 0.13	6.74 ± 0.09	0.96
17-18	S	5.7	13.01	-0.48 ± 0.04	-39.15 ± 0.30	-0.85	0.11 ± 0.03	5.03 ± 0.24	0.22
17	T	5.7	4.91	1.43 ± 0.08	-44.34 ± 0.22	0.94	0.40 ± 0.04	5.00 ± 0.13	0.73
18	U	5.7	4.91	1.64 ± 0.04	-47.12 ± 0.12	0.98	0.45 ± 0.08	5.89 ± 0.22	0.66
19	V	5.8	2.71	0.12 ± 0.15	-35.52 ± 0.24	0.15	-0.13 ± 0.16	11.74 ± 0.26	-0.15
20	W	5.8	4.87	0.13 ± 0.12	-41.15 ± 0.31	0.19	0.22 ± 0.08	11.18 ± 0.22	0.26
20	X	5.8	2.54	-1.26 ± 0.47	-33.02 ± 0.72	-0.66	0.59 ± 0.11	9.08 ± 0.36	0.79

in Table 5.4 but can be easily derived from the information provided. The radial velocity and line-width behaviors are, respectively, given in Columns 5-7 and Columns 8-10. Table 5.4 provides the steepness of each linear gradient (∇_v and ∇_β), the Y-intercept value for each relation ($v_{k,\mathrm{initial}}$ and $\beta_{k,\mathrm{initial}}$ with k being labeled between A and X in the text), and the Pearson correlation coefficients (Bevington 1969, Chapter 4) derived from least-squares fits applied to the straight lines. For the radial velocity investigation, a radial velocity gradient characterized by a positive (negative) slope will be referred to as a redshifted (blueshifted) tendency with respect to its Y-intercept value, $v_{k,\mathrm{initial}}$, the LSR radial velocity of the ionized gas in contact with the neutral material. Similarly, a positive (negative) slope related to a particular line-width gradient will be associated with a tendency toward line broadening (narrowing) compared to its Y-intercept, $\beta_{k,\mathrm{initial}}$.

Except for Flow S, each flow in Table 5.4 is chosen supposing a probable Champagne flow and is therefore traced out, as far as possible, such that its origin coincides with ionized material in contact with the eroded neutral feature. Table 5.5 presents a comparison in radial velocities between the neutral material (its nature, atomic or molecular, being given in Column 2) and this ionized component, respectively, in Columns 3 and 4. Column 4 corresponds to Column 6 of Table 5.4 except for Flows F, I, J, K, and X where an extrapolation from the origin of each flow to their associated molecular fragment was necessary (see Section 5.6.2). For these flows, the line-width gradient was also extrapolated, giving the new $\beta_{k,\mathrm{initial}}$ values in Column 5. The $\beta_{k,\mathrm{initial}}$ values remain unchanged with respect to Table 5.4 if no extrapolation is necessary. The range on the plane of the sky corresponding to the extrapolation is estimated in Column 6. The source of the radial velocities presented in Column 3 is given in Column 7. All radial velocities in Table 5.5 are measured with respect to the LSR.

5.6.2 Ionized gas' kinematics in the vicinity of molecular material

In order for the reader to identify (spatially) each flow in the context of W4-south, Hα peak intensity maps (i.e., for each pixel, the maximum photon counts obtained from the Gaussian fit procedure once the continuum properly subtracted) have been obtained for each field. Fields enclosing ionized gas flows likely related to the photoerosion of nearby molecular clumps are presented in Figures 5.5*a*-*c*, 5.6,

Table 5.5: Kinematical comparison between the spacially coinciding neutral and ionized material.

Flow[a]	Nature	$v_{k,\mathrm{neutral}}$ (km s^{-1})	$v_{k,\mathrm{initial}}$ (km s^{-1})	$\beta_{k,\mathrm{initial}}$ (km s^{-1})	Extrapolation (pc)	Source
A	Molecular	-44.0	-45.13 ± 0.08	9.30 ± 0.09	–	1
B	Molecular	-45.0	-43.98 ± 0.20	6.79 ± 0.17	–	1
C	Molecular	-46.0	-44.06 ± 0.10	9.21 ± 0.12	–	1
D	Atomic	[-42.0, -46.0]	-44.95 ± 0.49	9.43 ± 0.09	–	2
E	Molecular	-40.0	-40.54 ± 0.16	8.36 ± 0.10	–	1
F	Molecular	-43.0	-44.5	19.0	2.25	1
G	Molecular	-43.5	-43.97 ± 0.25	8.67 ± 0.18	–	1
H	Molecular	-51.0	-44.45 ± 0.18	6.52 ± 0.16	–	1
I	Molecular	[-45.0, -49.0]	-49.8	8.8	1.24	1
J	Molecular	[-45.0, -49.0]	-50.8	7.8	2.06	1
K	Molecular	[-45.0, -49.0]	-50.4	6.7	1.33	1
L	Molecular	[-38.0, -43.0]	-45.43 ± 0.11	12.28 ± 0.19	–	1, 3
M	Molecular	-42.0	-41.37 ± 0.21	6.97 ± 0.05	–	1, 3
N	Molecular	[-38.0, -43.0]	-45.52 ± 0.08	11.51 ± 0.13	–	1, 3
O	Molecular	-42.5	-43.95 ± 0.07	8.96 ± 0.07	–	1, 3
P	Molecular	-41.0	-41.96 ± 0.11	10.20 ± 0.14	–	1
Q	Molecular	-42.5	-41.81 ± 0.06	7.12 ± 0.14	–	1, 3
R	Molecular	-42.0	-42.21 ± 0.20	6.74 ± 0.09	–	1, 3
T	Atomic	[-43.0, -47.0]	-44.34 ± 0.22	5.00 ± 0.13	–	2
U	Atomic	[-43.0, -47.0]	-47.12 ± 0.12	5.89 ± 0.22	–	2
V	Molecular	-37.0	-35.52 ± 0.24	11.74 ± 0.26	–	1, 3
W	Molecular	[-28.0, -32.0]	-41.15 ± 0.31	11.18 ± 0.22	–	1
X	Molecular	[-28.0, -32.0]	-31.0	8.2	1.50	1

Sources : (1) FCRAO CO(1-0) observations (Heyer *et al.* 1998) ; (2) CGPS H I observations (Normandeau *et al.* 1997) ; (3) JCMT CO (2-1) observations (Taylor *et al.* 1999).

---

[a] Flows F, I, J, K, and X required an extrapolation of their origin on a certain range to their associated molecular cloud fragment.

and 5.8, whereas Figures 5.5*d* and 5.7, related to the photoerosion of H I material, will be discussed in Sections 5.6.3 and 5.7.3. The disposition of Fields 06-16, 19, and 20 allows us to obtain mosaicked images for Figures 5.6 and 5.8. Obvious lines of demarcation can be seen separating each field. This is mainly due to differences in exposure times and sky transparency. To avoid confusion, numbers used for field identification were voluntarily omitted in Figure 5.6. The reader can refer to Figures 5.1 and 5.2 to deduce the location of each field in the mosaicked image.

Each flow is properly identified by its appropriate letter (see Tables 5.4 and 5.5). The "slice-of-a-pie" regions enclose the pixels used in the investigation of each flow. Radial velocity and line-width gradients are always measured from "the center" to "the crust". In Figure 5.5, dotted lines indicate the orientation of the ionized shell. The bottom-right corner of Figure 5.6 coincides approximately with the star cluster IC 1805. Thirteen OB stars are drawn from the positions indicated by Massey *et al.* (1995). In many cases, the presence of molecular material (see Figure 5.2) at the origin of particular flows is clearly unmistakable from bright Hα rims pinpointing ionization fronts. Figure 5.9 is added to this work in order to visualize the presence or not of molecular material in the vicinity of Fields 17-19 (all located above the northern latitude of Figure 5.2). Even though Figure 5.2 clearly indicates the presence of molecular clumps, some sections of our FPI observations do not, a priori, show the same characteristic in Hα; the absence of bright rims was mitigated by adding black squares in Figures 5.5*a* and 5.8 at the position of molecular material (estimated from the FCRAO CO (1-0) observations).

The following results exclusively apply to ionized flows presenting a molecular nature in Column 2 of Table 5.5. The behavior in radial velocities has shown well-defined linear gradients pointing away from the individual cloud fragments (see Table 5.4). The kinematical tendency alternates between blueshifted and redshifted. In absolute value, the radial velocity slopes are found between 0.31 and 2.60 km s^{-1} pc^{-1}, all below the maximal Champagne gradient predicted (see Section 5.3). The most common trend is toward line broadening even though Flows F, G, and H, near the star cluster, show a line narrowing behavior (see Table 5.4). The line-width slopes are usually below 2 km s^{-1} pc^{-1} with peak values slightly above 3 km s^{-1} pc^{-1} for Flows L and N in the vicinity of the molecular fragment G134.9+1.4. The $\beta_{k,\mathrm{initial}}$ values, in contact with the molecular material, usually indicate a subsonic regime. However, supersonic values above 10 km s^{-1} are found for Flows L, N, and P, also associated with G134.9+1.4. A similar regime for Flows V and W is also observed near G134.6+1.9.

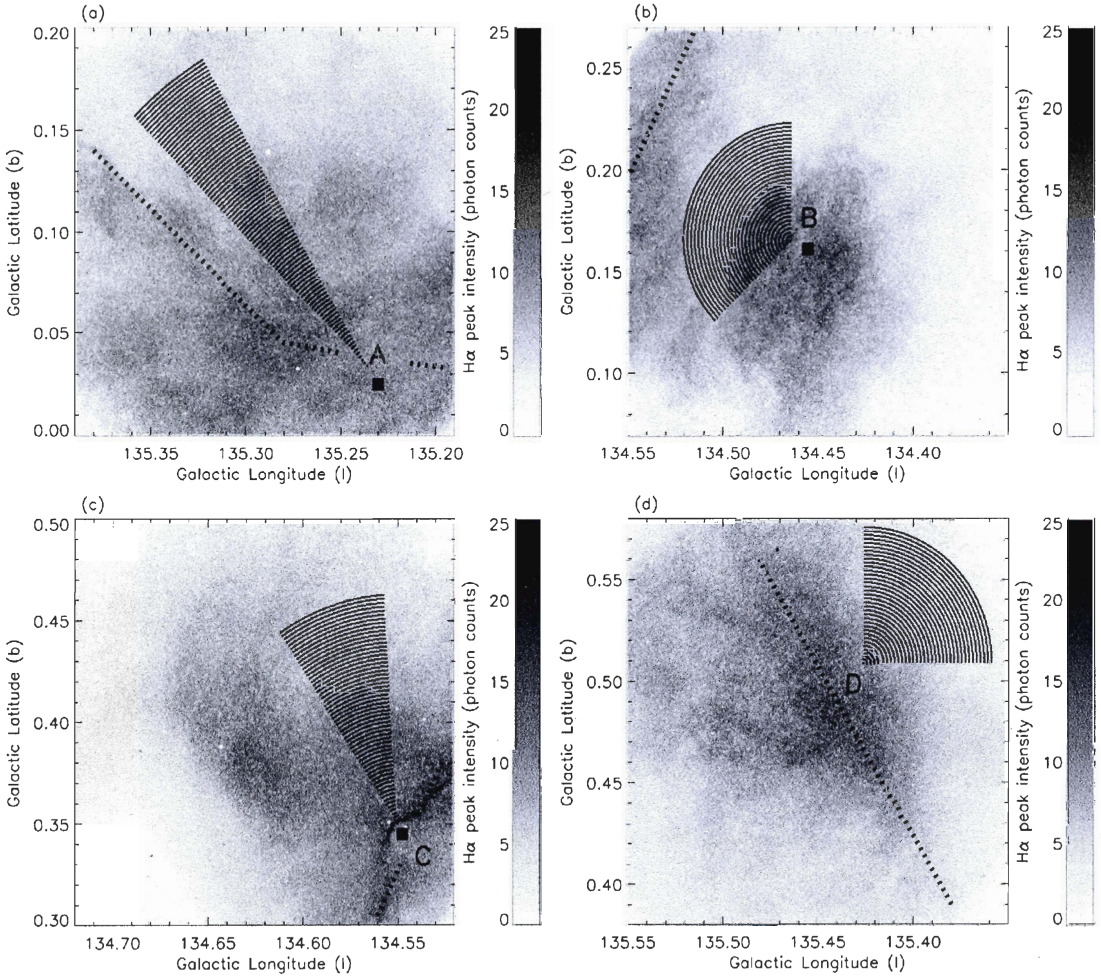

Figure 5.5: Hα peak intensity maps for Fields 01-04.

Hα peak intensity maps for : (a) Field 01, (b) Field 02, (c) Field 03, and (d) Field 04. Areas investigated for Flows A to D are represented by the "slice-of-a-pie" regions. Black filled squares coincide with the location of molecular material according to the FCRAO CO (1-0) observations. The dotted lines indicate the orientation of the ionized shell.

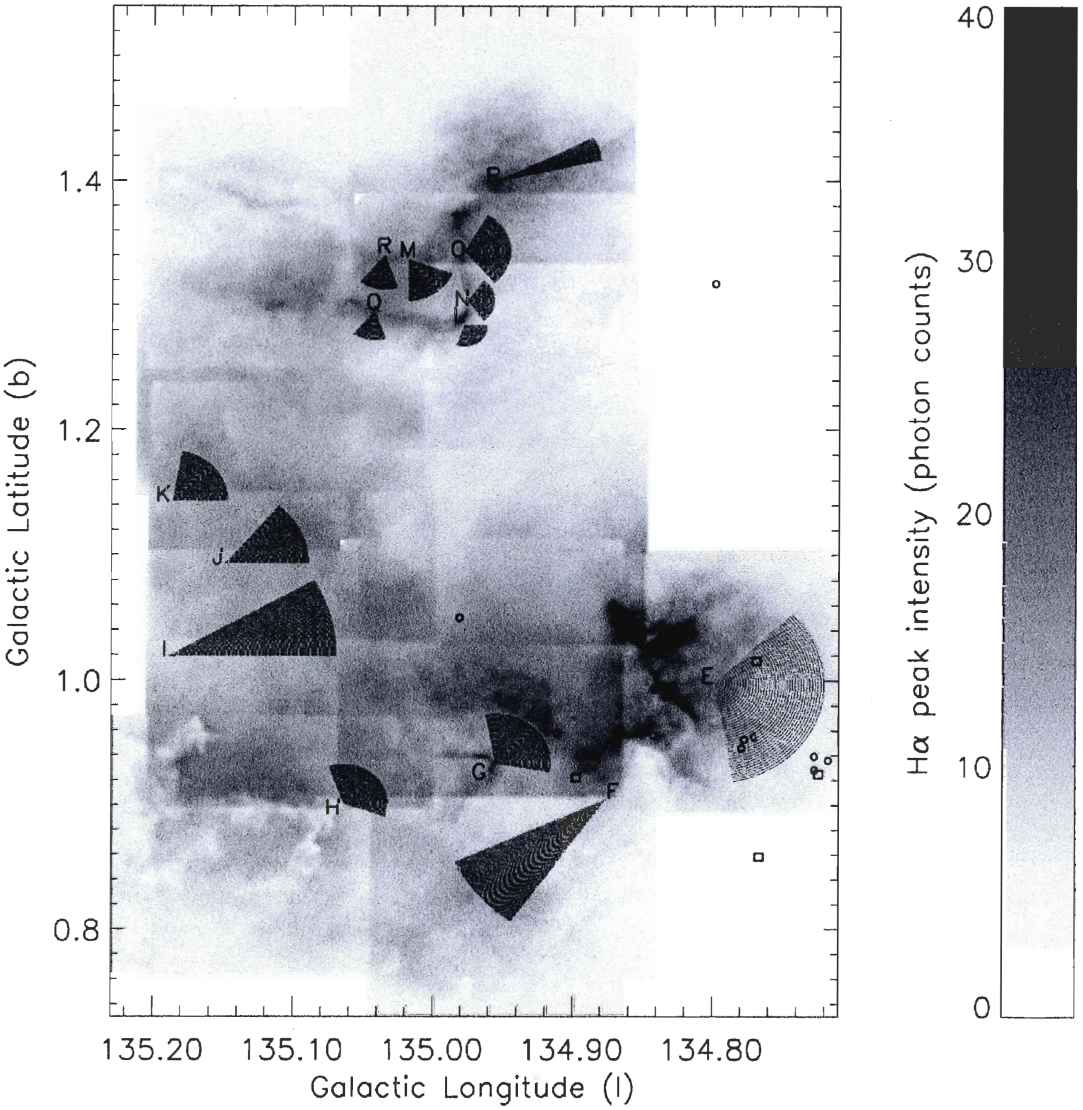

Figure 5.6: Mosaicked Hα peak intensity map for Fields 06-16.

Open squares (circles) coincide with massive O stars (B stars) associated with the star cluster IC 1805. B stars were considered only for spectral types B0 and B1. At least, eight other massive stars, with spectral types ranging between O7 and B1, are not shown in the mosaicked image ($l < 134°\!.71$)*. The reader is referred to Figures 5.1 and 5.2 in order to identify the location of the 10 fields. Areas investigated for Flows E to R are represented by the "slice-of-a-pie" regions.*

Unfortunately, it was not possible to extract precise kinematical information at the intersection of Fields 06 and 07 due to instrumental vignetting. Therefore, Flow F was investigated from an origin located slightly beyond the south-east boundary of Field 06 (see Figure 5.6). Extrapolation of the radial velocity gradient on the missing range to the extremely emissive Hα feature in Field 06 (estimated at 2.25 pc) leads, for the extended Flow F, to a new value for $v_{F,\text{initial}}$ near -44.5 km s^{-1} (see Table 5.5). This feature is particularly interesting as no molecular counterpart can be seen in Figure 5.2 (if not for really faint emission below 5 K km s^{-1} barely deduced from the FCRAO CO (1-0) observations). We, therefore, interpret the emissive structure as an old molecular fragment that has undergone almost full erosion. An extrapolation of Flows I, J, K, and X was also necessary since the associated molecular fragments are, respectively, located beyond the eastern and western boundaries of Fields 08-10 and 20 (see Figure 5.2). New extrapolated Y-intercept values (in radial velocities and line widths) are also presented in Table 5.5.

5.6.3 Ionized gas' kinematics in the vicinity of atomic material

Along the eastern wall of W4-south, Fields 04, 17, and 18 investigate at eroded shell segments likely formed of compressed atomic material. A faint molecular fragment seems to be detected slightly south of Field 18 in Figure 5.9 but has been ruled out since its radial velocity, near -60 km s^{-1}, does not match the kinematics of Flow S in Table 5.4. The small CO clump is, therefore, likely located well in front or behind W4-south. Figures 5.5*d* and 5.7 present the Hα peak intensity maps for the three fields. Dotted lines again indicate the orientation of the ionized shell.

Flows D (Field 04), T (Field 17), and U (Field 18) all present a roughly identical behavior in radial velocities. The gradients are estimated at roughly 1.5 km s^{-1} pc^{-1} along redshifted tendencies directed from the shell toward the center of the expanding bubble (see Table 5.4). For all three flows, the end radial velocities are found slightly above -40 km s^{-1}. Correlated to the radial velocity gradients, line broadening is observed similar to the majority of the flows presented in Section 5.6.2. The line-width slope is, however, much steeper in Flow D when compared to Flows T and U. In every case, the $\beta_{k,\text{initial}}$ values remain in the subsonic regime. A behavior similar to Flows D, T, and U can be observed in the southern portion of Field 03 (below Flow C in Figure 5.5*c*), but was not retained for Tables 5.4 and 5.5.

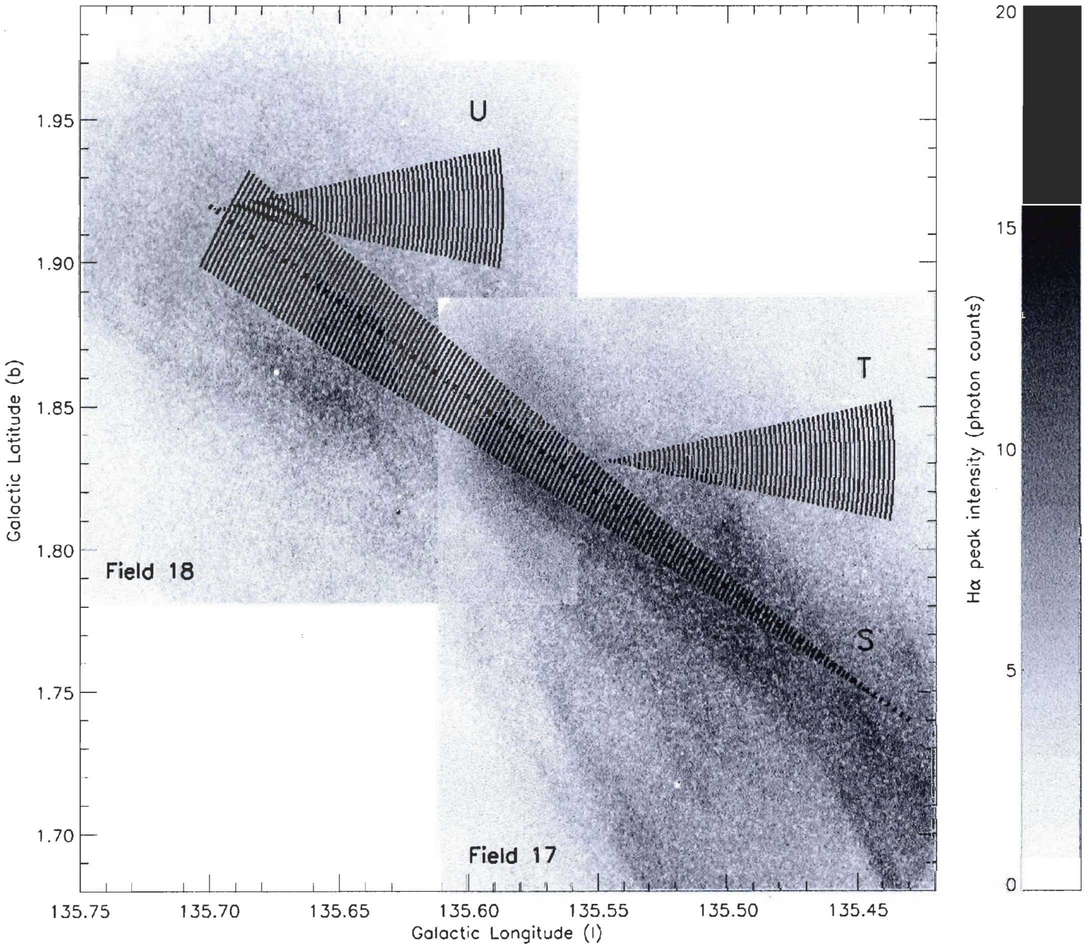

Figure 5.7: Mosaicked Hα peak intensity map for Fields 17 and 18.

Areas investigated for Flows S to U are represented by the "slice-of-a-pie" regions. The dotted line indicates the orientation of the ionized shell.

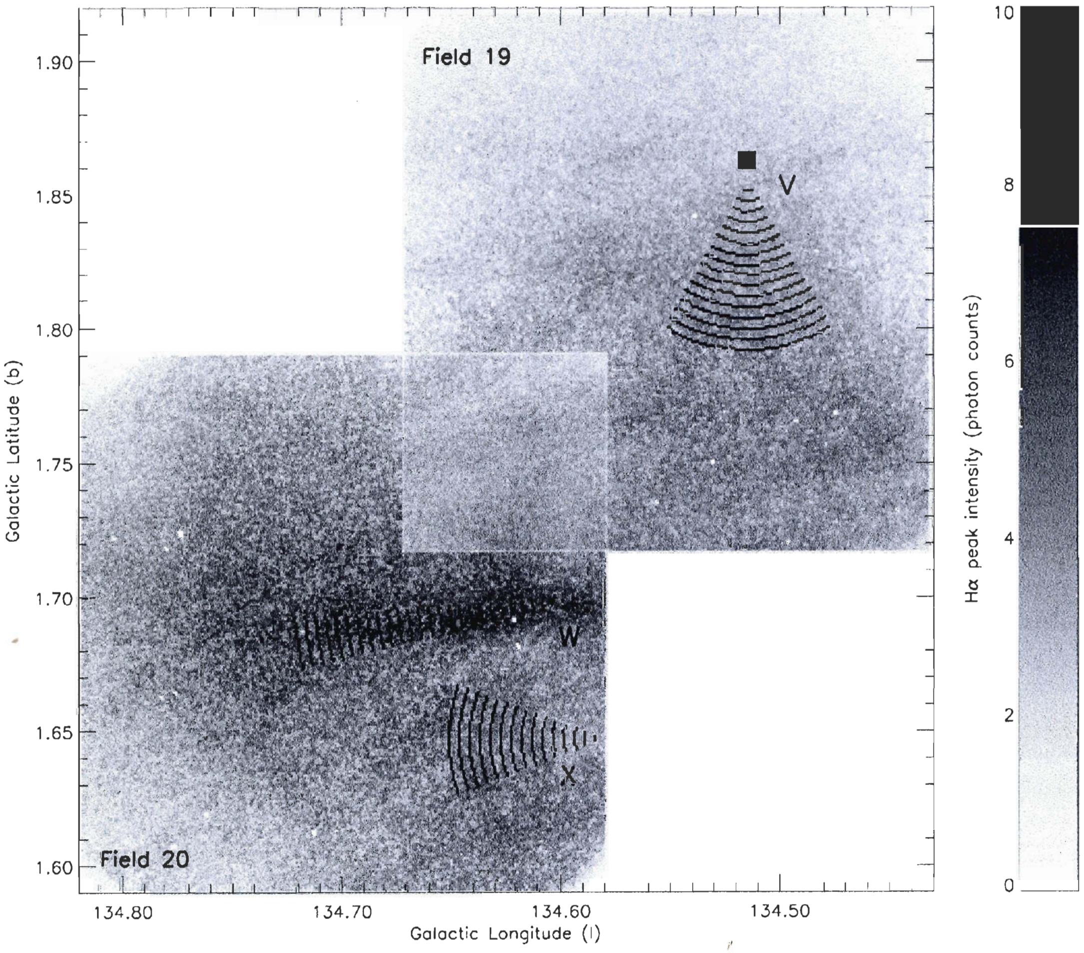

Figure 5.8: Mosaicked Hα peak intensity map for Fields 19 and 20. *Areas investigated for Flows V to X are represented by the "slice-of-a-pie" regions. The black filled square coincides with the location of molecular material according to the JCMT CO (2-1) observations.*

The mosaicked image of Figure 5.7 allows us to investigate the kinematical behavior of the eroded shell on a 13 pc range along the eastern wall of W4-south. Flow S shows a relatively flat but well-defined radial velocity gradient. The tendency is blueshifted along a south-north axis with radial velocities ranging from roughly -39 to -46 km s^{-1} near the origin of Flow U. The line-width behavior shows the ionized material (in contact with the expanding shell) with dispersion values roughly constant between 5 and 6 km s^{-1}.

Even though the ionized shell dominates the emission in both Fields 17 and 18, weaker filamentary structures can be seen near the southern portion of Figure 5.7 ($135.^{\circ}5 \leqslant l \leqslant 135.^{\circ}6$, $b \leqslant 1.^{\circ}75$). Relatively parallel to each other, the filaments are kinematically linked to the inner and brighter ionized shell with roughly identical radial velocities, approaching -40 km s^{-1}, centered on $b = 1.^{\circ}73$.

5.6.4 Interflow medium

Many areas of our Hα survey of W4-south have shown no indication of well-defined radial velocity and line-width gradients. These areas are referred to as the interflow medium in a sense that the ionized material is not specifically related to the photoerosion of a particular neutral feature, atomic or molecular. We identify these zones as the western portion of Field 05, Field 12, the southern portion of Fields 13 and 14, the eastern portion of Field 15, the northern portion of Field 16, and the eastern portion of Field 20. The eastern portion of Field 05 was not considered since the northern tip of a well-defined vertical filament of ionized material is detected (see Figure 5.2). The horseshoe-shaped structure undoubtedly points toward the star cluster. The filament's origin, roughly 15 pc below Field 05, is located slightly beyond the western boundary of Field 01 near the southern polar cap of W4. The enhanced Hα emission presents roughly constant radial velocities between -37 and -40 km s^{-1} and particularly low line widths slightly below 5 km s^{-1}.

The LSR radial velocity and corrected line-width distributions of the interflow medium are, respectively, shown in Figures 5.3 and 5.4 as the dotted histograms. In both figures, the black arrow indicates the position of the mean value of the distribution : $\langle v_{\mathrm{interflow},LSR} \rangle$ and $\langle \beta_{\mathrm{interflow},corr} \rangle$ are, respectively, estimated at -38.04 ± 0.01 km s^{-1} and 10.95 ± 0.01 km s^{-1}. The interflow medium, with a mean S/N of 35, is slightly more tenuous than the remaining of the ionized material investigated in our

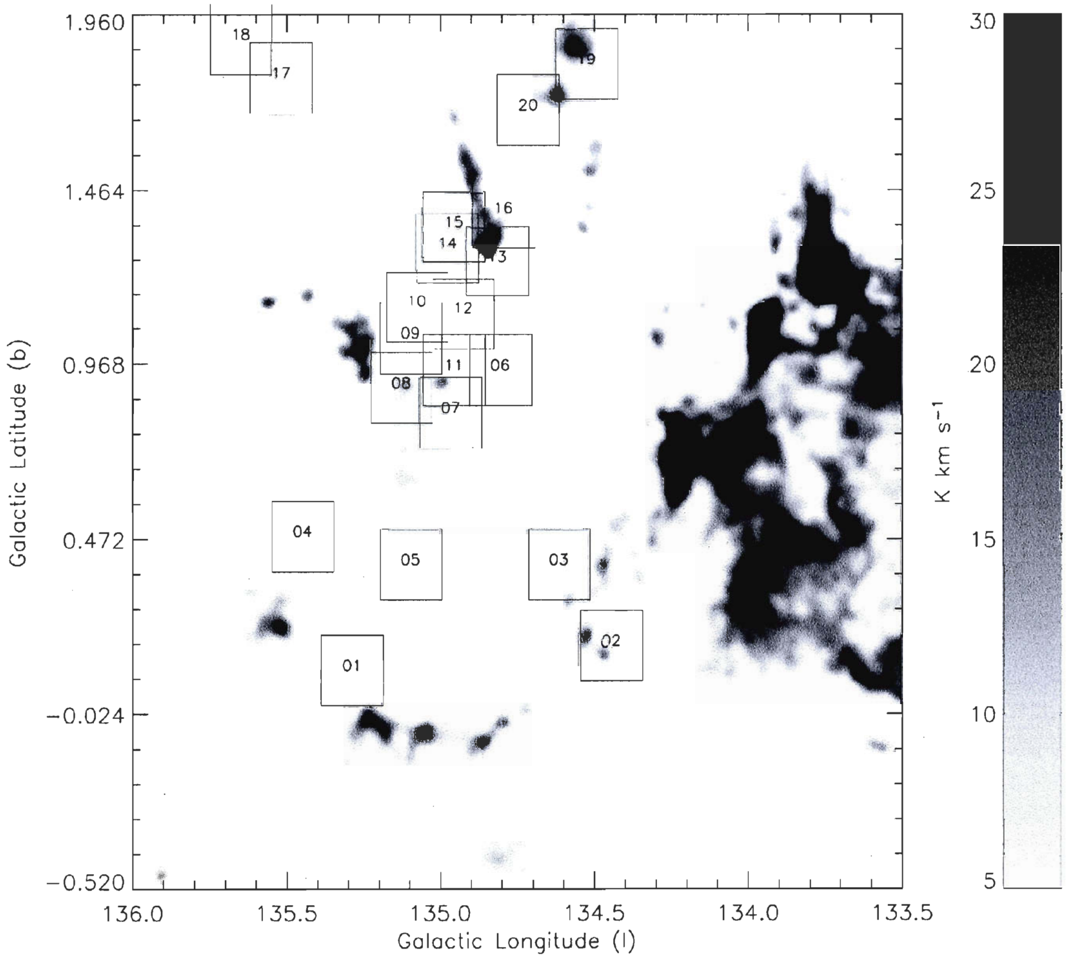

Figure 5.9: Integrated intensity map of the molecular emission found in the vicinity of the W4 region.

The spectral collapse of the FCRAO CO (1-0) transition data cube was made for LSR radial velocities between -22.90 and -63.30 km s^{-1}*. As in Figures 5.1 and 5.2, numbers coincide approximately with the location of the Fabry-Perot observations.*

Hα survey of W4-south (which presents a mean S/N of 44). Both the radial velocity and line-width distributions present particularly large asymmetry coefficients estimated, respectively, at 0.47 (toward the red tail of radial velocities) and 0.56 (toward the right tail of supersonic line widths). The zones used in our definition of the interflow medium correspond to roughly 12% of the total area covered by Fields 01-20.

5.7 Discussion

5.7.1 General overview

Investigation of the FCRAO CO (1-0) survey has revealed a mean LSR radial velocity of -47.2 ± 3.5 km s^{-1} for the molecular material observed in the vicinity of the W4 superbubble ($\langle v_{FCRAO,CO} \rangle$). Our value for $\langle v_{\rm survey,\mathit{LSR}} \rangle$ is, therefore, redshifted by nearly 5 km s^{-1} (see Section 5.7.4) compared to the last fragments of the giant molecular cloud that likely gave birth to W4. The standard deviation of the radial velocity distribution in Figure 5.3 presents a particularly small value considering the imposing dimensions of the superbubble. More important spreadings in radial velocities have been obtained from the Hα investigation of much smaller Galactic H II regions. The comparison is, however, debatable since the geometry of a given object will largely influence the kinematical disorder observed on the plane of the sky. For example, the Sh 2-158 H II region presents an Hα emissive component over a small area of 30 pc^2 and a 1σ deviation of its LSR radial velocity distribution estimated at 7.80 ± 0.02 km s^{-1} (Barriault & Joncas 2007). Since Sh 2-158 has an inclination of 60° with respect to the LOS, accelerated flows, therefore, present noticeable variations in radial velocities on surprisingly small distances. A similar argument can be used for the Sh 142 H II region (Joncas & Roy 1984) and the M17 nebula (Joncas & Roy 1986) presenting inclinations with respect to the LOS, respectively, estimated at 45° and 0° and radial velocity distributions characterized by standard deviations of 12.5 and 10.1 km s^{-1}. However, the Sh 269 H II region (Godbout *et al.* 1997), characterized by a face-on view, presents an inclination of roughly 90°, almost perfectly perpendicular to the LOS, and an extremely narrow distribution with a 1σ deviation estimated at 2.77 km s^{-1}. The relatively narrow radial velocity distribution of W4 might, therefore, be attributed to gas flows found mostly parallel to the plane of the sky, artificially attenuating the steepness of small-scale radial velocity gradients. This is likely related to a small angle of inclination (of the W4 superbubble) with respect to the plane of the sky (see Paper II).

The mean line width, slightly below 10 km s^{-1}, of our Hα survey suggests a rather complex kinematical behavior, along the LOS, of the ionized material embedded in W4-south. The fact that $\langle\beta_{\text{survey},corr}\rangle$ lies between subsonic and supersonic regimes is of great interest. Considering dimensions of the kiloparsec order for extragalactic H II regions, supersonic line widths could easily be explained through very complicated velocity systems (O'Dell & Townsley 1988). Embedded OB associations, being found dispersed in a single object, could lead to the mixing of numerous ionized flows provoked by the hydrodynamical interaction of stellar winds and the photoerosion of numerous molecular clouds. For giant H II regions encompassing a large amount of ionized material, this would likely result in a turbulent hot interior with an important overlap of strong radial velocity gradients along the LOS (Rosa & Solf 1984; Hippelein & Fried 1984). The link between small-size (<30 pc) Galactic and giant (>500 pc) extragalactic H II regions could, therefore, be provided by W4-type superbubbles.

Table 5.1 shows no indication for a large-scale radial velocity gradient pointing toward the Galactic corona, a kinematical behavior expected from the chimney model (Section 5.3). The $\langle v_{i,LSR}\rangle$ values are all, except for Field 19, within 1σ (± 5.204 km s^{-1}) of $\langle v_{\text{survey},LSR}\rangle$ (see Figure 5.3). The variations in radial velocities are, therefore, negligible to conclude for a large-scale trend. Either the chimney model does not allow us to properly interpret the kinematics of the ionized material enclosed in W4-south or a large-scale flow could be present but undetectable, perfectly parallel to the plane of the sky. This demands the W4 superbubble to be seen face-on with a 90° inclination. In Section 5.7.2, we confirm W4 as being slightly tilted toward the observer and, therefore, reject the latter assumption.

5.7.2 Ionized gas' kinematics in the vicinity of molecular material

Using the values and signs of the different radial velocity slopes presented in Column 5 of Table 5.4, a spatial scenario presenting the distribution of the molecular material along the LOS of W4-south has been obtained. The details, and particularly how ∇_v values in Table 5.4 provide an estimate of the angle of each flow with respect to the LOS, will be presented in Section 5.8. However, the reader can already refer to Figure 5.11 in order to have in mind a large-scale view of the CO distribution for the discussion to follow.

From Table 5.5, flows presenting a molecular nature in Column 2 have shown (in most cases) striking similitudes between $v_{k,\mathrm{neutral}}$ and $v_{k,\mathrm{initial}}$. This is in agreement with the Champagne model in which freshly ionized material initially retains the kinematics of the eroded material before being accelerated due to the pressure discontinuity (see Section 5.3). This argument confirms the observed kinematics as being roughly explained by a series of small-scale Champagne flows crisscrossing the nebula. Moreover, a possible contribution attributed to stellar winds cannot be properly identified from the low ∇_v values in Table 5.4. Comerón (1997) has shown Champagne flows, boosted by the addition of stellar winds, to present radial velocity gradients slightly steeper than the maximal gradient originally predicted by Bodenheimer *et al.* (1979). Therefore, two possibilities arise : (1) the stellar winds have only a negligible contribution on the kinematics of the ionized material or (2) supposing stellar winds to have a sizeable impact on the different flows, the particular geometry of W4-south does not allow us to observe important variations in radial velocities on the plane of the sky and, therefore, steeper gradients (see Section 5.7.1).

Intuitively, we would expect the ionized material in contact with the individual cloud fragments to present initial line widths in a subsonic regime, an assumption motivated by extremely narrow line widths usually obtained from the CO observations (Blitz *et al.* 1982; Digel *et al.* 1996; Lee *et al.* 1999). Flows L and N associated with the cloud fragment G134.9+1.4 present an interesting case in which supersonic values for $\beta_{k,\mathrm{initial}}$ are obtained (addressed below). From Table 5.4, the line broadening behavior ($\nabla_\beta > 0$) is also in agreement with the Champagne model (see Section 5.3). Many explanations are proposed for larger line widths down the Champagne flows. In particular, a sizeable source of broadening can be attributed to the growing depth of the W4 superbubble as the progression is made away from the small clump toward the star cluster; the constant increase of the investigated volume of embedded ionized material accentuates the probability of finding numerous ionized flows along the LOS, a kinematical contribution to line broadening. In particular for Flow C (see Figure 5.5*c*), the investigated depth across the W4 superbubble is estimated to vary from roughly 0 (near the shell) to 28 pc at a distance of 4.74 pc from the shell (assuming a radius of 24 pc between the molecular fragment and the star cluster). This diversity of flow may well be exacerbated by the ruggedness of the neutral fragment's surface. A molecular clump showing irregular, ragged edges could lead to a series of individual Champagne flows presenting slight differences in inclination with respect to the LOS. Roughly indistinguishable at the pressure discontinuity, this could possibly lead to an important broadening on a range of a few parsecs. This argument is expected for Flow B since the enhanced Hα emission in Figure 5.5*b* shows evidences of bumps and holes at the periphery of the molecular fragment (Felli *et al.* 1977). The porosity of the eroded material could additionally amplify the line splitting predicted in the modelization of Champagne flows (see Section 5.3). The spectral resolution of the FaNTOmM device system does not, however, allow us to detect evidences of line splitting. Finally, for molecular fragments in the immediate vicinity of the star cluster, line broadening can be due to numerous nearby sources of ionization. The approximation of an ionizing point source does not hold for Flow E where each star will likely initiate its own Champagne flow characterized by its own radial velocity gradient. In fact, this argument also applies to the radial velocity gradient where a mean value is determined.

Immediately, conclusive results can be deduced from Table 5.4. If we limit ourselves to the investigation of molecular clumps found exclusively at the boundaries of the H II region, a change of sign in the radial velocity gradients is observed from Flows A, B, and C to Flows I, J, and K. Normandeau *et al.* (1996) introduced the W4 H I supershell as being slightly tilted toward the observer (see Section 5.3). Assuming the center of rotation to coincide with the vicinity of star cluster IC 1805, a large fraction ($> 50\%$) of the superbubble's volume above (below) $b = 0\overset{\circ}{.}9$ should be located in front of (behind) the ionizing sources. This said, the majority of the cloud fragments found compressed on the outer shell should also be located in front or behind the star cluster depending on their latitude, above or below $b = 0\overset{\circ}{.}9$. Table 5.4 clearly confirms this behavior as Flows A, B, and C all indicate blueshifted tendencies related to forward accelerated flows and, therefore, molecular clumps found near the rear wall of W4-south (see Figure 5.11). Above the $b = 0\overset{\circ}{.}9$ threshold, Flows I, J, and K are associated with a large cloud fragment likely located in front of the ionizing sources as seen from the positive ∇_v values. This tends to confirm the W4 superbubble as being clearly tilted toward the observer. Moreover, supposing the cloud fragment associated with Flows I, J, and K as being also tilted toward the observer, a change in the angle of each flow with respect to the LOS is expected as one moves from $b = 1\overset{\circ}{.}0$ to $b = 1\overset{\circ}{.}2$ (see Figure 5.11). This is assumed supposing each flow to be roughly oriented toward the star cluster. Kinematically, this results in radial velocity gradients more and more steeper from Flows I to J and from Flows J to K (see Table 5.4).

The behavior in radial velocities for Flows F and G is perfectly in agreement with the expectations of the Champagne model. The discrepancy $v_{H,\text{neutral}}$ vs. $v_{H,\text{initial}}$ for Flow H (see Table 5.5) can be easily explained from the V-shaped absorption band at the location of the molecular fragment (see Figure 5.6). The latter is thus at a relatively large distance in front of the ionizing sources (probably beyond the boundaries of the H II region) since it blocks the W4-south Hα emission. The measurement of Flow H starts when it is already far from the neutral fragment. Extrapolating the gradient in order to obtain an initial radial velocity of -51 km s^{-1} (to coincide with the molecular material) demands the flow to have traveled roughly 9 pc before it "appears" near the western boundary of the molecular cloud. However, the three flows (F, G, and H) are all characterized by line narrowing gradients (see Table 5.4). Flow collimation is certainly not expected from the Champagne model (see Section 5.3). Even though the discrepancy seems to diminish in Flows I to K, negative ∇_β values are quite surprising. The simplest explanation for such collimation might reside in an important loss of kinematical information along the LOS due to absorption (induced by interstellar dust). From Figure 3.16 of West (2003), the 60 μm *Infrared Astronomical Satellite* (IRAS) image of the W3/W4/W5 complex shows particularly bright emission in the vicinity of the star cluster IC 1805.

The molecular fragment G134.9+1.4 represents a particularly complicated case. As predicted by Taylor *et al.* (1999), the sign of the radial velocity slopes for Flows L to R in Table 5.4 confirms the cloud as being located behind the star cluster. Combined to supersonic values obtained for $\beta_{L,\text{initial}}$ and $\beta_{N,\text{initial}}$, the slight discrepancies in radial velocities $v_{L,\text{initial}}$ vs. $v_{L,\text{neutral}}$ and $v_{N,\text{initial}}$ vs. $v_{N,\text{neutral}}$ are best explained by numerous ionized flows along the LOS of the fragment's southern tip. Above the bright ionization front seen in the northern portion of Figure 5.6, a secondary Hα rim is observed at the junction of Fields 13, 15, and 16, evidence of a molecular fragment not entirely smoothed out by tangential ionizing photons. Eroded material is, therefore, expected to flow from this secondary rim toward the southern tip of the cloud fragment. The value measured for $v_{M,\text{initial}}$, this time, coincides with the radial velocities of the molecular material (see Table 5.5). A similar conclusion is reached for $\beta_{M,\text{initial}}$, as expected, in the subsonic regime (see Table 5.5). Extrapolating the line broadening gradient to the origin of Flow L (i.e., to extend the range of Flow M in Table 5.4 from 1.35 to 2.72 pc) leads to end line widths of 9.8 km s^{-1}, roughly 2.5 km s^{-1} narrower than the value predicted by $\beta_{L,\text{initial}}$. The difference mainly results from the erosion of the fragment's southern tip and its associated ionized flow that "adds up" to the accelerated material observed in Flow M, a model that contributes for a sudden broadening excess. A direct comparison between $v_{L,\text{initial}}$ and the radial velocities of the (spatially) corresponding molecular material in Table 5.5 is, therefore, inappropriate since the Y-intercept value is clearly contaminated by northern flowing material. The end radial velocities of the extended Flow M are -47.6 km s^{-1} at the origin of Flow L, blueshifted by more than 2 km s^{-1} from $v_{L,\mathrm{initial}}$. If we assume Flow L to result from the merging of Flow M and the accelerated ionized flow (now referred as Flow L*) anticipated from the photoionization of the fragment's southern tip, we propose $v_{L,\mathrm{initial}}$ to roughly equal $0.5\times(v_{M,\mathrm{end}} + v_{L^*,\mathrm{initial}})$. This gives $v_{L^*,\mathrm{initial}} =$ -43.3 km s^{-1}, in agreement with $v_{L,\mathrm{neutral}}$ in Table 5.5. This simple model would explain why $v_{L,\mathrm{initial}}$ is blueshifted with respect to the molecular material. Moreover, since ∇_v for Flow L can be interpreted as a mean between the radial velocity gradients of Flows L* and M, we propose the former to be characterized by a steep gradient near -2.90 km s^{-1} pc^{-1} (in order to compensate for the "slow-down" brought by the latter). This value is almost in agreement with the maximal Champagne gradient theoretically predicted (see Section 5.3). Similar "back-to-the-envelope" calculations connecting Flows M and N give $v_{N^*,\mathrm{initial}} =$ -43.6 km s^{-1} and a radial velocity gradient of -2.57 km s^{-1} pc^{-1}. Finally, from $v_{O,\mathrm{initial}}$ ($\sim v_{L^*,\mathrm{initial}}$, $\sim v_{N^*,\mathrm{initial}}$) and $\beta_{O,\mathrm{initial}}$ (<10 km s^{-1}) in Table 5.4, we assume Flow O to remain uncontaminated by Flow M. A clear change in the angle of view along the western edge of G134.9+1.4 is, however, deduced from more and more flatter radial velocity slopes from Flows L* to N* and from N* to O. A similar argument also applies to the eastern edge of the cloud fragment along which Flow Q remains apparently unaffected by Flow R. As for Flow O, the two flows present initial line widths well in the subsonic regime and initial radial velocities in agreement with the FCRAO CO (1-0) and JCMT CO (2-1) observations (see Table 5.5).

The northernmost neutral feature associated with W4-south coincides with the molecular fragment G134.6+1.9. In their investigation of the CO (2-1) transition, Taylor *et al.* (1999) particularly noticed the apparent lack of continuum emission in its vicinity and the absence of ionization fronts at its periphery. This, obviously, is in agreement with the detection of particularly weak Hα lines throughout Fields 19 and 20. Combined effects of geometrical dilution of the UV flux and the photoabsorption of energetic photons at lower latitudes are proposed as an explanation. Assuming a weak photoionization to take place behind the cloud fragment, this could explain the absence of bright Hα rims in Field 19. The origin of Flow V (see Figure 5.8) roughly coincides with the southern tip of G134.6+1.9's Feature II according to the notation used by Taylor *et al.* (1999) (see the authors' Figure 2(b)). Table 5.5 gives $v_{V,\mathrm{initial}}$ roughly in agreement with $v_{V,\mathrm{neutral}}$. However, Table 5.4 provides no indication for accelerated ionized material in Flow V. A Champagne flow observed roughly parallel to the plane of the sky is ruled out since it would likely induce a well-defined line broadening gradient. Instead, the line-width behavior shows a relatively constant and supersonic regime from the optical center of Field 19 to its southern boundary, mostly in agreement with the interflow medium (see Section 5.7.4). Therefore, the kinematics of Field 19 does not reveal any sign for the photoerosion of the molecular fragment G134.6+1.9.

According to the FCRAO CO (1-0) observations, a southern extension of the roughly circular Feature I of Taylor *et al.* (1999) (see the authors' Figure 2(b)) is detected beyond the western boundary of Field 20 (see Figure 5.2). Flow X investigates the erosion of the cloud's eastern edge and reveals a kinematics very similar to Flow O (see above). The sign of the radial velocity slope (see Table 5.4) indicates a molecular fragment likely located behind the ionizing sources as opposed to the spatial scenario initially proposed by the JCMT CO (2-1) observations (see Section 5.4). Similar to Flow H, Flow W presents an important discrepancy (~ 10 km s^{-1}) in radial velocities between $v_{W,\text{initial}}$ and $v_{W,\text{neutral}}$ (see Table 5.5). This can be explained if the photoerosion of the horizontal molecular filament (see Figures 5.2 and 5.8) induces a forward ionized flow roughly parallel to the LOS. This scenario is also in agreement with Hα line widths slightly greater than expected along the filament (see Table 5.4). A similar explanation is also proposed for Flow P (see Figure 5.6) even though the discrepancy in radial velocities between $v_{P,\text{initial}}$ and $v_{P,\text{neutral}}$ is less obvious (see Table 5.5).

5.7.3 Ionized gas' kinematics in the vicinity of atomic material

In Section 5.6.3, kinematical results for Fields 04, 17, and 18 were presented as being roughly similar, all three fields being characterized by an emissive Hα shell likely formed of eroded atomic material. As for the majority of Champagne flows (see Section 5.7.2), Table 5.5 presents $v_{D,\text{initial}}$, $v_{T,\text{initial}}$, and $v_{U,\text{initial}}$ roughly in agreement with the radial velocities of the atomic counterpart. In each case, the eroded material, extracted from the compressed shell, flows toward the center of the expanding bubble along redshifted radial velocity gradients with respect to the outer H I component (see Table 5.4). In every case, tendencies toward line broadening are also observed (see Table 5.4). Rather than being interpreted as (roughly) identical Champagne flows, such similarities between Flows D, T, and U could be explained if each field (04, 17, and 18) is dominated by a process generalized to the whole H I supershell. The column densities of the atomic shell segments observed in all three fields are roughly equivalent ($\sim 9 \times 10^{20}$ cm^{-2} (K km s^{-1})$^{-1}$) leading, for a shell thickness between 10 and 20 pc (West 2003), to particle densities between n(H I) = 15 cm^{-3} and 30 cm^{-3}. These particle densities remain well below the expected densities (> 100 cm^{-3}) found on the outer envelope of typical molecular clouds (Kutner 1984). We, therefore, assume the pressure difference between the photoionized atomic shell and the embedded ISM to be insufficient in order to carry the eroded material along well-defined Champagne flows. However, the kinematics of Flows D, T, and U could be explained by lagging material, once extracted from the neutral shell, left behind the advancing (toward the observer) supershell. This assumption is best explained with the analogy of a solid body moving in a viscous fluid and the expected dynamics found in its wake (Landau & Lifshitz 1987, Chapter 2). The velocity of the fluid particles in the wake decreases with increasing distance to the solid body (here, the neutral shell). This is related to the monotonic dissipation of the kinetic energy due to viscosity. This model is in agreement with the "shell-to-interior" redshifted radial velocity gradients of Flows D, T, and U, which should, therefore, be interpreted as decelerated flows rather than accelerated flows directed toward the rear wall of W4. This decelerating material, therefore, has a sizeable contribution to the asymmetry coefficient found in the radial velocity distribution of Figure 5.3 (see Section 5.6.1) and will be referred to as a sizeable source for the interflow medium (see Section 5.7.4). A similar interpretation of lagging material, associated with the molecular fragment G134.9+1.4, was proposed by Taylor *et al.* (1999) in order to explain radial velocity gradients obtained from the JCMT CO (2-1) observations.

Another argument in favor of a generalized tendency associated with the erosion of the H I supershell comes from the apparent tilt of the W4 superbubble. In Section 5.7.2, we obtained evidences for W4 being slightly tilted toward the observer with the star cluster IC 1805 probably acting as the center of rotation. This was deduced from Champagne flows, initiated at the periphery of the expanding H II region and located above (below) the star cluster, being accelerated away from (toward) the observer. It could, therefore, be assumed that a similar pattern (a change of sign in the radial velocity gradients above and below $b = 0\overset{\circ}{.}9$) should be observed between Flow D and Flows T and U if we choose to categorize them as Champagne flows. Obviously, this is not the case here.

The line broadening gradients observed along the three flows could be partially explained by the "shell-to-interior" geometrical effect related to the constant increase of the investigated volume of ionized material along the LOS (an argument also mentioned in Section 5.7.2). Flow instabilities can also form, intuitively related to line broadening. In particular, turbulence driven by Kelvin-Helmholtz instabilities is likely to develop in ionized flows assuming a plasma's magnetic field roughly below $10\,\mu$G (Watson *et al.* 2004). From depolarization observations, West *et al.* (2007) presented estimates between 4 and $7\,\mu$G for the magnetic field inside the W4 supershell. Finally, vortex shedding is said to develop with time in uniformly decelerated flows (Wang & Dalton 1991).

In Table 5.4, the important discrepancy between the line-width slopes of Flow D and Flows T and U could be related to the particle density of the eroded shell. In fact, the particle density of the atomic shell in Fields 17 and 18 is likely below 15 cm^{-3} since the curvature of the shell is probably much smaller than in Field 04. This leads to a much greater shell thickness along the LOS. From Figures 5.5*d* and 5.7, the ionized shell in Fields 17 and 18 appears slightly more tenuous than in Field 04 (for roughly identical exposure times). This is not surprising since the particle density of the upstream neutral material is meant to decrease with latitude above the Galactic mid-plane (see Section 5.3). Considering larger line widths to be partially related to the accumulation of different radial velocity gradients along the LOS and itself highly favored in presence of dense erodible material (e.g., Flows L and N), the tenuous ionized material in Fields 17 and 18 could explain the particularly small values measured for $\langle\beta_{17,corr}\rangle$ and $\langle\beta_{18,corr}\rangle$ in Table 5.2.

The kinematical behavior of Flow S is best explained by the kinematics of the outer H I component found near the eastern boundaries of Fields 17 and 18 (see the interval of values for $v_{k,\mathrm{neutral}}$ presented for Flows T and U in Table 5.5). These radial velocities are roughly oriented along a south-north axis (between $b = 1\overset{\circ}{.}65$ and $b = 1\overset{\circ}{.}95$) toward a blueshifted tendency. Even though the value of -43 km s^{-1} does not particularly match $v_{S,\mathrm{initial}}$ (see Table 5.4), the ionized shell is likely to "follow" the kinematics of the atomic material.

Considering the 13 pc shell segment observed in Figure 5.7 as being density-bounded, the sustainment of each Hα filament, observed in the southern portion of Field 17, is likely provided by IC 1805. The filamentary structures (at least, three of them are identified) have the same radial velocities as the thicker ionized shell and can be interpreted as observational evidences for a series of earlier shocks in a diffuse H I medium. Each of these shocks is likely to have contributed to the expansion of the large superbubble, the compressed H I now being fully ionized. This is in agreement with the multigeneration star cluster model postulated by Dennison *et al.* (1997) for the formation of W4 (see Section 5.4).

5.7.4 Interflow medium

Before proceeding to the interpretation of the interflow medium, a quick return should be made on the eastern portion of Field 05, ignored in our definition of the interflow medium (see Section 5.6.4). A feature similar to the vertical ionized filament observed between the southern polar cap and Field 05 is seen emerging at roughly normal incidence from the dense western shell in the vicinity of Fields 02 and 03 (see Figure 5.2). The ionized filaments could correspond to dense fingers of shocked ISM material that have detached from the compressed shell (García-Segura *et al.* 1996; Capriotti & Kozminski 2001). Vishniac (1994) interpreted the streamers according to the theory of nonlinear thin shell instabilities where the shocked ISM material has a tendency to induce a momentum transfer directed in the opposite direction of the expansion. No particular radial velocity gradients are detected in the eastern portion of Field 05 and, therefore, suggest the ionized streamer to be observed perfectly parallel to the plane of the sky.

About the interflow medium, typical Galactic H II regions, in agreement with the Champagne model, present well-defined global radial velocity gradients encompassing the whole nebula. In Section 5.6.1, the range attributed to Flows A to X (see Table 5.4) was defined as the distance over which the radial velocity and line-width slopes for each flow remain roughly constant. Except for a few exceptions (e.g., Flows D, T, and U not associated with Champagne flows, Flow E limited by the FOV in Field 06, and Flow M voluntarily stopped in order to avoid overlap with the "slice-of-a-pie" regions of Flows L and N in Figure 5.6), this coincides, for a given flow, with the distance (on the plane of the sky) over which the ionized material has been carried away from its associated molecular feature. Compressive shocks are expected to be found at the end of these ranges (Shu *et al.* 2002). This can be seen from arched structures of compressed photoionized material beyond Flows G to K (see Figure 5.6) due to a large particle density of the ionized gas in the vicinity of the star cluster. W4-south, therefore, represents a very unique object since each detected Champagne flow expands in an interflow medium intrinsic to the superbubble and well-defined kinematically (see the dotted histograms in Figures 5.3 and 5.4). In order to avoid a kinematical contamination from ionized flows that could have been omitted in Table 5.4, only the ionized material observed in zones characterized by a low number of neutral features was considered in our investigation of the interflow medium. The star cluster vicinity was avoided since numerous cloud fragments are detected near $b = 0\overset{\circ}{.}9$ (see Figure 5.2). The value obtained for $\langle v_{\text{interflow},LSR} \rangle$ is redshifted by nearly 10 km s^{-1} with respect to $\langle v_{FCRAO,CO} \rangle$ (see Section 5.7.1) and barely in agreement with the reddest end of the radial velocity range (between -38.46 and -45.05 km s^{-1}) revealing the H I cavity (see Section 5.4). Certainly, this interflow medium contributes to the 5 km s^{-1} gap between $\langle v_{\text{survey},LSR} \rangle$ and the mean radial velocity of the molecular material found in the vicinity of the W4 superbubble. The particularly low S/Ns measured for the interflow medium are easily explained from a lack of neutral and erodible material in the targeted regions.

Exceeding $\langle \beta_{\text{survey},corr} \rangle$ by roughly 2 km s^{-1}, $\langle \beta_{\text{interflow},corr} \rangle$ in Figure 5.4 indicates particularly broadened Hα profiles. This is expected from Fields 05, 12 and 20 since the ionized material is probed through deeper LOSs and, therefore, subject to an important kinematical disorder. However, the overabundance of radial velocities and line widths, respectively, above -35 km s^{-1} and 12 km s^{-1} in the dotted histogram of Figures 5.3 and 5.4 could be related to ionized material that results from the inner erosion of the H I supershell. In Section 5.7.3, this flowing "shell-to-interior" ionized material was characterized by particularly redshifted radial velocities (with respect to the neutral shell) and line broadening gradients directed toward the center of W4 (see Flows D, T, and U in Tables 5.4 and 5.5). The analogy used in Section 5.7.3 must consider the wake of lagging material to have a finite dimension. Once these gradients peaked (say, on a range of a few parsecs beyond the western boundaries of Fields 04, 17, and 18), the end radial velocities and line widths are likely to coincide with the right tails of the dotted distributions (therefore, partially explaining the kinematics of the interflow medium). Since shell segments entirely enclosing atomic material constitute a large fraction of the total shell's area, we anticipate the lagging ionized component to account for a large fraction of the interflow medium.

On a much smaller scale, the transition from the intra- to the interflow medium has been investigated. Since the extensions of Flows C and X are quickly limited by the FOV in Fields 03 and 20, respectively (see Figures 5.5*c* and 5.8), an investigation of the flows associated with the cloud fragment G134.6+1.9 is more appropriate. The mosaicked Hα peak intensity map of Figure 5.6 allows to quantify the gas' motions on ranges that exceed the dimensions of a single FOV. Panels (a) and (b) of Figure 5.10 present the kinematical behavior of the ionized material found beyond Flow L. The 6.25 pc range reaches the optical center of Field 12. The southern tip of

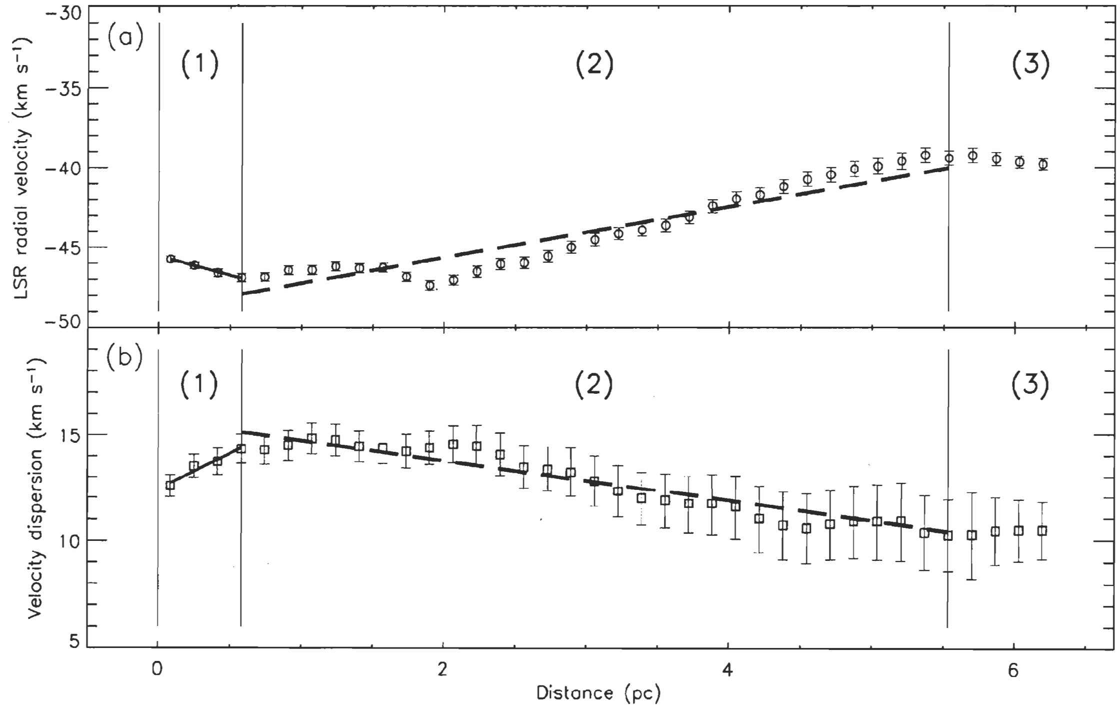

Figure 5.10: Kinematical behavior of the ionized material in and slightly beyond Flow L.

Panels (a) and (b), respectively, correspond to the radial velocity and Hα line-width profiles. The cloud fragment G134.9+1.4 is located at 0 pc. Three regions are defined : (1) the Champagne Flow L followed by (2) the transition zone that leads to (3) the interflow medium. The linear fits associated with regions (1) and (2) correspond, respectively, to the bold and long-dashed lines.

the cloud fragment is located at 0 pc. Both panels have been splitted into three distinctive regions : (1) the (Champagne) Flow L followed by (2) a transition zone that finally leads to (3) the interflow medium. Well-defined tendencies are observed in regions (1) and (2). The linear fits are, respectively, represented by the bold and long-dashed lines (the bold lines correspond to the radial velocity and line-width gradients presented for Flow L in Table 5.4). Beyond region (3), no particular trend is observed in agreement with our expectations of a "chaotic" interflow medium. The abrupt change of the radial velocity slope between regions (1) and (2) could be a strong indication for a Champagne shock. Intuitively, region (2) of Panel (a) looks very similar to the kinematical discontinuity, predicted between the upstream and downstream material of a shock (Shu 1992, Chapter 15). However, this discontinuity is expected to be only a few mean free paths thick, a fraction of a parsec. However, if we suppose the particle density at the boundary between regions (1) and (2) to be roughly equivalent to the mean density of the interflow medium in region (3), we could be confronted to a Champagne shock that has been almost fully dissipated[2]. Processes of diffusivity could be responsible for the return of ionized material in the upstream medium as the turbulent trapping becomes less and less efficient in the dissipating shock (Vainio & Laitinen 2007). The range of roughly 5 pc for region (2) in Figure 5.10 can be interpreted as the mixing length required for the escaping material to reach the local configuration of region (3). Beyond Flow L (in which end radial velocities are blueshifted with respect to the molecular material), the mixing length is characterized by a redshifted gradient estimated at 1.59 km s^{-1} pc^{-1}. The transition zone ends when the redshifted tendency vanishes near -41 km s^{-1}. The transition zone also shows a line narrowing gradient found at -0.96 km s^{-1} pc^{-1}. Even though the interflow medium was said to present particularly broadened Hα profiles (see above), the negative line-width gradient is explained by the efficiency of Flow L to induce line broadening. From end line widths near 15 km s^{-1} in Flow L, the transition zone ends with dispersion values slightly below 11 km s^{-1}, in agreement with $\langle \beta_{\text{interflow},corr} \rangle$.

Table 5.6 presents similar investigations made for Flows N and O along the western edge of G134.9+1.4. The transition zone of Flow N is very similar to region (2) in Figure 5.10, presenting identical mixing lengths and similar gradients. However, the change in the angle of view from Flow L (and N) to Flow O has a sizeable impact not only on the kinematics of the Champagne flow (see Section 5.7.2) but also on the transition zone. For a mixing length that slightly exceeds the transition zones beyond Flows L and N, a flatter radial velocity gradient is obtained beyond Flow O that also leads to radial velocities near -40 km s^{-1}. In Table 5.6, the small value extracted for ∇_β is mostly associated with end line widths for Flow O already in agreement with the interflow medium (see Table 5.4). The transition zone is, therefore, barely distinguishable if we limit ourselves to the line-width behavior beyond Flow O.

Flows I and J present extensions that approximately lead to the optical center of Field 12, in the vicinity of the extended Flow L of Figure 5.10 (a priori, these two flows are not kinematically contaminated by other accelerated flows in the vicinity of the star cluster). The radial velocity and line-width profiles, beyond both flows,

---

[2] An exponential decrease of the flow's particle density is predicted from the Champagne model as the photoionized material is carried away from the eroded neutral feature (Tenorio-Tagle 1979; Bodenheimer *et al.* 1979).

Table 5.6: **Transition zones from the intra- to interflow medium.**

Beyond...	Figure	Range	LSR radial velocities			Hα line widths		
		(pc)	∇_v (km s^{-1} pc^{-1})	$v_{\rm trans,initial}$ (km s^{-1})	Correlation	∇_β (km s^{-1} pc^{-1})	$\beta_{\rm trans,initial}$ (km s^{-1})	Correlation
Flow L	5.10	5.05	1.59 ± 0.07	-48.83 ± 0.26	0.95	-0.96 ± 0.04	15.68 ± 0.14	-0.96
Flow N	–	5.06	1.49 ± 0.15	-49.06 ± 0.56	0.95	-0.81 ± 0.05	15.53 ± 0.20	-0.96
Flow O	–	5.72	1.38 ± 0.09	-48.99 ± 0.39	0.97	0.12 ± 0.07	11.27 ± 0.29	0.62

present plateaux intersected by decreasing/increasing trends each of relatively small range (< 1 pc), a behavior we would anticipate from the interflow medium. The arched structures of compressed ionized material in Figure 5.6 indicate a particle density that likely exceeds the shock's density of Flows L, N, and O. The mixing length beyond Flows I and J might, therefore, be very restricted or even null if we suppose no ionized material to escape from the compressive shocks.

5.8 Spatial scenario

The interpretation of the radial velocity behavior of particular flows presented in Table 5.4 allows a three-dimensional representation of the molecular fragments found embedded or at the periphery of W4-south. A longitudinal cut of W4 in the latitude range between $b = 0\overset{\circ}{.}0$ and $b = 1\overset{\circ}{.}8$ is presented in Figure 5.11 (seen from above the Galactic plane). The dotted line represents the semineutral, semi-ionized supershell at the latitude of the star cluster, assuming a roughly elliptical shape (estimated from the distance separating the western and the eastern walls in Figure 5.2). Obviously, the size (or "depth" according to Figure 5.11) of the ellipse is meant to vary with latitude (practically null at $b = 0\overset{\circ}{.}0$ to roughly 60 pc near $b = 1\overset{\circ}{.}8$). From the 13 OB stars shown in Figure 5.6, only the four O stars were drawn in Figure 5.11. The location of each star and cloud fragment remains approximate but probably not too far from reality. Each flow is identified by the same letter as in Table 5.4. The angle of each flow with respect to the LOS is estimated from the ∇_v values in Table 5.4 and the maximal value expected from a Champagne flow. The solid arrows indicate the most plausible directions. The flatter gradients (e.g., A, C and I) generally indicate molecular material roughly coplanar with the photon flux orientation and, therefore, Champagne flows roughly perpendicular to the LOS. Inversely, steeper gradients (e.g., K, L, and N) are related to Champagne flows presenting an important velocity component parallel to the LOS and, therefore, propose the associated molecular fragments to be located either in front or behind the ionizing sources. Flows M and R were voluntarily omitted in order to avoid confusion in Figure 5.11.

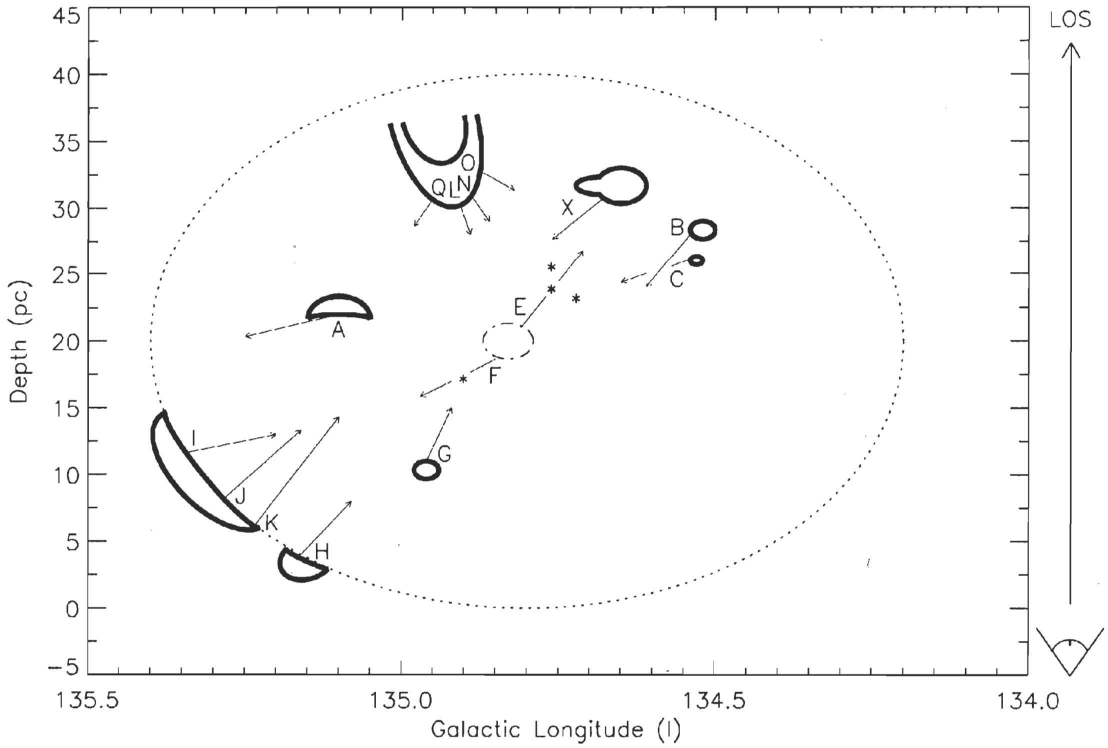

Figure 5.11: Longitudinal cut of W4-south.

Longitudinal cut, as seen from above, of the W4 superbubble between $b = 0\overset{\circ}{.}0$ *and* $b = 1\overset{\circ}{.}8$. *The dotted line is related to the semineutral, semi-ionized supershell. The molecular cloud fragments correspond to the thick solid lines. The central Hα feature in Field 06 is represented by the dash-dotted line since its molecular counterpart is hardly distinguishable from the FCRAO (1-0) observations. The approximate direction of each flow is shown by solid arrows. The star-symbols coincide with the four O stars in Figure 5.6. The observer is located "below" the figure.*

5.9 Conclusion

The use of an interferometric device system, especially designed to study particularly faint extended astronomical objects, has allowed us to extract the kinematical information associated with the ionized component found embedded in the southern portion of the Galactic superbubble/H II region W4. Prior to our investigation, the superbubble was presented as a promising candidate of Galactic chimney likely to energetically interact with the Galactic corona. From 20 Hα data cubes, the photoionization of numerous molecular clumps, found embedded or compressed along the expanding outer shell, leads to the detection of at least 10 independent flows of eroded ionized material in agreement with the Champagne model for the time-dynamical evolution of H II regions (Flows L to R, e.g, were interpreted as a unique flow since they all involve a single cloud fragment). Radial velocity gradients between 0.31 and 2.60 km s^{-1} pc^{-1} (in absolute value) are detected (Section 5.6.2). The steepness of each radial velocity gradient approximately indicates the angle of the ionized flow with respect to the LOS and, therefore, the position of the eroded material with respect to the ionizing sources. A spatial scenario is proposed for the distribution, along the LOS, of each investigated cloud fragment in W4-south (Section 5.8). Clearly, W4-south shows the last stage of the photoerosion of a large giant molecular cloud. At the periphery of the expanding bubble, cloud fragments, located above (below) the star cluster, present associated Champagne flows redshifted (blueshifted) with respect to the molecular material (Section 5.7.2). This is in agreement with the W4 superbubble being tilted toward the observer.

The radial velocity gradients all present slopes smaller than the maximal gradient expected from the Champagne phase (between 3 and 5 km s^{-1} pc^{-1}). Gas flows generally perpendicular to the LOS are proposed in order to explain the low kinematical disorder observed on the plane of the sky (Section 5.7.1). A kinematical contribution to the observed gradients attributed to stellar winds could not be verified and could be related to this geometrical effect (Section 5.7.2). However, stellar winds might also have a negligible contribution to the kinematics of the ionized material embedded in well-developed flows near the star cluster (Section 5.7.2).

The particle density contrast at the pressure discontinuity between the erodible neutral material and the surrounding ISM also presents sizeable repercussions on the observed kinematics. In particular, the inner erosion of the W4 supershell, formed of either partially compressed molecular clumps or atomic material, reveals different mechanisms. In the first case, accelerated (blueshifted or redshifted) flows in agreement with the Champagne model are observed as expected (Section 5.7.2). The photoerosion of the atomic shell, characterized by a local particle density roughly 3 to 10 times smaller than the minimal density expected on the outer envelope of molecular clouds, induces redshifted (with respect to the neutral H I shell) flows directed toward the center of the expanding bubble. Rather than being interpreted as backward Champagne flows, the eroded material is said to "hover", left behind the advancing (toward the observer) supershell. The kinematics of these particular flows has been largely compared to a wake of material behind a solid body moving in a viscous fluid (Section 5.7.3). This lagging material could have a sizeable impact on the kinematics of some restricted zones of our Hα survey of W4-south referred to as the interflow medium (Section 5.7.4).

Particular Champagne shocks present evidences of shock dissipation. The transition from the intra- to interflow medium shows a mixing length in which accelerated ionized material escapes the compressive shock and gradually evolves to recover the local kinematical state of the interflow medium (Section 5.7.4). The interflow medium partially explains the overall mean radial velocity of our Hα survey to be redshifted by roughly 5 km s^{-1} from the mean radial velocity of the molecular material observed in the vicinity of the W4 complex (Sections 5.7.1 and 5.7.4).

The investigation of the kinematical disorder along the LOS shows W4 to lie in a transient state between subsonic and supersonic regimes, in agreement with the apparent dimensions of the superbubble. The mean Hα line width is estimated at 9.213 ± 0.002 km s^{-1}. W4-type superbubbles, characterized by complicated radial velocity fields, are assumed to be the missing link between small-size (< 30 pc) Galactic and giant (> 500 pc) extragalactic H II regions (Section 5.7.1). The Hα line-width behavior, intrinsic to Champagne flows, is particularly investigated. Tendencies toward line broadening, in agreement with the theory, are mostly explained by a series of effects; the constant increase of the investigated volume of ionized material along the LOS, the addition of radial velocity gradients as the eroded material is carried away from the pressure discontinuities (between the molecular and interstellar material), a localized spreading of the ionizing sources in the vicinity of the erodible material, and porosity and imperfections on the outskirts of the neutral clumps (Section 5.7.2). The line broadening gradients for Champagne flows are found between 0.16 and 3.62 km s^{-1} pc^{-1} (Section 5.6.2). However, line narrowing gradients, in the vicinity of the star cluster, are attributed to absorption along the LOS, thus blocking a certain fraction of the kinematical information (Section 5.7.2).

The ionized material found embedded in W4-south being mostly dominated by small-scale ($\lesssim 10$ pc) Champagne flows, no large-scale gas flows are detected (Section 5.7.1). This is in disagreement with the model of Galactic chimney (Section 5.3). From the imposing distance (~ 180 pc) on the plane of the sky separating the northernmost portion of the superbubble and W4-south, we propose large-scale ionized flows to remain undetected below a certain threshold in latitude. In order to estimate the implication of the W4 superbubble in the sustainment of the Galactic corona, a similar investigation, carried out through Fabry-Perot interferometry in Paper II, will provide information on the kinematics and dynamics related to the ionized material found embedded in W4-north.

The authors thank the Natural Sciences and Engineering Research Council of Canada and the Fonds Québécois de la Recherche sur la Nature et les Technologies who provided funds for this research project. The Canadian Galactic Plane Survey is a Canadian project with international partners and is supported by a grant from the Natural Sciences and Engineering Research Council of Canada. Data from the Canadian Galactic Plane Survey are publicly available through the facilities of the Canadian Astronomy Data Centre (http ://www1.cadc-ccda.hia-iha.nrc-cnrc.gc.ca/cgps/).

D. L. is grateful to M.-A. Miville-Deschênes and Olivier Daigle who provided useful IDL routines to carry out data reduction. D. L. also thanks B. Malenfant, G. Turcotte, and P.-L. Lévesque for technical support during numerous observing nights at the Observatoire du mont Mégantic. Finally, D. L. thanks astro-imager R. Crisp for providing the Light from the Heart.

Chapitre 6

Cinématique du gaz ionisé associé à W4 $(3° < b \leqslant 7°)$

Sommaire

Référence : Lagrois, D., & Joncas, G. 2009b, *ApJ*, 693, 186

Titre original : *On the Dynamical Evolution of H*II *Regions : an Investigation of the Ionized Component of W4, a Galactic Chimney Candidate. II. Kinematics and Dynamics in the Latitude Range* $3° < b \leqslant 7°$.

Cet article traite de la portion nord de W4 dans l'intervalle en latitude de $b = 3°$ à $b = 7°$. L'article fut soumis le 22 juillet 2008 et accepté pour publication le 11 novembre 2008. Le manuscrit, tel que présenté au chapitre 6, parut dans l'édition du $1^{\underline{\text{er}}}$ mars 2009 de *The Astrophysical Journal.*

6.1 Résumé

Dans ce second d'une série de deux articles, nous présentons les résultats associés à une investigation Hα, obtenue suite à l'utilisation du système FaNTOmM, du matériel ionisé diffus confiné à la portion nord de W4. W4 est une candidate prometteuse de cheminée galactique, susceptible d'être en interaction avec la couronne galactique, présentant des indices de fragmentation au niveau de sa coquille. Nous présentons un modèle quantitatif d'identification de failles nous permettant de conclure que la supercoquille H I/région H II W4 renferme une cheminée galactique en formation. Sur une échelle d'environ 125 pc, deux gradients de vitesse sud-nord sont détectés, $\nabla_v = (\text{-})0.17$ km s^{-1} pc^{-1} ($3\overset{\circ}{.}5 \leqslant b < 6\overset{\circ}{.}3$) et $\nabla_v = (\text{-})3.13$ km s^{-1} pc^{-1} ($6\overset{\circ}{.}3 \leqslant b \leqslant 6\overset{\circ}{.}5$). Ceci mène à des vitesses radiales, légèrement au-delà de la calotte polaire, de -70 km s^{-1}, décalées [vers le bleu] par environ 25 km s^{-1} par rapport à la supercoquille H I. Le comportement cinématique est en accord avec un scénario de raréfaction si W4 montre une inclinaison dirigée vers l'observateur. Cet angle d'inclinaison est estimé entre 9° et 27° par rapport au plan du ciel. Un gradient montrant le rétrécissement des largeurs de raie est corrélé spatialement au gradient de vitesse. Les comportements, à grande échelle, en vitesse et en largeur de raie correspondent à des écoulements, accélérés et parallélisés, de matériel ionisé expulsé hors de la nébuleuse. Cette signature cinématique coïncide avec le modèle de cheminée galactique. L'âge dynamique de la cheminée de W4 est estimée à 4.1 Mans et, par le fait même, demande que des instabilités se soient développées au niveau de la coquille à des latitudes inférieures au seuil d'éclatement d'une bulle. Notre travail permet de confirmer que l'amas stellaire IC 1805 participe partiellement à l'ionisation de la basse couronne galactique au-dessus du bras de Persée.

6.2 Abstract

In the second of this two-paper series, we present results associated with an Hα investigation, obtained using the Fabry-Perot interferometer FaNTOmM, of the tenuous ionized material found embedded in the northern portion of W4. W4 is a promising candidate for a Galactic chimney, likely connected with the Galactic corona, and presents evidence of shell fragmentation. We present the quantitative method for identifying shell breakout that allows us to characterize the giant H I supershell/H II region W4 as enclosing a Galactic chimney in formation. On a range of approximately 125 pc, two south-north radial velocity gradients are detected, $\nabla_v =$ (-)0.17 km s^{-1} pc^{-1} ($3.^{\circ}5 \leqslant b < 6.^{\circ}3$) and $\nabla_v =$ (-)3.13 km s^{-1} pc^{-1} ($6.^{\circ}3 \leqslant b \leqslant 6.^{\circ}5$). This leads to radial velocities, slightly above the vicinity of the shell's polar cap, of -70 km s^{-1}, blueshifted by nearly 25 km s^{-1} with respect to the H I supershell. The kinematic behavior is in agreement with a rarefaction scenario if the W4 superbubble presents a tilt toward the observer. This angle of inclination is estimated between 9° et 27° with respect to the plane of the sky. A line-narrowing gradient is correlated with the radial velocity gradient. The large-scale trends in radial velocities and line widths correspond to highly accelerated, well-parallelized outflows of vented ionized material. This kinematic signature is expected from the chimney model. The dynamical age of the W4 chimney is estimated at 4.1 Myr and constraints shell instabilities to have developed at latitudes lower than the blowout threshold height. Our work contributes to the evidence that the star cluster IC 1805 partially sustains the low-galactic corona above the Perseus arm.

6.3 Introduction

The implication of Galactic chimneys (Norman & Ikeuchi 1989) in the sustainment of the hot, ionized Galactic corona has been investigated for the past three decades. Numerical models have shown the formation of ovoid supershells fueled by the action of supernova explosions (Chevalier & Gardner 1974), the mechanical deposit of Lyα radiation (Dove *et al.* 2000) and stellar winds (Basu *et al.* 1999) of large star clusters. Assuming an exponentially decreasing Galactic atmosphere model (Dickey & Lockmann 1990; Heiles 1991), blowout events occur once the polar cap of an expanding supershell overtakes the Galactic layer of neutral material. According to Mac Low *et al.* (1989), the blowout threshold is estimated at 2 to 3 times the vertical scale height of the H I distribution above mid-plane. There is a dramatic drop in particle density and pressure from the upstream interstellar medium (hereafter, ISM). This, in turn, leads to a sudden acceleration of the shell's polar cap segment. Dove *et al.* (2000) proposed this particular scenario as ideal for fast shell instability development, which is responsible for shell weaknesses and ultimately fracture. Shell openings, therefore, assure that a certain fraction of the energetic photons will exit the H II region. The evacuated photons will likely travel to interact with the Galactic corona contributing to the sustainment of the Reynolds layer (Reynolds 1989a).

Observational identification of shell breakouts usually relies on visual aspects. An investigation using a more quantitative method is required especially for superbubbles displaying observational evidence for ionization-bounded supershells. Due to the pressure difference between the warm interior and the outer ISM, openings found on some supershell will likely vent interior gas outwards. Induced at the point of fracture, a rarefaction wave will quickly develop and sweep out a large amount of embedded ionized material. That is, a discontinuity associated with the wave will propagate from the fracture toward the center of the superbubble, while the gas that is being rarefied will move in the opposite direction, toward the fragmenting shell of the superbubble. The shocked material is accelerated through the "interior-to-exterior" pressure gradient before being evacuated. For gas flows not strictly parallel to the plane of the sky, a kinematic discrepancy can be established between the high-velocity-accelerated component, being evacuated, and the unperturbed material found deeper in the superbubble. This model particularly resembles the kinematics anticipated from the embedded air in a pierced metal container (see Section 6.7.2). The Galactic superbubble/H II region W4 characterized by a slight tilt toward the observer (Normandeau *et al.* 1996) represents an ideal astronomical object to verify such a model.

In Section 6.4, we present the promising Galactic chimney candidate W4. Large-scale observations have led to the detection of two possible breaks located along the northern shell frame. Techniques used for data acquisition and reduction are described in Section 6.5. We provide, in Section 6.6, the results of our Fabry-Perot Hα investigation in the northern portion of W4, bounded in latitude between 3° and 7°. Our model of a pierced metal container will be presented in Section 6.7 and used in the interpretation of the observed gas motion. A review of the most important results and conclusion will be presented in Section 6.8.

6.4 The W4 superbubble

In our first paper (Lagrois & Joncas 2009a, hereafter Paper I), we introduced the Galactic wind-blown bubble/H II region W4 which was the central feature of the

CGPS pilot project (Normandeau *et al.* 1997). Observations in the radio regime have presented W4 as an impressive H I cavity aiming toward the Galactic corona and visible in the radial velocity range between -38.46 and -45.05 km s^{-1} as measured in the LSR (West *et al.* 2007). Outflows from the star cluster IC 1805 (Shi & Hu 1999) were said to be responsible for the actual superbubble expansion (Basu *et al.* 1999). A northern extension of the CGPS spectroscopic 21 cm line observations, used in Paper I, is presented in Normandeau (2000). The H I supershell is seen extending between $b = 0°$ and $b = 6°$ and presents no evidence for a neutral polar cap at the northernmost latitudes (Normandeau 2000). From polarization observations, West *et al.* (2007) outlined a roughly egg-shaped supershell reaching a height of roughly 245 parsecs above the Galactic mid-plane, considering a spectroscopic distance of 2.35 kpc to the star cluster (Massey *et al.* 1995). Considering the vertical scale height of the H I distribution estimated at 140 pc above the Perseus arm (Normandeau 2000), it is assumed that the shell's polar region is located slightly below the blowout threshold and should not, therefore, show signs of a re-accelerated expansion.

Dennison *et al.* (1997) obtained a large-scale view of the Hα emission associated with the W4 H II region. The 10° circular FOV revealed an ionized counterpart to the H I supershell. The neutral shell is apparently eroded from its inner side. The shell can, therefore, be referred as being semineutral, semi-ionized. A faint ionized polar cap seems to be detected roughly 230 pc above the Galactic mid-plane. Even though the outer shock wave of the expanding structure left very little material behind it, a diffuse ionized component is observed embedded in the superbubble. In Paper I, partial sources of material were identified as numerous and mostly molecular blobs found either inside or at the periphery of the supershell and exposed to the UV flux of the nearby star cluster. Generally located at low-galactic latitude, these eroded features contributed to establish a discrepancy in emissivity between what we referred as the southern ($0° \leqslant b \leqslant 3°$, hereafter W4-south) and northern ($3° < b \leqslant 7°$, hereafter W4-north) portions of W4 respectively made up of strong and faint Hα emission. This paper will mainly focus on the description and the kinematic investigation of W4-north.

At the boundary between W4-south and -north, slightly bended neutral filaments (hereafter, referred to the "H I horizontal sheets") are detected, covering in longitude an important fraction of the bubble's width. A second, but nonetheless important, atomic feature is observed near the shell's polar cap. Kinematically linked to the H I supershell, the intriguing vertical H I-spur (Normandeau 2000) is highly similar to worm-like structures obtained from numerical models of accelerated wind-blown bubbles and interpreted as filamentary remnants of unstable broken shells (De Avillez & Berry 2001). In fact, the investigation of the large-scale Hα (Dennison *et al.* 1997) and 1420/408 MHz continuum (CGPS) emissions has revealed particularly faint shell material in the direct vicinity of the H I-spur (West 2003; West *et al.* 2007). The authors interpreted the lack of emission as an observational evidence for a recent shell fracture. A second possible break is also detected along the western side of the W4 supershell. Combined with a lack of high-latitude ionizing photons (Terebey *et al.* 2003) and of erodible neutral clumps, dramatic gas venting might have deprived W4-north of its emissive material; all contributing to the discrepancy in emissivity between the two portions of the nebula. In order to visualize the location of each feature, the reader is referred to the schematic drawing of W4-north in Figure 6.1.

On a much larger scale of view, the Wisconsin Hα Mapper (WHAM) Northern Sky Survey (Reynolds *et al.* 2001) has revealed a large horseshoe-shaped Hα loop above the W3/W4/W5 complex, at a relatively low-galactic corona level (about 1 kpc above Galactic mid-plane). Striking similarities can be established between the bent H I capped structures observed above the known chimney associated with the Galactic supershell GSH 242-03+37 (McClure-Griffiths *et al.* 2006) and the giant ionized loop (hereafter, referred as the "Reynolds loop"). Mostly due to a remarkable alignment between the W4 superbubble and the Reynolds loop, Reynolds *et al.* (2001) proposed its sustainment to be partially attributed to the star cluster IC 1805.

In order to investigate the percolation of energetic photons through the possible shell breakouts, Hα observations via Fabry-Perot interferometry were carried out on the tenuous embedded material of W4-north. Since a strong disagreement exists (H I vs. Hα and polarization observations) regarding a possible polar cap, our own work becomes crucial to assess whether the W4 superbubble is a chimney or not. Our motivation is based on our model of a pierced metal container and the expected large-scale radial velocity gradients directed toward the shell openings. Such gradients, associated with gas venting outwards, have remained undetected in our kinematic investigation of W4-south in Paper I due to a north-south sound crossing time of the nebula estimated at 25 Myr, well above the proposed dynamical age of the superbubble (Dennison *et al.* 1997). Therefore, rarefaction waves emanating from unstable northern-shell segments and propagating in a roughly sonic regime would still be found well above $b = 3°$, leaving unperturbed the ionized material found in the vicinity of the star cluster. Additionally, a northern portion of W4 mostly dominated by accelerated outflows of ejected material would confirm the formation

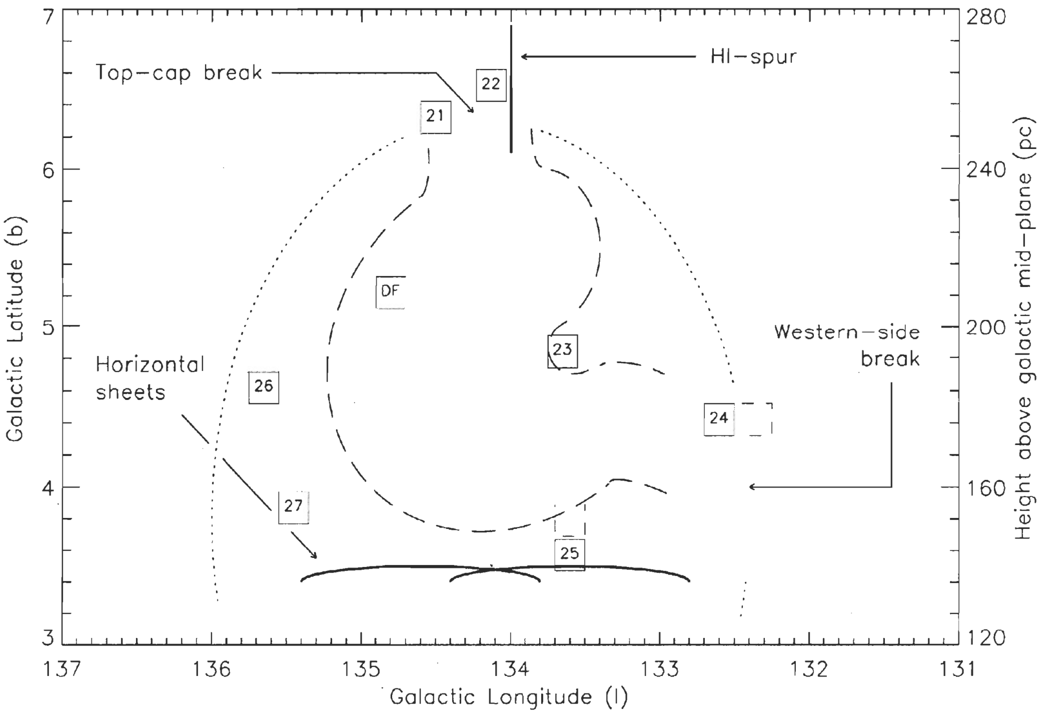

Figure 6.1: Schematic diagram of W4-north.

The numbers coincide with the optical centers of the seven observed fields. The field labeled "DF" coincides with the location of the Dark Field used for night-sky subtraction. Bounded boxes enclose the FOV obtained from the FaNTOmM device system. The right-hand vertical axis shows the height above Galactic mid-plane, assuming a spectroscopic distance of 2.35 kpc to the star cluster IC1805. Atomic hydrogen features are represented by the bold solid lines. The long-dashed line encloses the 2°×2° portion inside the W4 superbubble where the Hα and 1420/408 MHz continuum emissions are seen particularly low (referred as the Hα-poor cavity in the text). The dotted line is related to the semineutral, semi-ionized W4 supershell. Dashed line "empty fields" near Fields 24 and 25 correspond to areas that remain to be investigated in order to perfectly interpret the kinematics of W4-north.

of a Galactic chimney and an obvious interaction between the star cluster IC 1805 and the Reynolds loop.

6.5 Observations and data reduction

Hα observations of W4-north were performed in 2006 and 2007 using the Ritchey-Chrétien 1.6 m telescope of the OmM. Similar to Paper I, the FaNTOmM (Fabry-Perot of New Technology for the Observatoire du mont Mégantic) device system was again used for data gathering. Technical information about the ultrasensitive IPCS camera can be found in Hernandez *et al.* (2003). The central interference order of the FPI was fixed at 765 for a free spectral range of 8.56 Å centered on the Hα rest frequency. The finesse of the FPI varied slightly from night to night between 18 and 19. This allowed us to perform the spectral scanning at a fixed number of 44 steps (channels). All Hα emission spectra, therefore, presented a spectral resolution of 0.19 Å channel^{-1} (or 8.89 km s^{-1} channel^{-1}). The λ6598.95 Å Ne-line was used to produce interferograms for the radial velocity calibration, while narrow-band ($\Delta\lambda_{FWHM} = 10$ Å) filters allowed to isolate Hα lines from other ionized emission. Interference filters were chosen approximately in order to maximize flux transmission, that is, to consider the effect of blueshifting (-0.2 Å·K^{-1}) on transmission caused by cold ambient temperatures and to minimize the inclination of the different filters.

The use of the PANORAMIX f/2 focal reducer (Godbout *et al.* 1998) allowed us to obtain a square 12$'$.3×12$'$.3 FOV for a spatial resolution of 1$''$.45 pixel^{-1} using the hard binned 512×512 80 frames s^{-1} mode of the CCD detector. Data reduction was carried out using IDL procedure (Daigle *et al.* 2006) specially tailored to reproduce the method used for the TAURUS FP spectrometer (Atherton *et al.* 1982).

We emphasized, in Paper I, the difficulty arising from night-sky emission (Osterbrock *et al.* 1996). The problem was partially eliminated by applying a multi-component Gaussian fit to each emission spectrum. The method demands each spectral line to be clearly identifiable in each raw spectrum. However, this criterion does not hold in spatial regions above the H I horizontal sheets, where the W4 Hα component is highly dominated by the emissivity of the Earth's mesosphere.

In order to mitigate the problem of night-sky emission, we use a semi-parallel procedure of sky subtraction that allows us to extract, from highly contaminated spectra, extremely faint W4 Hα profiles. The problem of sky subtraction must initially be treated as dual, being both spatial and temporal. Skinner *et al.* (1998) brilliantly demonstrated the optical variability of the night-sky emission as being dependent on the pointing position and the local time of the observations. In particular, the authors pointed out that the photometric properties of the sky vary on periods as short as 15 minutes. Since the Hα emission from W4 fills our FOV, a patch of sky essentially devoided of emission was needed near the targeted areas. Examination of Figure 12 from West *et al.* (2007) shows a $2° \times 2°$ ionized gas trough centered on $(l, b) = (134\overset{\circ}{.}5, 4\overset{\circ}{.}9)$. This area is pictured in our Figure 6.1 using a long-dashed line and will be referred as the Hα-poor cavity. The small region labeled "DF", for Dark Field, was observed repeatedly during the night to measure the night-sky contamination. The sky subtraction scheme is shown in Figure 6.2. The angular separation between the Dark Field and individual W4 fields is $\gtrsim 1°$ and the telescope was moved back and forth between W4 and DF. A given cycle, either associated with W4 or DF, corresponds to a one-time scanning of the 60 Å-wide wavelength interval (see Paper I). Each cycle is completed in ~ 7 minutes. Hence less than 15 minutes elapses between two consecutive cycles, each Dark Field cycle labeled "j" can be subtracted from its associated W4 field cycle "j+1" (see Figure 6.2). From each DF subtracted observation, a faint but uncontaminated Hα profile is extracted. The procedure is repeated from $j = 1$ to M-1 (W4 field cycle 01 and DF cycle M are naturally rejected from the procedure). The resulting Hα profiles are all summed in order to show a clear, high S/N, detection of the ionized material in W4-north. Once sky subtraction was completed, a Gaussian-fitting routine allowed us to extract, from each profile, the centroid position (radial velocity), the observed line width value (dispersion), and the amplitude of the fitted line. The M value for each W4 field (Figure 6.1) is listed in Table 6.1 (see Section 6.6).

6.6 Kinematical results

We present the large-scale kinematic behavior of the ionized component associated with W4-north. The schematic diagram of Figure 6.1 indicates the location of the FPI observations. A total of seven fields were obtained in order to detect the anticipated signature related to our model of a pierced metal container (that is the kinematic impact on the embedded ionized material attributed to rarefaction waves originating from the possible top-cap and western-side breaks). In order to pursue the terminology used for W4-south in Paper I, the new Hα observations were labeled

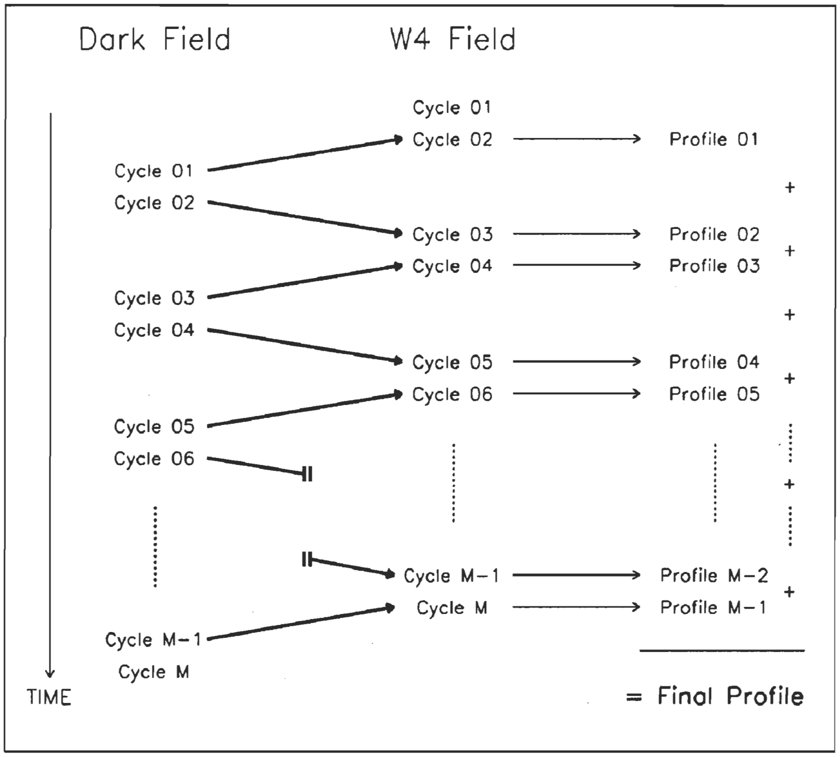

Figure 6.2: Scheme of the night-sky subtraction method.

Schematic diagram of the night-sky subtraction method used during the observations and data reduction. Each cycle corresponds to an exposure time of ~ 7 min. The total number of cycles gathered for each field (Dark and W4) is labeled "M". Cycles 01 and M, respectively for the W4 Field and the Dark Field, were rejected in every case. Solid thick arrows are to be translated as "... subtracted from ...". The method is duplicated for every spatial pixel of the raw data cubes.

from 21 to 27. The observations were carried out in order to investigate four specific areas of W4-north : the top-cap break (Fields 21, 22, and 23), the western-side break (Field 24), the H I horizontal sheets (Field 25), and the high-latitude W4 eastern wall (Fields 26 and 27). Each investigated area will be related to a particular subsection in Section 6.7.

Since the Hα emission is very faint, spatial binning was necessary in order to obtain significant S/Ns. Each field was spatially degraded to produce 4×4 pixel^2 raw data cubes before proceeding to sky subtraction (except for Field 26, observed in poor meteorological conditions, where a 2×2 pixel^2 cube produced better results).

The number of points available, to establish a reliable kinematic model of W4-north, is, therefore, reduced to less than a 100. Figures 6.3-6.9 present the resulting three-dimensional cubes respectively for Fields 21 to 27. Each panel (i.e. pixel) corresponds to a 2.1×2.1 pc^2 area at the distance of W4 (4.2×4.2 pc^2 in Figure 6.8). The data points are represented by open circles. Gaussian fits to the observed W4 Hα profiles correspond to bold solid lines. Since more than a degree separates the Dark Field from individual W4 fields, it can be assumed that sky profiles will always be an approximation of the nearby night-sky emission to be subtracted. Induced by a less than perfect subtraction of the λ6553.6 Å OH line and the λ6562.8 Å geocoronal Hα line[1], small remnants are detected near the right wing of different Hα profiles in (the faintest) Fields 21, 22, and 23 (see, in particular, the lower panels in Figures 6.3, 6.4, and 6.5). The fact that these remnants show important variations on the FOV suggests that the night-sky emission varies on angular distances of less than $12'$ on the plane of the sky. Gaussian fits were also applied on these remnants (not shown in Figures 6.3-6.5 to avoid unnecessary complexity). The reader is, however, referred to the residuals of the fits symbolized by the small black dots in Figures 6.3-6.9. The base line (continuum) at zero was also traced out to help estimate the relative importance of the residuals. Finally, the vertical and horizontal thick solid lines are respectively associated with the centroid position and the observed line width of each fitted Hα profile. In order to extract purely kinematic broadening effects from the observed line widths, the method of quadratic subtraction presented in Paper I was again used. For every panel, the LSR radial velocity, $v_{i,LSR}$, the corrected line width value, $\beta_{i,corr}$, and the S/N of the fitted line are given. For Figures 6.3-6.9, error bars on $v_{i,LSR}$ and $\beta_{i,corr}$ correspond to kinematic uncertainties and are derived from the method introduced by Lenz & Ayres (1992).

Table 6.1 presents a review of the kinematic information extracted from Fields 21 to 27. For each field, the mean LSR radial velocity and mean corrected line width are given respectively in Columns 4 and 5. From now on, the label "i" will be referring to the field's identification number (e.g., $\langle v_{21,LSR} \rangle$ corresponds to the mean radial velocity observed in Field 21). The number of cycles (M) accumulated for both the

---

[1] The top abscissa, in Figures 6.3-6.9, corresponds to the scanned wavelength interval of the FPI's central interference order. Paper I mentioned a spectral scanning that covers seven interference orders for a 60 Å range (roughly seven times the free spectral range on rest Hα). Each order wraps around the others and is summed on each channel at the end of the acquisition. A given channel, therefore, corresponds to more than one wavelength. However, the central interference order dominates the flux at roughly every step except at the particular spectral positions of the contaminant night-sky lines. Peripherical orders do not account for the detected spectra, flattened out by the narrow-band filters.

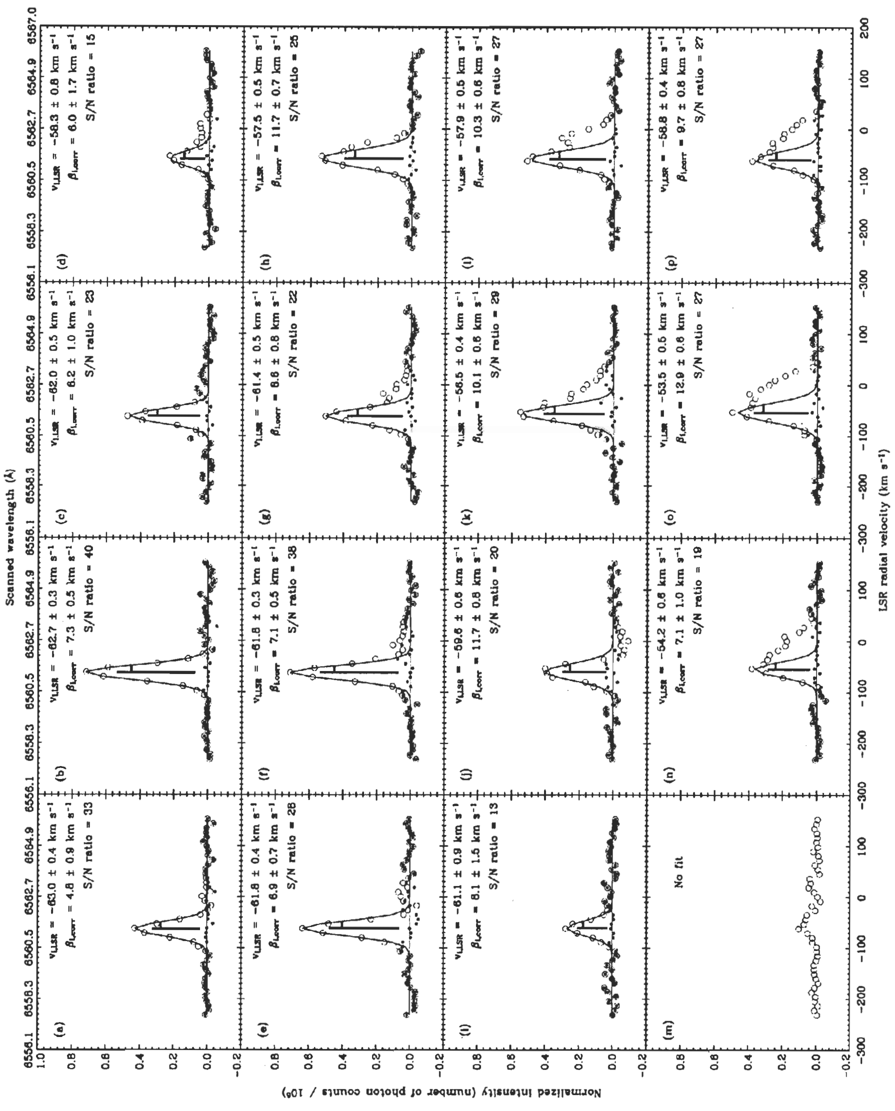

Figure 6.3: Hard binned Hα profiles for Field 21.

The data points are represented by open circles. Gaussian fits to the observed W4 Hα profiles correspond to bold solid lines. Remnants of sky subtraction can often be found near the right wing of the different Hα profiles. Gaussian fits (not shown) were also applied on these remnants. The small dot, for each channel, corresponds to the residual of the total fit (the added contributions in emission of the Hα profile and the remnants of sky-emission). The base line (continuum) at zero is traced out to help estimate the relative importance of the residuals. The vertical and horizontal thick solid lines respectively correspond to the centroid position and the observed line width of each fitted Hα profile.

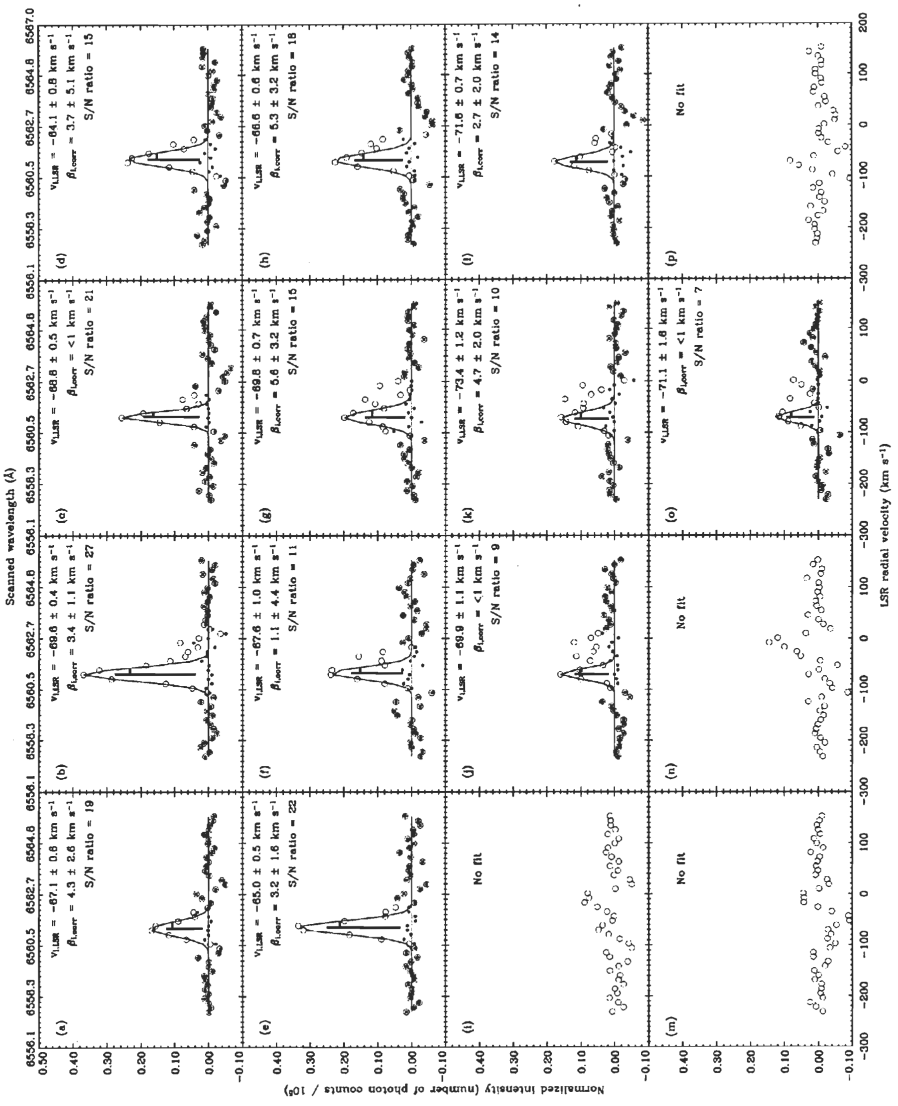

Figure 6.4: Hard binned Hα profiles for Field 22.

See caption of Figure 6.3 for more details.

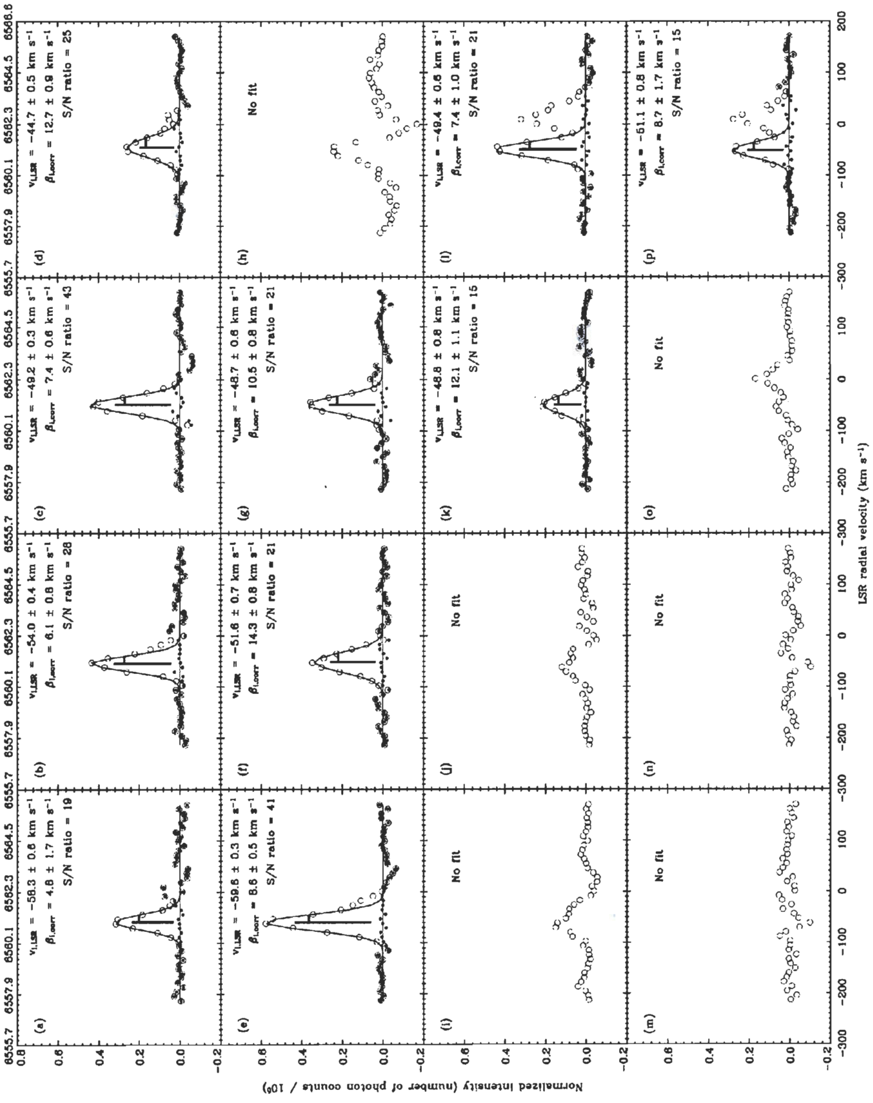

Figure 6.5: Hard binned Hα profiles for Field 23.

See caption of Figure 6.3 for more details.

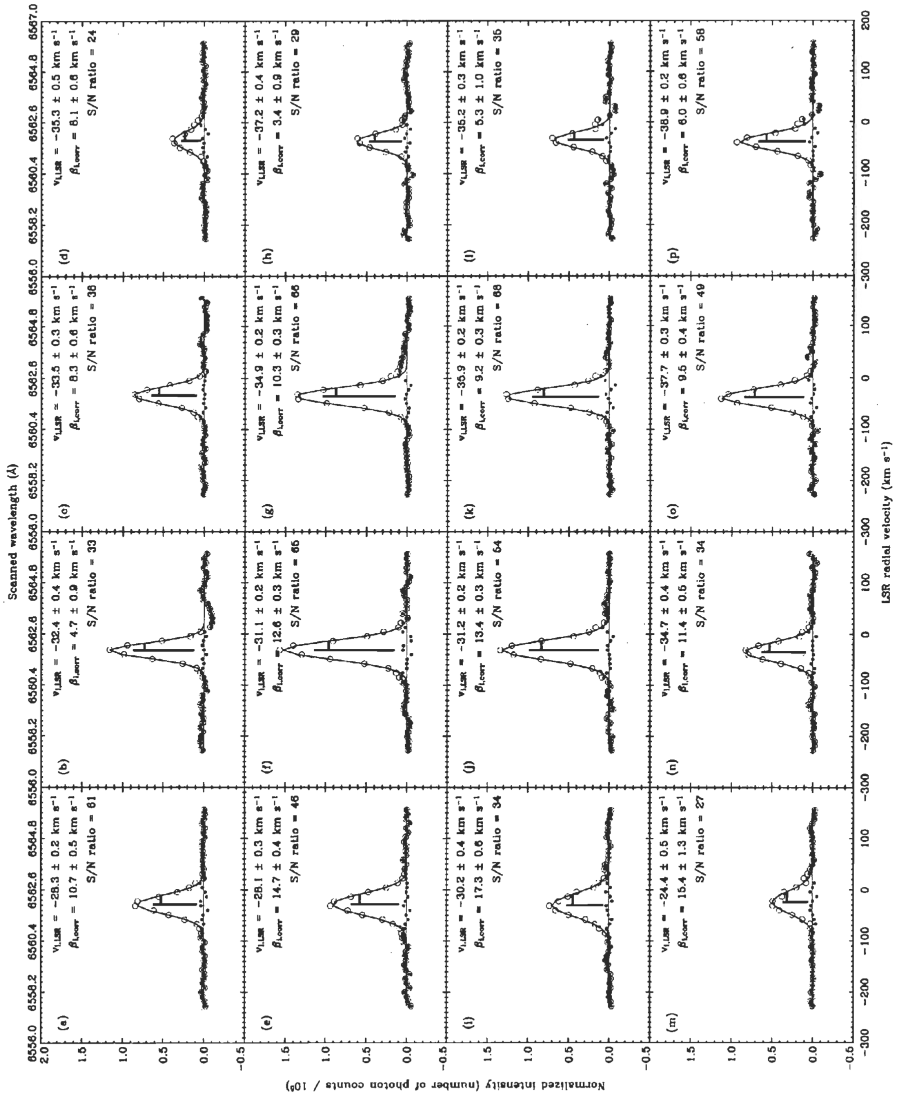

Figure 6.6: Hard binned Hα profiles for Field 24.

See caption of Figure 6.3 for more details.

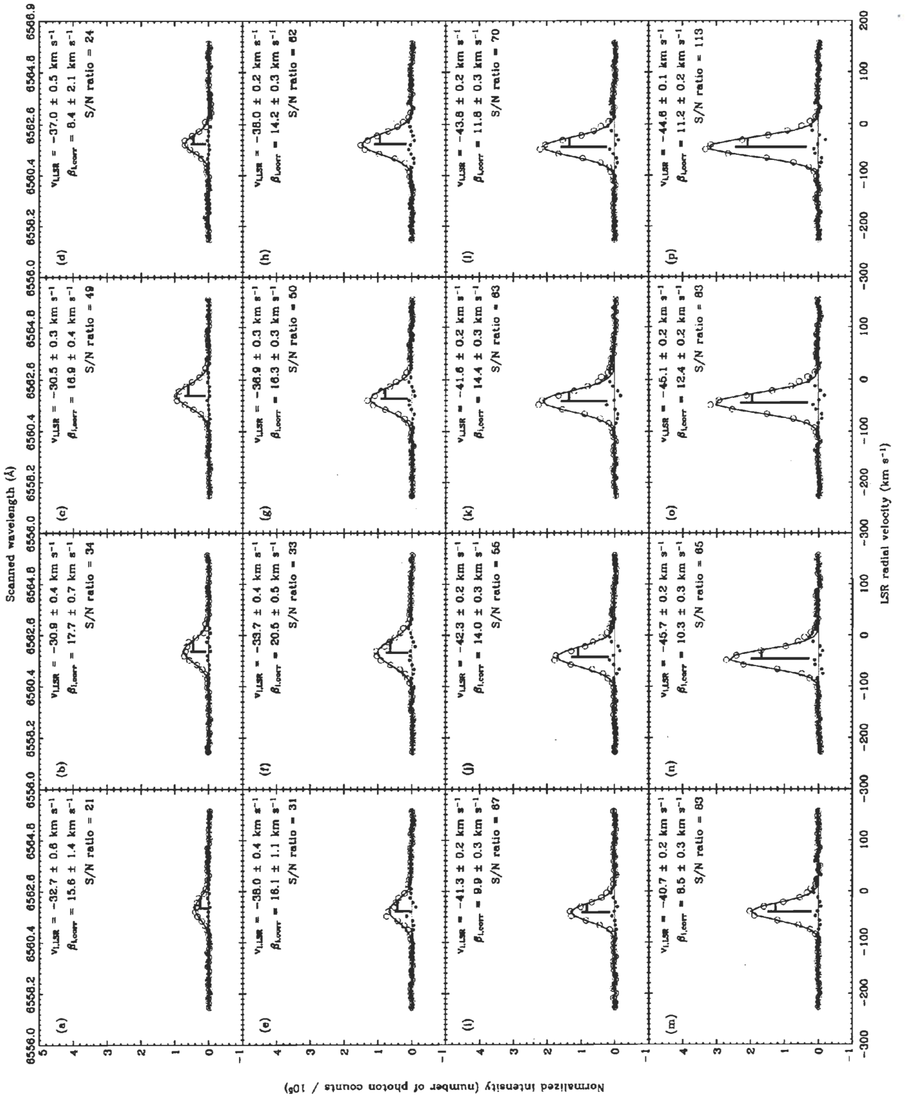

Figure 6.7: Hard binned Hα profiles for Field 25.

See caption of Figure 6.3 for more details.

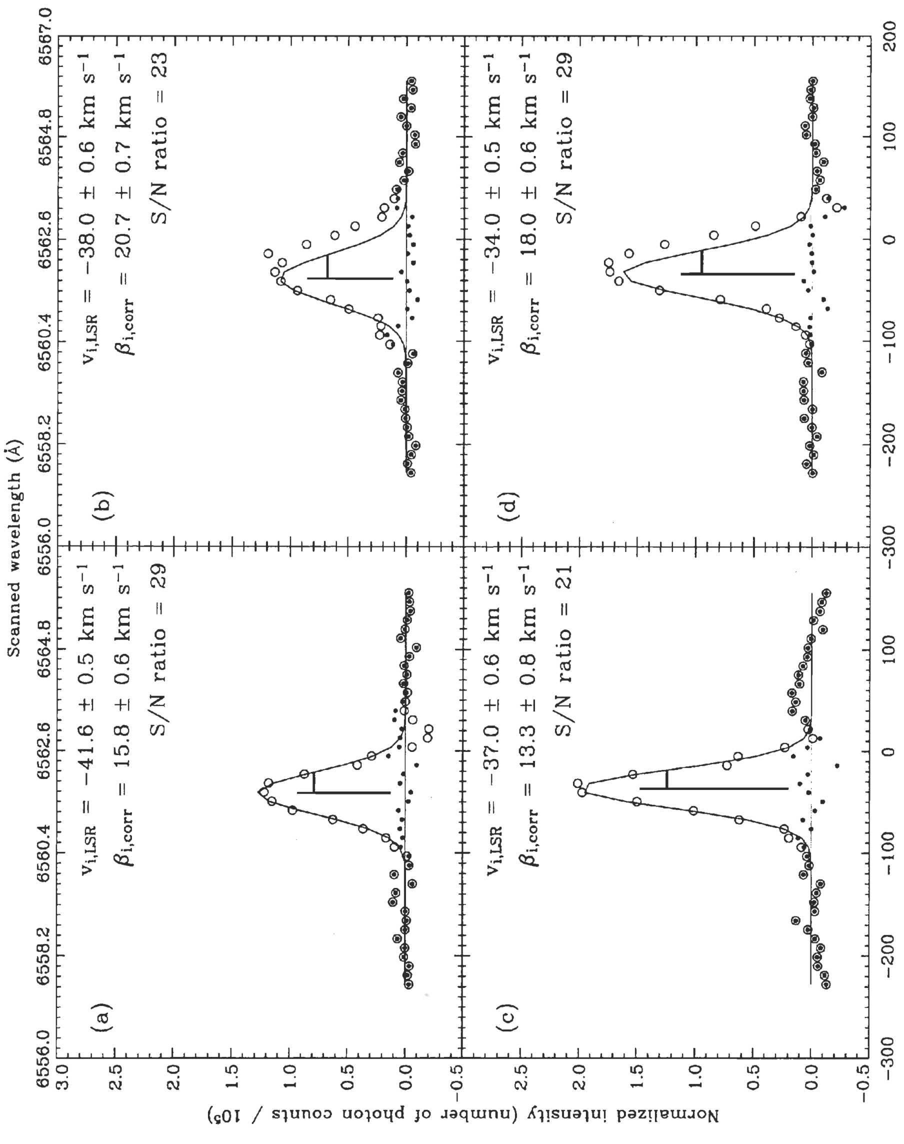

Figure 6.8: Hard binned Hα profiles for Field 26.

See caption of Figure 6.3 for more details.

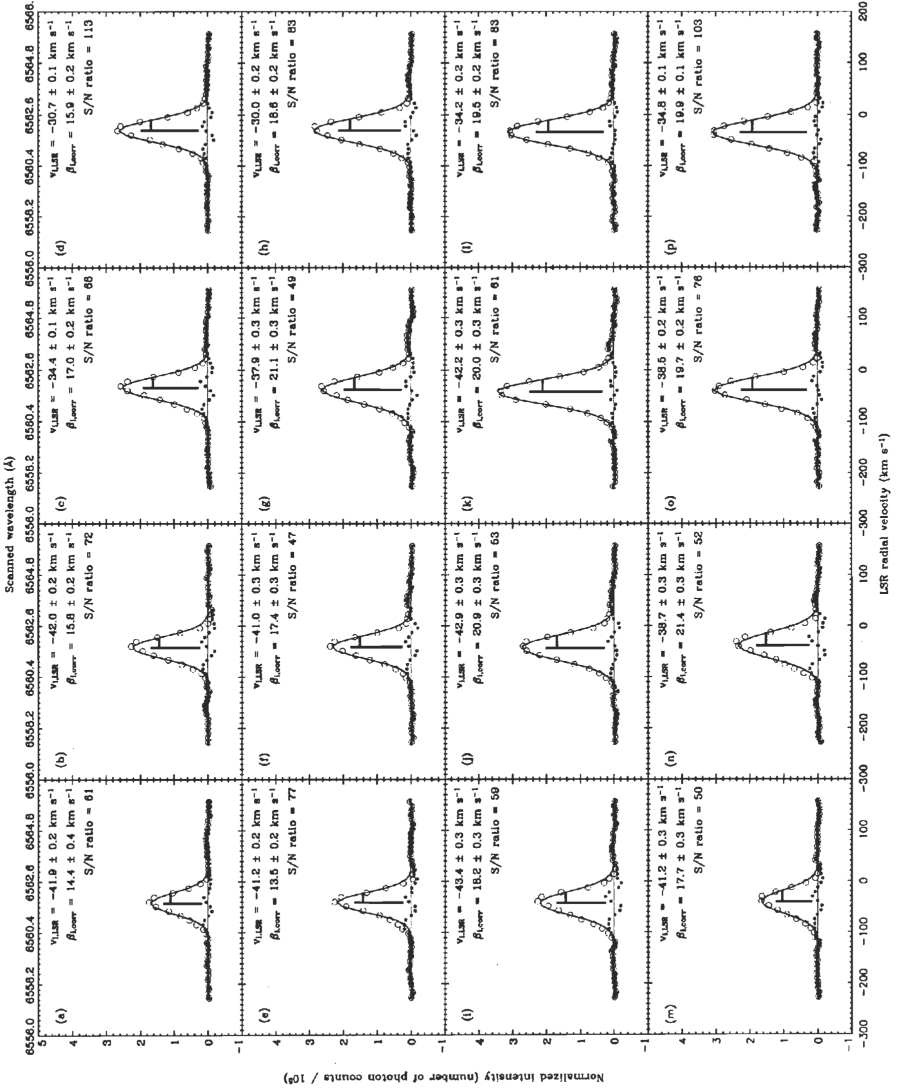

Figure 6.9: Hard binned Hα profiles for Field 27.

See caption of Figure 6.3 for more details.

Table 6.1: LSR radial velocity and line-width investigations in W4-north.

Field	Figure	Optical center (l,b)	$\langle v_{i,LSR} \rangle$ (km s^{-1})	$\langle \beta_{i,corr} \rangle$ (km s^{-1})	M	Separation (°)	Location
21	6.3	(134°.45, 6°.35)	-59.3 ± 0.5	8.6 ± 0.8	22	1°.21	Top-cap break
22	6.4	(134°.00, 6°.50)	-68.7 ± 0.8	$< 3.7^a$	28	1°.54	Top-cap break
23	6.5	(133°.85, 4°.75)	-51.5 ± 0.7	9.3 ± 1.3	26	1°.05	Top-cap break
24	6.6	(132°.60, 4°.40)	-33.1 ± 0.3	10.0 ± 0.6	28	2°.34	Western-side break
25	6.7	(133°.65, 3°.55)	-38.9 ± 0.3	13.6 ± 0.6	20	2°.01	Horizontal sheets
26	6.8	(135°.65, 4°.60)	-37.7 ± 0.6	17.0 ± 0.7	18	1°.04	Eastern shell
27	6.9	(135°.40, 3°.80)	-38.4 ± 0.2	18.2 ± 0.3	18	1°.46	Eastern shell
DF	–	(134°.80, 5°.20)	–	–	–	–	Dark Field

Note : For Fields 21 to 23, panels labeled "No Fit" were not considered in the calculation of $\langle v_{i,LSR} \rangle$ and $\langle \beta_{i,corr} \rangle$.

---

[a] An upper limit is found due to Hα line widths estimated below 1 km s^{-1}. These particular panels were not statistically considered in the calculation of $\langle \beta_{22,corr} \rangle$.

Dark and W4 fields (see Figure 6.2) is presented in Column 6. Exposure times for each W4 field can be estimated at 7×M minutes. This time does not take into account the time spent on DF (for a given W4 field, the total time of telescope required to obtain a reliable kinematics is, therefore, estimated at 7×2×M minutes). Column 7 gives the angular separation (between optical centers) between each W4 field and the Dark Field. Finally, a brief comment on the particular location of each field is provided in Column 8. The value for $\langle\beta_{22,corr}\rangle$ was treated as an upper limit due to particular Hα profiles (see Panels (c), (h), (j), and (l) in Figure 6.4) that revealed undefined (numerically) $\beta_{i,corr}$ values (see Section 4.1 in Paper I). Kinematically, these profiles were interpreted as being extremely narrow with line widths below 1 km s^{-1}, but were ignored in the calculation of the mean corrected line width of Field 22 (see Section 6.7.3). Uncertainties, in Columns 4 and 5, correspond to kinematic uncertainties obtained from the mean Hα profile associated with each field.

In the following section, we compare the kinematics of each field to see if there may be flows between fields. Relevant characteristics are presented in Table 6.2 for those fields in our Hα survey of W4-north which are probably connected in this way. The linear radial velocity and line-width gradients are presented respectively in Columns 2 and 3. In Column 4, the range corresponds to the distance on the plane of the sky separating the two connected fields. The gradients were calculated using mean values in Columns 4 and 5 of Table 6.1. Of course, we assume the flow to be continuous between the fields. Table 6.2 is mainly relevant to the verification of our model of a pierced metal container discussed in Section 6.7.2.

6.7 Discussion

6.7.1 Motivation

To determine whether or not ionized material is escaping the H II region through the fragmented shell, a large-scale investigation of the ionized gas' kinematics of W4-north is necessary. A particular kinematic signature, directed from the center of the superbubble toward the breaks, should be observed if indeed ionized material flows beyond the boundaries of W4 (see Section 6.3). A large-scale trend in radial velocities is immediately deduced from Table 6.1. On a south-north direction, apparently directed toward the top-cap break (see Figure 6.1), radial velocities change

Table 6.2: Linear kinematic connections between individual fields in W4-north.

Fields	∇_v (km s^{-1} pc^{-1})	∇_β (km s^{-1} pc^{-1})	Range (pc)
21 → 22	(-)0.49	< (-)0.26[a]	19
23 → 21	(-)0.11	(-)0.01	70
25 → 23	(-)0.24	(-)0.09	49

Note : Arrows in column 1 should be translated as "From Field XX to Field YY".

---

[a] The line-width gradient was calculated using $\langle\beta_{22,corr}\rangle = 3.7$ km s^{-1} and is therefore likely to be slightly steeper than presented. The "<" symbol signifies that the gradient can only be more negative.

approximately from -40 km s^{-1} (in Fields 25 and 27) to -70 km s^{-1} (in Field 22). In particular, values measured for $\langle v_{21,LSR}\rangle$ and $\langle v_{22,LSR}\rangle$ are clearly blueshifted with respect to the H I supershell (see Section 6.4). We believe that the kinematic behavior of the embedded material in W4-north resembles the behavior predicted by pressurized air in a metal container suddenly pierced along its wall. A simple model of this rarefaction scenario is derived in Section 6.7.2, which allows us to obtain the velocity of the rarefied material expanding toward the wall opening. In our interpretation of our Hα survey, particular attention will be given to the ionized material found in the vicinity of the possible top-cap (see Section 6.7.3) and western-side breaks (see Section 6.7.4).

6.7.2 Analogy : W4-north as a pierced metal container

We previously presented our intuition that a shell opening associated with W4-north could eventually be modeled by a rarefaction wave propagating inside a pierced metal container (see Sections 6.3 and 6.4). Figure 6.13 foreshadows the model suggested by our analysis (see Sections 6.7.3-6.7.6). To simplify the description, we will assume (for now) that only the shell's polar cap has been proned to fracture. The rarefaction wave is bordered, in Figure 6.13 by the two weak discontinuities moving in opposite directions (see Section 6.7.8) ; Discontinuity-N is moving toward the Galactic corona and Discontinuity-S toward the Galactic mid-plane. Discontinuity-N is labeled by a question mark since no kinematic information is provided by our Hα survey above Field 22. This field, still showing evidence for an accelerated ionized component (see Table 6.1), indicates that Discontinuity-N can be located somewhere above $b \sim 6\overset{\circ}{.}5$ (see Section 6.7.7). The location of Discontinuity-S in Figure 6.13 is investigated in detail in the discussion to follow.

We follow Landau & Lifshitz (1987, Chapter 10), who present textbook examples of semi-infinite cylindrical pipes in which rarefaction waves dominate the kinematics of the embedded gaseous material. The particle density and pressure of any gas element within a pipe decrease as the wave moves. This basically defines rarefaction. Rearranging the authors' equation (99.15), we obtain the relation for the velocity v_ρ of the gaseous material behind (above) Discontinuity-S with respect to the gas said at rest located in front of (below) it :

$$v_\rho = \frac{2c_0}{(\gamma - 1)} \times \left[1 - \left(\frac{\rho}{\rho_0}\right)^{\frac{\gamma-1}{2}}\right], \tag{6.1}$$

where c_0 is the speed of sound in the vicinity of the gas at rest, γ is the heat capacity ratio of the accelerated material, and ρ_0 is the particle density of the gas at rest. The variable ρ is the local particle density of the rarefied material. For W4, the speed of sound was estimated at 10 km s^{-1}. The heat capacity ratio of a monoatomic ideal gas, neutral or ionized, is 5/3. However, the lack of energetic photons at high-galactic latitudes (Terebey *et al.* 2003; Dennison *et al.* 1997; West 2003) suggests that the plasma in W4-north can be interpreted as a mixture of perfect gases still undergoing ionization (this can be seen, in particular, from a thin H I supershell above $b = 4°$ and the presence of the H I horizontal sheets). The heat capacity ratio's equation for atomic hydrogen is provided by Cox & Giuli (1968, Chapter 9) and is shown in Figure 6.10 for an ionization rate between 0 and 1. A portion of the curve is isolated for an ionization rate between 0.95 and 0.99, a range of values we consider plausible for W4-north. The heat capacity ratio is, therefore, estimated between 1.10 and 1.30.

From equation (6.1), a family of curves is traced out in Figure 6.11 for five different values of γ (1.10, 1.15, 1.20, 1.25, and 1.30). The relations show the expected behavior in velocities as the gaseous material is rarefied (toward Discontinuity-N) following the passing of Discontinuity-S (see Figure 6.13). Since the value for ρ/ρ_0 diminishes as the material moves away from Discontinuity-S, a relation is likely to exist between a particular gas element's particle density and the distance it has tra-

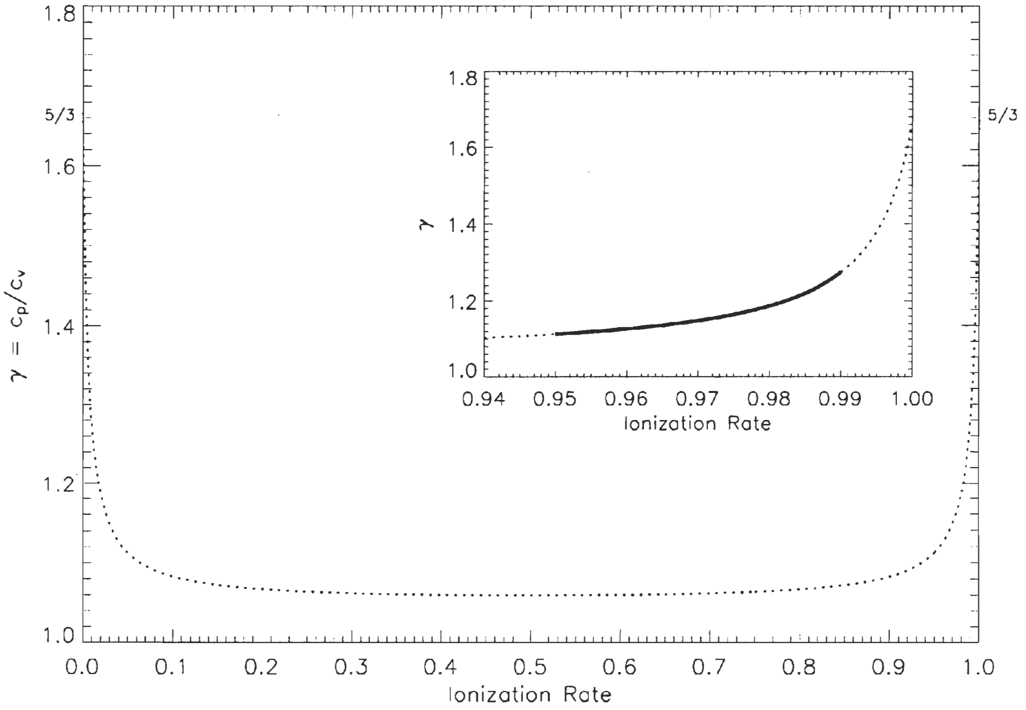

Figure 6.10: Heat capacity ratio for monoatomic hydrogen undergoing ionization.

The dotted curve is obtained from equation (9.169) of Cox & Giuli (1968) assuming an electron temperature of 7400 K. The magnified curve (solid line) isolates the heat capacity ratio for an ionization rate between 0.95 and 0.99.

veled inside the rarefaction wave (i.e., between the two discontinuities). The abscissa in Figure 6.11 is, therefore, an indicative of the distance (increasing from right to left) separating the accelerated material and the discontinuity moving into the gas at rest. The velocity gradient remains constant until the ratio ρ/ρ_0 reaches approximately 10%. Over the same range, the variations of γ do not seem to have sizeable repercussions on the kinematic behavior (this remains true for roughly any value of γ below 1.50). Below 10%, however, the velocity gradient becomes much steeper and presents a larger dispersion with the heat capacity ratio since the $(\gamma - 1)^{-1}$ term dominates the exponent in equation (6.1). In every case, the peak velocity is found at $2c_0/(\gamma - 1)$ when the rarefied material becomes so tenuous that its local particle density can be interpreted as 0 with respect to the density of the gas at rest ($\rho/\rho_0 \rightarrow 0$). For the analogy of a pierced metal container, this corresponds to the maximal velocity at which the embedded pressurized air can be ejected through the opening (using, obviously, the correct values for c_0 and γ).

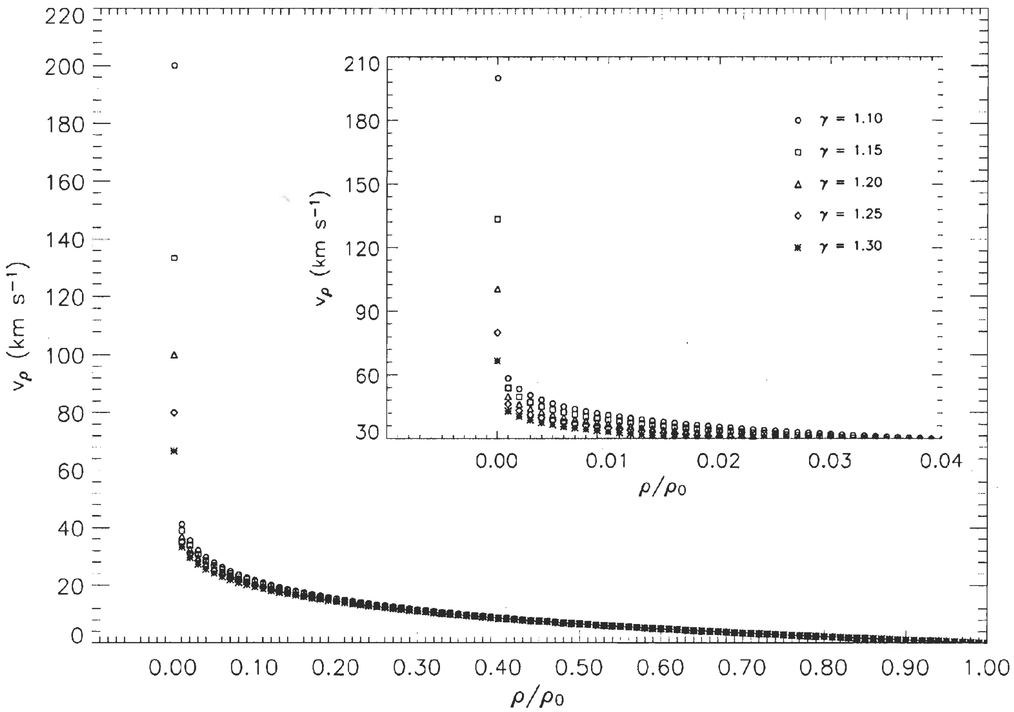

Figure 6.11: Behavior in velocities expected in a rarefaction wave.

Equation (6.1) was plotted using $c_0 = 10$ *km* s^{-1}. *The velocity* v_ρ *of the rarefied material (measured with respect to the gas at rest) is traced out w.r.t.* ρ/ρ_0. *The variable* ρ *indicates the local particle density of the rarefied material while* ρ_0 *indicates the particle density of the gas at rest. Discontinuity-S is located at* $\rho/\rho_0 = 1$ *and Discontinuity-N, at* $\rho/\rho_0 = 0$ *(see Figure 6.13). The five curves correspond to different values of the heat capacity ratio :* $\gamma = 1.10$ *(open circles), 1.15 (open squares), 1.20 (open triangles), 1.25 (open diamonds), and 1.30 (stars). The magnified curves correspond to the possible solutions for W4-north.*

The model presented here is unidimensional and would be appropriate if we suppose chimneys to form in a roughly cylindrical shape. In this case, only a corrective term, required from the fact that we measure radial velocities and, therefore, taking into account the angle of inclination of the "cylinder" with respect to the observer, would need to be applied to the curves in Figure 6.11. However, the W4 region, in particular, brings some geometrical constraints. For example, the apparent size of the top-cap break is much smaller ($\sim 10\%$) than the maximal width of the large superbubble (West *et al.* 2007). We, therefore, assume the zone of rarefaction, between the two discontinuities in Figure 6.13, to resemble the shape of an inverse light bulb. Our model might, therefore, be proned to uncertainties as we investigate at ionized material located more and more away from a central vertical axis passing by $l \sim 134.°2$. Moreover, a probable western-side break (see Section 6.7.4) would certainly induce a rather complicated kinematics in W4-north since the embedded ionized material would be dominated by two rarefaction waves instead of one. All of these reasons demand a three-dimensional model to be eventually derived.

Our one-dimensional model also does not provide indications for the behavior in line widths as the ionized material travels away from the discontinuity moving into the gas at rest. First, we must consider the fact that the gas at rest, in W4, probably presents a kinematics in agreement with what we referred to as the "chaotic" interflow medium in Paper I. From its location close to the center of the W4 superbubble, this component likely present a large diversity of radial velocity gradients along the line of sight (a large volume of embedded ionized material being investigated). Moreover, freshly ionized material is constantly provided resulting from the photoionization of the atomic shell. The sustainment in gas likely contributes to turbulence in the interflow medium. These arguments are all related to the large Hα profiles observed in Paper I. Intuitively, we can anticipate line widths will decrease above the southern discontinuity in Figure 6.13 for two reasons. First, the production of turbulence being suppressed following the passing of a rarefaction wave (Gol'dfel'd *et al.* 1987), we expect a monotonic dissipation of the vorticity as the material travels away from the southern discontinuity. Secondly, the fact that the rarefied material converges straight at the shell opening diminishes the number of radial velocity gradients along the line of sight in the zone of rarefaction. Our assumptions, therefore, propose the ionized material found above Discontinuity-S to generally appear more and more "ordered" with latitude. For our Hα survey, this would result in a narrowing of the observed line widths with spatial change (from Discontinuity-S to -N). This line narrowing gradient (see the definition used in Section 4.1 of Paper I) should, therefore, be correlated with the large-scale radial velocity gradient expected from Figure 6.11.

6.7.3 Top-cap break

Gathered in the vicinity of the H I-spur filament (Normandeau 2000), Fields 21 and 22 coincide with the northernmost latitudes investigated in our Hα survey. We reiterate the fact that this particular region of W4 appears as a closed shell lining in Hα images but also reveals a fracture according to the atomic observations (see Section 6.4), therefore, pinpointing a possible top-cap break in a very low density H I shell. From Figure 6.1, Fields 21 and 22 are located slightly above the hypothetical H I fracture. At this height above the star cluster IC 1805, the ionized material is extremely tenuous (Dennison *et al.* 1997). This can be seen from Figures 6.3 and 6.4 where the extraction of reliable information has not been possible for particularly faint areas labeled "No Fit". We assume the faint Hα emission detected in both fields to be associated with the polarized data (tracing the superbubble) of West *et al.* (2007) rather than, say, foreground objects.

Examination of Table 6.1 shows that the northern Field 22 is more blueshifted, and has narrower lines, than the lower latitude Field 21. This can be interpreted as a south-north flow. The fact that $\langle v_{21,LSR} \rangle$ and $\langle v_{22,LSR} \rangle$ do not coincide with the radial velocity range of the H I supershell (see Sections 6.4 and 6.7.1) makes it difficult to associate the ionized gas with the shell. From our model presented in Section 6.7.2, the orientation indicated by the line narrowing gradient should be correlated with the direction of the ionized flow itself. From the slight tilt toward the observer expected from the W4 superbubble (Normandeau *et al.* 1996; Lagrois & Joncas 2009a) and the well-defined blueshifted radial velocity gradient directed toward the Galactic corona, we propose the observed behavior to correspond precisely with the signature anticipated from the passing of a rarefying discontinuity, the rarefaction wave itself being induced by the appearance of an opening near the shell's polar cap.

In Figure 6.3, the south-north tendency toward line narrowing is also well-defined intrinsically in Field 21. From a roughly sonic regime in Panels (j) to (l), northern edge's line widths present values slightly above 6 km s^{-1}. The south-north blueshifted radial velocity gradient is also easily detected within Field 21 in agreement with the tendency presented on a larger scale in Table 6.1. Particularly visible along the two middle columns from Panels (n) and (o) to (b) and (c) respectively, the kinematic trend leads to northern radial velocities slightly more negative than -60 km s^{-1}.

On an intermediate scale, estimated at roughly 19 pc between Fields 21 and 22, the radial velocity and line-width gradients are found respectively at $\nabla_v = (\text{-})0.49$ km s^{-1} pc^{-1} and $\nabla_\beta = (\text{-})0.26$ km s^{-1} pc^{-1} (see Table 6.2). The larger (in absolute value) radial velocities obtained from our Hα survey are found in Figure 6.4 where lower panels show radial velocities slightly below -70 km s^{-1}, blueshifted by nearly 25 km s^{-1} with respect to the neutral expanding supershell. The Hα line widths also show a clear continuity from Field 21 to 22 as the highly accelerated ionized material evacuates the W4 superbubble, aiming toward the Galactic corona. In fact, four panels in Figure 6.4 present Hα profiles so narrow that the spectral resolution of our interferometric device system does not allow us to properly resolve the width of the fitted lines. Hence, either (1) the kinematic disorder (including turbulence) is minimal along the line of sight (see Section 6.7.7), (2) the electron temperature is smaller than the canonical value (7 400 K) used so far in this work, or (3) all of the above. A good estimate of the electron temperature is critical in order to convert observed line widths in purely kinematic line widths (see Section 3 in Paper I). Certainly, a slight overestimation of the electron temperature[2] in W4-north is plausible if we assume a large fraction of the most energetic photons (of the star cluster IC 1805) to be absorbed by neutral material embedded in W4-south (see Paper I). The overestimation will lead (numerically) to line widths narrower than it should be. However, the fact that the abundance of neutral material in W4-north is relatively small (see Section 6.7.2), we can argue that the electron temperature is probably constant in W4-north and does not decrease with latitude. Therefore, the line narrowing gradient pointing toward the Galactic corona is genuine. On the other hand, the overestimation of the thermal broadening likely contributes to undefined $\beta_{i,corr}$ values (< 1 km s^{-1}) in Field 22.

From our investigation of Fields 21 and 22, it is reasonable to assume that a discontinuity associated with a rarefaction wave had previously accelerated and forced the ejection of ionized material beyond the boundaries of the W4 superbubble. In order to estimate the distance over which this discontinuity, traveling toward southern latitudes, has affected the embedded ionized material, Field 23 was observed. The field resides halfway between the northern polar cap and the possible western-side break (West *et al.* 2007). A particularly weak signal is observed near

---

[2] The lower limit for the electron temperature of the Galactic diffuse ionized medium (hereafter, DIM) has been estimated to 5 400 K from forbidden line intensities (Reynolds 1989b).

its south-east boundary. Six panels in Figure 6.5 have failed to show well-defined profiles mainly due to a slight overlap with the Hα-poor cavity observed in the middle of W4-north (see Figure 6.1). In agreement with Fields 21 and 22, Figure 6.5 shows a clear tendency toward line narrowing from the middle Panels (f), (g), and (k) to the north-east boundary in Panels (a), (b), and (e). The line-width gradient is precisely oriented toward the top-cap break. The anticipated blueshifted radial velocity gradient is also observed as northern radial velocities are found barely more positive than -60 km s^{-1}, slightly redfshifted with respect to the radial velocities in the northern portion of Field 21. This is however in agreement with Field 23 being located closer to the southern discontinuity than Field 21 and, therefore, presenting a kinematics slightly more in agreement with what we expect from the gas at rest (see Figure 6.11). From the values obtained in Table 6.1 for $\langle v_{21,LSR} \rangle$ and $\langle v_{23,LSR} \rangle$, we calculated a particularly flat radial velocity gradient estimated at $\nabla_v = (\text{-})0.11$ km s^{-1} pc^{-1} in Table 6.2. The gradient is however likely limited (in steepness) from the fact that it is measured on a more or less oblique axis (see Section 6.7.7). Moreover, considering the W4 superbubble to be only slightly tilted toward the observer (an argument used in Paper I to explain the low kinematic disorder on the plane of the sky), relatively flat radial velocity gradients are not surprising in W4-north. Hence, our model presented in Section 6.7.2 essentially uses kinematic observations in order to describe a scenario of outward gas venting occurring over a particularly extended range, rather than associated with a very steep gradient.

A well-defined signature in the northern portion of W4-north allowed us to confirm striking similarities between our model of a rarefaction scenario and the kinematics of Fields 21 to 23. A kinematic impact on the embedded ionized material has been observed on a range estimated at 72 pc between Fields 22 and 23 and was attributed to a rarefying discontinuity associated with the top-cap break and propagating toward the Galactic mid-plane. An investigation on a larger scale will however be provided in Section 6.7.7. We will also compare, in Section 6.7.8, the rate of escape of the ionized material through the chimney with respect to the filling rate in W4-north (provided by the inner erosion of the atomic shell). The fact that the polar cap, in particular, has been proned to shell instabilities (and, therefore, fracture) is not surprising since a low particle density is expected from upstream ISM material more and more tenuous with the increasing galactic latitude. A low electron density is directly correlated with a low recombination rate of the ionized shell (Dyson & Williams 1980, Chapter 5). Numerical simulations have shown the amplitude of developing instabilities to enter a growth regime when recombination processes are turned off or highly diminished (Mizuta *et al.* 2005). The kinematic confirmation of a top-cap break is of great importance as it clearly indicates that the W4 superbubble is currently evolving into a chimney. Considering the remarkable alignment (toward the Galactic corona) taken by the top-cap break, escaping photons (through the hole) will undoubtedly contribute to the sustainment of the high-latitude Reynolds loop (Reynolds *et al.* 2001).

6.7.4 Western-side break

The investigation of the second breakout identified by West *et al.* (2007) is provided by Field 24. A brief review should however bemade on Field 23. We already demonstrated its upper half to enclose ionized material kinematically in agreement with the presence of a top-cap break (see Section 6.7.3). On the other hand, a second gradient toward line narrowing is possible, from the middle to the lower panels in Figure 6.5, oriented toward the western-side break. However, Figure 6.6 (for Field 24) does not favor any connection with Field 23 as its eastern boundary shows supersonic line widths. From our model (see Section 6.7.2), we would expect a significant decrease in line widths from the lower panels in Figure 6.5 to the easternmost panels in Figure 6.6 as the ionized flows converge toward the western-side break.

Certainly, we anticipate the embedded material in W4-north to be kinematically dominated by two possible regimes : the erosion of the embedded atomic material (H I walls and horizontal sheets) or the large-scale trend expected from rarefaction waves. The former possibility was largely discussed in Section 5.3 of Paper I in which we suggest the eroded material to lag behind the advancing (toward the observer) bubble. This is similar to the wake of material behind a solid body moving in a viscous fluid. The resulting kinematics is likely to show an ionized component redshifted with respect to the H I supershell. This is what was found for Fields 04, 17, and 18 in Paper I. However, the radial velocities approaching -50 km s^{-1}, in Panels (k), (l), and (p) of Figure 6.5, do not coincide with this scenario. Even though a possible implication of the western-side break near $b = 5°$ has been ruled out by the disconnection in line widths between Fields 23 and 24, the kinematics of Field 23 seems to be entirely attributed to the passing of a rarefying discontinuity propagating toward southern latitudes. We, therefore, assume that the kinematic repercussions attributed to the top-cap break can be found on a distance that likely exceeds the 72 pc range previously estimated (see Section 6.7.5).

On the other hand, the investigation of Field 24 provides inconclusive results for the presence of a western-side break. Certainly, the blueshifted radial velocity gradient combined with a line narrowing gradient (both being precisely oriented toward the western wall) represent a signature identical to the kinematic behavior observed in Field 21. However, radial velocities between -30 and -40 km s^{-1} do not present a significant discrepancy with the radial velocity range of the H I supershell. In fact, interpreting Figure 6.6 along a west-east direction, the kinematic behavior appears very similar to what we would expect from the erosion of atomic material. The radial velocity gradient presents a redshifted tendency estimated between 1.1 and 2.3 km s^{-1} pc^{-1} (these are respectively the flatter and steeper gradients measured from the four rows in Figure 6.6), perfectly matching our results for Flows D, T, and U in Paper I. A line broadening gradient is found slightly below 2 km s^{-1} pc^{-1}, also coinciding with Flow D. However, the investigation of the CGPS H I observations clearly indicates that the shell is ill-defined in the vicinity of Field 24 (Normandeau *et al.* 1997). This argument alone favors the large side break detected by (West *et al.* 2007) while the striking similarities established between Field 24 and Fields 04, 17, and 18 are likely coincidental.

Two reasons are proposed to explain why the kinematics of Field 24 does not indicate the presence of a shell opening along the western wall of W4. First, if the outflows are oriented roughly perpendicular to the line of sight (in other words, if the outflows do not "follow" the tilt of the superbubble as we would expect), this particular geometry would artificially maintain the radial velocities roughly in agreement with the gas at rest. The important discrepancy in radial velocities between the ionized material and the H I supershell (see Section 6.7.3) would remain undetected. Secondly, it can be assumed that the western-side break is relatively young or, at least, much younger than the top-cap break. We can reiterate the fact that the development of shell instabilities in an expanding superbubble is supposed to initially occur near the shell's polar cap (Dove *et al.* 2000). In this case, it is reasonable to assume that the rarefaction near Field 24 would still be very low (that is, to assume a ρ/ρ_0 value, introduced for Figure 6.11, very close to 1). This assumption, we believe, supercedes the first one; not only does it explain radial velocities almost in agreement with the atomic shell but it is also in agreement with the east-west gradients (in radial velocities and line widths) observed in Field 24. We, therefore, propose a scenario in which a discontinuity, probably located not too far away from the field's eastern boundary, travels toward larger longitudes. In order to further investigate on a possible western-side break, a western extension to Field 24 is required (e.g., the dashed line "empty field" on the right of Field 24 in Figure

6.1). This extension would certainly enclosed ionized material more rarefied (than in Field 24) and, therefore, radial velocities slightly more different than the atomic shell.

Similar to the top-cap break, the implication of a western-side break is also important from the point of view of the dynamical evolution of the expanding wind-blown bubble (see Section 6.7.8). However, its hypothetical orientation, favoring evacuated flows of ionized material roughly parallel to the Galactic mid-plane, would not allow for an efficient connection with the Galactic corona. On the other hand, the escaping photons would certainly contribute to the photoionization and sustainment of the DIM found at low-galactic latitudes (Mathis 1986).

6.7.5 Horizontal sheets

The H I horizontal sheets mark the boundary between the relatively emissive W4-south region and the much fainter W4-north. The spectroscopic 21 cm line observations of the CGPS revealed the horizontal sheets on a LSR radial velocity range between -38 and -45 km s^{-1} (Normandeau *et al.* 1997). Roughly located at the geometrical center of the expanding superbubble, Field 25 investigates the kinematic behavior of the tenuous ionized material found below the Hα-poor cavity (see Figure 6.1).

Similar to Field 23, the north-east portion of Field 25 is (spatially) close to the imposing dark region almost fully deprived of Hα emission. In Figure 6.7, this leads to weaker Hα profiles in Panels (a), (b), and (e). Radial velocities approaching -45 km s^{-1} can be found in Panels (n) to (p), slightly blueshifted with respect to the horizontal sheets ; the neutral features are particularly well-defined at this specific location with radial velocities between -41 and -42 km s^{-1} (Normandeau *et al.* 1997). From the four columns in Figure 6.7, a south-north radial velocity gradient, directed toward the top-cap break, is estimated to be between 1.2 and 2.3 km s^{-1} pc^{-1}. The gradient is redshifted (with respect to the southern panels in Figure 6.7) and, therefore, cannot be related to the same dynamical process described for Fields 21 and 22 (see Section 6.7.3). On the other hand, the gradient's steepness perfectly matches the radial velocity gradients observed for Flows D, T, and U in Paper I. In fact, the kinematics of Field 25 is almost identical to what was found for Fields 04, 17, and 18 ; the ionized material, eroded from the horizontal sheets, could be observed in the wake of the advancing (toward the observer) neutral filaments. This supposes the horizontal sheets to be located in front of the star cluster, tilted in a way that their southern edge is slightly in front of their northern edge (from a side point of view). Assuming this scenario, the lagging material would certainly be in agreement with the redshifted radial velocity gradient.

Disregarding the western column from Panel (p) to (d), a line broadening gradient, pointing away from the atomic material, is estimated at 0.8 km s^{-1} pc^{-1} in Figure 6.7. The gradient is much flatter than 2.1 km s^{-1} pc^{-1}, the value measured for ∇_β in Flow D (see Table 4 in Paper I). However, the steepness coincides very well with the line width gradients estimated for Flows T and U (see Table 4 in Paper I). The discrepancy in line widths between Flow D and Flows T and U was explained by much more tenuous atomic material in Fields 17 and 18 when compared to Field 04 (see Section 5.3 in Paper I). Larger line widths can be partially related to the accumulation of different radial velocity gradients along the line of sight and this scenario is highly favored in presence of dense erodible material. If we assume the particle density of the horizontal sheets to roughly equal the one of the W4 eastern shell near Fields 17 and 18, it could explain the line-width behavior in Field 25. The fact that $\langle\beta_{25,corr}\rangle$ (see Table 6.1) is well into the supersonic regime, and roughly in agreement with $\langle\beta_{\mathrm{interflow},corr}\rangle$ (see Figure 4 in Paper I), could indicate a kinematics also partially explained by the interflow medium (see Section 6.7.7). This is expected since the location of Field 25 allows for deep lines of sight through the W4 superbubble (see Section 6.7.2).

However, the proximity of Field 25 to the Hα-poor cavity (see Figure 6.1) may also be a factor that explains the relatively flat south-north line broadening gradient in Figure 6.7. In Section 6.7.3, the kinematics of Fields 21, 22, and 23 were presented as being directly related to the passing of a rarefying discontinuity propagating toward the Galactic mid-plane and associated with an opening near the shell's polar cap. If we assume that Discontinuity-S has reached the vicinity of Field 25 (see Figure 6.13), the Hα-poor cavity in Figure 6.1 could be filled of accelerated ionized material (flowing toward the top-cap break), rarefied to such a degree that it becomes roughly invisible (see Section 6.7.7). The ionized component of Field 25 could, therefore, be the most recently material "incorporated" into the evacuation process (in Figure 6.11, this corresponds to material found at $\rho/\rho_0 = 1$).

The transition (from unperturbed to accelerated and rarefied material) could initially be characterized by a localized attenuation of the line broadening gradient (expected from the erosion of the H I material) before becoming the line narrowing trend observed on a larger scale (see the kinematic connections between Fields 23 and 21 and Fields 21 and 22 in Table 6.2). If this attenuation takes place on a range of a few parsecs on the plane of the sky, the line-width gradient's flatness in Field 25 might correspond to it. However, a northern extension of Field 25, at the periphery of the Hα-poor cavity (e.g., the dashed line "empty field" above Field 25 in Figure 6.1), would be required in order to precisely detect the kinematic signature anticipated from a rarefaction wave. The kinematic connection between Field 25 and Field 23 is presented in Table 6.2. A factor of two is measured between the radial velocity gradient connecting Fields 25 and 23 and the one connecting Fields 23 and 21. Again, this is due to the particularly oblique connection linking the two latter fields (see Sections 6.7.3 and 6.7.7). On the other hand, the line narrowing gradient between $\langle \beta_{25,corr} \rangle$ and $\langle \beta_{23,corr} \rangle$, nine times steeper than for Fields 23 to 21, is probably associated with more than just a geometrical effect (see Section 6.7.7).

The investigation of Field 25 proposes the southern discontinuity (associated with the polar cap's rarefaction wave) not to have traveled below the threshold fixed by the H I horizontal sheets. Even though the particular kinematic signature expected from our model in Section 6.7.2 could not be explicitly identified near $b = 3\overset{\circ}{.}5$, we anticipate the southernmost signs of gas venting outwards to appear slightly below the Hα-poor cavity. This would give a range of roughly 125 pc separating the southern discontinuity and Field 22 slightly above the top-cap break's vicinity (see Section 6.7.7).

6.7.6 High-latitude eastern wall

The investigation of the W4 eastern wall at high galactic latitude ($b > 3°$) is provided by Fields 26 and 27. Non-photometric sky conditions, absorbing high-altitude cirrostratus, and a lack of accumulated cycles have constrained us to spatially degrade the raw data cube of Field 26 to obtain 2×2 images. Even though the statistics are poor (only four points being available in Figure 6.8), the detected motion of the ionized material is nonetheless in agreement with the kinematic behavior observed in Fields 04, 17, and 18 (see Paper I). From the inner erosion of the eastern wall, lagging material seems to flow toward the center of the wind-blown bubble. On an east-west direction, the redshifted radial velocity gradient is estimated as slightly below 1.1 km s^{-1} pc^{-1}. From the location of Field 26, roughly 5 to 8 pc separates it from the eastern wall. Extrapolating the radial velocity gradient leads to radial velocities roughly in agreement with the 21 cm line observations showing the neutral shell with velocities between -43 and -46 km s^{-1} (Normandeau *et al.* 1997). In Figure 6.8, the expected east-west line broadening gradient is found at 1.2 km s^{-1} pc^{-1}, a steepness that coincides with an intermediate case scenario between Flow D and Flows T and U. Eastern line widths in Panels (a) and (c), well above 10 km s^{-1}, also clearly indicate a gradient "in progress" since a transition from a subsonic to a supersonic regime is expected from the inner erosion of the neutral wall (see Section 5.3 in Paper I). Extrapolating the line-width gradient for the missing range between Field 26 and the compressed shell leads to line widths between 4 and 8 km s^{-1} in agreement with dispersion values associated with the shell material in Fields 04, 17, and 18 (see Paper I).

Similar to Field 26, Field 27 is characterized by a redshifted radial velocity gradient again directed away from the neutral wall toward the Hα-poor cavity and is estimated to be just below 1.5 km s^{-1} pc^{-1} in Figure 6.9. A 30 pc interval separates the optical center of Field 27 from the nearby eastern shell. Extrapolation, on this range, of the radial velocity gradient leads to radial velocities more negative than -80 km s^{-1}, obviously in disagreement with the 21 cm line observations (Normandeau *et al.* 1997). The inner erosion of the eastern wall does not properly explain the kinematic behavior of Field 27. Table 6.1 presents a slightly blueshifted value for $\langle v_{27,LSR} \rangle$ when compared to $\langle v_{26,LSR} \rangle$. Given a larger distance separating Field 27 from the neutral shell (than Field 26), we would expect a redshifted tendency between mean radial velocities from Field 26 to Field 27. The complicated kinematic behavior seen in Figure 6.9 could be related to a contribution of radial velocities more negative than -38 km s^{-1}. This blueshifted material (with respect to $\langle v_{27,LSR} \rangle$) is likely to be associated with the photoerosion of the H I horizontal sheets. At the longitude of Field 27, the neutral filaments present radial velocities just below -45 km s^{-1}, slightly blueshifted from the H I material found in the vicinity of Field 25 (Normandeau *et al.* 1997). Criss-crossing ionized flows resulting from the proximity of two distinct erodible features (the filaments and the H I wall segment) could explain the accumulation of different gradients along the line of sight of Field 27. This would also explain the value for $\langle \beta_{27,corr} \rangle$, about 20 km s^{-1} which is the largest observed in both W4-south and -north.

6.7.7 A large-scale trend in W4-north

The investigation of the ionized material in W4-north (see Sections 6.7.3-6.7.6) implies there are kinematic connections, in radial velocities and line widths, between four of our Hα fields (see Table 6.2). Figure 6.12 provides, on a vertical scale of roughly 125 pc, the large-scale trends of W4-north. Field 25 (see Table 6.1) coincides with the kinematics of the gas at rest near the southern discontinuity caused by the top-cap break's rarefaction wave. Every radial velocity and line-width point in Figure 6.12 is measured with respect to $\langle v_{25,LSR} \rangle$ and $\langle \beta_{25,corr} \rangle$, respectively. This can be justified from the fact that Field 25 displays mean values of radial velocity and line width in agreement with $\langle v_{\mathrm{interflow},LSR} \rangle$ and $\langle \beta_{\mathrm{interflow},corr} \rangle$ for the interflow medium (see Section 6.7.5). The interflow medium was introduced, for W4-south, as ionized material not a priori associated with a well-identified or well-defined Champagne flow (see Paper I). These areas seem to be partially formed of material that results from the inner photoerosion of the H I supershell. In Paper I, we supposed this interflow medium to account for a large fraction of the embedded ionized material in W4 and, therefore, likely constitute the medium in which the weak discontinuity propagates (toward the Galactic mid-plane). The abscissa in Figure 6.12 corresponds to the distance on the plane of the sky separating each field from Field 25. Each panel shows two particular trends : relatively flat radial velocity ($\nabla_v = (\text{-})0.17$ km s^{-1} pc^{-1}) and line-width ($\nabla_\beta = (\text{-})0.04$ km s^{-1} pc^{-1}) gradients between Fields 25, 23, and 21 while Fields 21 and 22 are spatially connected by much steeper relations ($\nabla_v = (\text{-})3.13$ km s^{-1} pc^{-1}, $\nabla_\beta = (\text{-})1.63$ km s^{-1} pc^{-1}). The gradients differ in steepness from Table 6.2 due to the fact that the connections were often made on a relatively oblique axis (e.g., 21 → 22, 23 → 21) rather than on a roughly vertical axis, the most plausible direction taken by the ionized outflows. Similarities can nonetheless be found between Figure 6.12 and Table 6.2 (in particular, the 21 → 22 connection showing the steeper gradients).

From the one-dimensional model of Landau & Lifshitz (1987, Chapter 10), equation (6.1) predicts a peak velocity of $v_{\rho,max} = 2c_0/(\gamma - 1)$ for the rarefied material expanding behind Discontinuity-S (see Section 6.7.2). At this point (when $\rho/\rho_0 = 0$), the rarefied material overtakes Discontinuity-N to enter either a regime of constant velocity or a zone in which the velocity gradient quickly vanishes (see below, the last paragraph of this subsection). In Figure 6.12, no indications are provided for a break in the radial velocity gradient, which suggests that Discontinuity-N is undoubtedly located above or precisely at the location of Field 22, beyond the boundaries of the

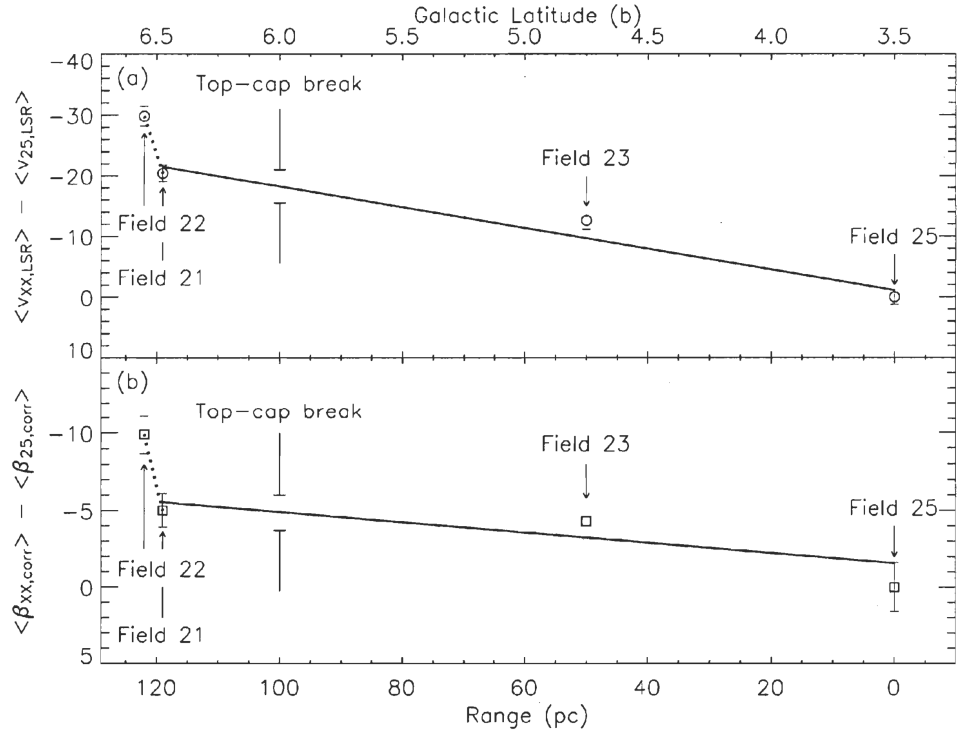

Figure 6.12: Large-scale radial velocity and line-width trends in W4-north.

Large-scale (a) radial velocity, and (b) line-width gradients in W4-north. The two ordinates are in units of km s^{-1}. *Open circles and open squares correspond to the data points. On a range of 125 pc between Fields 25 and 22, each panel presents two trends. The kinematic connections between Fields 25, 23, and 21 show radial velocity and line-width gradients (solid lines) estimated at* $\nabla_v = (\text{-})0.17 \pm 0.04$ *km* s^{-1} *pc*$^{-1}$ *and* $\nabla_\beta = (\text{-})0.04 \pm 0.02$ *km* s^{-1} *pc*$^{-1}$ *respectively. The Pearson correlation coefficents applied to the straight lines are found to be -0.97 and -0.85 respectively. The kinematic connections between Fields 21 and 22 show radial velocity and line-width gradients (dotted lines) estimated at* $\nabla_v = (\text{-})3.13$ *km* s^{-1} *pc*$^{-1}$ *and* $\nabla_\beta < (\text{-})1.63$ *km* s^{-1} *pc*$^{-1}$ *respectively. The inequality for* ∇_β *comes from the fact that we used* $\langle \beta_{22,corr} \rangle = 3.7$ *km* s^{-1}, *the upper limit on the mean line width of Field 22. In other words, the line narrowing gradient can only be more negative than (-)1.63 km* s^{-1} *pc*$^{-1}$. *The top abscissa gives approximately the galactic latitude for each field. At* $b = 6°$, *the position of the top-cap break is indicated in both panels.*

H II region. On the other hand, the sudden change of slope between Fields 21 and 22 resembles the kink in velocities predicted near $\rho/\rho_0 = 0.05$ in Figure 6.11 (this abrupt acceleration is indicated in Figure 6.13). The model, therefore, implies that the ionized material, initially swept-up by Discontinuity-S and presently ejected through the top-cap break, has been rarefied to at most 5% of the particle density of the ionized material near Field 25. In the vicinity of the shell opening, Field 22 shows a 30 km s^{-1} difference from the kinematics of the gas at rest in Field 25. Since we only measure radial velocities, the velocity jump between Fields 25 and 22 is undoubtedly larger. The section of our model showing velocity points larger than 30 km s^{-1} is isolated in Figure 6.11. The "solution" for W4-north is likely found in these points. The large-scale blueshifted radial velocity gradient confirms the W4 superbubble to be tilted toward the observer, given the arguments in Section 6.7.3. The extremely small line widths near $b = 6\overset{\circ}{.}5$ (see Figure 6.4) indicate that the angle of inclination, with respect to the plane of the sky, is relatively small since Field 22 does not seem to probe the ionized material to a significant depth through the radial velocity gradient ; otherwise, an important spreading in radial velocities would be anticipated along the line of sight. An estimation of its value can be made by assuming the 30 km s^{-1} difference to correspond to the peak (radial) velocity reached by the rarefied material (that is, to put Discontinuity-N in Figure 6.13 at the exact latitude of Field 22). Even though our survey cannot properly confirm the theoretical peak velocity to have been reached at the northernmost latitudes of W4-north, the kink detected between Fields 21 and 22 in Figure 6.12 could indicate that the vented material (see Figure 6.13) in the latter field presents a velocity near $v_{\rho,max}$. If so, the inclination with respect to the plane of the sky is likely to be between 9° ($\gamma = 1.10$) and 27° ($\gamma = 1.30$).

The behavior in line widths is precisely in agreement with our expectations presented in Section 6.7.2. The much greater steepness characterizing the line narrowing gradient between Fields 25 and 23 when compared to the connection between Fields 23 and 21 (see Table 6.2) could be partially related to vortex dissipation immediately behind Discontinuity-S. In particular, supersonic turbulence will likely decay quickly once the material is incorporated inside the zone of rarefaction (Shu 1992, Chapter 14). The zone of turbulence dissipation is indicated in Figure 6.13. From Table 6.1, values for $\langle \beta_{23,corr} \rangle$ and $\langle \beta_{21,corr} \rangle$ indicates a roughly constant trend in line widths between Fields 23 and 21. Even though we used a straight line to connect Fields 25, 23 and 21 in Panel (b) of Figure 6.12, one can immediately acknowledge roughly identical values, near -5 km s^{-1}, associated with the two latter fields. Above the zone of dissipation, we, therefore, assume the ionized material to be roughly

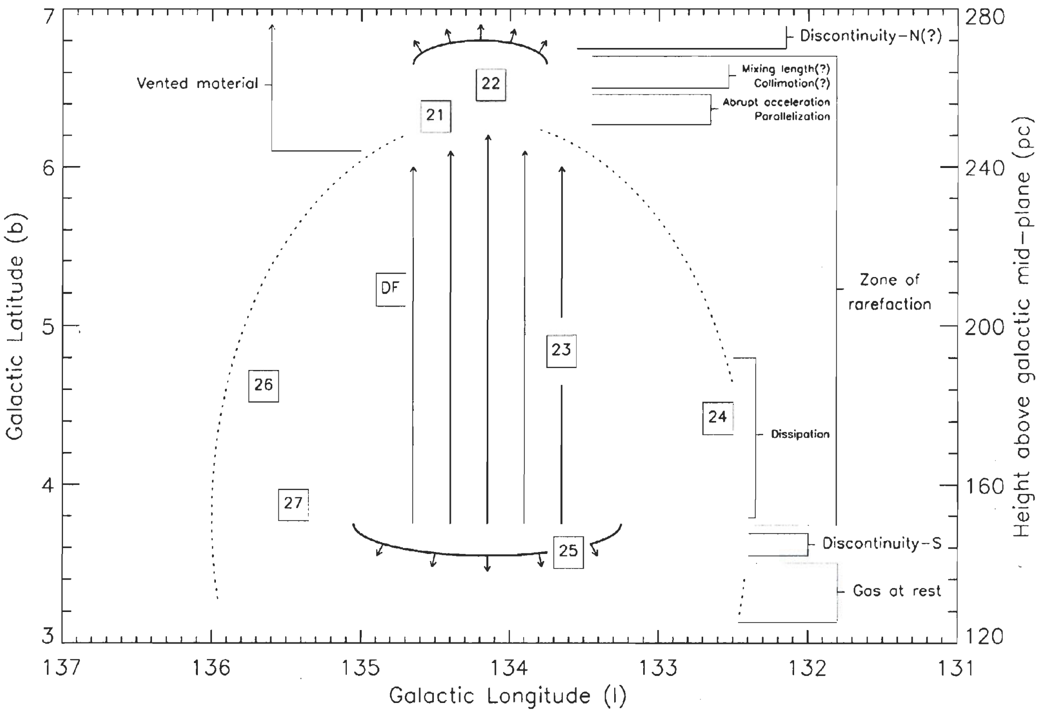

Figure 6.13: A rarefaction scenario in W4-north.

Application to W4-north of our model of a pierced metal container governed by the propagation of a rarefaction wave. The different regions (gas at rest, discontinuities, zone of rarefaction) are traced out following our kinematic analysis of Fields 21-27 in Sections 6.7.3-6.7.7 (see the text). Small arrows indicate the direction of motion associated with the two discontinuities enclosing the rarefaction wave. Long arrows show the direction of motion of the rarefied material between the two discontinuities. The threshold $b = 6°$ *marks the latitude above which the ionized material has been vented beyond the boundaries of the H* II *region, above the top-cap break.*

deprived of turbulent motions; only a weak tendency related to the parallelization of the outflows could be responsible for the slight decrease in line widths (see below).

In Section 6.7.5, we interpreted the Hα-poor cavity (see Figure 6.1) as enclosing accelerated ionized material, rarefied by the passing of Discontinuity-S. The rarefaction is directed toward the top-cap break. From this assumption, the ionized material should appear more and more tenuous as the progression is made away from the weak discontinuity : that is, the rarefying discontinuity moves toward the horizontal sheets at $b = 3\overset{\circ}{.}5$ while the gas becomes more and more rarefied towards $b = 6\overset{\circ}{.}5$. According to our one-dimensional model, Field DF, used for sky subtraction (see Section 6.5), should, therefore, display an Hα emissivity greater than Fields 21 and 22 since it is located closer to Discontinuity-S and, therefore, should have a greater ρ/ρ_0 value (hence, less rarefied material). Field DF was used as a night-sky indicator due to the fact that it is located relatively far from the H I walls of W4-north. On the other hand, Field 21, in the vicinity of the shell's polar cap, might be constantly fed by freshly photoeroded material. The contribution of this material artificially accentuates the local particle density contrast, ρ/ρ_0. This allows a clear detection even at high galactic latitudes whereas the material in DF does not have sufficient contrast. However, the kinematics predicted by the model remain unchanged as the newly ionized component immediately acquires the high velocities of the nearby rarefied material. In Figure 6.3, there is no evidence for radial velocities near -45 km s^{-1}, a value locally associated with the H I wall.

Located relatively far (roughly 20 pc) from the H I shell (similarly to Field DF), the contribution in material mentioned in the previous paragraph cannot explain the "high" Hα emissivity in Field 22. A possible scenario can however be deduced if we make a few assumptions regarding the geometry of the ionized flows beyond the top-cap break. In Section 6.7.2, we mentioned that the width of the top-cap break represents only a fraction of the superbubble's width. Intuitively, this should lead to well-parallelized outflows as the material evacuates the superbubble. That is, there will be fewer orientations of velocity vectors to contribute to the line of sight measurement, resulting in a steep line narrowing gradient between Fields 21 and 22 (see Table 6.2). If the outflows eventually collimate above the shell opening, this would lead to the accumulation of ionized material in a small, restricted region above the top-cap break and, therefore, a localized increase of the particle density. Due to this increase in density, the ionized material will be more emissive than expected in Field 22. The accumulation of material directly favors the development of turbulent motions. This scenario (of collimation leading to turbulence) seems however more significant in the northern portion of Field 22 (see Panels (g) and (h) of Figure 6.4 with line widths slightly above 5 km s^{-1}) while the lower panels show a minimal kinematic disorder along the line of sight (see Section 6.7.3). Although an increase in density due to collimation causes line broadening, this could possibly be compensated by the parallelization of the outflows (which likely dominates the overall dynamics in Field 22 according to the small value found for $\langle \beta_{22,corr} \rangle$ in Table 1).

Additionally, collimation could even lead to a slowdown of the vented outflows (see Panels (d), (e), and (h) in the northern portion of Figure 6.4 with radial velocities slightly more positive than $\langle v_{22,LSR} \rangle$). This is deduced from the mass flow rate (i.e., the product of the particle density, the velocity, and the flow's cross sectional area) treated as being constant in Field 22. This is plausible since (from a previous argument) the field is located at a latitude above the eroded shell and, therefore, no ionized material is constantly added near $b = 6\overset{\circ}{.}5$. From the observed behavior in line widths, we already proposed in the previous paragraph that collimation becomes more and more significant with latitude inside Field 22. However, the fact that the particle density and the cross-sectional area of the outflows respectively increase and decrease on a south-north direction inside the FOV is not enough to definitively show that the velocities will also decrease. If the increase in density perfectly balances (numerically) the decrease in area, the velocities would remain unaffected by the collimating "bottleneck" effect. However, this possible deceleration of the outflows also favors (similarly to localized increase in particle density) the development of turbulent motions (Wang & Dalton 1991), again in agreement with larger line widths in the upper panels of Figure 6.4.

To the simplistic collimation model described above, a second dynamical scenario can also be considered in order to explain the kinematics observed in the northern portion of Field 22 (a kinematics, on a south-north direction, against the large-scale trends identified in Figure 6.12). From the formalism of Landau & Lifshitz (1987, Chapter 10), the large-scale velocity gradient in Figure 6.12 is expected to vanish above Discontinuity-N (see Figure 6.13) if :

$$P_e < P_0 \times \left(\frac{2}{\gamma + 1}\right)^{\frac{2\gamma}{\gamma - 1}}, \qquad (6.2)$$

where γ is the heat capacity ratio of the accelerated material (see Figure 6.10), P_e is the external pressure to the superbubble, and P_0 is the pressure of the gas at rest embedded inside the superbubble. Substituting our possible values for γ (between 1.10 and 1.30) and using the equation of state of a classical ideal gas leads (for the particular case of W4-north) to :

$$\frac{n_e}{n_0} \cdot \frac{T_e}{T_0} < 0.30 - 0.34. \tag{6.3}$$

We used canonical ratios of T_e/T_0 (0.01 to 0.1), between the cold, outer ISM and the warm, embedded material, and $n_e \sim 1$ cm^{-3} for the particle density of the atomic material found roughly 245 pc above mid-plane. The inequality of equation (6.3) is not satisfied only if n_0, the density in the gas at the rest near Field 25, is $\lesssim 0.1$ cm^{-3}. This value, which is well below the mean density of the Galactic DIM (Mathis 1986), is unrealistic and hence we suppose that the rarefied material that overtakes the northern discontinuity dynamically evolves into the kinematic configuration of the local DIM beyond the boundaries of the large W4 H II region. This scenario is precisely identical to the concept of "mixing length" introduced in Paper I. Table 1 of Reynolds *et al.* (2001) gives the kinematic behavior of the DIM component located a few parsecs above Field 22 ; a mean radial velocity of roughly -45 km s^{-1} and a corrected line width of 16 km s^{-1}. Both the redshifted radial velocity and line broadening gradients observed from the two lower to two upper rows in Figure 6.4 could indicate material flowing above Discontinuity-N and mingling with the local DIM. This assumption contributes to put Discontinuity-N at a latitude of $b = 6.°5$, coincident with Field 22. We firmly believe that this simple model of rarefied, vented material/DIM mixing supercedes the collimation scenario since it leads to an elegant connection with the data of the WHAM Northern Sky Survey.

6.7.8 The W4 Galactic chimney : suggestion of a timescale scenario

From our analysis of subsections 6.7.3-6.7.7, we have strong evidence of a rarefaction scenario in W4-north which ultimately leads to gas venting outwards in the vicinity of the shell's polar cap. This corroborates the notion that a Galactic chimney is currently forming inside the W4 superbubble. In the following subsection, a timescale scenario will be proposed in order to determine when W4 enters the chimney phase of its expansion ; that is, to estimate at which time in the past the first signs of shell fragmentation would have been observed. Our model remains however approximate since it highly depends of the growth rate of the zone of rarefaction (see Figure 6.13) and, therefore, the velocity of the two weak discontinuities bounding the rarefaction wave. This information could only be roughly estimated from our observations. Finally, the rate of mass input associated with the photoerosion of the H I shell will be compared to the rate of escape of ionized material through the chimney.

Inconclusive results for a western-side break in Section 6.7.4 are of great importance (relative to the dynamical evolution of the W4 superbubble) as it implies the development of shell instabilities on a timescale much smaller than expected. This follows from our argument in Section 6.7.5 proposing that the large Hα-poor cavity (see Figure 6.1) formed by the evacuation of ionized material through the top-cap break alone. Dove *et al.* (2000) proposed the development of Rayleigh-Taylor instabilities that could lead to shell fragmentation once a supershell enters the reacceleration phase of its expansion above the blowout threshold. We already demonstrated in Section 6.4 that W4 barely reaches the required height above the Galactic mid-plane. However, three-dimensional models have shown that magnetohydrodynamic instabilities, in particular, are likely responsible for shell fragmentation at earlier stages (De Avillez & Breitschwerdt 2005; West *et al.* 2007). We expect the chimney to keep forming as long as the Hα-poor cavity does not occupy all the volume available inside W4 and the rarefaction wave does not dissipate.

From the kinematics observed in Fields 21, 22, 23, and 25, a simple time-dependent scenario, regarding the fragmentation of the shell's polar cap, can be derived. The fragmentation of the shell has necessarily occurred at a time when the shell's polar cap was located between 145 and 245 pc above the Galactic mid-plane. The lower limit coincides with Field 25 ; otherwise, the Hα-poor cavity would be observed below the H I horizontal sheets and probably well into W4-south (see Section 6.7.5). The higher limit corresponds to the actual height reached by the egg-shaped supershell of West *et al.* (2007). The fragmentation of the shell coincides with the appearance of the two weak discontinuities associated with the rarefaction wave. The formalism of rarefaction waves (Landau & Lifshitz 1987, Chapter 10) demands that the two discontinuities travel either along the same direction (toward the gas at rest) or in opposite directions. Since observational evidence suggests that Discontinuity-N is presently located above the W4 superbubble (see Section 6.7.7), this discontinuity is propagating toward the Galactic corona. Otherwise, the discontinuity would be evident above Discontinuity-S in Figure 6.13 but still well below the actual height of the superbubble. The change of sign (from blueshifted to redshifted) of the large-scale radial velocity gradient, apparent in the northern portion of Field 22 (see Section 6.7.7), would, therefore, be observed at a latitude well below the top-cap break (which is not the case; see Figure 6.12). The fact that the two discontinuities are moving away from each other allows us to estimate the dynamical age of the zone of rarefaction.

Equation (4) of Dennison *et al.* (1997) defines the timescale t_D to be the time required for a superbubble to expand one scale height above the Galactic mid-plane. Considering $H = 140$ pc above the Galactic mid-plane (Normandeau 2000) and using the same values for the actual mechanical luminosity of the star cluster IC 1805 ($L_0 = 0.3 \times 10^{38}$ ergs s^{-1}) and the ambient particle density of the ISM exterior to the superbubble at the Galactic plane level ($n_{\text{plane}} = 5$ cm^{-3}), we obtain a new estimate of roughly 5.6 Myr for t_D, compared to 3.2 Myr proposed by Dennison *et al.* (1997). Assuming the superbubble to have expanded on a timescale between $1.5 \times t_D$ and $2.5 \times t_D$ (this type of approximation was also used by Dennison *et al.* (1997)) in order to reach its actual height (estimated at $1.85 \times H$), we propose the dynamical age of the W4 superbubble to lay between 8.4 and 14.0 Myr. The lower limit is similar to the dynamical age of 9 Myr obtained by West *et al.* (2007).

The behavior in velocities of the two discontinuities associated with a rarefaction wave is particularly complicated as it involves viscosity and thermal conductivity in the gas at rest which ultimately lead to the dissipation of the wave in the subsonic regime (Landau & Lifshitz 1987, Chapter 10). The velocities are however comparable to the speed of sound in the ambient plasma. If we assume both discontinuities to have a velocity of 15 km s^{-1}, the zone of rarefaction in Figure 6.13 is expected to have grown at a rate of 30 km s^{-1} (since the discontinuities are moving away from each other). Assuming Discontinuity-N to coincide precisely with Field 22 (an assumption largely discussed in Section 6.7.7), the point of shell fracture is estimated near $b = 5°$ (halfway between $b = 3\overset{\circ}{.}5$ and $b = 6\overset{\circ}{.}5$), at a latitude coincident with Field 23 (roughly 200 pc above the mid-plane). For a distance of 2.35 kpc to the star cluster IC 1805 (Massey *et al.* 1995), this height corresponds to $1.4 \times H$, roughly 30% below the predicted blowout threshold (see Section 6.3). In order to cover, at a grown rate of 30 km s^{-1}, the distance of 125 pc between Fields 25 and 22, roughly 4.1 Myr is required. This can be interpreted as the dynamical age of the top-cap break and, consequently, the chimney. By subtracting the chimney's age from the range of dynamical ages obtained for the W4 superbubble (see above), shell instabilities are, therefore, likely to have developed 4.3 to 9.9 Myr following the ignition of the first stellar generation. As a check on this range of ages, we assume the mechanical luminosity to have remained constant (that is, near L_0) from one stellar generation to the other and we obtain, using equation (1) of Mac Low & McCray (1988), the time required for a superbubble to reach a height of Z parsecs above the Galactic mid-plane :

$$t(Z) = \left(\frac{Z}{1\,\mathrm{pc}}\right)^{\frac{5}{3}} \left(\frac{H}{1\,\mathrm{pc}}\right)^{-\frac{5}{3}} t_D. \tag{6.4}$$

For the W4 superbubble, roughly 10.1 Myr are necessary to reach 200 pc and initiate shell fragmentation. Adding the age derived for the chimney, our timescale scenario is in agreement with a dynamical age of 14 Myr for the superbubble, a value greater than the first estimate between 6.4 and 9.6 Myr proposed by Dennison *et al.* (1997). The authors, however, do not provide uncertainties on their estimate.

The velocity of 15 km s^{-1}, proposed in particular for Discontinuity-N, is probably not too far from reality. Our previous arguments have already demonstrated that Discontinuity-N, moving toward the Galactic corona, is presently located slightly above the actual height of the superbubble, probably near the latitude of Field 22 (see Figure 6.13). In other words, the velocity of the discontinuity is probably slightly greater than the polar region's mean expansion velocity between 200 pc (at fracture) and 245 pc (actual height) above mid-plane. From equation (13.5) of Lozinskaya (1992, Section 13), giving the expansion velocity (with respect to time) of a wind-blown bubble in its phase of energy conservation, we predict a deceleration from 10.9 km s^{-1} (at $Z = 200$ pc and $t = 10$ Myr) to 9.6 km s^{-1} (at $Z = 245$ pc and $t = 14$ Myr). This is obtained using a mean particle density[3] of roughly 2 cm^{-3} for the upstream material between 37 pc (the height above mid-plane of the star cluster IC 1805) and 245 pc. For a mean expansion velocity of 10 km s^{-1}, the difference of 5 km s^{-1} between the region of the shell's polar cap and Discontinuity-N signifies

---

[3] This value is justified by the exponentially decreasing Galactic atmosphere model mentioned in Section 6.3. The atomic material displays a particle density of $n(Z) = n_{\mathrm{plane}} \times \mathrm{e}^{-Z/H}$. Assuming $n_{\mathrm{plane}} = 5$ cm^{-3}, we obtain $\overline{n} = 2.01$ cm^{-3} for Z varying between 37 and 245 pc. The CGPS 21 cm line observations (Normandeau *et al.* 1997) in W4-south exhibit an expansion velocity of 9.75 km s^{-1} for the W4 region (see Figure 6.14). Also, the W4-south region is used for the determination of the expansion velocity since both the front and rear walls of the supershell are ill-defined at the latitude of W4-north.

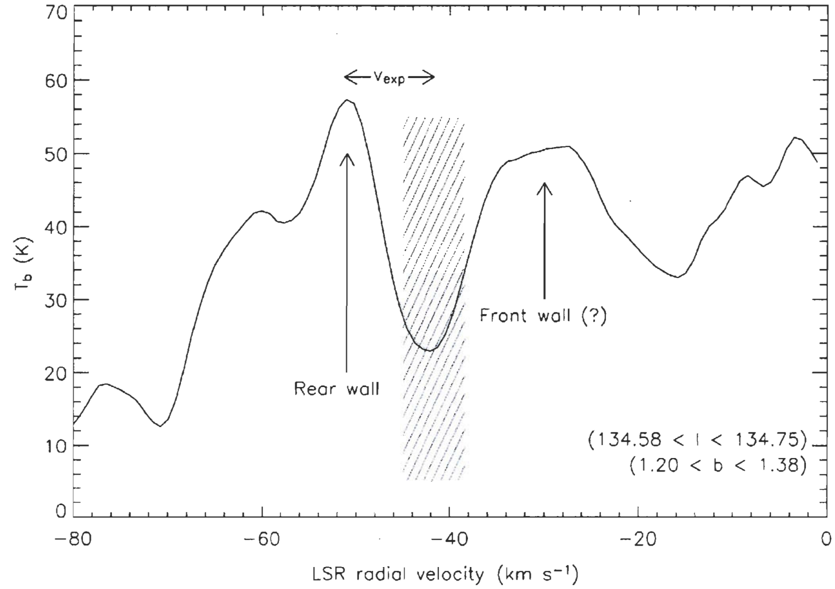

Figure 6.14: Velocity profile in W4-south : the expansion velocity of the supershell.

Radial velocity profile extracted from the CGPS 21 cm line observations along the line of sight of W4-south. The rear wall of W4 is clearly detected from the well-defined peak near -51.3 km s^{-1}*. The front wall peak, much broader, is likely to be contaminated by a large-scale neutral feature located between the expanding bubble and the observer. The dashed area shows the radial velocity range associated with the H*I *cavity revealing the W4 H*II *region. The actual expansion velocity of W4 is estimated at 9.75 km* s^{-1} *from the radial velocity range between the H*I *cavity and the position of the rear wall.*

that the weak discontinuity would have traveled an additional 20 pc during the last 4 Myr (corresponding to the age of the chimney). This simple argument puts Discontinuity-N at an height of 265 pc above the Galactic mid-plane, in agreement with the location of Field 22 (see the right-hand axis of Figures 6.1 and 6.13).

Finally, an investigation is here provided that should help validate the relations established between our model of a rarefaction scenario and the kinematics of W4-north. The fact that the Hα-poor cavity is well-detected demands the rate at which the ionized material evacuates the superbubble to exceed the discharge (toward the interior) of freshly photoeroded material that results from the ionization of the neutral supershell. The rate $\dot{M}_{\rm in}$ at which the photoeroded material "falls" into the W4 superbubble is adapted (to our work) from the investigation of the photoevaporation of molecular clumps (Joncas & Roy 1984) and is estimated at :

$$\dot{M}_{\rm in} = \rho_{\rm HII}\, v_{\rm HII}\, S_{\rm shell}, \tag{6.5}$$

where $\rho_{\rm HII}$ correspond to the density (in units of mass per volume) of the ionized material in contact with the neutral shell, $v_{\rm HII}$ is the velocity of this material with respect to the neutral shell, and $S_{\rm shell}$, the area covered by the shell. In order to avoid distortions of the velocity measurements due to a possible western-side break, we estimate $v_{\rm HII}$ to be roughly 1 km s^{-1} using Fields 04, 17, and 18 (Paper I, Table 5). The neutral supershell envelops an ionized superbubble. Thus using the characteristics determined by West *et al.* (2007), such as an half-radius and half-height of the W4 superbubble respectively of 82 and 123 pc, a particle density $\rho_{\rm HII}$ of $\sim$0.40 cm^{-3}, and noting that the zone of rarefaction covers about 30% of the superbubble area, we estimate $\dot{M}_{\rm in} \sim 3.4\times10^{-4}$ M$_\odot$ yr^{-1}.

Using the same formalism as equation (6.5), we obtained $\dot{M}_{\rm out}$, the rate of evacuation through the top-cap break, as :

$$\dot{M}_{\rm out} = \rho_{\rm break}\, v_{\rm evac}\, S_{\rm break}, \tag{6.6}$$

where $\rho_{\rm break}$ is the density (in units of mass per volume) of the ionized material in the vicinity of the shell opening, $v_{\rm evac}$ is the velocity of the rarefied material passing above $b = 6°$, and $S_{\rm break}$, the area of the Top-cap break. We assume $n_{\rm break}$ (in units of particle per volume) to be roughly equivalent to the electron density, n_e, of Point I displayed in Table 4.2 and Figure 4.2 of West (2003). The value is estimated near 0.20 cm^{-3}. Using the large-scale radial velocity gradient of Figure 6.12 (solid line), we estimate the radial component of the velocity of evacuation (with respect to the gas at rest) to approximately 17 km s^{-1} at the position of the top-cap break ($b = 6°$). Using the range of values proposed for the superbubble's angle of inclination in Section 6.7.7, the velocity of evacuation $v_{\rm evac}$ is estimated between 37 km s^{-1} ($\theta = 27°$) and 110 km s^{-1} ($\theta = 9°$). West *et al.* (2007) gives 20 pc for the diameter of the top-cap break for a roughly circular shape of 315 pc^2. The value for $\dot{M}_{\rm out}$ is estimated between 5.9×10^{-5} and 1.8×10^{-4} M$_\odot$ yr^{-1}.

Our model of a W4 superbubble that looses ionized material at a rate faster than it gains material does not hold even for large values of $v_{\rm evac}$. This could be explained by (1) a value for $v_{\rm evac}$ greater than expected (this would demand an ionization rate below 95% in W4-north leading to an angle of inclination with respect to the plane of the sky below 9°), (2) a sizeable contribution to the rarefied cavity attributed to the (young ?) western-side break, (3) an underestimation of the break's dimensions, or (4) all of the above. For example, an angle of inclination slightly below 5° (instead of $\geqslant 9°$) or a shell opening characterized by a diameter of 28 pc (instead of 20 pc) would give $\dot{M}_{\rm out}$ greater than $\dot{M}_{\rm in}$, in agreement with our initial assumption. However, the increase in diameter (from 20 to 28 pc) would demand that the top-cap break, at the distance of W4, is more than 10 pixels wider than its current estimated width (according to the $\sim 1'$ spatial resolution of the CGPS observations). Such a large difference with the CGPS images displayed in West *et al.* (2007) is highly questionable. A possible explanation might however be related to the shape of the top-cap break ; rather than assuming a circular opening, an irregular, asymmetric break (that likely has a larger dimension along the line of sight compared to the dimension observed on the plane of the sky) could contribute for a larger $S_{\rm break}$ value. This is plausible since the edge-on view with the W4's polar cap does not allow to conclude on the shape of the shell opening.

6.8 Conclusion

The use of FaNTOmM, an interferometric device system especially designed to study particularly faint extended astronomical objects, has allowed us to extract the kinematic information associated with the ionized component found embedded in the northern portion of the Galactic superbubble/H II region W4. Our motivation was based on the possible discovery that two faint H I segments along the northern shell could be interpreted as evidence of shell fragmentation (see Section 6.4). We propose a method of quantitatively identifying shell breakout (see Section 6.3). The method relies on the kinematic perturbation by (inward) propagating rarefaction waves. The results from using this method suggest a situation that is similar to a model of a pierced metal container (see Section 6.7.2).

A total of seven fields were observed in the galactic latitude range between 3° and 7°. Two kinematic regimes are identified. First, the embedded ionized material below $b = 5°$ and found at the periphery of the H II region seems to be mostly dominated by the inner erosion of the compressed H I shell (see Section 6.7.6), a behavior largely discussed in Paper I. However, a clear south-north gas flow is identified on a vertical axis of 125 pc between $b = 3\overset{\circ}{.}5$ and $b = 6\overset{\circ}{.}5$ (roughly centered on $l = 134°$), in agreement with the passing of a weak discontinuity (labeled Discontinuity-S in text) associated with a rarefaction wave (see Section 6.7.7). The discontinuity is propagating toward the Galactic mid-plane and the rarefaction wave itself results from a shell opening near the polar cap. The second discontinuity of the wave (labeled Discontinuity-N in text) is propagating toward the Galactic corona (see Section 6.7.8). Our investigation did not show conclusive results for ionized flows through a possible western-side break (see Section 6.7.4).

A 30 km s^{-1} radial velocity difference is found between Field 25 (which appears to be associated with the gas at rest near the southern discontinuity of the wave) and Field 22, enclosing the gas located slightly beyond the boundaries of the H II region (see Section 6.7.7). Between both these regions, a large Hα-poor cavity (see Figure 6.1) encloses accelerated and rarefied material expanding northward above (behind) Discontinuity-S (see Figure 6.13). Two trends in radial velocities are detected : a roughly flat gradient between Fields 25 and 21 estimated at (-)0.17 km s^{-1} pc^{-1} and a much steeper gradient found at (-)3.13 km s^{-1} pc^{-1} between the northern Fields 21 and 22 (see Figure 6.12). The sudden change of slope corresponds to the abrupt increase in velocities predicted from our model for highly rarefied material (see Figure 6.11). The behavior in radial velocities confirms that the W4 superbubble is tilted toward the observer and substantiates the formation of a Galactic chimney (see Section 6.7.7).

The dynamical age of the chimney phase is estimated at 4.1 Myr assuming both discontinuities, associated with the wave, to travel with very similar velocities. This implies that the shell opening appeared when the shell's polar cap was roughly located 200 pc above Galactic mid-plane (see Section 6.7.8). In this case, shell instabilities developed in W4 at latitudes well below the blowout threshold, which is between 280 and 420 pc above mid-plane at the distance of the star cluster IC 1805. Magnetohydrodynamic instabilities are likely to have occurred at the earlier stages of the expansion (see Section 6.7.8). According to a simple model of expanding wind-blown bubbles, roughly 10 Myr was necessary to reach 200 pc and initiate shell fragmentation in W4. Adding the age of the chimney phase, we propose the dynamical age of the superbubble to be approximately 14 Myr (see Section 6.7.8), a value apparently greater than any previous estimations.

The H I walls do not seem to have a kinematic impact on the vented outflows of ionized material. On the other hand, their inner erosion contributes to the local particle density of particular areas. Otherwise, the fields observed would have enclosed extremely rarefied material which would likely be invisible, according to the model (see Section 6.7.7).

Our one-dimensional model does not provide indications on how the Hα line widths vary inside a rarefaction wave (see Section 6.7.2). However, the behavior in line widths can be best explained by a few assumptions regarding the hydrodynamics of the rarefied material and the particular geometry of W4-north. A zone characterized by a dissipation of the turbulence (see Figure 6.13) could be located immediately behind the southern discontinuity (see Section 6.7.7). Correlated with the abrupt acceleration observed between Fields 21 and 22 (see Figure 6.12), the steep line narrowing gradient could be related to a parallelization of the outflows through the top-cap break (see Section 6.7.7). Collimation could eventually explain the particular kinematic behavior in radial velocities and line widths observed in the northern portion of Field 22. Another scenario demands the northern discontinuity of the wave to be located precisely at the latitude of Field 22 ; ionized material, that flows through the top-cap break and beyond the zone of rarefaction, might evolve for a certain distance to reach the kinematic configuration of the local DIM material above the superbubble (see Section 6.7.7). Finally, the particularly low $\beta_{i,corr}$ values in Field 22 indicate a small inclination of the W4 superbubble with respect to the plane of the sky. Using evidence that Discontinuity-N coincides in latitudes with Field 22, we obtain an angle of inclination between 9° and 27° (see Section 6.7.7).

Using observations in Paper I, we can estimate how much photoeroded material is added per year to the warm ISM enclosed by the H I shell. The rate at which W4-north loses ionized material through the top-cap break is slightly less than this rate. However, the presence of the Hα-poor cavity indicates that the rate of evacuation should clearly dominate. The proposed explanations are mostly associated with geometrical effects : a larger maybe asymmetric top-cap break, a smaller angle of inclination of the superbubble with respect to the plane of the sky, or a sizeable contribution to the evacuation attributed to the western-side break, although the latter is not detected in Hα. Since the uncertainties on each measurement are difficult to quantify, no particular explanation clearly emerges from the others.

The kinematic confirmation of a shell opening near the polar region of W4 signifies that a certain fraction of the UV flux will likely exit the large superbubble through the hole. The formation of a dynamic chimney inside the superbubble/H II region W4 is the evolutionary stage that establishes an energetical connection between the star cluster IC 1805 and the Reynolds loop located at low-galactic corona level.

The authors would like to thank the Natural Sciences and Engineering Research Council of Canada and the Fonds Québécois de la Recherche sur la Nature et les Technologies who provided funds for this research project. The Canadian Galactic Plane Survey is a Canadian project with international partners and is supported by a grant from the Natural Sciences and Engineering Research Council of Canada. Data from the Canadian Galactic Plane Survey are publicly available through the facilities of the Canadian Astronomy Data Centre (http ://www1.cadc-ccda.hia-iha.nrc-cnrc.gc.ca/cgps/).

D. L. is grateful to M.-A. Miville-Deschênes and Olivier Daigle who provided useful IDL routines to carry out data reduction. D. L. would also like to thank B. Malenfant, G. Turcotte and P.-L. Lévesque for technical support during numerous observing nights at the Observatoire du mont Mégantic.

Chapitre 7

Investigation multi-ionique de la cinématique de NGC 595

Sommaire

Référence : Lagrois, D., & Joncas, G. 2009c, *ApJ*, sous presse

Titre original : *A Multi-Ionic Kinematic Investigation of NGC 595, a Giant Extragalactic H*II *Region in M33.*

Cet article présente une étude multi-ionique de NGC 595. L'article fut soumis le 6 mars 2009 et accepté pour publication le 9 juin 2009 par *The Astrophysical*

Journal. La publication de l'article scientifique est actuellement prévue pour le 10 août 2009 dans le volume 701 du dit journal. Le manuscrit, tel que présenté au chapitre 7, est donc appelé à être légèrement modifié d'un point de vue lexicologique et grammatical. Les résultats scientifiques demeureront inchangés. L'auteur remercie les membres du jury, et plus particulièrement Gilles Joncas et Laurent Drissen, de même que l'arbitre anonyme pour leurs judicieux conseils ayant permis l'amélioration de ce travail.

7.1 Résumé

Une série d'observations spectro-interférométriques des raies d'émission optiques Hα, [O III] et [S II] sont combinées à des observations radio de la raie à 21 cm dans le but d'obtenir un portrait cinématique fiable de NGC 595, la seconde région H II géante extragalactique la plus imposante dans M33. Les observations Hα et [O III] montrent que la nébuleuse est encline à deux régimes cinématiques distincts. Alors que des profils de vitesse symétriques, habituellement supersoniques, dominent une fraction importante de l'étendue ionisée, des indices de dédoublement de raies sont observés dans une région de faible dimension au voisinage des étoiles les plus massives de l'amas stellaire. Une investigation quantitative propose que deux bulles de vents stellaires en expansion pourraient être tenues responsables du dédoublement de raies observé. La cinématique du matériel ionisé caractérisé par des profils en vitesse ne comportant qu'une seule composante indique que des écoulements Champagne sont présents en périphérie de la composante moléculaire forçant ainsi l'accélération du matériel fraîchement ionisé dans le milieu interstellaire ambiant. Dans les portions de l'objet non-dominées par l'érosion des nuages moléculaires, le matériel H^+ et S^+ montre un comportement cinématique en accord avec le gaz atomique. Les largeurs de raie non-thermiques montrent des valeurs relativement élevées et supersoniques, spécialement en [O III]. La modélisation de fonctions de structure indique que les composantes Hα et [O III] pourraient être exposées à différents mouvements turbulents pouvant expliquer l'excès en largeur de raie observé pour ce dernier. Sur toute la surface ionisée de la nébuleuse, le matériel S^+ montre des largeurs de raie plus étroites que les deux autres ions. Combinées à l'absence de dédoublement de raies, ces caractéristiques particulières indiquent que la composante [S II] est certainement située en périphérie de la nébuleuse et ne coexiste possiblement pas avec Hα et [O III]. L'allure de la fonction de structure en [S II] est en accord avec un nombre relativement faible de gradients de vitesse à grande échelle ce qui explique partiellement les profils étroits observés. La densité électronique moyenne dans la nébuleuse est estimée à $162 \pm 106(1\sigma)$ cm^{-3}, en accord avec les études antérieures de régions H II géantes extragalactiques similaires. Nous présentons la première carte bidimensionnelle en densités électroniques d'une nébuleuse géante extragalactique.

7.2 Abstract

Spectro-interferometric observations of the Hα, [O III], and [S II] optical emission-lines are combined with radio observations of the 21 cm line in order to obtain a reliable kinematic image of NGC 595, the second largest giant extragalactic H II region in M33. The Hα and [O III] observations reveal that the nebula is exposed to two distinct kinematical regimes. While symmetric, broad velocity profiles dominate a sizeable fraction of the ionized extent, evidence for line splitting is detected in a small region near the most massive stars of the star cluster. A quantitative investigation proposes that two expanding wind-blown bubbles could be held responsible for the observed line splitting. The kinematics of the ionized material presenting 1-component velocity profiles likely indicates that Champagne flows are present at the periphery of the molecular component leading to accelerated ionized material in the ambient interstellar medium. In areas not dominated by the photoionization of the molecular clouds, the H$^+$ and S$^+$ material shows a kinematical behavior roughly in agreement with the atomic gas. Mean non-thermal line widths show relatively large, supersonic values especially in [O III]. Models of structure functions indicate that the Hα and [O III] components could be exposed to different turbulent motions which could explain the broadening excess observed for the latter ion. On the full ionized extent of the nebula, the S$^+$ material shows narrower line widths than the two other ions. Combined with the absence of line splitting, these peculiar characteristics indicate that the [S II] component is likely located at the periphery of the nebula and probably does not coexist with Hα and [O III]. The shape of the [S II] structure function is in agreement with a relatively low number of large-scale velocity gradients which partially explains the narrower profiles observed. The mean electron density in the nebula is estimated at $162 \pm 106(1\sigma)$ cm^{-3}, in agreement with previous studies of similar extragalactic H II regions. We provide the first bidimensional electron density map ever presented for a giant extragalactic nebula.

7.3 Introduction

From their imposing sizes up to a kiloparsec (Castañeda *et al.* 1992) and the presence of massive star clusters (Abbot 1982), giant extragalactic H II regions (GEHRs) represent ideal structures to quantify the dynamic interaction between gigantic volumes of interstellar medium (ISM) and the combined effect of strong stellar winds and large amount of ionizing photons, both induced by several tens (or even hundreds) hot stars ($T_{eff} \geqslant 30\,000$ K). Even though large distances are generally involved, high-sensitivity optical detectors can track the embedded ionized material and usually provide a reliable kinematic estimate of the internal motions. In particular, supersonic velocity line widths ($\sigma \geqslant 10$ km s^{-1}) were often found in integrated emission-line profiles of GEHRs (e.g., Smith & Weedman 1970; Melnick 1977; Skillman & Balick 1984; Roy *et al.* 1986) and contributed to differentiate these objects from their Galactic, much smaller, equivalent (O'Dell & Townsley 1988). Melnick *et al.* (1999) summarized the possible sources for the observed excess in line broadening : gravitationally bound systems (stars, gas, and dust) and the expected virialized motions (Terlevich & Melnick 1981), embedded wind-blown bubbles and expanding shells likely related to line splitting (Dyson 1979), and the intrinsic radial velocity dispersion associated to each object which accounts for different velocity gradients along the line of sight (LOS) and turbulent motions (Arsenault & Roy 1988), and Champagne flows (Tenorio-Tagle 1979; Bodenheimer *et al.* 1979).

Numerous investigations, spectroscopic or interferometric, have shown rather complex and often different kinematical properties depending on the targeted nebula. Melnick *et al.* (1999) obtained Hα line profiles of the 30 Doradus nebula that revealed a faint, broad ($\sigma \sim 45$ km s^{-1}) component located roughly at the radial velocity of the nebula. The authors interpreted this component as a diffuse and highly turbulent mixture observed at all LOSs that could have its origin in the Champagne phase. The largest and most luminous H II region of M33, NGC 604, shows an integrated velocity profile characterized by a relatively broad ($\sigma \sim 18$ km s^{-1}), central, emissive component flanked by two extended wings (Yang *et al.* 1996). These wings were attributed to embedded shells expanding in the giant ionized region. Specifically, the brightest regions of the nebula were best fitted by a single, supersonic component, attributed to gravity and virialized motions, while the fainter parts presented evidence for line splitting (two resolved components) and were said to be mostly dominated by wind-blown bubbles. Rozas *et al.* (2006a) presented a sample of GEHRs in which the majority of the observed nebulae also show similar profiles generally characterized by a 3-component fit ; a central, emissive feature accompanied by two broad, low intensity components at high velocities. Skillman & Balick (1984) obtained asymmetric Hα and [O III] line profiles of the NGC 2363 and NGC 5455 regions that were well fitted using a combination of narrow and broad components separated by a few km s^{-1}. The authors particularly noted that the asymmetries were always more pronounced in the [O III] line profiles. The spectral discrepancies observed between each study are certainly dependent of the geometry of each object but could also be related to a different stage of evolution. Muñoz-Tuñón *et al.* (1996) mentioned that young GEHRs are most likely dominated by gravity and virialized motions while winds from massive stars and supernovae are responsible for the overall kinematics in much older objects. This results from massive stars (forming at a later stage in the giant molecular cloud) eventually developing strong shocks (i.e., winds, supernovae) that sweep up the surrounding ionized mixture and literally "erase" the kinematic signature of virialization. Objects with intermediate ages (e.g., NGC 604) show an hybrid kinematics in which both mechanisms contribute. This, however, does not consider the kinematic impact attributed to previous generations of star clusters.

In addition to the different broadening sources mentioned earlier, Roy *et al.* (1992) proposed that the blowout of a superbubble could lead to supersonic motions as the ionized gas is accelerated and vented outwards. Lagrois & Joncas (2009b) confirmed the existence of a rarefaction scenario, correlated to the formation of a dynamic chimney, in the large W4 Galactic H II region (Dennison *et al.* 1997; Basu *et al.* 1999; Normandeau 2000; West *et al.* 2007). The authors measured a 30 km s^{-1} difference in radial velocities between the highly rarefied, accelerated material (being ejected from the superbubble) and the embedded ionized component said to be at rest. This value was however limited by the small inclination of the object with respect to the plane of the sky (roughly between 9° and 27°). Assuming a particular case in which the vented outflows would be directed toward or away from the observer (that is, assuming a superbubble tilted at roughly 90° w.r.t. the plane of the sky), a large range of radial velocities would be expected along the LOS. The resulting emission profile would show a strong peak (with a potentially supersonic width) at the velocity of the undisturbed, embedded material found deep inside the superbubble and a very weak but long tail (blueshifted or redshifted depending on the direction of the outflows) associated to the rarefied, accelerated component. Extremely broad profiles ($\sigma \gtrsim 100$ km s^{-1}) are therefore not expected but the tail's asymmetry could lead to observed line widths up to a few tens of km s^{-1}. Without investigating the line-width behavior, Tenorio-Tagle *et al.* (2000) found kinematic evidence in radial velocities for multiple blowouts in the NGC 604 region. The particular geometry of the nebula allowed to measure a 100 km s^{-1} difference between the rest component and the highly accelerated material.

We present, in this work, our latest investigation of the GEHR NGG 595 located in M33. High-resolution (< 15 km s^{-1}) velocity profiles of the Hα λ6563 Å, [O III] λ5007 Å, and [S II] $\lambda\lambda$6716, 6731 Å optical lines were obtained providing the kinematical information of the most emissive parts of the ionized nebula. The interferometric 21 cm atomic line and CO (1-0) transition emissions of NGG 595 are also provided. To our knowledge, this work represents one of the most complete kinematical study ever presented for a GEHR. In particular, the neutral material's data are crucial since it provides the reference velocities needed to carry out a reliable interpretation of the ionized gas' motions. Our goals are to (1) obtain a large scale kinematic view of the nebula's neutral and ionized gas components, (2) explain the observed gas motions, (3) estimate the contribution of the different broadening mechanisms on the observed line widths, (4) quantify the implication of embedded wind-blown bubbles on the observed line profiles, and, (5) verify if NGC 595, on account of its H I appearance, is a dynamic chimney candidate. We present, in Section 7.4, the giant H II region NGC 595 and the previous work associated with the nebula. Information related to the observations and data reduction are detailed in Section 7.5. Results of our multi-ionic Fabry-Perot interferometry measurements are given in Section 7.6 and analyzed and discussed in Section 7.7. Summarized results and general conclusions will be given in Section 7.8.

7.4 NGC 595, a giant H II region

NGC 595 is the second biggest GEHR of the late-type Sc galaxy M33. Viallefond *et al.* (1983) identified a core-halo morphology in Hα with apparently no indication of non-thermal radio emission (i.e., no sign of recent supernovae). The diffuse halo presents particularly rich filamentary structures (Courtès *et al.* 1987). We adopt a distance of 847 ± 60 kpc to the nebula according to the photometric investigation of Galleti *et al.* (2004). Viallefond & Goss (1986) used a distance of 600 kpc to M33 and estimated the total masses of H I and H II material in the nebula for a diameter of 110 pc, the dimension of the bounded area which enclosed the majority of the emissive material. Correcting for the distance to the galaxy, we obtain $M_{HI} = 1.2 \times 10^6$ $M_\odot$ and $M_{HII} = 4.6 \times 10^5$ $M_\odot$ in NGC 595 for a diameter of 155 pc. Kennicutt (1984) presented a much larger diameter for the extended nebula estimated at 400 pc for a distance of 800 kpc to M33. This dimension potentially encloses all the gaseous material (even the faintest emission) associated with NGC 595. The (full) diameter of NGC 595 can therefore be estimated at roughly 425 pc as seen on the plane of the sky using our adopted distance. Drissen *et al.* (1990) estimated an age between 4 and 6 Myr for the nebula. NGC 595 therefore appears to be slightly more evolved than the similar GEHRs NGC 604 (Pellerin 2006) and 30 Doradus (Hunter *et al.* 1995).

Drissen *et al.* (1993, 2008) identified ten Wolf-Rayet (WR) stars (nine of those being WN-stars and one WC-star) located near the bright central core of NGC 595. Malumuth *et al.* (1996) obtained, via photometric HST/WFPC-2 observations, a color-magnitude diagram in agreement with a cluster model having an age estimated at 4.5 ± 1.0 Myr. This signifies that the NGC 595 region is likely to have been formed by the mechanical deposit of Lyα radiation and stellar winds of a single generation of stars (i.e., the present one). Integrating their derived initial mass function, the authors obtained a stellar mass of 7.35×10^3 M$_\odot$ down to a lower mass limit of 4 M$_\odot$ (corresponding to B-stars and heavier). This result is similar to the value of 7 000 M$_\odot$ obtained by Kennicutt (1984) for OB-stars only. The total stellar mass (accounting for all stars) is estimated at $M_{\mathrm{stars}} = 18\,000$ M$_\odot$. The ionizing luminosity of the star cluster is estimated at 5.0×10^{50} photons s^{-1} (with $\lambda < 912$ Å), roughly half the rate of ionizing photons predicted by the radio flux density (Viallefond & Goss 1986) and the Hα luminosity. Malumuth *et al.* (1996) mentioned that a certain reconciliation can be reached if we allow for a spread in the stellar ages between 3.5 and 5.5 Myr (within the range of uncertainties obtained for the cluster's age). An on-line (and partially incomplete) table presenting the photometric data (filters : F170W, F336W, F439W, F547M) of nearly 600 star-candidates in NGC 595 is also presented by the authors (see Section 7.6).

Deul & van der Hulst (1987) made a 21 cm line survey of M33 at a resolution of $12'' \times 24'' \times 8.2$ km s^{-1}. Inspection of their Figure 8 (N_{HI} map) shows the presence of a partially opened, elliptical, empty H I shell surrounding the location of NGC 595. The top, northernmost, section of the shell is opened to the ISM. In fact, Deul & den Hartog (1990) made a study of all such structure in M33. For NGC 595, the velocity of the H I gas varies between -202 and -164 km s^{-1} with a maximum contrast obtained at -191 km s^{-1}. The authors used a distance of 724 kpc to M33. Corrected to our adopted distance, the ellipse has a size of 140×210 pc^2, an H I density of ~ 0.3 cm^{-3}, and a mass of 5.0×10^4 M$_\odot$. The shell has an expansion velocity of 18 km s^{-1}. For this work, we intend to use new H I observations of NGC 595 with a higher sensitivity and characterized by better spatial and spectral resolutions (see Section 7.5).

Single dish and interferometric observations of the CO (1-0) transition emission in NGC 595 are provided by Wilson & Scoville (1992). The integrated intensity map [over the full range in velocity] of the CO emission reveals two close knots labeled N595-1 ($\alpha_{2000} = 01^h33^m33^s.87$, $\delta_{2000} = 30°41'22''.3$) and N595-2 ($\alpha_{2000} = 01^h33^m33^s.16$, $\delta_{2000} = 30°41'22''.3$). The authors could not conclude if the two dense clouds are either separate objects or belong to a single molecular structure. The single dish flux corresponds, once corrected to our adopted distance to the nebula, to a total H_2 gas mass of $5.8 - 9.2 \times 10^5$ $M_{\odot}$. The low signal-to-noise ratio (S/N) of the CO line makes it difficult to obtain reliable information on the kinematics of the molecular gas in NGC 595. Table 2 of Wilson & Scoville (1992) gives however an estimate of the line's centroid position for each knot; -186 and -189 km s^{-1} respectively for the eastern (N595-1) and western (N595-2) clouds. All radial velocities in this work are measured with respect to the local standard of rest (LSR). The integrated intensity map of the CO emission was made available for our study of NGC 595 (Pr. Christine Wilson, private communication). In this work, we will consider the two clouds as separate.

7.5 Observations and data reduction

The Hα observations of NGC 595 were performed during the nights of 2006 November 22-23, 23-24 using the Ritchey-Chrétien 1.6m telescope of the Observatoire du mont Mégantic (OmM). The data were gathered using the FaNTOmM (Fabry-Perot of New Technology for the Observatoire du mont Mégantic) device system composed of a f/2 focal reducer, a Fabry-Perot Interferometer (FPI) and an Image Photon Counting System (IPCS). Technical information about the IPCS camera can be found in Hernandez *et al.* (2003). Both the parallelism and the spacing between the plates of the FPI were monitored using a servo-control system. A finesse of 18 was measured for the two observing nights. This allowed us to perform the spectral scanning at a fixed number of 44 steps (channels). The central interference order of the FPI was fixed at $m_0 = 765$ for a free spectral range of 8.56 Å (391.77 km s^{-1}) centered on the Hα rest frequency, and, therefore, a channel step of 0.19 Å channel^{-1} (8.89 km s^{-1} channel^{-1}). The spectral scanning covers seven interference orders[1] (labeled m_0, $m_{\pm1}$, $m_{\pm2}$, $m_{\pm3}$) for a total range of 60 Å (7 orders × 8.56 Å orders^{-1}). The calibration interferogram was obtained using the λ6598.95 Å Ne-line. A narrow-band ($\Delta\lambda_{FWHM} = 15$ Å) interference filter, slightly redshifted from λ6562.78 Å in order to compensate for blueshifting effects (-0.2 Å·K^{-1}) caused by cold ambient temperatures, was used. Emission attributed to the peripherical scanned orders ($m_{\pm2}$, $m_{\pm3}$) was therefore flattened out by the narrow transmissive band. This greatly reduces the possibility of finding two or more lines (of different wavelengths) superimposed on a given channel. The focal reducer allowed a spatial resolution of 1ʺ61 pixel^{-1} and a field of view (FOV) of 13ʹ7×13ʹ7 using the hard binned 512×512 80 frames per second mode of the CCD detector.

The [O III] observations were performed at the Canada-France-Hawaii Telescope (CFHT) on 1987 December 2-3, 3-4, and 4-5 using the same focal reducer[2], the Université Laval FPI, and an IPCS camera. The central interference order of the FPI was fixed at $m_0 = 1003$ for a free spectral range of 4.98 Å (298.51 km s^{-1}) centered on the [O III] rest frequency. The seven interference orders therefore covered a 35 Å-band (7 orders × 4.98 Å orders^{-1}) in wavelength. The free spectral range was scanned in 40 steps (channels) for a channel step of 0.12 Å channel^{-1} (7.46 km s^{-1} channel^{-1}). A narrow-band ($\Delta\lambda_{FWHM} = 15$ Å) interference filter centered on λ5006.85 Å was used. The calibration interferogram was obtained using the λ4861 Å Hβ-line. The focal reducer allowed a spatial resolution of 1ʺ16 pixel^{-1} for 256^2 pixels and a FOV of 4ʹ9×4ʹ9.

The [S II] observations were also performed with the OmM facilities on 2008 August 28-29, September 1-2, and 2-3 using the FaNTOmM device system (see above). The finesse of the FPI (∼18), the number of scanned channels (44), the spatial resolution (1ʺ61 pixel^{-1}), and the FOV (13ʹ7×13ʹ7) were the same as the Hα observations. The free spectral range of the FPI was 8.99 Å (401.21 km s^{-1}) centered on λ6724 Å. The channel step was therefore estimated at 0.20 Å channel^{-1} (9.12

---

[1] Note that the seven interference orders are scanned simultaneously in parallel. Each order wraps around the others and is summed on each channel. Theoretically, a given channel therefore indicates the contribution in emission of seven different wavelengths, one for each interference order. Obviously, each of these wavelengths does not coincide with a nebular or atmospheric line. However, two lines can be potentially superimposed on a given channel. For this particular case, a difficulty arises since the observer must separate these lines (using a multi-component fit) in order to carry out a reliable kinematical study of the targeted object.

[2] Note that the focal reducer used for the [O III] observing run was slightly modified in the late '90s. More details on the "upgraded" PANORAMIX focal reducer, used for the Hα and [S II] observations, can be found in Section 2.1 of Godbout *et al.* (1998).

km s^{-1} channel^{-1}). The λ6717.04 Å Ne-line was used to produce the interferogram for the radial velocity calibration while an intermediate-band ($\Delta\lambda_{FWHM} = 45$ Å) interference filter enabled the simultaneous observation of both lines ($\lambda\lambda$6716, 6731 Å) of the [S II] doublet. The use of a larger transmissive band implies that each scanned order of the FPI (m_0, $m_{\pm1}$, $m_{\pm2}$, $m_{\pm3}$) likely contributed to the emission at each channel. The spectral scanning of the [S II] observations covered a 63 Å-band (7 orders × 8.99 Å orders^{-1}) between λ6692 Å and λ6755 Å. A priori, this should not lead to spectral disruptions, anomalies or asymmetries [expected from overlapping emission-lines found in different orders] since the [S II] doublet represents the only two optical lines (nebular or atmospheric) observed in this range of the electromagnetic spectrum. Both lines of the [S II] doublet are observed in adjacent interference orders due to the 15 Å interval separating them, a value greater than the FPI's free spectral range (see above).

For all observing runs, each channel was exposed to the nebular light for 10 seconds. The spectral scanning (i.e., cycle) of the 60, 35, and 63 Å-bands in wavelength (respectively in Hα, [O III], and [S II]) was therefore completed in 440, 400, and 440 seconds respectively. These times are roughly a factor two shorter than the 15-minutes time-interval estimated for the photometric variations of the sky (Skinner *et al.* 1998). The total numbers of gathered cycles are 30, 65, and 140 respectively in Hα, [O III], and [S II]. We therefore estimated the total acquisition times to 3 hours and 40 minutes spread over two nights, 7 hours and 13 minutes spread over three nights, and to 17 hours and 6 minutes spread over three nights respectively for the Hα, [O III], and [S II] observations.

Data reduction of our interferometric optical observations was carried out using the ADHOCw[3] software (Laval *et al.* 1987) specially tailored to reproduce the method used for the TAURUS FP spectrometer (Atherton *et al.* 1982). For each observing run (Hα, [O III], and [S II]), computation of the phase map and its application to the observed interferogram allowed us to obtain a three dimensional (α, δ, λ) raw data cube. For the [O III] and [S II] observations, no contaminant night-sky lines are found in their respective scanned wavelength intervals. Sky subtraction was therefore omitted. For the Hα observations, three atmospheric lines can be found in the transmissive band of the narrow-band filter used; the $\lambda\lambda$6553.6, 6568.8 Å OH lines and the λ6562.8 Å geocoronal Hα line (Osterbrock *et al.* 1996). Fortunately, each of these contaminant lines are detected at channels relatively far from the mean velocity of NGC 595 and therefore do not affect the shape of the Hα profiles. To

---

[3] http ://www-obs.cnrs-mrs.fr/adhoc/adhoc.html

avoid spectral disruptions caused by a less than perfect subtraction of the night-sky emission, we also chose to omit sky subtraction in our Hα observations. Nonetheless, a multi-component Gaussian fit giving the intensity (in units of photon counts), the spectral position (or radial velocity) and the observed line width ($\sigma = \mathrm{FWHM}/2.354$) of each component was applied on each emission spectrum of our Hα cube. We explicitly imposed that the fitting procedure adjusts components at the specific positions of the contaminant lines mentioned above [in order to clearly separate them from the Hα lines]. The same multi-component Gaussian fit (without, obviously, the condition on night-sky lines) was also applied on the [O III] and [S II] cubes. In every case (atmospheric lines included), the minimal S/N allowed for a fitted line was fixed at three. The measured S/Ns spread from 3 to 746 with a mean of 69 in Hα and from 3 to 71 with a mean of 12 in [O III]. For the [S II] observations, the λ6716 Å line was used to estimate the kinematics of the S^+ material in NGC 595 (see Section 7.6.3). For this line, the S/Ns spread from 3 to 77 with a mean of 14.

In order to extract purely kinematic broadening effects from the observed Hα, [O III], and [S II] line widths, the method of quadratic subtraction presented in Lagrois & Joncas (2009a) was used. For each ion, the broadening excess caused by thermal motions was estimated and subtracted assuming a constant electron temperature of 8 500 K in NGC 595. The electron temperature was calculated considering a galactocentric radius of 1.54 kpc for NGC 595 (Comte & Monnet 1974) and using the galactocentric electronic temperature gradient for known H II regions in M33 (Magrini *et al.* 2007). The instrumental contribution was taken as the width of the Ne-lines (for Hα and [S II]) and Hβ-line (for [O III]) obtained from the calibration profiles. Following the quadratic subtraction, the resulting σ values will be referred, in the next sections, as the corrected (or non-thermal) Hα, [O III], and [S II] line widths.

For the detector's pixels restricted to the study of NGC 595 (see Section 7.6.1), Figure 7.1 provides the mean instrumental profiles obtained from the velocity calibration of our Hα and [S II] observations. The width of these calibration profiles defines the spectral resolution of our optical observations : 8.39 ± 0.02 km s^{-1}, ~ 12.2 km s^{-1} (figure not available), and 10.19 ± 0.01 km s^{-1} respectively in Hα, [O III], and [S II]. For a given ion, each corrected line width, mentioned in this manuscript with a defined (i.e., positive) value, therefore implied an associated observed line width greater than the corresponding spectral resolution.

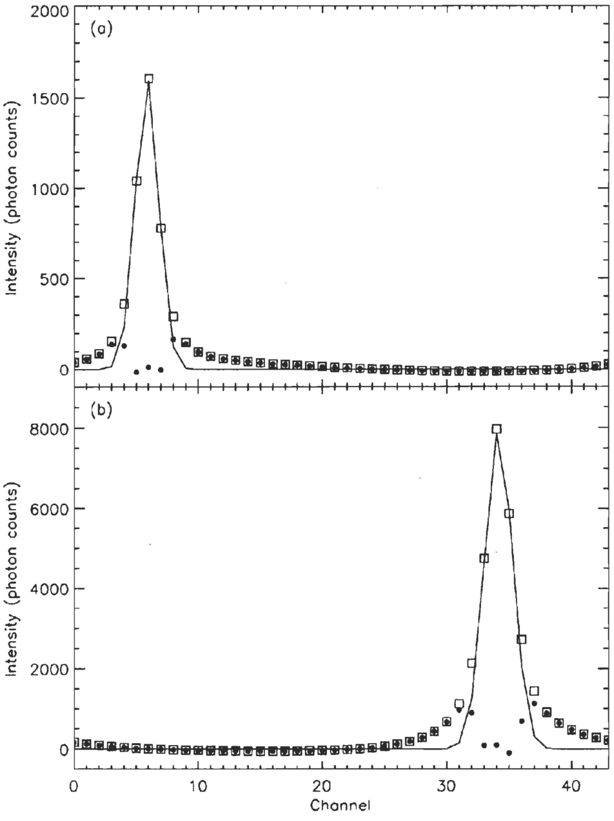

Figure 7.1: Mean Ne-lines calibration profiles for NGC 595.

Mean Ne-line calibration profiles (open squares) obtained from our (a) : Hα and, (b) : [S II] observations. The solid lines show the Gaussian fit on each profile. Filled circles correspond to the residual of the fit for each channel. The dispersions (σ's) of the Gaussian curves are estimated at 8.39 ± 0.02 km s^{-1} *and 10.19 ± 0.01 km* s^{-1} *respectively in Panels (a) and (b). These values respectively define the spectral resolution of our Hα and [S II] observations. As expected, the extended wings of the Airy profiles are not well-fitted by the Gaussian shape. However, the goodness of fit remains particularly reliable from the peak of maximal intensity down to a width of roughly 3σ. The spectral resolution of our [O III] observations is estimated at 12.2 km* s^{-1}*. We cannot provide the Hβ-line calibration profile since it is not available in digitized form.*

The distribution and kinematics of H I in M33 were measured (Thilker *et al.* 2009) during survey observations undertaken at the Very Large Array (VLA) and the Green Bank Telescope (GBT). The interferometric dataset combined visibility data recorded in multiple configurations of the VLA. B- and C-array observations were obtained with a mosaic of six synthesis pointings designed to optimize sensitivity and uniformity of coverage across M33's disk. Visibility measurements in the D-array were obtained over a larger survey area spanning $3° \times 4°$, employing the VLA's raster offset mode to define a Nyquist sampled grid of pointings. All the VLA data were calibrated within AIPS, according to usual convention. More detail will be provided in Thilker *et al.* (2009). Total power H I data covering a $5° \times 5°$ area were obtained at the GBT using an on-the-fly observing strategy. The angular resolution of the GBT observations ($9\overset{\prime}{.}1$ FWHM) was well-suited to compensate for the short spacing information missing from the VLA interferometry. The M33 GBT data is similar to a companion M31 survey described more fully by Thilker *et al.* (2004).

Joint deconvolution of all VLA pointings was completed with MOSSDI in Miriad on a channel-by-channel basis, after forming a weighted sum of the linearly combined synthesis image (created with uniform weighting then a subsequent Gaussian taper) and the GBT total power image at matching velocity. Deconvolved H I data cubes were generated at a variety of angular and velocity resolutions (reaching down to observational limits of $5''$ pixel^{-1} and 1.3 km s^{-1}). The H I data were obtained, reduced and provided by Dr. David A. Thilker (private communication).

7.6 Results

7.6.1 Peak intensity maps

Figures 7.2 and 7.3 present respectively the Hα and [O III] peak intensity maps for a 1-component fit. Similarly, Figure 7.4 shows the [S II] peak intensity map for a 2-component fit applied to the [S II] doublet. The figures show $4' \times 4'$ areas centered on NGC 595 and, therefore, correspond to sub-regions of our original FOVs (see Section 7.5). The [O III] observations were spatially degraded (from $1\overset{\prime\prime}{.}16$ pixel^{-1} to $1\overset{\prime\prime}{.}61$ pixel^{-1}) in order to match the resolution of our Hα and [S II] observations (see Section 7.5). Using the adopted distance to NGC 595 (see Section 7.4), the spatial

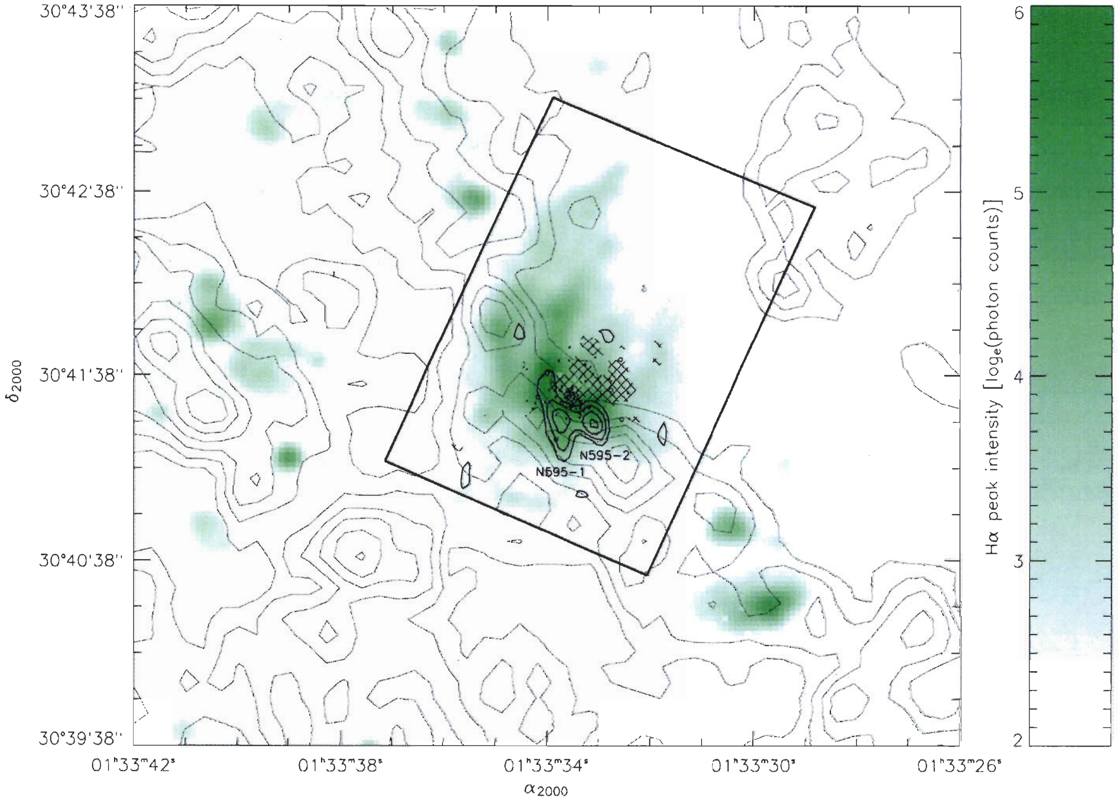

Figure 7.2: Hα peak intensity map in NGC 595.

The value of each pixel indicates the peak photon count obtained from the fitting procedure assuming 1-component profiles everywhere in the FOV. The minimal S/N for a fitted line was fixed at three. We applied a log_e*-scale to the map in order to emphasize faint emission. The black rectangle indicates the approximate ionized extent of NGC 595. The hatched region encompasses velocity profiles showing line splitting (discussed as 2-component profiles in Section 7.7.3). Open circles (black dots) show the position of WR-stars (main-sequence O-stars). The molecular emission, in brightness temperatures, corresponds to the thick contours of the CO (1-0) integrated intensity map with four levels between 2 and 8 K and a spacing of 2 K. The atomic emission, in brightness temperatures, corresponds to the regular contours of the H*I *integrated intensity map with seven levels between 15 and 75 mK and a spacing of 5 mK. The two molecular clouds, associated with NGC 595, are identified (see text).*

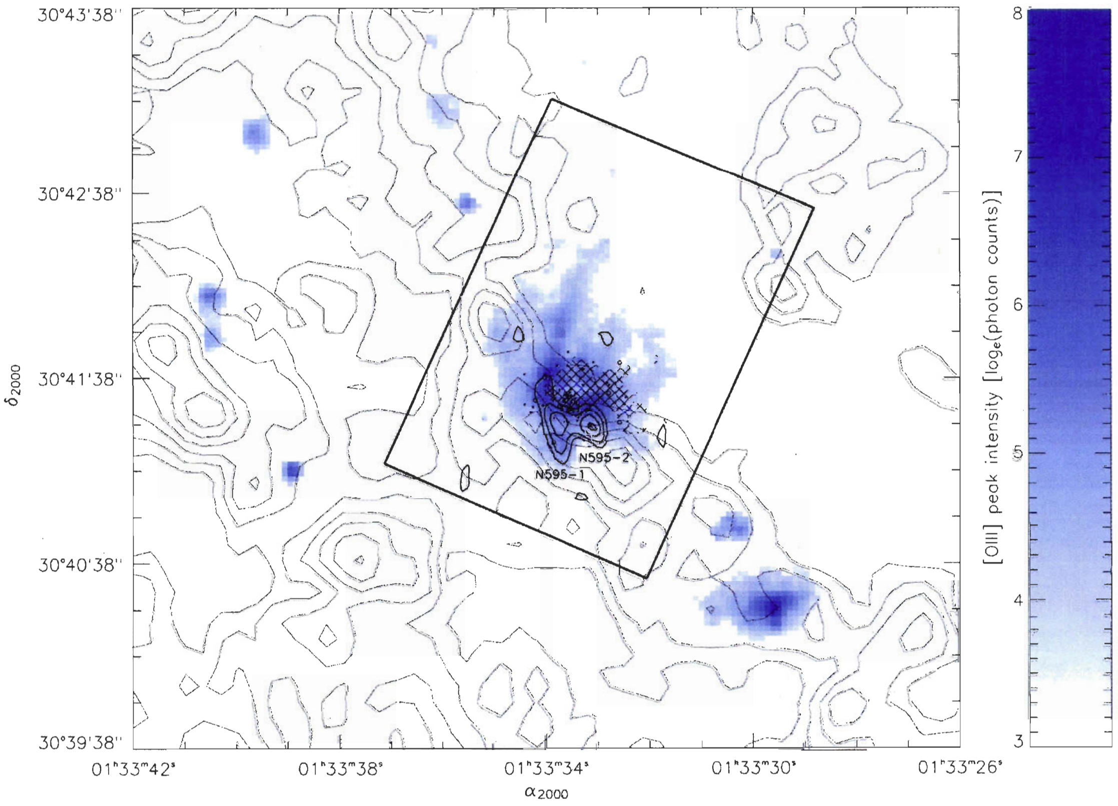

Figure 7.3: [O III] peak intensity map in NGC 595.

The contours, star symbols, and hatched region all kept the same definitions as in Figure 7.2.

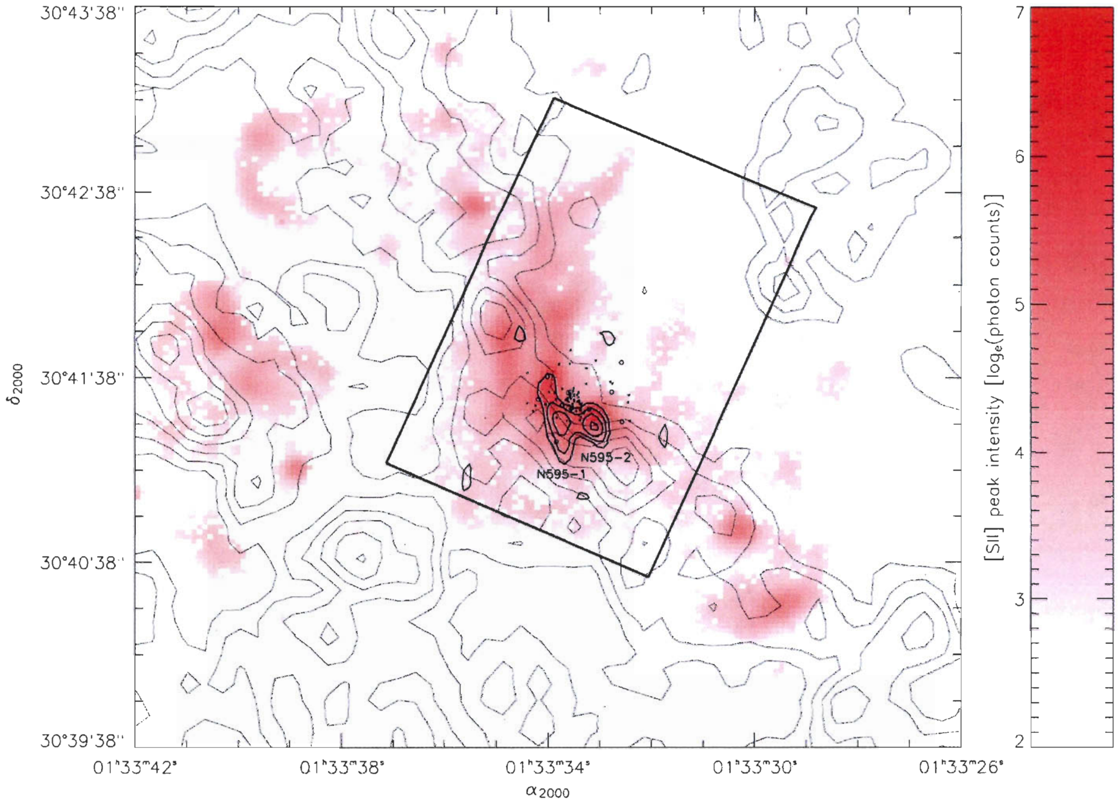

Figure 7.4: [S II] peak intensity map in NGC 595.

A 1-component fit has been applied on each line of the [S II] doublet. The peak intensity corresponds to the sum of the two peak photon counts obtained. The contours and star symbols all kept the same definitions as in Figure 7.2. Note that the [S II] data show no indication for line splitting (no hatched region).

resolution of our Fabry-Perot observations is therefore 6.61 pc pixel^{-1} in Figures 7.2 to 7.4.

A particular area of NGC 595 shows a clear indication of line splitting in both Hα and [O III]. These profiles were fitted using 2-component Gaussians while the corresponding pixels are identified, in Figures 7.2 and 7.3, by the overplotted hatched region. These pixels will be treated independently from the 1-component profiles since they likely indicate a much different kinematic origin (see Section 7.7.3). No indication of line splitting was found in the [S II] data.

We added, to the ionized emission of Figures 7.2 to 7.4, contour plots of the interferometric 21 cm line observations (Thilker *et al.* 2002) and the interferometric CO (1-0) emission (Wilson & Scoville 1992). The $4' \times 4'$ FOV of the H I observations used in this work shows a mean noise level estimated at roughly 4 mK. The spatial and spectral resolutions are $5''$ pixel^{-1} and 3.9 km s^{-1} respectively. The mean noise level of the CO data cube is estimated at 1 K. In all three figures, the two molecular knots (see Section 7.4) can be seen near the brightest ionized material. In order to avoid crowding in the subsequent figures, the N595-1 and N595-2 molecular clouds are only identified in Figures 7.2 to 7.4. The H I observations were kept at their original spatial resolution while the original spatial resolution ($1''.50$ pixel^{-1}) of the CO observations was slightly degraded in order to match the resolution of our Fabry-Perot measurements ($1''.61$ pixel^{-1}).

The ten WR-stars, identified by Drissen *et al.* (1993, 2008), are indicated by open circles in Figures 7.2 to 7.4. Of the 600-star candidates found by Malumuth *et al.* (1996), 267 stars present observations for all F336W, F439W, and F547M filters. Binary systems, supergiants and WR-stars, found in the authors' on-line table, were ruled out. The CHORIZOS IDL procedure (Maíz-Apellániz 2004) uses the three observed magnitudes in order to compute the most probable effective temperature for each star. We used the extinction law provided by Cardelli *et al.* (1989). We obtained 76 main-sequence candidates[4] presenting an effective temperature hotter than 33 000 K (which corresponds to main-sequence stars earlier than B0V). The 76 O-stars are represented by black dots in Figures 7.2 to 7.4.

Finally, the black rectangle defines the region, we believe, encloses the majority of the ionized emission attributed to NGC 595. The box has dimensions of 500 × 325

---

[4] Note that this value is slightly different from the 98 O-stars estimated by Malumuth *et al.* (1996). However, the authors used a lower limit in temperature of 30 000 K.

pc^2 on the plane of the sky which correspond roughly to the 425 pc diameter for NGC 595 estimated by Kennicutt (1984) (see Section 7.4). The rectangle encloses the H I shell identified by Deul & van der Hulst (1987) (see Section 7.4). However, it is particularly difficult to estimate the extent of the atomic component (beyond the H I shell) associated to the nebula. Instead, the rectangle's dimensions were chosen specifically in order to avoid contamination by the emissive ionized material of smaller H II regions surrounding NGC 595.

7.6.2 Radial velocity profiles : a few examples

Figure 7.5 presents a series of examples of radial velocity profiles obtained from our Hα and [O III] observations. Panels (a) and (c) correspond to typical profiles, in Hα and [O III] respectively, spatially located near the bright central core of the nebula along the LOS of the molecular cloud. Panels (b) and (d) are found in the hatched region displayed in Figures 7.2 and 7.3 that reveals evidence for line splitting. A profile example associated to our [S II] observations of NGC 595 was judged unnecessary since the [S II] doublet is apparently "normal" throughout the whole area bounded by the black rectangle (see Figure 7.4). The λ6716 Å line usually shows intensities greater than the λ6731 Å component, indicating relatively small ($\ll 500$ cm^{-3}) electron densities throughout the nebula (see Section 7.6.5).

7.6.3 1-component radial velocity profiles in Hα, [O III], and [S II]

Figures 7.6, 7.7 and 7.8 summarize the investigation of the 1-component profiles obtained respectively from the Hα, [O III], and [S II] observations (note that we will refer to the [S II] observations as presenting 1-component profiles in a sense that no evidence for line splitting was found in the [S II] doublet, see Section 7.6.1). The pixels associated with the overplotted hatched region in Figures 7.2 and 7.3 have therefore been removed from Figures 7.6 and 7.7 and will be investigated separately in the next subsection (Section 7.6.4). We reiterate the fact that the radial velocities and the corrected line widths of the [S II] doublet were measured using the λ6716 Å line. Statistical parameters for the radial velocity and corrected line-width distributions are provided in Table 7.1 : mean values ($\langle v_{1-comp} \rangle$, $\langle \sigma_{1-comp} \rangle$), one-standard

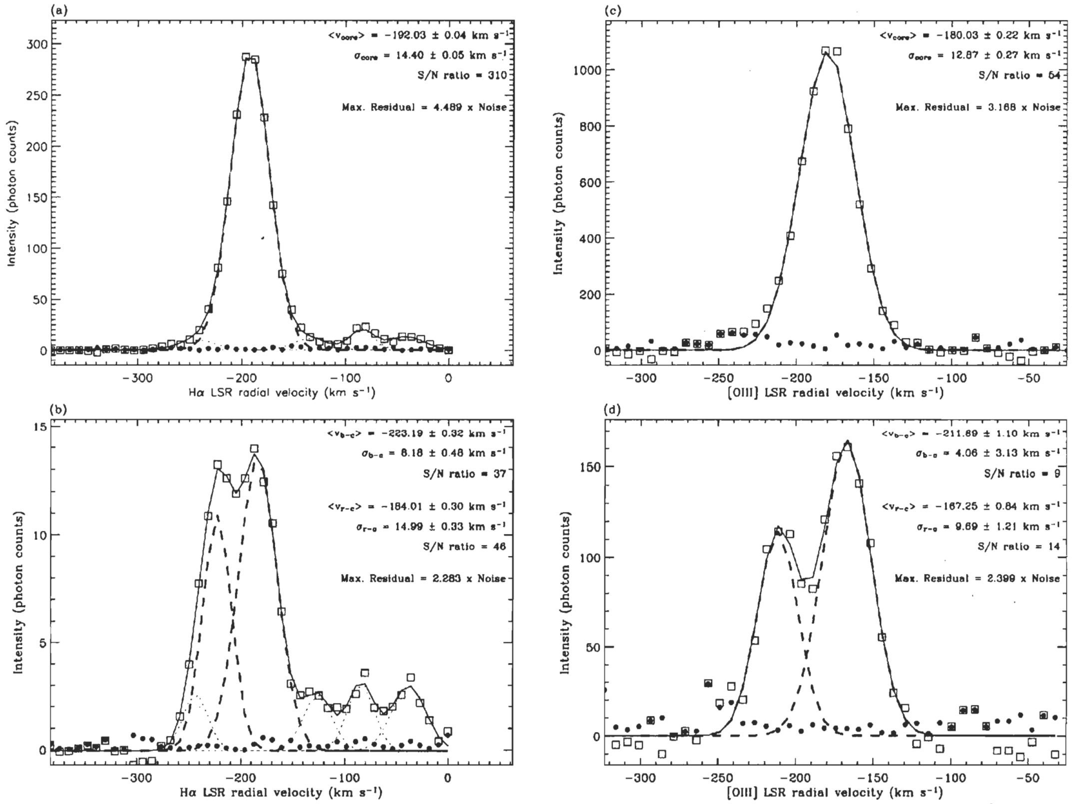

Figure 7.5: Examples of radial velocity profiles.

Panel (a) : 1-component Hα profile located inside the black rectangle of Figure 7.2 (outside the hatched region). Panel (b) : 2-component Hα profile located inside the hatched region of Figure 7.2. Panel (c) : 1-component [O III] profile located inside the black rectangle of Figure 7.3 (outside the hatched region). Panel (d) : 2-component [O III] profile located inside the hatched region of Figure 7.3. For each panel, the open squares correspond to the observational data. The bold long-dashed lines indicate the fit to the Hα and [O III] profiles. In Panels (a) and (b), the thin dotted lines correspond to the contaminant night-sky lines found in the wavelength interval covered by the Hα observations (see Section 3). In every case, the solid line shows the total fit on the observational data (the sum of all fitted components ; long-dashed and thin dotted lines). For each channel, the filled circle represents the residual of the total fit. In each panel, the radial velocity, the corrected (non-thermal) line width, and the S/N are provided for each Hα and [O III] component. Also included is the intensity of the maximal residual with respect to the noise level for each spectrum.

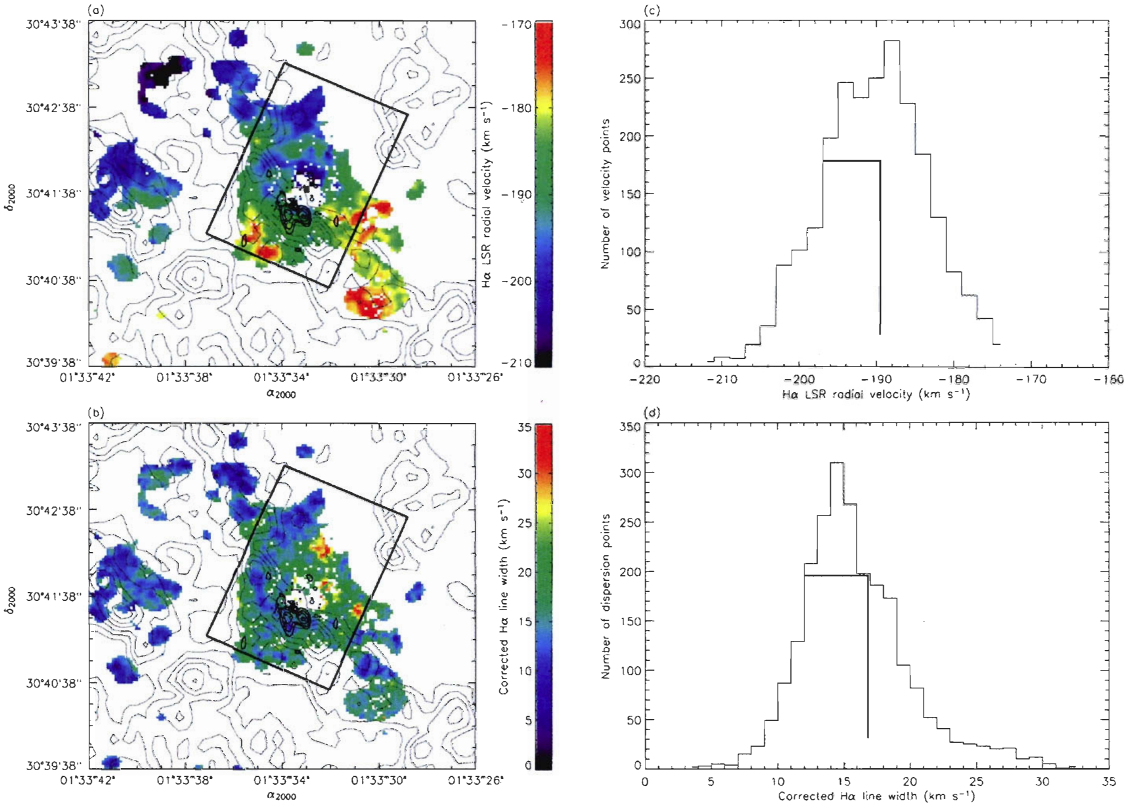

Figure 7.6: Investigation of the 1-component profiles in Hα.

Open circles, black dots, and thick and regular contours all kept the same definitions as in Figure 7.2. White pixels are undefined values (with S/N< 3). The hatched region's pixels are also treated as undefined for the cause. Panel (a) : Radial velocity map measured with respect to the LSR. Panel (b) : Non-thermal Hα line-width map corrected for the thermal broadening, the instrumental response, and the natural width of the Hα-line. Panel (c) : Radial velocity histogram of all defined velocity points encompassed by the black rectangle of Panel (a). Panel (d) : Corrected line-width histogram of all defined dispersion points encompassed by the black rectangle of Panel (b). In the two latter panels, the vertical and horizontal thick lines respectively indicate the mean and one-standard deviation of the distribution. These values are listed in Table 7.1.

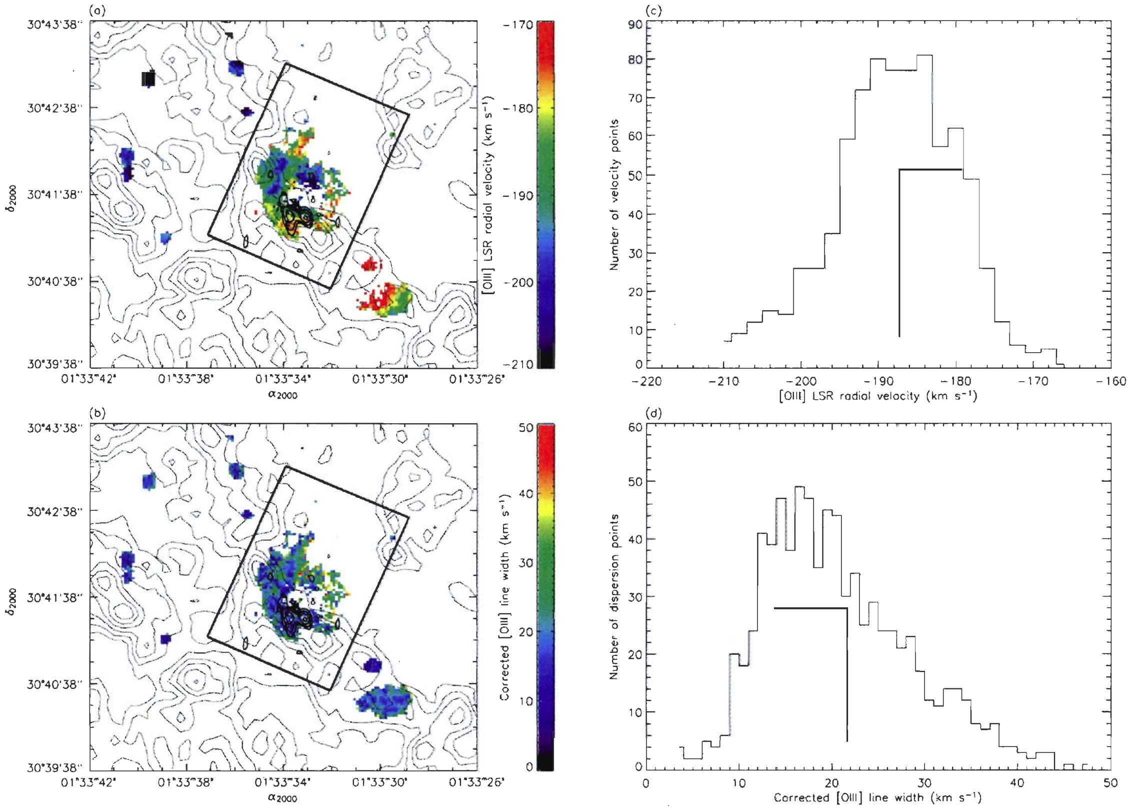

Figure 7.7: Investigation of the 1-component profiles in [O III].

Each panel has the same signification as in Figure 7.6. The statistical parameters of the radial velocity and corrected line-width histograms are provided in Table 7.1.

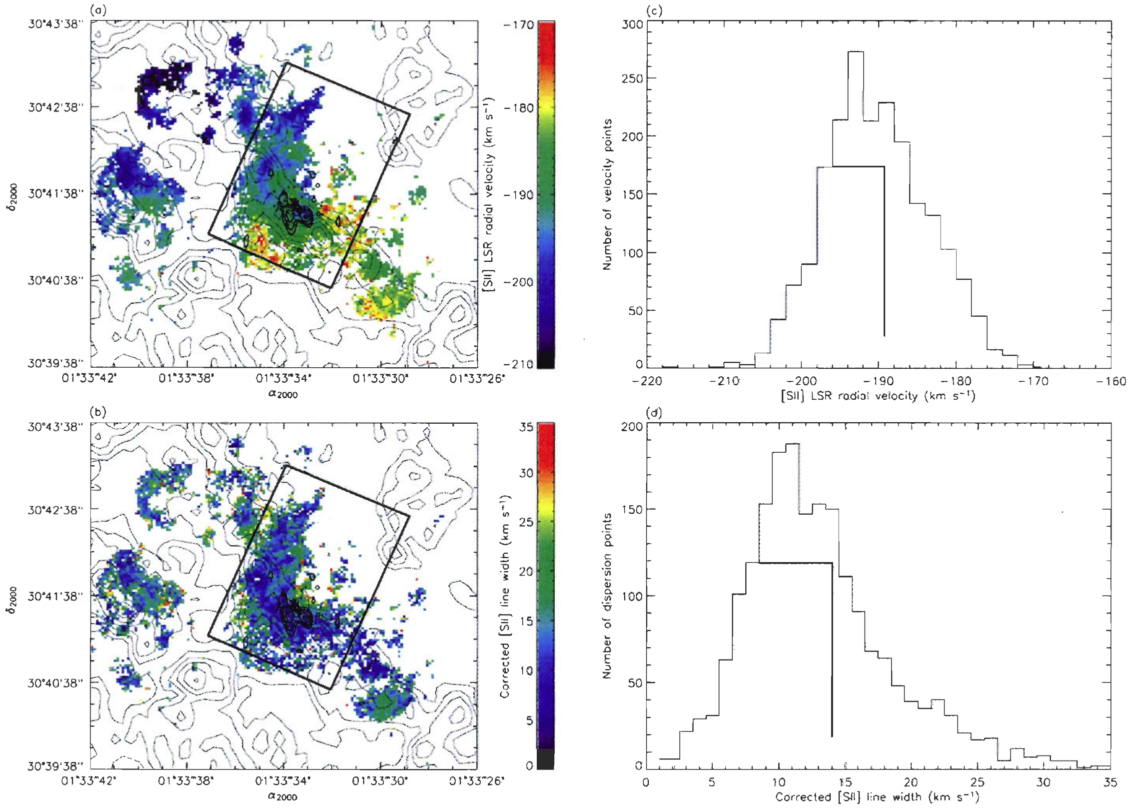

Figure 7.8: Investigation of the 1-component profiles in [S II].

The λ6716 Å line of the [S II] doublet was used for the measurements. Each panel has the same signification as in Figure 7.6. The statistical parameters of the radial velocity and corrected line-width histograms are provided in Table 7.1.

Table 7.1: Kinematical investigation of the 1-component profiles in NGC 595.

Line	Figure	LSR radial velocities				Corrected line widths			
		$\langle v_{1-comp} \rangle$ (km s^{-1})	β_v (km s^{-1})	Skewness	N$_{pts}$	$\langle \sigma_{1-comp} \rangle$ (km s^{-1})	β_σ (km s^{-1})	Skewness	N$_{pts}$
Hα	7.6	-189.52 ± 0.14	6.95 ± 0.10	-0.119	2 343	16.83 ± 0.09	4.12 ± 0.06	0.818	2343
[O III]	7.7	-187.28 ± 0.29	8.12 ± 0.20	-0.315	812	21.63 ± 0.28	7.88 ± 0.20	0.607	804
[S II]	7.8	-189.26 ± 0.15	6.69 ± 0.10	0.091	2 054	14.02 ± 0.13	5.95 ± 0.09	1.563	1 989
H I	7.16, 7.17	-186.06 ± 0.15	7.25 ± 0.11	-0.396	2 320[a]	–	–	–	–
CO (N595-1)	–	-186	2.3	–	–	–	–	–	–
CO (N595-2)	–	-189	6.0	–	–	–	–	–	–

Note : The kinematics of the CO clouds (N595-1, N595-2) is provided by Table 2 of Wilson & Scoville (1992).

---

[a] The number of points results from the spatial rescaling of the H I data cube.

deviations (β_v, β_σ), asymmetry coefficients (skewness), and the corresponding total number of points (N_{pts}).

For the [O III] and [S II] observations, slight differences can be noted between the N_{pts} values of Columns 6 and 10. This simply results from a few velocity profiles, for both ions, presenting an observed line width (from the fitting procedure) smaller than the instrumental width. These points were rejected from the line-width analysis but were nevertheless preserved for the investigation of the radial velocity behavior. The mean kinematic characteristics of the CO (Wilson & Scoville 1992) and H I (see Section 7.7.2.4) components associated to NGC 595 are also provided in Table 7.1.

7.6.4 2-component radial velocity profiles in Hα and [O III]

Similarly to Panels (b) and (d) of Figure 7.5, each velocity profile in the hatched region of Figures 7.2 and 7.3 has shown evidence for line splitting. Figures 7.9 to 7.12 present a closer view of the kinematical properties of these particular profiles. The Hα splitted lines are investigated in radial velocities and corrected line widths respectively in Figures 7.9 and 7.10. Figures 7.11 and 7.12 provide a similar investigation for the [O III] profiles. For a given profile, each component will be referred as either blue or red depending on its velocity relative to the other (i.e., the blue component will always refer to the component presenting the most negative velocity and the red component, the most positive velocity). Note that, as opposed to Figures 7.2 to 7.4, the $1'\!.3 \times 1'\!.3$ FOV used here allows for a better insight of the star distribution in the vicinity of the molecular clouds. For both the blue and red components, histograms in radial velocities and corrected line widths of the hatched region displayed in Figures 7.2 and 7.3 are provided in all four Panels (d). Statistical parameters for each of these distributions are provided in Table 7.2 : mean values ($\langle v_{b-c} \rangle$, $\langle v_{r-c} \rangle$, $\langle \sigma_{b-c} \rangle$, $\langle \sigma_{r-c} \rangle$), one-standard deviations ($\beta_{v,b}$, $\beta_{v,r}$, $\beta_{\sigma,b}$, $\beta_{\sigma,r}$), and the total number of points (N_{pts}) in each histogram. In addition, the mean value of each Panel (c) is provided ($\langle \Delta v \rangle$ for Figures 7.9 and 7.11, and $\langle \Delta\sigma \rangle$ for Figures 7.10 and 7.12). This value is also indicated in Figures 7.9 to 7.12 by the small solid line in the color bar adjacent to Panel (c).

Similarly to the investigation of the 1-component profiles (see Section 7.6.3), a certain number of components (either blue or red) in Hα and [O III] have shown observed line widths smaller than the instrumental width (i.e., unresolved lines).

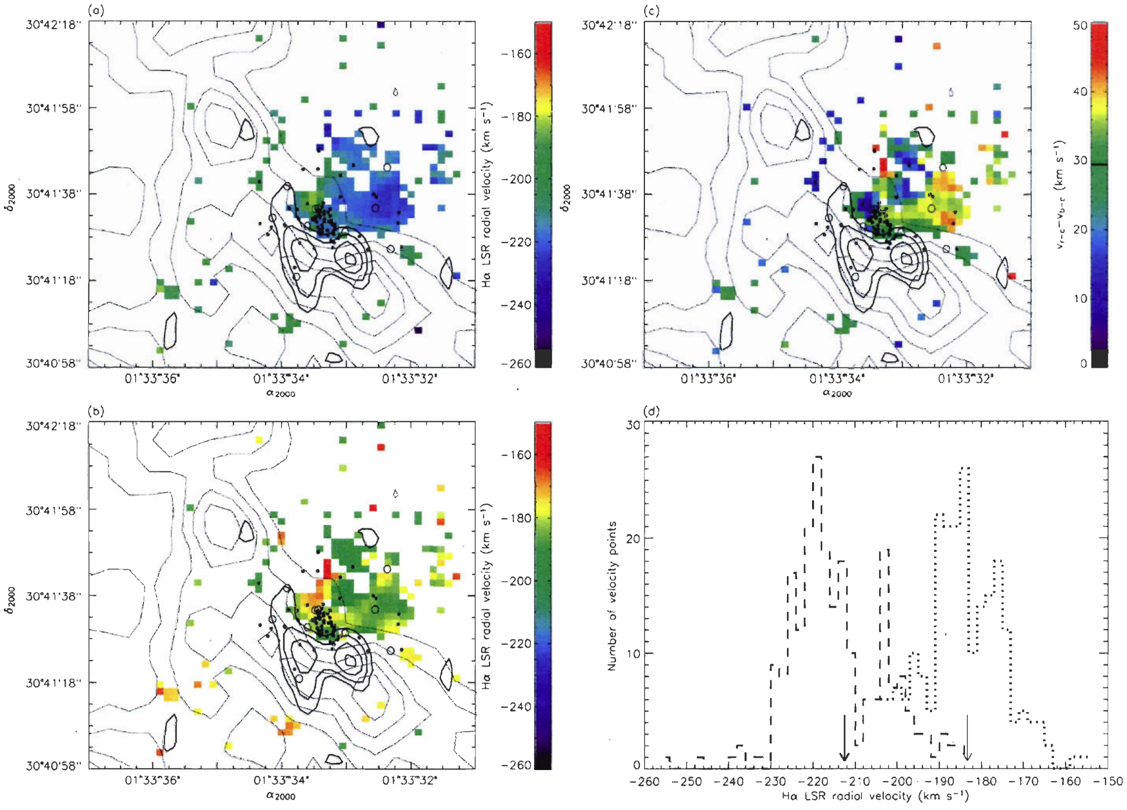

Figure 7.9: Investigation of the 2-component profiles in Hα : the behavior in radial velocities.

Open circles, black dots, and thick and regular contours all kept the same definitions as in Figure 7.2. White pixels are undefined values (these also include, for the cause, 1-component profiles surrounding the hatched region of splitted lines). The component of a given splitted profile having the most negative (positive) velocity is defined as the blue (red) component. Panel (a) : Radial velocity map of the blue component measured with respect to the LSR. Panel (b) : Radial velocity map of the red component measured with respect to the LSR. Panel (c) : Difference in velocities, pixel-to-pixel, between Panels (a) and (b). The blue component's velocities are always subtracted from the red component's velocities in order to obtain positive values. The mean value of Panel (c) is indicated by the small solid line in the adjacent color bar. Panel (d) : Histograms of the radial velocity points displayed in Panels (a) and (b). The dashed (dotted) distribution is associated to the blue (red) component. The thick (regular) arrow indicates the mean value of the blue (red) component's distribution. These values are listed in Table 7.2.

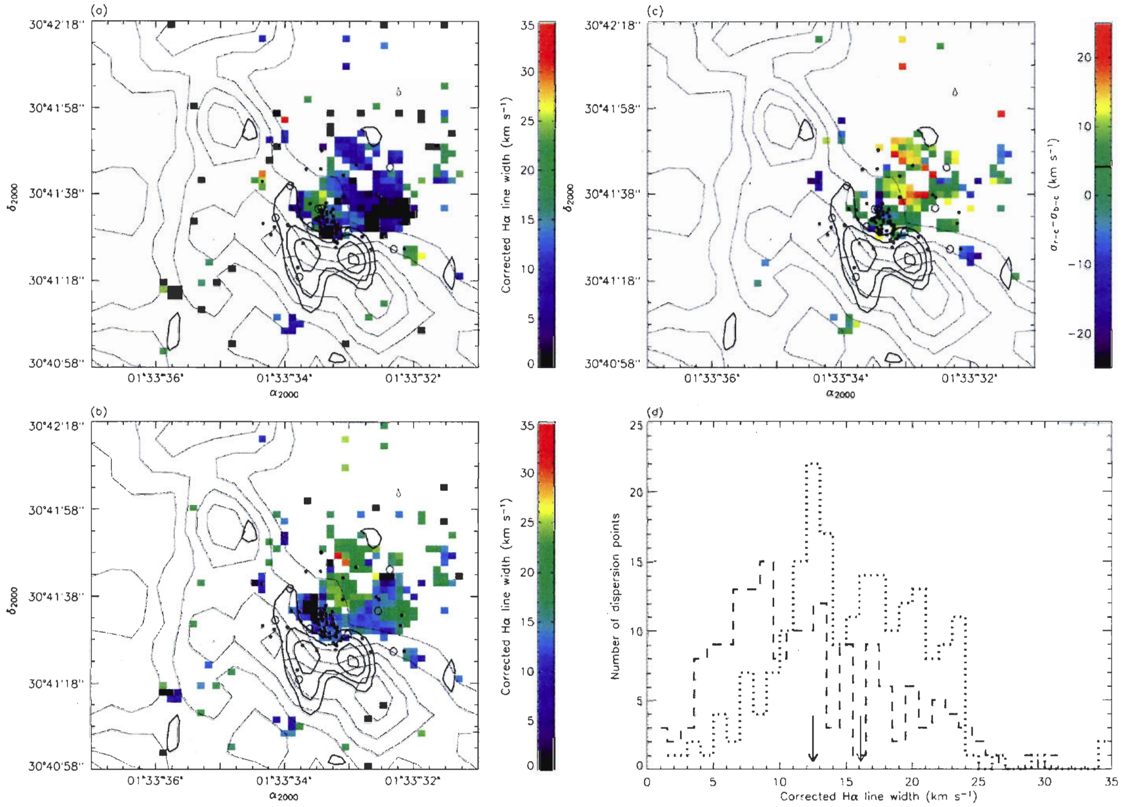

Figure 7.10: Investigation of the 2-component profiles in Hα : the behavior in corrected line widths.

Open circles, black dots, and thick and regular contours all kept the same definitions as in Figure 7.2. White pixels are undefined values (these also include, for the cause, 1-component profiles surrounding the hatched region of splitted lines). Black pixels belong to the hatched region of splitted profiles but show an observed line width narrower than the instrumental profile (i.e., unresolved lines). These pixels can also be regarded as undefined. Panel (a) : Corrected line-width map of the blue component displayed in Figure 7.9a. Panel (b) : Corrected line-width map of the red component displayed in Figure 7.9b. Panel (c) : Difference in line widths, pixel-to-pixel, between Panels (a) and (b). The blue component's widths are always subtracted from the red component's widths. In this case, positive and negative are obtained. The mean value of Panel (c) is indicated by the small solid line in the adjacent color bar. Panel (d) : Histograms of the corrected line-width points displayed in Panels (a) and (b). The dashed (dotted) distribution is associated to the blue (red) component. The thick (regular) arrow indicates the mean value of the blue (red) component's distribution. These values are listed in Table 7.2.

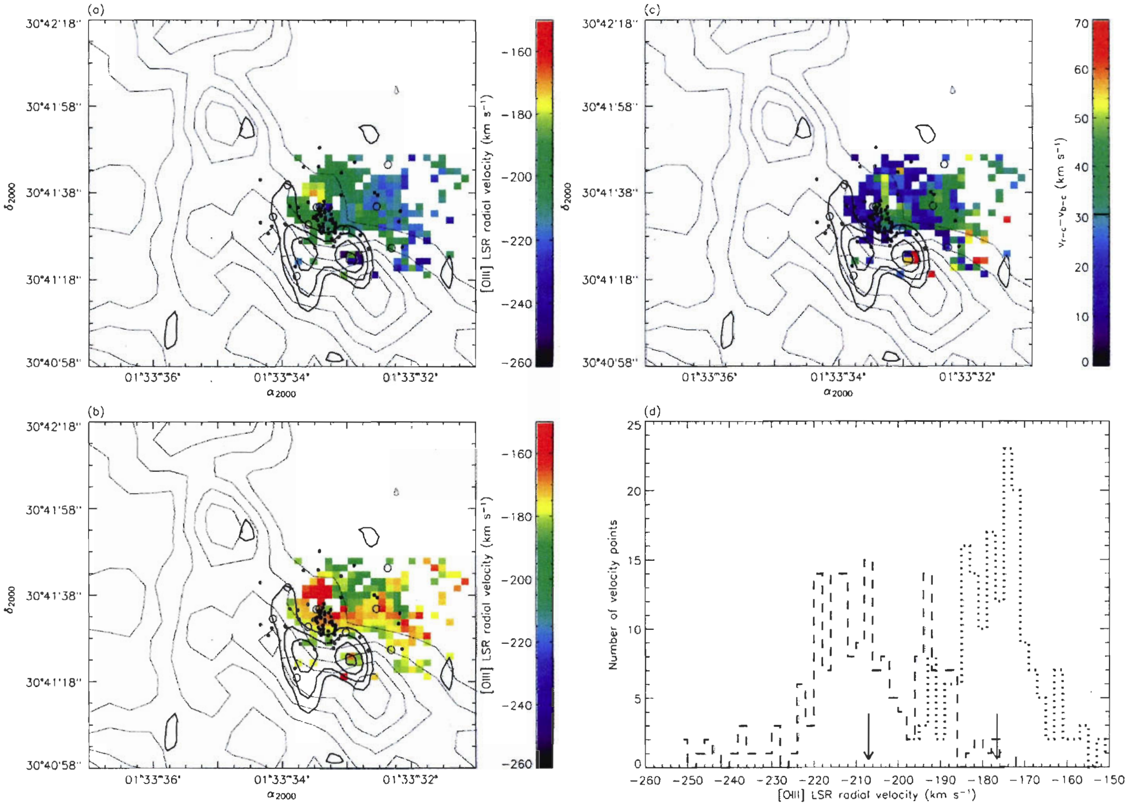

Figure 7.11: Investigation of the 2-component profiles in [O III] : the behavior in radial velocities.

Each panel has the same signification as in Figure 7.9. The statistical parameters of the radial velocity histograms are provided in Table 7.2.

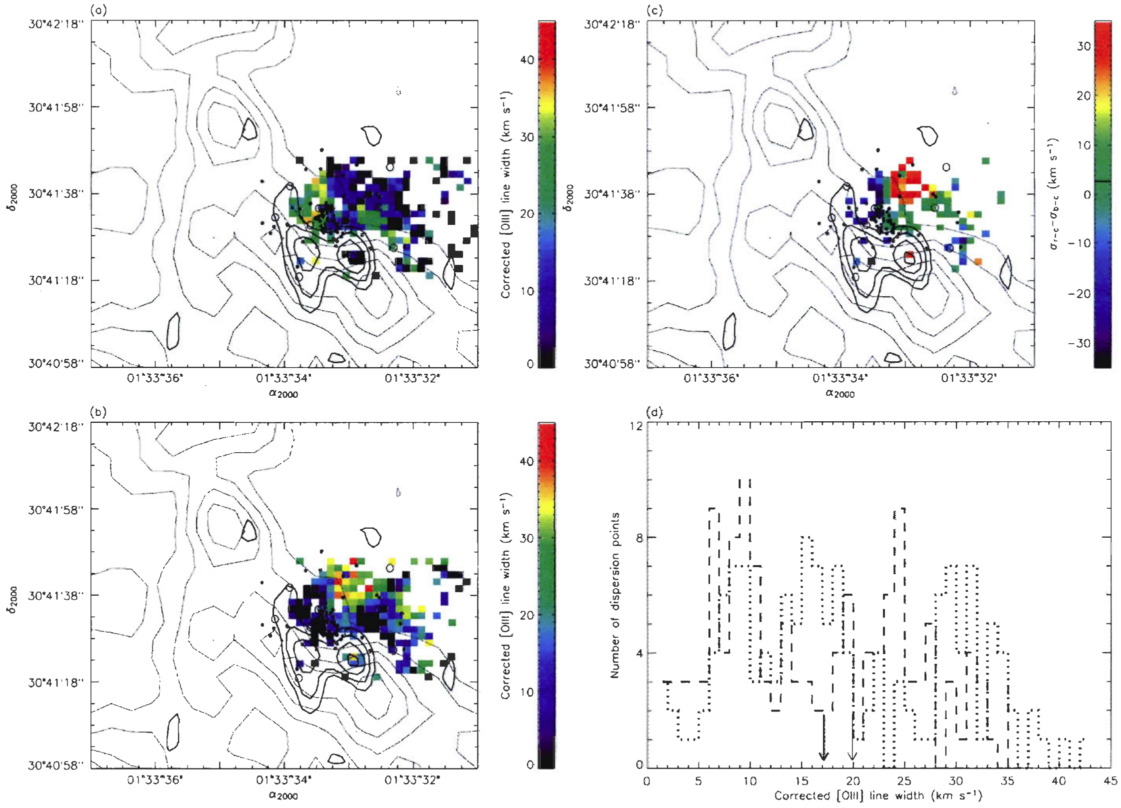

Figure 7.12: Investigation of the 2-component profiles in [O III] : the behavior in corrected line widths.

Panel (a) : Corrected line-width map of the blue component displayed in Figure 7.11a. Panel (b) : Corrected line-width map of the red component displayed in Figure 7.11b. Panel (c) : Difference in line widths, pixel-to-pixel, between Panels (a) and (b). Panel (d) : Histograms of the corrected line-width points displayed in Panels (a) and (b). More details can be found in the caption of Figure 7.10. The statistical parameters of the corrected line-width histograms are provided in Table 7.2.

Table 7.2: Kinematical investigation of the 2-component profiles in NGC 595.

		LSR radial velocities						
			Blue component			Red component		
Ion	Figure	$\langle\Delta v\rangle$ (km s^{-1})	$\langle v_{b-c}\rangle$ (km s^{-1})	$\beta_{v,b}$ (km s^{-1})	N$_{pts}$	$\langle v_{r-c}\rangle$ (km s^{-1})	$\beta_{v,r}$ (km s^{-1})	N$_{pts}$
Hα	7.9	29.51	-212.55 ± 0.76	11.45 ± 0.54	229	-183.30 ± 0.64	9.68 ± 0.45	229
[O III]	7.11	30.31	-206.97 ± 1.12	15.09 ± 0.79	183	-176.66 ± 0.74	9.99 ± 0.52	183
		Corrected line widths						
			Blue component			Red component		
Ion	Figure	$\langle\Delta\sigma\rangle$ (km s^{-1})	$\langle\sigma_{b-c}\rangle$ (km s^{-1})	$\beta_{\sigma,b}$ (km s^{-1})	N$_{pts}$	$\langle\sigma_{r-c}\rangle$ (km s^{-1})	$\beta_{\sigma,r}$ (km s^{-1})	N$_{pts}$
Hα	7.10	4.15	12.50 ± 0.48	6.24 ± 0.34	171	16.13 ± 0.38	5.45 ± 0.27	209
[O III]	7.12	2.63	17.14 ± 0.80	9.23 ± 0.57	133	19.91 ± 0.86	10.61 ± 0.61	140

These particular profiles are identified by black pixels in Panels (a) and (b) of Figures 7.10 and 7.12. A black pixel, in either Panel (a) or (b), directly results in a white, undefined pixel in Panel (c). This undefined pixel is therefore rejected from the calculation of $\langle \Delta\sigma \rangle$. Even though some would be tempted to reject the possibility of a double component if one of the two fitted lines presents an undefined corrected line width, we believe that these velocity profiles (associated to the hatched region of Figures 7.2 and 7.3) all present indubitable evidence for line splitting (see Section 7.7.3) ; black pixels in Panels (a) and (b) of Figures 7.10 and 7.12 simply result from the fact that the device systems used for the data acquisition were clearly limited in spectral resolution (see Figure 7.1) and therefore did not allow to properly resolved these extremely narrow components.

7.6.5 Electron densities

The FIVEL fortran procedure (De Robertis *et al.* 1987), assuming a constant electron temperature of 8 500 K throughout the nebula (see Section 7.5), was used in order to obtain an estimate of the mean electron density (n_e) along each LOS to NGC 595. Rola & Pelat (1994) suggested that only velocity profiles presenting both doublet-lines with a S/N greater than seven should be used in the calculation of the electron densities. In order to increase the S/N of our [S II] observations, a 2×2 spatial bin was applied to the data cube. For the density investigation, the spatial resolution is therefore 13.22 pc pixel^{-1}. Using a mean geocentric radial velocity of -212 km s^{-1} for the S^+ material (the LSR correction for the [S II] observations is estimated at roughly +23 km s^{-1}), the [S II] doublet is observed at wavelengths corresponding to $\lambda\lambda$6711.6, 6726.0 Å ($\lambda_{\rm obs} - \lambda_{\rm rest} \sim$ -4.8 Å). According to the transmission profile of the intermediate-band interference filter used for the [S II] observations (see Section 7.5), we calculated that, for equal intensities, the λ6731 Å line would appear roughly 5% fainter than the λ6716 Å line. Therefore, each λ6731 Å line profile was rescaled to compensate for this instrumental effect. For a given line, the flux is calculated by summing the contribution in intensity for each channel under the velocity profile. The integrated intensity is then multiplied by the channel step of our [S II] observations (see Section 7.5).

Figure 7.13 shows the electron density map obtained, at each point, by the flux ratio of the [S II] doublet (Osterbrock 1989, Chapter 5). As expected, the electron density spatial distribution agrees with the morphology of the H I component. The

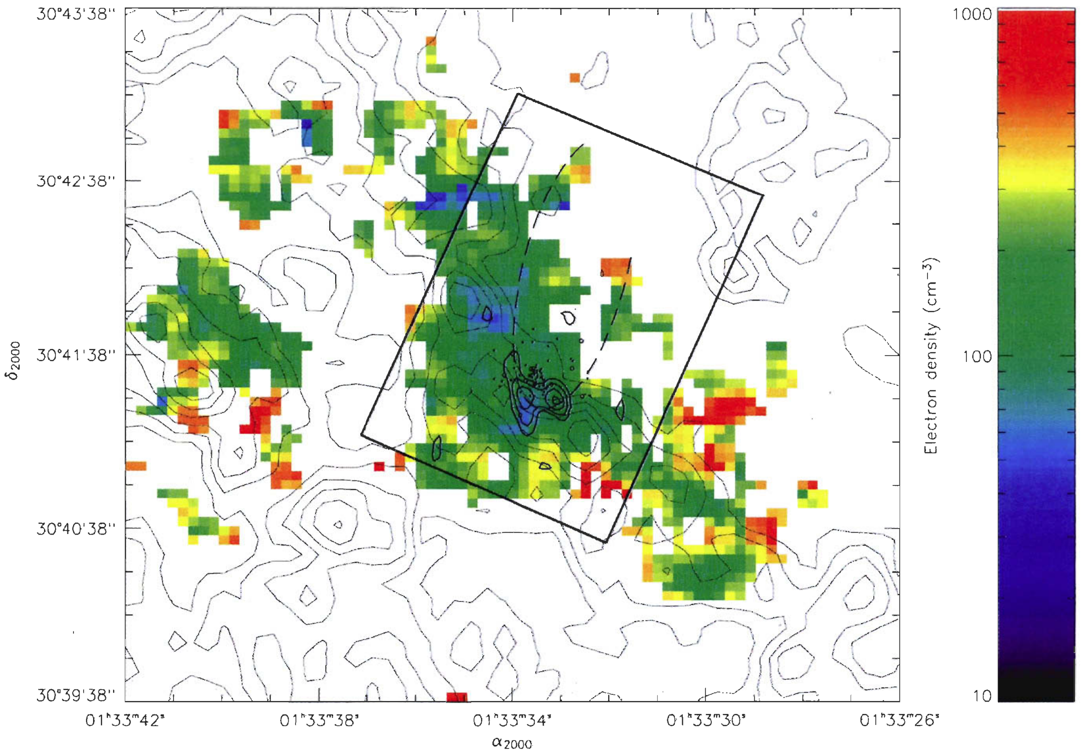

Figure 7.13: Electron density map in NGC 595.

Obtained from the flux ratio of the [S II] *doublet* ($F_{\lambda 6716}/F_{\lambda 6731}$). *The partial ellipse indicates approximately the ovoid supershell associated with NGC 595 and is traced out using the filamentary extensions that seem to originate from the molecular clouds. The color bar is logarithmic ranging from 10 to 1 000* cm^{-3}. *Open circles, black dots, and thick and regular contours all kept the same definitions as in Figures 7.2 to 7.4.*

partial ellipse (long-dashed line) fits well the H^+ and S^+ filamentary extents that seem to originate from the molecular clouds' vicinity (see Figures 7.2 and 7.4) and will be further discussed in Sections 7.7.2.1 and 7.7.2.2. We provide, in Figure 7.14, the distribution of the 551 density points located inside the black rectangle of Figure 7.13. Statistical parameters of the distribution are provided in Table 7.3. Note that Column 6 corresponds to the range of S/Ns measured, in our electron density investigation, for the λ6731 Å line (once rescaled for the instrumental effect discussed above). For NGC 595, this line is the weakest of the [S II] doublet (see Section 7.6.2) and therefore indicates if a given velocity profile respects or not the criterion of Rola & Pelat (1994). The upper limit in Column 6 is substantially greater than the range of S/Ns, indicated in Section 7.5, for the [S II] observations. This, obviously, results from the 2×2 spatial bin (see above). The value for $\langle n_e \rangle$ matches relatively well the results obtained in previous investigations (e.g., Viallefond & Goss 1986; Castañeda *et al.* 1992; Yang *et al.* 1996; Malmann *et al.* 2002; Magrini *et al.* 2007)

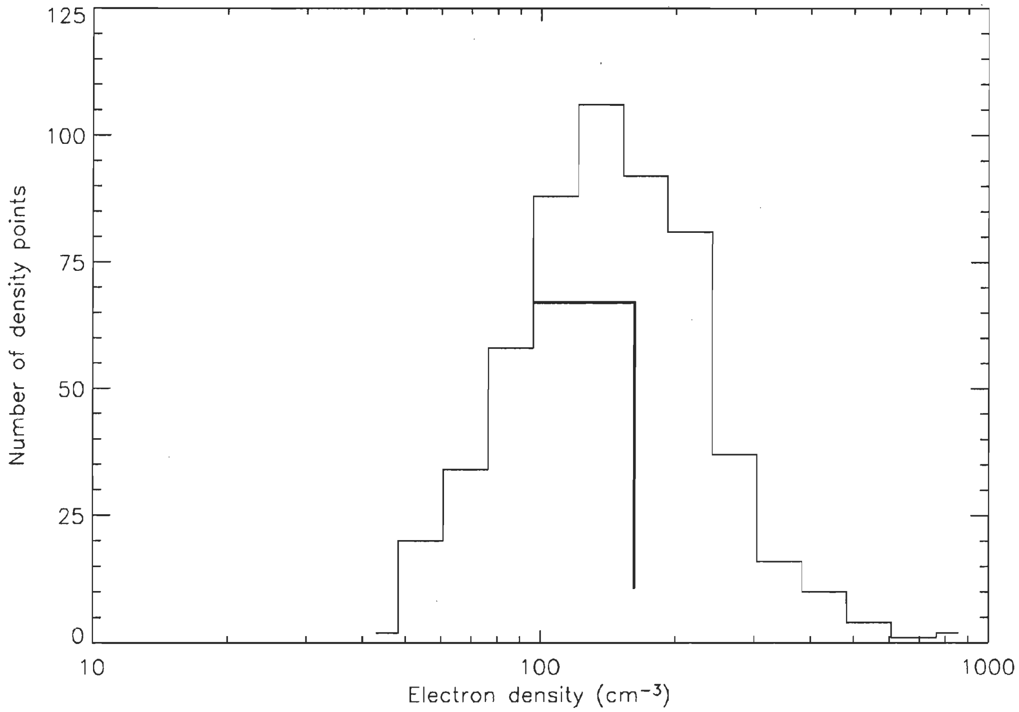

Figure 7.14: Electron density distribution in NGC 595.

The abscissa is logarithmic ranging from 10 to 1 000 cm^{-3}. The vertical and horizontal thick lines respectively indicate the mean and one-standard deviation of the distribution. These values are listed in Table 7.3.

Table 7.3: Electron densities in NGC 595.

Figure	$\langle n_e \rangle$ (cm^{-3})	β_{n_e} (cm^{-3})	Skewness	N_{pts}	$\mathrm{S/N}_{\lambda 6731}$
7.14	162 ± 5	106 ± 3	0.229	551	$[7-198]$

of the $\mathrm{F}_{\lambda 6716}/\mathrm{F}_{\lambda 6731}$ flux ratio in local GEHRs. Densities ranging from a few tens up to a few hundreds of particles per cm^3 were commonly found, in agreement with our mean density of NGC 595.

Error bars on mean values and standard deviations in Tables 7.1 to 7.3 are statistical uncertainties. For a kinematic parameter "X" characterized by a distribution of mean $\langle X \rangle$ and of one-standard deviation β_X, the statistical uncertainties on the two latter values are respectively $\beta_X/\sqrt{N_{pts}}$ and $\beta_X/\sqrt{2(N_{pts}-1)}$ (Bevington 1969, Chapter 5).

7.7 Discussion

7.7.1 Peak intensity maps : a general overview

Figures 7.2 to 7.4 reveal bright ionized material along the LOSs of the molecular material in NGC 595. This suggests a source of ionization located in front of the dense clouds. Therefore, the large majority of the 86 massive stars (WR-, O-stars) identified in the star cluster are likely found in front of N595-1 and -2. The eastern edge of the nebula shows a sharp cutoff in all three ionic lines. A prominent north-south Hα filament at $\alpha_{2000} \sim 01^h33^m35^s$ extends on $\sim 1'\!.5$ (~ 370 pc) and fits snugly against the H I gas. That side of the nebula seems ionization-bounded. This filament is also detected in [S II] but appears shorter and more diffuse in [O III] possibly from a lack of energetic photons through a mixture of geometrical dilution and dust absorption. The filament will be referred as the outer ionized filament. A second filament is detected centered on $\alpha_{2000} \sim 01^h33^m34^s$. This inner ionized filament could indicate an old remnant of neutral material that has undergone full erosion (see Section 7.7.2.4). Interestingly, the inner ionized filament has very similar dimensions

($\sim$240 pc) in all three ionic emission-lines giving credence to its proposed origin and proximity to the star cluster. The two filaments would thus be independent structures explaining the dearth of emission between them (referred as the inter-filaments medium in Section 7.7.2.4).

The western and north-western sides of NGC 595 are ill-defined in ionized emission showing a smoother decline in emissivity. In fact, we would expect, from a typical nebula expanding in the plane of its galaxy, to be circumscribed in radio emission by an H I cavity, revealing how far the ionizing photons have traveled away from the star cluster. The absence of H I material in these zones of NGC 595 can be explained by : (1) a localized lack of atomic material in this particular region of the galactic plane of M33, (2) an extremely extended ionized nebula, density-bounded along its western and northern axes, or (3) a possible blowout of the superbubble. Rosolowsky *et al.* (2007) indicate that N595-1 and -2 (treated by the authors as a single, giant cloud) could be located at the periphery of a spiral arm. The H I cavity, detected west of NGC 595, could therefore be associated to the inter-arm medium, likely characterized by a very weak atomic gas' density. In Figure 7.2, the diffuse ionized component observed beyond the western boundary of the black rectangle likely indicates that the nebula is density-bounded toward the inter-arm (see Section 7.7.2.1). However, considering that the $4' \times 4'$ FOV of Figures 7.2 to 7.4 probably encloses a certain number of hot, massive stars besides the 86 stars identified previously, we cannot a priori confirm that the ionizing photons responsible for the diffuse mixture are necessarily associated with the star cluster of NGC 595. In particular, Hoopes & Walterbos (2000) mentioned that roughly 40% of the diffuse ionized gas in M33 is sustained by OB-stars located outside H II regions. On the other hand, different studies present series of disk GEHRs showing observational evidence for density-bounded regions and important leakage in ionizing photons (Castellanos *et al.* 2002; Rozas *et al.* 2006b).

The north-western side of NGC 595 shows no indication for diffuse ionized material above $\delta_{2000} = 30°42'55''$. However, evidence are given in Figures 7.2, 7.4 and 7.13 for a possible ovoid-shaped nebula as traced out by the eastern filaments (see Section 7.7.2.1). This particular elongated shape favors the development of shell instabilities (Dove *et al.* 2000) which could lead to the formation of dynamic chimneys (Norman & Ikeuchi 1989). In Section 7.7.2.2, the blowout scenario in NGC 595 is more deeply investigated.

7.7.2 Kinematics of the 1-component profiles

In Lagrois & Joncas (2009a), the authors identified broad, 1-component Hα profiles ($\sigma \sim 10$ km s^{-1}) in the southern portion of the W4 Galactic H II region. A double kinematic regime was observed depending on the nature of the different eroded features ; molecular or atomic. In the first case, the photoerosion of the molecular clumps led to well-defined Champagne flows mainly directed toward the ionizing sources and resulting from the important pressure discontinuity between the molecular component and the ambient ISM (Tenorio-Tagle 1979; Bodenheimer *et al.* 1979). Overall, at least 10 independent accelerated flows were observed, criss-crossing the nebula.

The photoionization of the H I shell was, on the other hand, interpreted according to the model of a growing wake behind a solid body moving in a viscous fluid. This scenario indicates that the eroded material, extracted from the expanding atomic shell [or filament], would appear redshifted (blueshifted) with respect to the ionized component still in contact with the neutral material if the latter is moving toward (away from) the observer with negative (positive) LSR radial velocities.

These different kinematical mechanisms, mixed in a single object, explain the relatively large, nearly supersonic, corrected line widths observed. The authors mentioned that W4-type superbubbles could correspond to the missing link between typical small H II regions and the larger GEHRs. Since an important fraction of our interferometric observations of NGC 595 presents 1-component velocity profiles in Hα, [O III], and [S II], we expect numerous similarities between W4 and NGC 595. This said, we intend to use the same dynamical approach in order to interpret the observed kinematics in the large nebula of M33. Note, however, that we do not wish to dynamically connect the two H II regions since both objects are extremely different in age, dimensions and in massive stars' content.

7.7.2.1 A star cluster too hot for [S II] ?

The fact that the hatched region of Figures 7.2 and 7.3 is not duplicated in Figure 7.4 could indicate that the S$^+$ material does not spatially coincide with the Hα and [O III] components. This is supported kinematically by relatively low line-width material in [S II] as seen by the $\langle \sigma_{1-comp} \rangle$ value in Table 7.1. In fact, considering the relatively high ionizing luminosity of the star cluster (see Section 7.4), we assume S^{++} ions to dominate in the vicinity of the ionizing sources (Rosa 1993) while the S^{+} material would be located at the periphery of the H II region. Tenorio-Tagle *et al.* (2000) reached a similar conclusion for NGC 604 also based on the absence of line splitting and on the measurements of particularly blueshifted velocities in [S II]. For the case of NGC 595, however, the mean velocity of the S^{+} material remains quite in agreement with the kinematics of the molecular and Hα components (see Table 7.1).

The partial ellipse, traced out in Figure 7.13, could correspond approximately to the ionized supershell expected at the periphery of NGC 595. The eastern side is bordered by the two prominent filaments discussed in Section 7.7.1. The western side, very diffuse in Figures 7.2 and 7.4, is partially defined in electron densities. The southernmost portion of the shell is most likely stalled by the dense material of the molecular clouds. In Section 7.7.3, we propose that the portion of the nebula dominated by stellar winds is restricted to a localized region near the molecular clouds. The partial shell might therefore be attributed to ionization fronts induced by the strong Lyman continuum of the massive star cluster (see Section 7.4). The fact that the western wall remains partially defined in Figure 7.13 up to declinations near 30°42′00″ favors the possibility of a density-bounded shell segment and that UV photons eventually percolated through the shell to ionize the tenuous neutral material found in the inter-arm medium (see Section 7.7.1).

7.7.2.2 An hypothetical blowout in NGC 595 ?

As expected from the absence of high-declination S^{+} material in Figure 7.4, the partial ellipse of Figure 7.13 remains opened to the ISM toward the northern and north-western axes. This obviously could result from an acquisition time, for the [S II] observations, too short in order to detect the very tenuous (?) northern shell. On the other hand, a broken/fragmented shell should be considered due to its elongated shape, a morphology typically associated to shell fracture (see Section 7.7.1).

Lagrois & Joncas (2009b) discussed the kinematical signature expected from the embedded ionized mixture of superbubbles evolving into dynamic chimneys. From Figures 7.6 and 7.8, the particularly blue velocities and low line-width material detected near the northernmost declinations of the nebula's eastern side might indicate a possible blowout if NGC 595 is slightly tilted toward the observer. The possibility therefore arises that NGC 595 might be currently evolving into a dynamic chimney. However, it is not clear where the hypothetical ejected outflows would be directed. Usually, blowouts occur perpendicular to the plane of the galaxy, allowing an efficient connection with the galactic halo (Dove *et al.* 2000) and/or the formation of high- and intermediate-velocity clouds at high latitudes (Shapiro & Field 1976). However, considering the particular positioning of NGC 595 in M33 (see Section 7.7.1), a blowout in the inter-arm medium remains a possible scenario.

Except for the northernmost portion of the outer ionized filament, our optical observations have not allowed to track the diffuse ionized material at high declinations. Therefore, the kinematical signature, expected from ejected outflows, cannot be undoubtedly identified from our Fabry-Perot measurements of NGC 595. Lagrois & Joncas (2009b) demonstrated that the vented material would certainly be rarefied to such a degree that it becomes particularly difficult to obtain reliable emission profiles with significant S/Ns. This scenario could explain why the high-declinations portion of the nebula seems to be apparently deprived of both ionized and atomic material.

7.7.2.3 The photoerosion of the molecular clouds : application of the Champagne model

Exposed to the UV flux of the nearby star cluster, the photoerosion of the molecular clouds should lead theoretically to an ionized material's dynamics in agreement with the Champagne model. The ionized flows, initiated at the periphery of the molecular fragments and directed toward the ambient ISM, have usually shown well-defined linear velocity gradients on the plane of the sky (Joncas & Roy 1984; Miville-Deschênes *et al.* 1995; Barriault & Joncas 2007). Numerical simulations (Bodenheimer *et al.* 1979; Tenorio-Tagle & Bedjin 1981; Tenorio-Tagle *et al.* 1982; Franco *et al.* 1990) predicted that the accelerated material could reach velocities up to 30 km s^{-1} [w.r.t. the velocity of the molecular component] when large density contrasts are involved ($n_{\rm cloud}/n_{\rm inter\text{-}clouds} > 1000$). Cyganowski *et al.* (2003) also mentioned a tendency toward line broadening (larger line widths) down the Champagne flow. The line-width gradient is directed along the flow's expansion and therefore spatially correlated to the velocity gradient.

Figure 7.15 shows an enlargement of Figure 7.6. Radial velocity and corrected line-width maps of the Hα material observed toward the molecular clouds are provided in Panels (a) and (b). Two gradients are detected (each associated to its own molecular knot) on a roughly south-north direction precisely oriented toward the star cluster. These velocity and line-width gradients are shown respectively in Panels (c) and (d), traced out by the black arrows[5] of the two former panels. Similar investigations, using the same arrows as in Figure 7.15, were also carried out for the [O III] and [S II] observations (figures not provided). The gradients are labeled A and B for Hα, C and D for [O III], and E and F for [S II]. The subscripts "v" and "σ" refer to the investigation in radial velocities and line widths respectively. Table 7.4 presents the parameters obtained from the different linear fits for Flows A to F : initial velocities ($v_{k,\mathrm{initial}}$) and line widths ($\sigma_{k,\mathrm{initial}}$), slopes ($\nabla_v$, ∇_σ), final velocities ($v_{k,\mathrm{final}}$) and line widths ($\sigma_{k,\mathrm{final}}$), and Pearson correlation coefficients (where "k" will be referring below to the identification letter of each flow). The range (i.e., the arrow's length) on which each gradient remains approximately well-detected on the plane of the sky is also provided. Except for the investigation in line widths for the O^{++} material (see C_σ and D_σ in Table 7.4), linear relations seem quite obvious from correlation coefficients approaching 1 (in absolute value).

Certainly, we anticipate that the velocity variations of the CO component itself must have a kinematic repercussion on the measured velocities of the ionized material. Wilson & Scoville (1992) observed a 3 km s^{-1} difference in mean velocities, blueshifted from N595-1 to N595-2 (see Table 7.1). This explains why open squares (Flow B, N595-2) in Figure 7.15*c* are always blueshifted by 2 to 5 km s^{-1} with respect to the open circles (Flow A, N595-1). Note that both $v_{D,\mathrm{initial}}$ and $v_{F,\mathrm{initial}}$ appear blueshifted in a similar way with respect to $v_{C,\mathrm{initial}}$ and $v_{E,\mathrm{initial}}$. However, since we do not have a more precise kinematic image of the molecular clouds in NGC 595, we cannot state at this point if the intrinsic velocity dispersion of the CO material has a sizeable repercussion on the measured slopes for Flows A_v to F_v. If so, we can state that each gradient is similarly affected. This said, the reader can note that Flows E_v and F_v in [S II] show the flatter Champagne gradients. This will be addressed in Section 7.7.2.5. Finally, the negative velocity slopes (see $\nabla_v < 0$

---

[5] Each point of the velocity and line-width gradients associated to Flows A to F is estimated by a 3-pixel wide horizontal band for each line of pixels crossed by the black arrows. At each declination, a mean between the pixel crossed and the two adjacent pixels is computed. For eight and seven rows of pixels crossed by Flows A and B respectively, eight and seven points are displayed in Panels (c) and (d) of Figure 7.15.

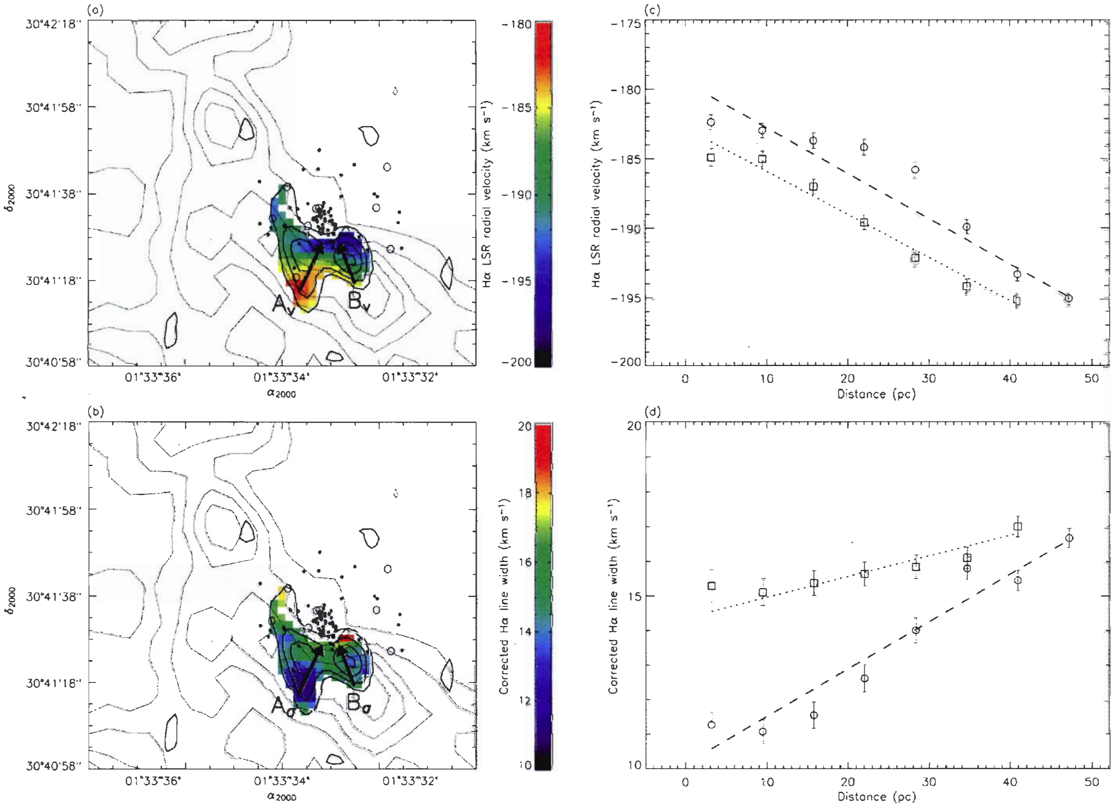

Figure 7.15: Investigation of the Hα emission near the molecular clouds. *White pixels are not considered and therefore treated as undefined. All defined pixels strictly imply 1-component profiles. Panel (a) : Radial velocity map measured with respect to the LSR. Panel (b) : Non-thermal line-width map corrected for the thermal broadening, the instrumental response, and the natural width of the Hα-line. In both panels, two well-defined gradients are identified by the black arrows. Panel (c) : Radial velocity gradients traced out by the black arrows in Panel (a). Open circles (squares) are associated to Flow A_v (B_v). The origin (at 0 pc) of both flows coincides with their respective arrow's tail. The dashed (dotted) line, associated to Flow A_v (B_v), shows the least-square fit applied to a straight line. Panel (d) : Line-width gradients traced out by the black arrows in Panel (b). Symbols and line types all kept the same definition as in Panel (c). All values (slopes, Y-intercepts...) associated to the linear fits are listed in Table 7.4.*

Table 7.4: The Champagne model applied to NGC 595.

			Radial velocity gradients				
Flow	Ion	Figure	Range (pc)	$v_{k,\text{initial}}$ (km s^{-1})	∇_v (km s^{-1} pc^{-1})	$v_{k,\text{final}}$ (km s^{-1})	Correlation
A_v	Hα	7.15	47.20	-182.67 ± 0.06	-0.33 ± 0.05	-195.08 ± 0.08	-0.94
B_v	Hα	7.15	40.91	-184.97 ± 0.09	-0.31 ± 0.02	-195.19 ± 0.04	-0.98
C_v	[O III]	–	47.20	-169.83 ± 0.18	-0.32 ± 0.05	-182.97 ± 0.24	-0.93
D_v	[O III]	–	40.91	-174.09 ± 0.17	-0.41 ± 0.12	-183.16 ± 0.19	-0.83
E_v	[S II]	–	47.20	-186.41 ± 0.16	-0.19 ± 0.02	-194.57 ± 0.17	-0.98
F_v	[S II]	–	40.91	-189.26 ± 0.14	-0.21 ± 0.03	-197.13 ± 0.15	-0.94

			Line-width gradients				
Flow	Ion	Figure	Range (pc)	$\sigma_{k,\text{initial}}$ (km s^{-1})	∇_σ (km s^{-1} pc^{-1})	$\sigma_{k,\text{final}}$ (km s^{-1})	Correlation
A_σ	Hα	7.15	47.20	11.31 ± 0.26	0.14 ± 0.02	16.62 ± 0.32	0.96
B_σ	Hα	7.15	40.91	15.33 ± 0.29	0.06 ± 0.01	17.09 ± 0.33	0.83
C_σ	[O III]	–	47.20	13.71 ± 0.98	0.11 ± 0.09	20.78 ± 1.22	0.56
D_σ	[O III]	–	40.91	22.86 ± 2.20	-0.28 ± 0.20	16.71 ± 1.19	-0.67
E_σ	[S II]	–	47.20	8.65 ± 0.79	0.13 ± 0.03	14.63 ± 0.41	0.87
F_σ	[S II]	–	40.91	9.73 ± 0.87	0.10 ± 0.03	15.34 ± 0.51	0.82

in Table 7.4) indicate forward, accelerated flows and therefore confirm the ionizing sources to be located in front of the molecular clouds.

Line broadening gradients, oriented toward the star cluster, are particularly in agreement with the Champagne model (see $\nabla_\sigma > 0$ in Table 7.4). Hence, the line-width gradients are attributed to the constant accumulation of different velocity gradients down the ionized flows; at the position of the arrows' head in Figure 7.15, the velocity profiles likely reveal the individual contributions of a series of accelerated flows initiated at different [southern] positions on the clouds' surface and all directed toward the star cluster. This simple geometrical scenario causes line widths to consistently increase at each LOS on a south-north axis. Three Champagne flows in W4 were found to have a line narrowing behavior ($\nabla_\sigma < 0$), in disagreement with the Champagne model (Lagrois & Joncas 2009a). The peculiar kinematics corresponds to ionized gas spatially coincident with particularly bright 60 μm emission according to the IRAS image, a strong indication for interstellar dust. Flow D may be similarly affected.

In Lagrois & Joncas (2009a), the authors obtained a series of independent Champagne flows associated to the W4 region in which a majority shows remarkable similitudes in velocities between $v_{k,\mathrm{initial}}$ and v_{neutral}, the velocity of the neutral material located at the pressure discontinuity with the ambient ISM (see the authors' Table 7.5). This is expected from the Champagne model since the velocity gradient is initiated by dense, ionized material still in contact with the neutral medium. In Table 7.4, $v_{A,\mathrm{initial}}$ and $v_{B,\mathrm{initial}}$ are slightly redshifted with respect to the mean velocity of N595-1 and N595-2 (see Table 7.1). However, these values for $v_{A,\mathrm{initial}}$ and $v_{B,\mathrm{initial}}$ potentially agree with the kinematics of the molecular material as they both are included in the range of velocities covered by the low-signal, integrated CO profiles of N595-1 and -2 (see Figures 3*e* and 3*f* of Wilson & Scoville (1992)). For Flows C_v and D_v, the discrepancy in velocities with the CO component is even more important with $v_{C,\mathrm{initial}}$ and $v_{D,\mathrm{initial}}$ found between -170 and -175 km s^{-1}. As mentioned above, absorption along the LOS might have deformed the kinematic information obtained from the blue light (see also Section 7.7.1). On the other hand, the [S II] investigation leads to values for $v_{E,\mathrm{initial}}$ and $v_{F,\mathrm{initial}}$ in agreement with the molecular gas' kinematics. Combined with the particularly flat slopes obtained for Flows E_v and F_v (see above), this tends to confirm our assumption that the S^+ material is probably not exposed to the violent medium in which the H^+ and O^{++} components likely evolve (see Section 7.7.2.1).

More than a simple line broadening gradient down the ionized flow, the Champagne model also demands the initial line widths to be roughly similar to the typical narrow line widths obtained from the CO observations (Blitz *et al.* 1982; Digel *et al.* 1996). A supersonic regime is however found for $\sigma_{A,\mathrm{initial}}$ and $\sigma_{B,\mathrm{initial}}$ in Table 7.4. This could be explained if the ionized material found near the arrows' tail in Figure 7.15 is already contaminated by some other flows, accelerated to different velocities and differently oriented. This is expected from a star cluster relatively dispersed over the molecular surface. Each ionizing star can potentially initiate its own Champagne flow at the periphery of the molecular clouds whose edges are, in addition, certainly ragged. This is the case, in particular, for WR-stars being found in a $20'' \times 20''$ FOV, roughly the area covered by the CO emission. Note that this scenario of multiple flows all directed toward different orientations could also partially explain our difficulty to reconciliate $v_{k,\mathrm{initial}}$ and v_{neutral} in the previous paragraph. The fact that $\sigma_{B,\mathrm{initial}} > \sigma_{A,\mathrm{initial}}$, $\sigma_{D,\mathrm{initial}} > \sigma_{C,\mathrm{initial}}$ and $\sigma_{F,\mathrm{initial}} > \sigma_{E,\mathrm{initial}}$ in Table 7.4 is in agreement with N595-2 presenting a larger dispersion in velocities when compared to N595-1 (see Table 7.1). Another factor for large initial line widths could be simply related to the [relatively] poor spatial resolution (6.61 pc pixel^{-1}) of our optical observations; the large area being covered by each pixel accentuates the probability of measuring important velocity variations.

Again, the [S II] component shows a kinematical behavior clearly distinct from the two other ions. The trend toward large $\sigma_{k,\mathrm{initial}}$ values is slightly attenuated for Flows E_σ and F_σ (see Table 7.4), showing narrower, subsonic profiles. In particular, the low value for $\sigma_{E,\mathrm{initial}}$, associated with N595-1, is indicative of the "stable" kinematical behavior of this cloud (see Table 7.1). The fact that, generally, $\sigma_{[\mathrm{O\,III}]} > \sigma_{\mathrm{H}\alpha} > \sigma_{[\mathrm{S\,II}]}$ (see Table 7.1) will be largely discussed in Section 7.7.2.5.

7.7.2.4 The atomic component as zones of photoionization

The area enclosing the majority of the CO emission in NGC 595 (see Section 7.7.2.3) is estimated at 80×80 pc^2, roughly 25 times smaller than the surface covered by the black rectangle in Figures 7.2 to 7.4. We, therefore, expect that a certain fraction of the ionized material in the nebula will likely show a kinematics governed by the H I material. Roughly 60% (100 000 pc^2) of the area covered by the black rectangle shows atomic emission with $\mathrm{S/N} > 3$. This value represents a factor three larger than the extent of the H I shell proposed by Deul & den Hartog (1990).

Figure 7.16*a* shows the LSR H I radial velocity map obtained from the 21 cm observations of NGC 595. To facilitate the kinematical comparisons with the Fabry-Perot measurements, the map has been rescaled to match the spatial resolution of our optical observations (i.e., artificially improving the resolution of the radio observations). The centroid position of the H I line was calculated using a 1-component fit on each velocity profile. The distribution of the 2 320 H I velocity points encompassed by the black rectangle is displayed in Figure 7.16*b*. The characteristics of the histogram are provided in Table 7.1.

Our H I velocities for NGC 595 are roughly consistent with the work of Deul & van der Hulst (1987). The interval in velocities covered by the histogram in Panel (b) matches the values obtained by Deul & den Hartog (1990). However, the mean H I velocity associated to the nebula (see Table 7.1) is redshifted by roughly 5 km s^{-1} from the value of maximal contrast obtained by the authors (see Section 7.4). Panel (a) in Figure 7.16 indicates a large-scale south-north radial velocity gradient associated to the H I component in the vicinity of NGC 595. The center of M33 being located roughly $3'$ to $4'$ beyond the south-east boundary of our $4' \times 4'$ FOV displayed in Figure 7.16*a* (Comte & Monnet 1974), the gradient seems spatially correlated to a line of isoradius. Even though the rotation curve of M33 is particularly abrupt at the galactocentric radius of NGC 595 (Corbelli & Salucci 2000), this kinematical trend cannot be attributed to the rotation of the galaxy. We therefore state that the atomic material, in this portion of M33, is exposed to important velocity variations on a range of a few hundreds of parsecs. In fact, a second component, near -197 km s^{-1}, is deduced from the histogram shown in Panel (b). This could signify that two distinct H I clouds, showing slightly different kinematics, are likely found in the vicinity of NGC 595.

Similarly to the photoerosion of the molecular clouds (see Section 7.7.2.3), we expect the velocities of the H I and ionized material to be roughly similar where the two components spatially coincide. Figure 7.16*c* clearly indicates Hα clumps, at low-to-intermediate declinations, blueshifted by 5 to 15 km s^{-1} with respect to the corresponding atomic material. In the vicinity of the CO clouds, this high-velocity ionized component likely results from Champagne flows as described in the previous subsection. The Hα clumps reach the northernmost declinations associated with the inner ionized filament, partially filling the inter-filaments medium. This indicates that the inner filament is most likely an extension of N595-1 (see Section 7.7.1). Moreover, this could signify that the two giant clouds could have been previously part of a supergiant (> 100 pc) molecular complex (Wilson *et al.* 2003). The rela-

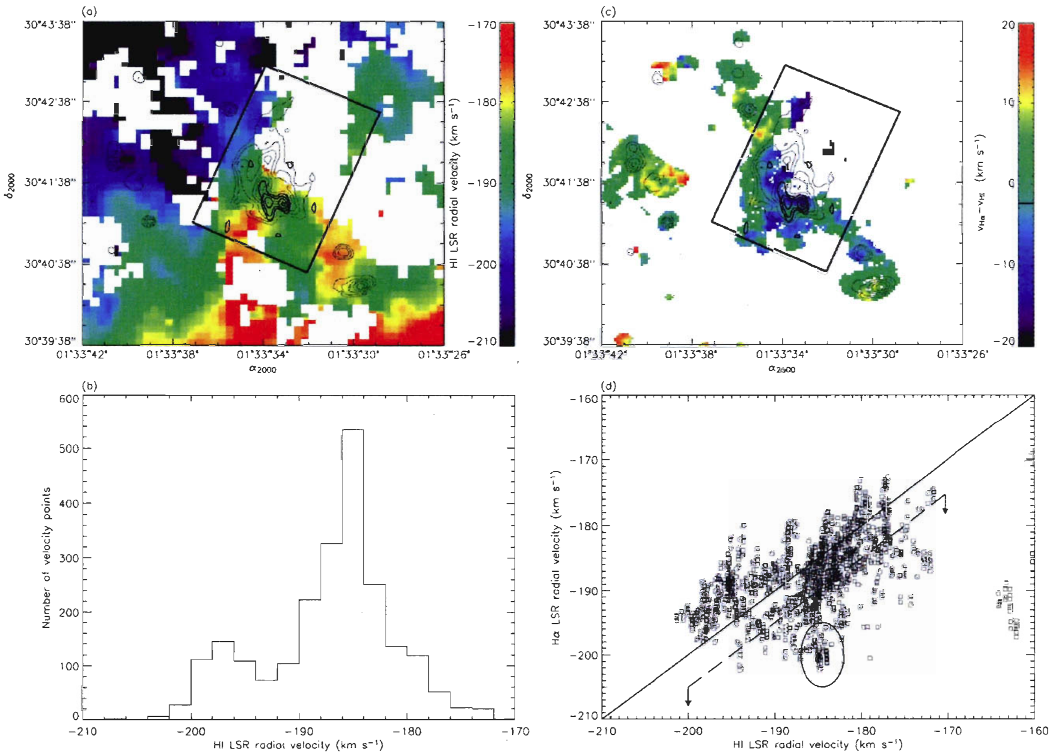

Figure 7.16: Investigation of the kinematical behavior of the H I component : comparison with the Hα material.

Panel (a) : H I LSR radial velocity map. White pixels are treated as undefined, implying H I profiles with S/N<3. Thick contours show the CO (1-0) emission in the vicinity of NGC 595 (see Figure 7.2). Regular contours correspond to the Hα emission shown in Figure 7.2. Seven Hα contours are drawn between e^3 and e^6 photon counts with a $\log_e$-spacing of 0.5. Panel (b) : H I radial velocity distribution of all defined velocity points encompassed by the black rectangle in Panel (a). The characteristics of the histogram are listed in Table 7.1. Panel (c) : Difference in velocities, pixel-to-pixel, between defined H I velocity points in Panel (a) and defined Hα velocity points in Figure 7.6a. The H I velocities are always subtracted from the Hα velocities. The value of each pixel therefore gives the excess in velocities of the H^+ material with respect to the atomic gas. The mean value encompassed by the black rectangle is indicated by the small solid line in the adjacent color bar. Panel (d) : Point-plot diagram (v_{HI} vs. $v_{H\alpha}$) of all defined velocity pairs found inside the black rectangle of Panel (c). All points located below the long-dashed line are likely contaminated by Champagne effects. Points associated to an hypothetical blowout in NGC 595 and/or to unrelated H I material are circumscribed by the black ellipse (see text).

tively important abundance of high-velocity points in Panel (c) leads to a negative mean difference (between the H I and Hα components) of -2.31 $\pm 7.05(1\sigma)$ km s^{-1} in NGC 595. This value is indicated by the small solid line in the adjacent color bar.

The fact that Champagne effects seem to regulate the kinematics of the ionized material, on a relatively large extent of NGC 595, is therefore directly related to the important number of points located below the solid line of kinematic agreement in Panel (d). The points located below the long-dashed line could be regarded as being dominated by the photoerosion of the dense, molecular material. The black ellipse indicates velocity points located near the northernmost portion of the outer ionized filament. This region was investigated in Section 7.7.2.2 in order to detect kinematical evidence for a possible blowout in NGC 595. Figure 7.16*c* shows a strong disagreement of nearly 15 km s^{-1} between the ionized material and the coinciding atomic gas. According to Figure 7.6*a*, the H$^+$ material, along the full extent of the outer filament, follows well the large-scale velocity gradient associated with the H I component in NGC 595 (see Figure 7.16*a*). The strong H I vs. Hα disagreement could originate from unrelated atomic material, more redshifted than expected, and likely located either in front or behind the nebula. However, the fact that the H$^+$ component near the northern tip of the filament follows relatively well the south-north behavior of the H I material does not favor the blowout alternative, the ionized material being apparently not accelerated with respect to the (nearby) neutral component. Obviously, this argument is dependent of the nebula's geometry ; if ejected outflows are indeed present but oriented almost perfectly parallel to the plane of the sky, no radial acceleration would be discernible.

Except for its northern tip, the outer ionized filament shows a much better agreement in velocity with the atomic gas, being usually redshifted by 1 to 5 km s^{-1} with respect to the H I material (points usually located above the solid diagonal of Figure 7.16*d*). This behavior directly arises from the thermal conduction between the shocked H I shell and the much hotter, ionized plasma inside the nebula (Capriotti & Kozminski 2001). Eventually, the conduction leads to the detachment of freshly eroded material from the expanding, neutral shell. Lagrois & Joncas (2009a) interpreted the observed kinematics of the ionized, detached material as uniformly decelerated flows, trailing behind the moving shell (see Section 7.7.2).

Figure 7.17 presents the same investigation, as described above, comparing the H I and S$^+$ material. High-velocity [S II] clumps are again observed in the vicinity of the molecular clouds (see Figure 7.17*c*), regulated by Champagne flows. These

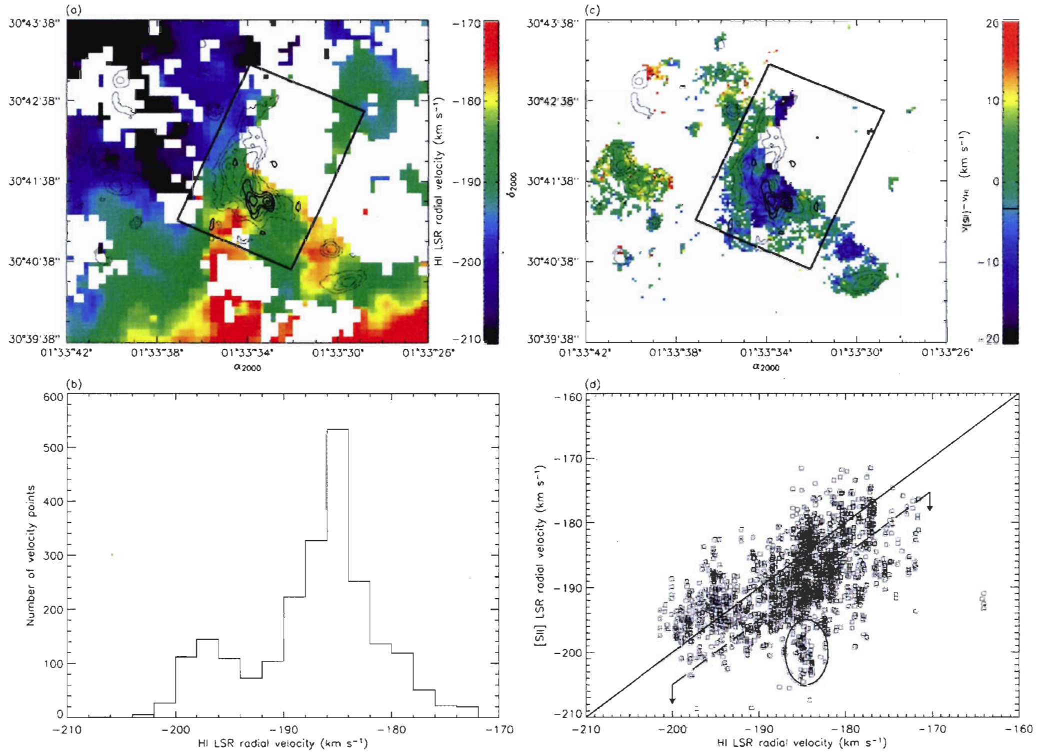

Figure 7.17: Investigation of the kinematical behavior of the H I component : comparison with the [S II] material.

Panel (a) : H I LSR radial velocity map. Regular contours correspond to the [S II] emission shown in Figure 7.4. Seven [S II] contours are drawn between $e^{3.5}$ *and* $e^{6.5}$ *photon counts with a* $\log_e$*-spacing of 0.5. Panel (b) : H I radial velocity distribution of all defined velocity points encompassed by the black rectangle in Panel (a). Panel (c) : Difference in velocities, pixel-to-pixel, between defined H I velocity points in Panel (a) and defined [S II] velocity points in Figure 7.8a. The H I velocities are always subtracted from the [S II] velocities. The value of each pixel therefore gives the excess in velocities of the* S^+ *material with respect to the atomic gas. Panel (d) : Point-plot diagram (*v_{HI} *vs.* $v_{[S\,II]}$*) of all defined velocity pairs found inside the black rectangle of Panel (c). More details can be found in the caption of Figure 7.16.*

points are also identified in Figure 7.17*d* below the long-dashed line. A 17 km s^{-1} discrepancy in velocities is observed with the atomic component near the northern tip of the outer ionized filament. The peculiar zone is again circumscribed by the black ellipse in Panel (d). The mean difference in velocities between the S^+ and atomic gas, inside the black rectangle of Panel (c), is estimated at $-3.25 \pm 6.26(1\sigma)$ km s^{-1}. The 1 km s^{-1} difference between this value and the one obtained from Figure 7.16*c* could be associated to the fact that Champagne flows in [S II], favoring negative velocities with respect to the atomic gas, are likely present in the zone spatially corresponding to the hatched region of splitted profiles in Hα. These pixels were rejected from Figure 7.16*c* and will be discussed in Section 7.7.3 as velocity profiles associated to wind-blown bubbles near the central core of NGC 595.

7.7.2.5 The line broadening excess in NGC 595 : a melting pot between turbulent motions and large-scale velocity gradients

We already provided a series of evidence, kinematic and dynamic, suggesting that the S^+ material is not spatially coincident with the H^+ and O^{++} components in NGC 595 (see Sections 7.7.2.1 and 7.7.2.3). In particular, relatively low $\sigma_{k,\mathrm{initial}}$ in [S II] flows are opposed to largely supersonic values found in Hα and [O III] (see Table 7.4). We believe that the mechanisms responsible for line broadening (see Section 7.3) are less efficient at the periphery of the nebula where the S^+ material seems to abound. Since the deepest ionized regions of the nebula are likely formed of H^+ and O^{++} material, the stars themselves can be looked as a potential source for large non-thermal line widths.

In particular, the *Cometary Stirring Model*, proposed by Tenorio-Tagle *et al.* (1993), is an interesting variant of the gravitation/virialization model (Terlevich & Melnick 1981; Rozas *et al.* 2007). The model is simple, easily testable, and fortunately our data set fulfills all the observational requirements. The *Cometary Stirring Model* proposes that low-mass stars, initially forming in a collapsing molecular cloud, communicate, via winds and bow shocks, their velocity dispersion to the nearby gaseous component (at which point, $\sigma_{\mathrm{stars}} = \sigma_{\mathrm{gas}}$). Muñoz-Tuñón *et al.* (1996) indicated that the σ vs. Intensity diagnostic diagram represents a powerful tool that could help separate the different contributions to the line broadening including virialized motions. The σ's are the non-thermal line widths obtained via a 1-component fit of the optical observations. Panels (a) and (b) of Figure 7.18 provide the σ vs. Intensity

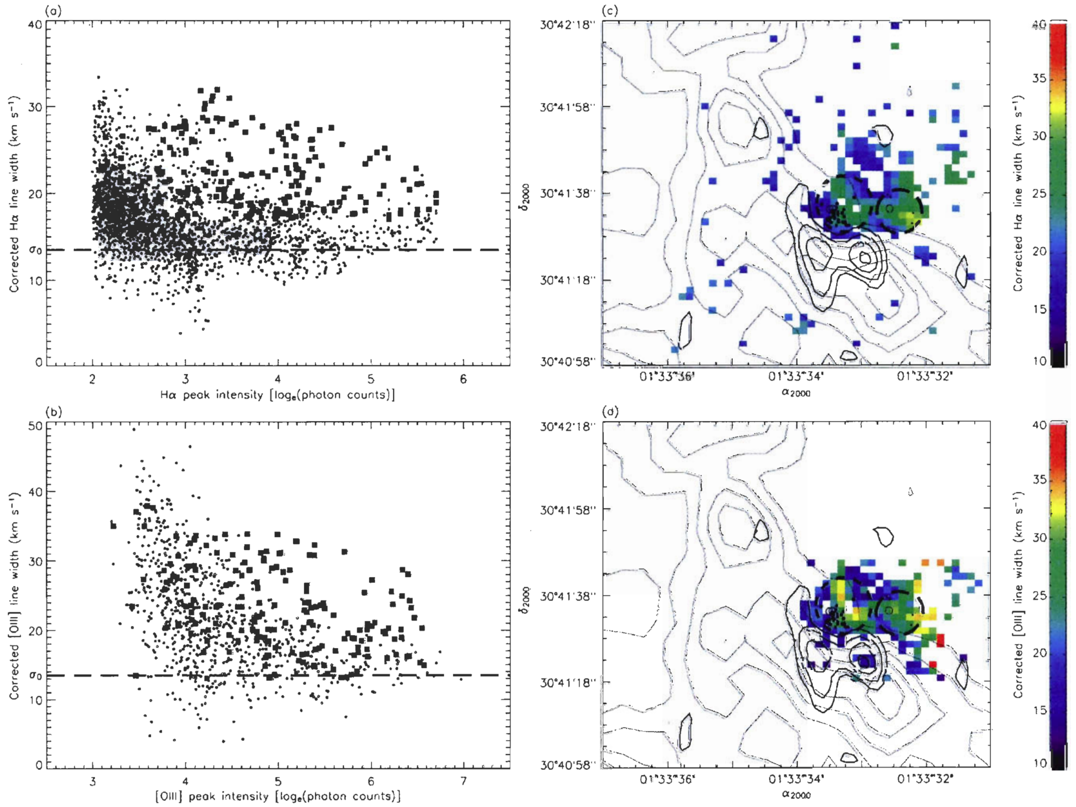

Figure 7.18: The σ vs. Intensity diagnostic diagrams.

Panel (a) : for Hα, (b) : for [O III]. Black dots correspond to 1-component profiles. Filled squares correspond to 2-component profiles associated to the hatched region of Figures 7.2 and 7.3 but fitted here, for the cause, with a single component. The low-limit plateau in line widths found at all intensities (σ_0) is indicated by the long-dashed line. Panel (c) : Corrected line-width map in Hα of the filled squares displayed in Panel (a). Panel (d) : Corrected line-width map in [O III] of the filled squares displayed in Panel (b). From the expected kinematical signature of expanding wind-blown bubbles (see text), two hypothetical shells are identified and traced out by the dashed and long-dashed circles. In both Panels (c) and (d), open circles, black dots, and thick and regular contours all kept the same definitions as in Figures 7.2 and 7.3. Note that massive stars located outside the two hypothetical shells were removed from Panels (c) and (d).

diagrams for, respectively, Hα and [O III], the two ions most likely affected by the nearby stars' motions. Muñoz-Tuñón *et al.* (1996) argued that the lower limit in line width (σ_0) that is observed at all intensities can be interpreted as the local random speed of motions induced by the large amount of low-mass stars moving in the ambient medium. The *Cometary Stirring Model* predicts that σ_0 should be roughly equivalent to the virialized broadening, σ_{vir}, estimated at :

$$\sigma_{vir} = \left(\frac{GM_T}{R}\right)^{\frac{1}{2}}, \tag{7.1}$$

where G is the gravitational constant, M_T is the total mass of the system, and R is the radius of the nebula. The total mass of the system is estimated at 2.25-2.60×10^6 $M_\odot$ using the values for M_{H_2}, M_{HI}, M_{HII}, and M_{stars} discussed in Section 7.4. Equation (7.1) gives a value for σ_{vir} estimated at 12.0 km s^{-1} using a radius of 75 pc for NGC 595 (depicted, in Section 7.4, as the radius around the molecular clouds enclosing the majority of all the emissive material associated to the nebula). This matches relatively well our estimate for σ_0 provided by Figure 7.18. However, Bosch *et al.* (2009) recently indicated that the velocity dispersion of the ionizing cluster in the 30 Doradus nebula is consistent with the mass of the cluster itself; the stellar motions are therefore kinematically linked to the cluster's mass but not to the (much larger) mass of the surrounding gaseous material (neutral and ionized). This single argument contributes to discredit the *Cometary Stirring Model.*

On the other hand, isotropic turbulence, similarly to the gravitational motions, has long been investigated as a line broadening mechanism in GEHRs (Arsenault & Roy 1988; Castañeda 1994; Medina-Tanco *et al.* 1997). In particular, Firpo *et al.* (2005) referred to the non-thermal line widths of their sample of GEHRs as simply "turbulent velocities". In fact, velocity gradients along the LOS also contribute, similarly to turbulent motions, to induce broadening in non-thermal line widths. Two statistical tools are often used to characterize the turbulent behavior in the ISM, the second-order structure function (hereafter, SF) and the auto-correlation function (hereafter, ACF). In order to carry out a reliable statistical investigation of the gas turbulence, weakly stationary velocity fields in Hα, [O III] and [S II] must first be obtained. In particular, Scalo (1984) mentioned that all large-scale velocity gradients should be initially removed from the observational data. This can be done using, for example, a two-dimensional linear wavelength filtering procedure (Zurflueh 1967; Miesch & Bally 1994; Grosdidier *et al.* 2001). The application of these kind of filters is a particularly complicated task and will be part of a subsequent paper (Lagrois & Joncas 2009d) in which a more robust, quantitative investigation of the isotropic turbulence in NGC 595 will be carried out. A posteriori, Medina-Tanco *et al.* (1997) tried to subtract the velocity gradients out of the ACF curve associated to NGC 604. Even though they were able to reproduce the expected theoretical ACF shape, we are not convinced that the result is quantitatively accurate as it could be. To demonstrate the contaminating effect induced by the presence of large-scale velocity gradients on the statistical analysis, we focus on the calculation of SFs.

For this work, we intend to compute the SF (Scalo 1984; Kleiner & Dickman 1985; Miville-Deschênes *et al.* 1995; Medina-Tanco *et al.* 1997) for all three observed ionic lines in order to determine why the S^+ material in NGC 595 generally shows narrower line widths than H^+ while the latter usually has narrower velocity profiles than the O^{++} material (see Section 7.7.2.3). The SF, $F_2(r)$, is defined as :

$$F_2(r) \;=\; N(r)^{-1} \sum_{i,j} [u(i,j) - u(i+r, j+r)]^2, \tag{7.2}$$

where $u(i,j)$ is the peculiar LSR radial velocity of the emitting material at a given pixel (i,j) (i.e., $u(i,j) \equiv v(i,j) - \langle v \rangle$ where $v(i,j)$ is the measured velocity obtained via Doppler shift and $\langle v \rangle$ is the mean velocity calculated over the full extent of the nebula). The lag r ranges from a minimal value fixed by the observational seeing during the acquisition and a maximal value determined by the diameter of the investigated nebula. Finally, $N(r)$ is the number of pixel-pairs in the peculiar velocity map separated by a lag r. Figure 7.19 shows, respectively in Panels (a), (b), and (c), the observational SFs for Hα, [O III] and [S II]. The pixels where line-splitted profiles were observed were ignored from the calculations since the corresponding nebular gas is affected by a violent interaction with stellar winds (see Section 7.7.3). In order to compare similar gas volumes, the Hα and [S II] SFs were computed over areas equal to the [O III] gas extent. The SFs range from 16.5 pc (corresponding to a lag of roughly 2.5 pixels in agreement with the seeing limitation estimated at $3\farcs5$ or 2.2 pixels during the acquisition nights) and 294 pc which corresponds approximately to the diameter of the [O III] extent in the black rectangle of Figure 7.3. In all three panels of Figure 7.19, we identified three distinct linear regimes, fitted by solid lines. The statistical parameters of the linear fits are provided in Table 7.5. Note that Columns 3 and 4 give respectively the mean radial velocities and the mean non-thermal line widths of the resulting profiles following the spatial diminution of the

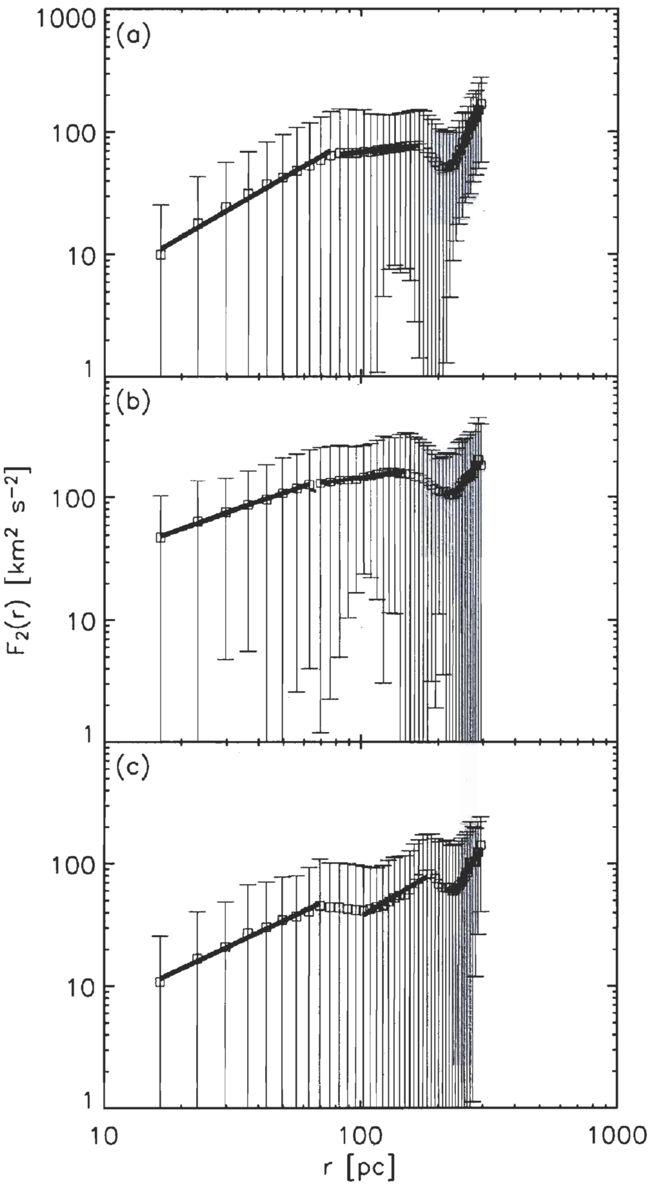

Figure 7.19: Observational structure functions in NGC 595.

Observational structure functions obtained from our (a) : Hα, (b) : [O III], and (c) : [S II] measurements. Open squares correspond to the data points. In each panel, we identified three linear regimes, labeled Regimes 1, 2, and 3 from left to right, respectively on small, intermediate, and large scales. Solid lines show the linear fits. The statistical parameters for each fit are provided in Table 7.5. For each lag r, the error bars correspond to the standard deviation associated to each average point given by equation (7.2). The abscissae are logarithmic ranging from 10 to 1 000 pc.

Table 7.5: Structure functions in NGC 595.

Ion	Figure	$\langle v \rangle$ (km s^{-1})	$\langle \sigma \rangle$ (km s^{-1})	Regime	Scale (pc)	∇_{F_2} (km^2 s^{-2} pc^{-1})	log[F$_2$(0)] (km^2 s^{-2})	Correlation
Hα	7.19*a*	-191.93 ±0.22	16.11 ±0.12	1	[16.53 – 76.02]	1.21 ±0.05	-0.42 ±0.09	0.99
				2	[82.63 – 168.6]	0.23 ±0.01	1.37 ±0.03	0.98
				3	[221.4 – 294.1]	4.25 ±0.10	-8.28 ±0.24	0.99
[O III]	7.19*b*	-187.28 ±0.29	21.63 ±0.28	1	[16.53 – 62.80]	0.72 ±0.01	0.82 ±0.02	0.99
				2	[69.41 – 148.7]	0.32 ±0.03	1.53 ±0.06	0.96
				3	[228.0 – 287.5]	2.73 ±0.17	-4.42 ±0.40	0.98
[S II]	7.19*c*	-190.87 ±0.19	12.88 ±0.17	1	[16.53 – 69.41]	0.99 ±0.04	-0.14 ±0.06	0.99
				2	[102.5 – 181.8]	1.26 ±0.09	-0.95 ±0.20	0.97
				3	[228.0 – 294.1]	3.33 ±0.20	-6.10 ±0.49	0.98

Hα and [S II] velocity maps. For [O III], $\langle v \rangle$ and $\langle \sigma \rangle$ obviously correspond to $\langle v_{1-comp} \rangle$ and $\langle \sigma_{1-comp} \rangle$ given in Table 7.1. The $\langle v \rangle$ values were used in equation (7.2) for the calculation of the different observational $F_2(r)$. On the ionized extent of the O^{++} material, the [S II] component still shows the narrower line widths followed by Hα and, finally, [O III]. The same trend was also observed in Table 7.1. The slope for each regime (∇_{F_2}), the Y-intercepts ($\log[F_2(0)]$), and the correlation coefficients of the fits are given in Columns 7 to 9 respectively.

As mentioned earlier, the SF is highly sensitive to the presence of gradients in the velocity fields. Since the gradients affect the key parameters provided by the SF (slope of the inertial range and cascading energy [or Y-intercept]), we ran a series of simulations in which a pseudo-velocity field formed of pure Gaussian (white) noise was initially used. The noisy map had a mean of 0 km s^{-1} and a root mean square of 7 km s^{-1}, roughly matching the values for β_v found in the first three rows of Table 7.1. The map was cut to match the relatively small ionized extent of the O^{++} component (see Figure 7.7*a*). The SF (figure not shown) of the noisy map was calculated using equation (7.2). As expected, the function is perfectly flat, $F_2(r)$ being constant over all lags. Contaminating radial velocity gradients were then added to the map. The spatial extent of the gradients was approximately limited to the pixels covered by the molecular material in NGC 595 where we observed large-scale Champagne flows (see Sections 7.7.2.3 and 7.7.2.4, and Figures 7.16*c* and 7.17*c*). The free parameters in the simulations were (1) the strength, or slope, of the gradients (i.e., weak, intermediate or strong), and (2) the number of added gradients (between 1 and 3). The classification of the gradients' strength was made according to the slopes measured for Champagne flows in Table 7.4. Note that the velocity gradients were often disposed, in the noisy map, so that they criss-cross each other as we would expect in typical giant nebulae.

At this point, the reader should note that we do not try to reproduce, through simulations, the observational SFs obtained for NGC 595 since turbulent hydrodynamical codes (Miville-Deschênes *et al.* 2003) with scale-dependent velocity fluctuations are unavailable to us. Nine simulations were performed and the resulting SFs are all displayed in Figure 7.20. The change in the SF's shape by the monotonic addition of velocity gradients of different strength is unmistakable. Note that the spatial resolution of our simulated runs was considered the same as our observations (6.61 pc pixel^{-1}) so that each panel in Figure 7.20 shows the same abscissa as Figure 7.19.

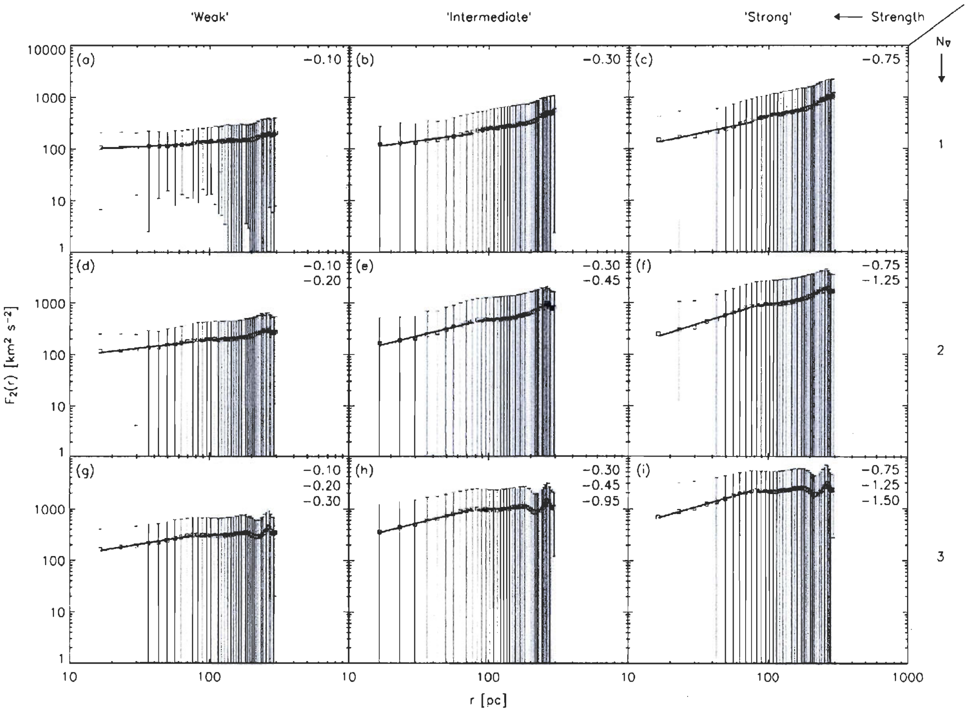

Figure 7.20: Structure functions obtained from simulated runs.
A Gaussian (white) noise map, of mean 0 km s^{-1}, *was created with a root mean square of 7 km* s^{-1}, *matching relatively well our values obtained for* β_v *in Table 7.1. The map was cut to reproduce the ionized extent of our* [OIII] *observations (see Figure 7.3). Simulations were performed by adding a series of radial velocity gradients to the noise fluctuations. All added gradients were spatially limited to the vicinity of the molecular material in NGC 595 (i.e., where large-scale flows are expected to dominate the observed kinematics). Structure functions for each run are provided here with logarithmic abscissae ranging from 10 to 1 000 pc.. Each row gives the number* N_∇ *of added gradient, 1 to 3 from up to bottom. The slope of each added gradient is provided in the upper-right corner of each panel in units of km* s^{-1} pc^{-1}. *These values have the same sign and remain relatively similar to the different* ∇_v *provided in Table 7.4. Each column corresponds to the intensity (or "strength") of the added gradients as defined by the gradients' slopes, weak to strong from left to right. In each panel, we applied least-square fits (solid lines) on three different scales corresponding to the three distinct regimes identified in Figure 7.19. The statistical parameters for each fit are provided in Table 7.6. For each lag r, the error bars are the standard deviation associated to each average point given by equation (7.2).*

According to Figure 7.20*i*, the addition of velocity gradients and the constant increase of these gradients' strength lead to the same three regimes identified in Figure 7.19. Solid lines show the linear fits. Even though all three regimes are not properly identified in all nine panels, linear relations on the same scales as in Panel (i) were calculated. The results are shown in Table 7.6. The number of added artificial gradients (N_∇) and their relative strength (weak (W), intermediate (I), or strong (S)) are provided in Columns 3 and 4 respectively. Columns 7 to 9 kept the same definitions as in Table 7.5. The reader should note that the strongest velocity gradients provide for the largest SF regime slopes (see Table 7.6).

Comparing the observational SFs, it appears that the [S II] curve suggests a different behavior. First, the intermediate-scale Regime 2 for Hα and [O III] has a flatter correlation than for [S II] and is less distinct from the small-scale Regime 1. Secondly, the inflexion point between Regimes 2 and 3 (largest scales) is somewhat shallower in [S II] than for the other two ions. Quantitatively, as seen in Table 7.5, all slopes are different whatever the regime. The only connection is that the slope ratios between Regimes 2 and 3 are roughly similar for the three ions. The slope ratio, for Regimes 1 and 2, decreases by a factor $\sim$2.5 from Hα to [O III] to [S II] ($5.3 \rightarrow 2.2 \rightarrow 0.8$). As expected, none of the slopes are close to the Kolmogorov prediction found at 0.66 (Kolmogorov 1941).

The simulations shown in Figure 7.20 roughly reproduce the observed behavior. The reader is reminded that absolute quantitative comparisons are not possible. Using against slope ratios, the Hα and [O III] SFs resemble most simulation S_9 and S_5 respectively while the [S II] SF resembles a mix between S_1 and S_2. The observed Y-intercepts vary a lot between the different ions contrarily to the simulations. Obviously, it is hard to separate the influence of the large-scale coherent flows from the chaotic turbulent velocity fluctuations.

Based on our crude simulations, we propose that the S^+ component likely encloses a lower number of large-scale gradients than the two other ions. This could partially explain the relatively narrow [S II] profiles since numerous velocity gradients along the LOS should naturally lead to broad non-thermal line widths (see above). Moreover, these gradients seem to be relatively weak explaining the particularly flat slopes measured for E_v and F_v (see Table 7.4). The H^+ component could encompass the strongest and/or the most numerous number of large-scale gradients explaining the broader Hα line widths with respect to [S II]. On the other hand, the connection with the [O III] SF seems more complicated than expected. Table 7.5 reveals that the

Table 7.6: Simulations of structure functions : the effect of large-scale velocity gradients.

Run	Figure	N_∇	Strength	Regime	Scale (pc)	∇_{F_2} (km^2 s^{-2} pc^{-1})	log[F$_2$(0)] (km^2 s^{-2})	Correlation
S$_1$	7.20*a*	1	W	1	[16.53 – 76.02]	0.12 ±0.02	1.87 ±0.03	0.94
				2	[82.63 – 181.8]	0.14 ±0.02	1.85 ±0.03	0.92
				3	[221.4 – 261.1]	0.90 ±0.16	0.11 ±0.39	0.93
S$_2$	7.20*b*	1	I	1	[16.53 – 76.02]	0.36 ±0.04	1.61 ±0.06	0.96
				2	[82.63 – 181.8]	0.37 ±0.01	1.64 ±0.03	0.99
				3	[221.4 – 261.1]	1.57 ±0.19	-1.09 ±0.44	0.97
S$_3$	7.20*c*	1	S	1	[16.53 – 76.02]	0.58 ±0.05	1.43 ±0.09	0.97
				2	[82.63 – 181.8]	0.49 ±0.01	1.64 ±0.03	0.99
				3	[221.4 – 261.1]	1.77 ±0.20	-1.29 ±0.47	0.97
S$_4$	7.20*d*	2	W	1	[16.53 – 76.02]	0.32 ±0.03	1.65 ±0.05	0.97
				2	[82.63 – 181.8]	0.14 ±0.02	2.00 ±0.05	0.86
				3	[221.4 – 261.1]	0.87 ±0.28	0.37 ±0.67	0.81
S$_5$	7.20*e*	2	I	1	[16.53 – 76.02]	0.67 ±0.04	1.36 ±0.07	0.98
				2	[82.63 – 181.8]	0.29 ±0.03	2.09 ±0.07	0.92
				3	[221.4 – 261.1]	1.17 ±0.38	0.14 ±0.91	0.81
S$_6$	7.20*f*	2	S	1	[16.53 – 76.02]	0.85 ±0.04	1.31 ±0.07	0.99
				2	[82.63 – 181.8]	0.35 ±0.04	2.27 ±0.08	0.93
				3	[221.4 – 261.1]	1.23 ±0.41	0.31 ±0.98	0.80
S$_7$	7.20*g*	3	W	1	[16.53 – 76.02]	0.44 ±0.02	1.65 ±0.04	0.99
				2	[82.63 – 181.8]	0.16 ±0.03	2.16 ±0.07	0.79
				3	[221.4 – 261.1]	2.40 ±0.38	-3.19 ±0.91	0.94
S$_8$	7.20*h*	3	I	1	[16.53 – 76.02]	0.68 ±0.02	1.71 ±0.03	0.99
				2	[82.63 – 181.8]	0.19 ±0.03	2.61 ±0.07	0.83
				3	[221.4 – 261.1]	2.93 ±0.42	-3.96 ±0.99	0.95
S$_9$	7.20*i*	3	S	1	[16.53 – 76.02]	0.75 ±0.02	1.92 ±0.03	0.99
				2	[82.63 – 181.8]	0.19 ±0.03	2.95 ±0.07	0.84
				3	[221.4 – 261.1]	3.03 ±0.42	-3.87 ±1.00	0.96

slope ratio between Regimes 1 and 2 is in agreement with relatively strong velocity gradients but also with a potentially lower number of large-scale gradients than in Hα (i.e., S_5 vs. S_9). The flatter slope for Regime 3, compared to Hα, also leads to a similar conclusion. This [O III] SF behavior cannot be reconciled with the [O III] line profiles showing the largest non-thermal line widths.

The only way to reconcile the [O III] SF results with the line-width behavior is to suppose that turbulence is stronger within the O^{++} ionic volume and that the ionization structure of NGC 595 is such that S^+ has the smallest volume (limited to the periphery) and H^+, the largest. O^{++} being close to the high-mass stars, the mixture of stellar winds and Champagne flows would do much to increase the turbulent motions. However, if we suppose that the H^+ and O^{++} volumes are spatially coincident hence both would be affected the same way by Champagne flows and stellar winds (contrary to the previous hypothesis). Therefore, turbulence would be very similar for both ions and could not provide a reasonable explanation for the observed differences in line widths (see Table 7.5) and in SFs (see Figures 7.19*a* and 7.19*b*). This is hard to reconcile hydrodynamically. If the observed differences are indeed due to different turbulent motions for H^+ and O^{++}, this can only be explained if the two ions are not spatially coincident. Since the Hα material seems to enclose more velocity gradients (see above our interpretation of the simulated SFs), only strong turbulent motions could compensate for the large $\langle\sigma\rangle$ value measured for [O III] in Table 7.5. This will be addressed in our forthcoming paper (Lagrois & Joncas 2009d). Whatever the outcome, our results do not support the *Cometary Stirring Model* since, according to Panels (a) and (b) of Figure 7.18, H^+ and O^{++} should exhibit a similar turbulent behavior (deduced from very similar σ_0 values).

7.7.3 Kinematics of the 2-component profiles

In their kinematic investigation of NGC 604, Yang *et al.* (1996) noticed that the faintest portions of the nebula showed velocity profiles in Hα often characterized by two distinct components. These portions of NGC 604 were said to be dominated by embedded, expanding wind-blown bubbles which cause the observed line splitting. This is similar to NGC 595 in which the line-splitted spectra are confined to a specific area surrounded by 1-component velocity profiles. The hatched region of Figures 7.2 and 7.3 is also spatially coincident with the majority of the most massive stars of the star cluster. The line splitting therefore likely indicates the kinematic impact of strong stellar winds on the surrounding nebular gas.

The reader should note that a series of spectral conditions were used in order to qualify a given profile as having two defined components. For example, we specified that the two components should have similar observed line width (within a few channel units). Dynamically, we have no reason to believe that the two components, of a given profile, should differ in corrected widths by more than a few tens of km s^{-1}. Moreover, this condition prevents the fit of particularly broad profiles that could be related to the warm ionized medium of the galaxy (Reynolds 1989b; Wang & Heckman 1997; Reynolds 2004). The S/Ns of the two components should be comparable within a factor five. Finally, we demand a separation in velocity greater than 0.75 times the channel step of our optical observations (see Section 7.5). The latter condition is used in order to avoid 2-component fits to very symmetric velocity profiles. Therefore, separated lines or [at least] well-defined asymmetric profiles were required. This probably underestimates, by a few pixels, the extent of the hatched region in Figures 7.2 and 7.3 (see Section 7.7.3.2) but it also prevents the creation of artificial 2-component profiles.

7.7.3.1 The σ vs. Intensity diagnostic diagram : a quest for embedded wind-blown bubbles

The σ vs. Intensity diagnostic diagram (see Figure 7.18), introduced by Muñoz-Tuñón *et al.* (1996), has a double purpose : (1) estimate the value for σ_0 which indicates, according to the authors, the kinematic impact of low-mass stars moving in the ambient ionized plasma (see Section 7.7.2.5) and (2) track the presence of expanding shells embedded inside GEHRs. The latter purpose is here investigated. Assuming 1-component profiles everywhere in each object, the authors described the line-width behavior, in the σ vs. Intensity diagram, of an optically thin idealized bubble. Each bubble should normally take the form of an inclined band in the diagram directed from a low intensity, high σ point to a high intensity, low σ point (see their Figure 3*c*). The low intensity, high σ point corresponds to a LOS oriented toward the center of the bubble where the contribution in intensity is mostly attributed to the thin front and rear walls (seen roughly at normal incidence) and where the separation in radial velocity between the two splitted lines is maximal (a 1-component fit to such velocity profile leads to a large σ value). The high intensity, low σ point results from a LOS tangential to the edge of the shell. This particular angle of view favors a more important amount of compressed material along the LOS (and therefore a relatively strong intensity). On the other hand, the radial velocity separation is minimal as the front and rear walls "meet" at the shell's edge (leading to a small σ value). Muñoz-Tuñón *et al.* (1996) identified at least three of these inclined bands in their σ vs. Intensity diagram of NGC 604. This tends to confirm the presence of wind-blown bubbles as suggested by Yang *et al.* (1996).

In Panels (a) and (b) of Figure 7.18, filled squares correspond to velocity profiles showing evidence for line splitting but nonetheless fitted, for the cause, by a single, Gaussian component. As opposed to the observations of Yang *et al.* (1996), splitted lines can even be found at large intensities. These points are found at the periphery of N595-1 and -2 where the hatched region and the molecular emission are superimposed (which explains the bright ionic emission). According to the model of Muñoz-Tuñón *et al.* (1996), well-defined inclined bands, among the filled square symbols, should indicate the presence of expanding shells in NGC 595. Unfortunately, it is not clear if such signature is present or not in both diagrams. However, the filled squares can be used to obtain 1-component corrected line-width maps in Hα and [O III] of the hatched region displayed in Figures 7.2 and 7.3. These maps are presented respectively in Panels (c) and (d) of Figure 7.18. Considering that the σ value should decrease from the center to the edge of the shell, we can identify at least one structure that could likely be related to an expanding wind-blown bubble. The dashed circle centered on (α_{2000}, δ_{2000}) = ($01^h33^m33^s.3$, 30°41′36″) indicates approximately the outer edge of the bubble (traced out by the low line-width material). The lower portion of the shell "sits" on the molecular clouds, probably slowed down by the dense material (similarly to the partial ellipse of Figure 7.13, see Section 7.7.2.1). A certain number of massive stars lie inside the dashed circle and likely correspond to the sources of energy for the expansion (see Section 7.7.3.2). The brightness temperature contours traced out by the atomic material are in agreement with the presence of a compressive shock wave ; a circular H I cavity can be deduced from Figures 7.18*c* and 7.18*d*, almost perfectly matching the shape of the dashed circle.

A second, but much less obvious, bubble could be located near the westernmost portion of the hatched region. The long-dashed circle, centered on (α_{2000}, δ_{2000}) = ($01^h33^m32^s.3$, 30°41′34″), indicates a shell relatively well-defined by low line-width material along its left-hand edge. The right-hand edge, on the other hand, extends to the periphery of the hatched region where no indication for low σ values in Hα and [O III] can be found. Smaller in dimensions [when compared to the dashed circle], the long-dashed shell also encloses a much smaller number of ionizing stars (see Section 7.7.3.2). In the next subsection, a quantitative investigation, using our optical observations, will be carried out in order to claim whether or not the two hypothetical shells are physically viable.

7.7.3.2 Wind-blown bubbles in NGC 595 : a quantitative investigation

The dashed circle in Panels (c) and (d) of Figure 7.18 (now referred as Shell-1) encloses an hypothetical bubble of radius $R_{\mathrm{shell}} = 24.5$ pc (roughly 3.75 pixels on the plane of the sky). The fact that the massive stars found [apparently] inside the bubble are generally located between the center of Shell-1 and the molecular clouds probably indicates an asymmetric, ovoid-shaped bubble. Shell-1 has likely expanded farther away from the ionizing sources on the direction pointing away from the molecular material (i.e., along the less-resistance direction). Notice that the whole NGC 595 nebula shows a similar morphology (see the ovoid-shaped supershell displayed in Figure 7.13). However, we chose to treat the shell as circular to simplify the following discussion. The shell's mass [of ionized hydrogen] is given by equation (2) of Rozas *et al.* (2006b) :

$$M_{\mathrm{shell}}(H^+) = (1+Y) \times 4\pi R_{\mathrm{shell}}^2 \times \Delta R_{\mathrm{shell}} \times n_{\mathrm{shell}} \times m_p, \tag{7.3}$$

where Y is the helium mass fraction, $\Delta R_{\mathrm{shell}}$ is the thickness of the shell, n_{shell} is the electron density of the ionized shell, and m_p is the mass of atomic hydrogen. Similarly to Rozas *et al.* (2006b), we adopt $Y = 0.25$. Chu & Kennicutt (1994) mention a $\Delta R_{\mathrm{shell}}/R_{\mathrm{shell}}$ ratio of roughly 0.08 during the adiabatic phase of a wind-blown bubble's expansion. This gives $\Delta R_{\mathrm{shell}} = 1.96$ pc. We circumscribed, in Figure 7.13, the area covered by Shell-1. The shell shows an electron density estimated at $118 \pm 13(1\sigma)$ cm^{-3}. We therefore obtained a shell's mass of 5.35×10^4 M$_\odot$.

The kinetic energy of the shell corresponds to :

$$K_{\mathrm{shell}} = \frac{1}{2} \times M_{\mathrm{shell}}(H^+) \times v_{\mathrm{exp}}^2, \tag{7.4}$$

where $v_{\rm exp}$ is the expansion velocity of the shell and is estimated at half the difference in velocities between the blue and red components measured through to center of the expanding bubble. From Panel (c) of Figures 7.9 and 7.11, the velocity difference between the two components is estimated at 36.9 km s^{-1} in Hα and 43.8 km s^{-1} in [O III]. We therefore found $v_{\rm exp}$ between 18 and 22 km s^{-1} for Shell-1 and we adopt a mean value of 20 km s^{-1}. This value agrees with the expansion velocity of the large H I shell said to partially circumscribe NGC 595 (Deul & den Hartog 1990, see Section 7.4). The kinematic energy of the shell is finally estimated at 2.14×10^{50} ergs.

Since less than 1% of the stellar UV emanating from a massive star can be converted in kinetic energy into the ambient ISM (Dyson & Williams 1980, Chapter 7), the source of the shell's kinetic energy can be entirely attributed to the mechanical deposit associated to stellar winds. A total of 35 star-candidates are observed inside Shell-1 (see Figures 7.18*c* and 7.18*d*) ; 33 of them being main-sequence O-stars and 2 WR-stars (N-type). Table 7.7 provides the wind properties estimated for each of the 35 star-candidates. In Column 3, the ID numbers correspond to the identification numbers used in Table 2 of Drissen *et al.* (2008), for WR-stars, and in the on-line table of Malumuth *et al.* (1996), for O-stars. The effective temperatures for O-stars in Column 6 are the values we obtained from the CHORIZOS procedure (see Section 7.6.1). The spectral class (SC, Column 7) of each O-star is estimated using its derived effective temperature and Figure 1 of Mokiem *et al.* (2007). We considered only the data points associated with the Large Magellanic Cloud (hereafter, LMC) since its metallicity is roughly coincident with the metallicity of M33 (Viironen *et al.* 2007). We provide, in Columns 8 and 9, estimates for the mass-loss rate and the terminal velocity associated to the winds of each star. To do so, we referred to a series of previous articles discussing the wind properties of numerous Galactic and LMC hot stars (Leitherer 1988; Prinja *et al.* 1990; Niedzielski & Skórzyński 2002; Crowther 2007; Mokiem *et al.* 2007). LMC observations were highly priorized but Galactic studies were also considered. In particular, Table 2 of Crowther (2007), mostly restricted to Galactic observations, was used to quantify the wind properties of the two WR-stars since WNL winds do not seem to be influenced by the metallicity (Niedzielski & Skórzyński 2002). We can approximate the total mechanical luminosity, $L_{\rm tot}$, attributed to the stellar winds of the 35 star-candidates presented in Table 7.7 as :

Table 7.7: Wind properties of the star-candidates in Shell-1.

	Type	ID	α_{2000} (01^h33^m)	δ_{2000} ($30°41'$)	T_{eff} (K)	SC	M_w (10^{-6} $M_\odot$ yr^{-1})	v_∞ (km s^{-1})
1	WR	2a	$33^s.76$	$34''.0$	–	WNL	[5-20]	[700-2200]
2	WR	2b	$33^s.72$	$34''.2$	–	WNL	[5-20]	[700-2200]
3	O	189	$33^s.75$	$32''.7$	43 118	O5(V)	[0.5-5.0]	2750
4	O	201	$33^s.74$	$32''.7$	41 604	O5.5(V)	[0.5-4.5]	2500
5	O	241	$33^s.68$	$33''.1$	40 732	O6(V)	[0.5-4.0]	2250
6	O	313	$33^s.55$	$33''.5$	40 642	O6(V)	[0.5-4.0]	2250
7	O	207	$33^s.74$	$32''.8$	40 056	O6(V)	[0.5-4.0]	2250
8	O	233	$33^s.63$	$31''.2$	39 875	O6(V)	[0.5-4.0]	2250
9	O	186	$33^s.72$	$31''.9$	39 436	O6(V)	[0.5-4.0]	2250
10	O	151	$33^s.90$	$35''.5$	39 279	O6(V)	[0.5-4.0]	2250
11	O	319	$33^s.58$	$35''.1$	38 772	O6.5(V)	[0.5-3.5]	2150
12	O	266	$33^s.64$	$33''.7$	38 578	O6.5(V)	[0.5-3.5]	2150
13	O	256	$33^s.61$	$32''.1$	38 454	O6.5(V)	[0.5-3.5]	2150
14	O	161	$33^s.78$	$32''.3$	38 008	O7(V)	[0.5-3.0]	2000
15	O	307	$33^s.52$	$32''.5$	37 930	O7(V)	[0.5-3.0]	2000
16	O	311	$33^s.49$	$31''.6$	37 672	O7(V)	[0.5-3.0]	2000
17	O	165	$33^s.77$	$32''.4$	37 591	O7(V)	[0.5-3.0]	2000
18	O	200	$33^s.71$	$31''.7$	36 674	O7.5(V)	[0.5-2.5]	1875
19	O	269	$33^s.65$	$34''.3$	36 496	O7.5(V)	[0.5-2.5]	1875
20	O	227	$33^s.70$	$33''.2$	36 367	O7.5(V)	[0.5-2.5]	1875
21	O	280	$33^s.69$	$36''.2$	36 196	O7.5(V)	[0.5-2.5]	1875
22	O	235	$33^s.68$	$32''.8$	35 342	O8(V)	[0.5-2.0]	1750
23	O	172	$33^s.75$	$32''.1$	35 303	O8(V)	[0.5-2.0]	1750
24	O	175	$33^s.76$	$32''.5$	35 253	O8(V)	[0.5-2.0]	1750
25	O	304	$33^s.51$	$32''.1$	35 126	O8(V)	[0.5-2.0]	1750
26	O	293	$33^s.59$	$34''.3$	35 043	O8(V)	[0.5-2.0]	1750
27	O	242	$33^s.70$	$34''.0$	35 003	O8(V)	[0.5-2.0]	1750
28	O	228	$33^s.71$	$33''.7$	34 871	O8.5(V)	[0.5-1.5]	1600
29	O	287	$33^s.55$	$32''.2$	34 687	O8.5(V)	[0.5-1.5]	1600
30	O	243	$33^s.71$	$34''.5$	34 641	O8.5(V)	[0.5-1.5]	1600
31	O	229	$33^s.74$	$34''.5$	34 212	O8.5(V)	[0.5-1.5]	1600
32	O	388	$33^s.48$	$38''.2$	33 707	O9(V)	[0.5-1.0]	1500
33	O	257	$33^s.62$	$32''.6$	33 265	O9.5(V)	[0.5-1.0]	1500
34	O	331	$33^s.46$	$31''.7$	33 240	O9.5(V)	[0.5-1.0]	1500
35	O	267	$33^s.69$	$35''.3$	33 163	O9.5(V)	[0.5-1.0]	1500

$$\begin{aligned} L_{\text{tot}} &= \frac{1}{2} \times \sum_{\text{WR-stars}} \dot{M}_w \times \left[\frac{1}{N_{WR}} \cdot \sum_{\text{WR-stars}} v_\infty \right]^2 \times t_{WR} \\ &+ \frac{1}{2} \times \sum_{\text{O-stars}} \dot{M}_w \times \left[\frac{1}{N_O} \cdot \sum_{\text{O-stars}} v_\infty \right]^2 \times t_O, \end{aligned} \tag{7.5}$$

where $N_{WR} = 2$ WR-stars and $N_O = 33$ O-stars, and t_{WR} and t_O are estimated at 500 000 yr and 4.5 Myr respectively. Equation (7.5) indicates that the Wolf-Rayet phase, in NGC 595, has begun 500 000 years ago, which can be interpreted as an upper limit (Meynet & Maeder 2005). We therefore neglected the wind contribution of the two O-stars that preceded the Wolf-Rayet phase. Equation (7.5) also assumes that all O-stars have formed simultaneously in a violent starburst 4.5 Myr ago, which corresponds to the age of the star cluster (see Section 7.4).

We obtained $L_{\text{tot}} = [0.28\text{-}1.57] \times 10^{52}$ ergs depending on the use of lower or upper limits on $\dot{M}_w$ and v_∞ in Table 7.7. From the range of proposed values for L_{tot}, the $K_{\text{shell}}/L_{\text{tot}}$ ratio for Shell-1 varies between 1% and 8%. Theoretically, Dyson & Williams (1980, Chapter 7) predicted that 20% of the mechanical luminosity of a star cluster can be converted in kinetic energy into the expanding shell.

The same exercise can be carried out for Shell-2 using $R_{\text{shell}} = 18.5$ pc (roughly 2.75 pixels on the plane of the sky, see Figure 7.18) and $n_{\text{shell}} = 161 \pm 30(1\sigma)$ cm^{-3} (from Figure 7.13). We obtained an ionized mass of 3.14×10^4 M$_\odot$ for Shell-2. From Figures 7.9 and 7.11, we estimate an expansion velocity, v_{exp}, of 19.5 km s^{-1} and, finally, a shell's kinetic energy of 1.19×10^{50} ergs. Only 5 massive stars are found inside Shell-2 in Figure 7.18; 1 WR-star and 4 main-sequence O-stars. Table 7.8 indicates the wind properties for each star. The spectral class of each O-star is again deduced using the derived effective temperature and the work of Mokiem *et al.* (2007) related to the LMC. Using the same values for $\dot{M}_w$ and v_∞ presented in Table 7.7, L_{tot} is estimated, from equation (7.5), between $[0.03\text{-}0.15] \times 10^{52}$ ergs for Shell-2. Our observations therefore indicate a $K_{\text{shell}}/L_{\text{tot}}$ ratio for Shell-2 between 8% and 40%.

From a judicious choice of $\dot{M}_w$ and v_∞ values in Table 7.8, theory and observations can be reconciled for Shell-2. The upper ratio of 40%, obtained using lower limits for $\dot{M}_w$ and v_∞, could indicate a lack of hot, massive stars inside the expanding shell. This is the scenario often found in similar investigations of wind-blown bubbles

Table 7.8: Wind properties of the star-candidates in Shell-2.

	Type	ID	α_{2000} (01^h33^m)	δ_{2000} ($30°41'$)	T_{eff} (K)	SC	$\dot{M}_w$ (10^{-6} $M_\odot$ yr^{-1})	v_∞ (km s^{-1})
1	WR	4	$32^s.95$	$36''.2$	–	WN	[5-20]	[700-2200]
2	O	486	$33^s.04$	$39''.9$	36 374	O7.5(V)	[0.5-2.5]	1875
3	O	558	$32^s.63$	$36''.6$	36 282	O7.5(V)	[0.5-2.5]	1875
4	O	551	$32^s.61$	$34''.2$	34 028	O8.5(V)	[0.5-1.5]	1600
5	O	495	$32^s.99$	$39''.4$	33 387	O9.5(V)	[0.5-1.0]	1500

embedded in GEHRs. Yang *et al.* (1996) mentioned, in particular, a sizeable contribution to the mechanical deposit in the ISM attributed to supernova remnants. Even though no non-thermal radio sources have been observed in NGC 595 (see Section 7.4), an appreciable number of stars have already evolved to the Wolf-Rayet phase. We can therefore suppose that a low but non-null number of extremely massive (> 60 $M_\odot$) O-stars were formed in the initial cloud collapse. These stars have likely evolved into supernovae shortly in the life of the nebula. Hence, their non-thermal emission undoubtedly vanished long before the modern observations (Crowther 2007). Supernovae might therefore have contributed to the expansion of Shell-2. Relaño & Beckman (2005) also mentioned that radiation driving via dust coupling could also accentuate the energy deposit that forces the expansion of ionized shells. Can also be added to this list, the neglected contribution of large amounts of B-stars in the different star clusters.

On the other hand, our investigation of Shell-1, in particular, indicates that $K_{\text{shell}}/L_{\text{tot}}$ is well below the theoretical ratio. The discrepancy between theory and observations imply that (1) the ionized shell is not as energetic as expected, (2) the stars, inside Shell-1, are too numerous and/or have too much wind momentum, or (3) both factors play a sizeable role. For the ionized shell, we stand by our measurements for the expansion velocity (Figures 7.9 and 7.11) and the electron density (Figure 7.13) for the reasons mentioned above. However, since the kinetic energy of the shell is dependent of R^3_{shell}, a slight over or underestimation of the shell's radius can lead to much different $K_{\text{shell}}/L_{\text{tot}}$ ratios. For example, if we put $R_{\text{shell}} = 34$ pc and using the lower limit on L_{tot}, we find a ratio, for Shell-1, in agreement with the theory. This would correspond to a misjudgment of roughly 1.5 pixel on the plane of the sky in our first estimate of R_{shell}. This is highly plausible since we can reiterate that the extent of the hatched region of splitted profiles was likely underestimated by a few pixels (see Section 7.7.3). Moreover, the outer pixels in Figures 7.18*c* and 7.18*d* that were used to trace out Shell-1 (see Section 7.7.3.1) still indicate supersonic values near 15 km s^{-1}. Certainly, we can assume that the splitted lines of a given velocity profile will probably show a subsonic velocity separation at the periphery of the shell, where the front and rear walls "meet" (see Section 7.7.3.1). This favors a larger value for R_{shell}, a more energetic Shell-1, and therefore a larger $K_{\text{shell}}/L_{\text{tot}}$ ratio that could approach the 20% theoretical value.

Alternatively, stars listed in Table 7.7 can be lowered in number if we assume that a certain fraction of them are independent of Shell-1, located either in front or well behind the blown bubble. However, this is hard to reconcile with Figure 7.18 since all stars are aggregated, in the (α, δ)-plane, inside a relatively small portion of the bubble. The low spatial dispersion observed on the plane of the sky probably indicates, similarly, a low spatial dispersion along the LOS and, therefore, very close stars embedded inside the shell and all contributing to its expansion. On the other hand, equation (7.5) remains a crude approximation of the total mechanical luminosity attributed to the stellar winds of a series of massive stars. In order to reconcile the Shell-1's properties with the theory of expanding wind-blown bubbles, numerical models, similar to the ones presented by Leitherer *et al.* (1992), should be used in order to obtain a reliable estimate of the star formation history in NGC 595. In particular, depending if we choose to modelize the star cluster as an instantaneous starburst (considered here) or with a continuous star formation rate can lead to different rates of wind momentum transferred to the local ISM. This could affect the measured $K_{\text{shell}}/L_{\text{tot}}$ ratio. In particular, Malumuth *et al.* (1996) give evidence for stars of slightly different ages in NGC 595 (see Section 7.4). This is opposed to the instantaneous starburst scenario. The reader should note that if we wish to lower the dynamical impact of the stars presented in Table 7.7 (in order to increase the $K_{\text{shell}}/L_{\text{tot}}$ ratio), supernova remnants must be ruled out in Shell-1. A different conclusion was reached for Shell-2. Finally, the wind momentum contribution attributed to the two WR-stars located inside Shell-1 is likely less important than first expected. Assuming a very young Wolf-Rayet phase (i.e., $t_{WR} \ll 100\,000$ yr in eqn. (7.5)), the $K_{\text{shell}}/L_{\text{tot}}$ ratio for Shell-1 can only be increased at 10%, still well below the theoretical value.

Considering all stars listed in both Tables 7.7 and 7.8, we obtained, using equation (7.5), a range of values for L_{tot} between 0.31 and 1.72×10^{52} erg. Considering a mean electron density of 140 cm^{-3} between Shell-1 and -2, a large, single shell of radius R_{shell} between 55 and 100 pc would show a certain agreement with the theory. Interestingly, the low-limit radius (~ 9 pixels) agrees with the area covered by both shells fused at one (see Figures 7.18*c* and 7.18*d*). However, the kinematical analysis of the shells seems to favor two distinct objects that should be investigated separately (see Section 7.7.3.3).

7.7.3.3 Shell-1 vs. Shell-2 : a kinematical comparison

We already mentioned that the position of the 35 massive stars lying in Shell-1 likely indicates an asymmetric bubble, probably ovoid-shaped (see Section 7.7.3.2). Kinematically, Table 7.2 also favors an asymmetric expansion in velocities inside the hatched region of line-splitted profiles. With respect to the velocity of the molecular material, we found a mean red component redshifted by roughly 4 and 10 km s^{-1} respectively in Hα and [O III]. On the other hand, the mean blue component is blueshifted with respect to the molecular clouds by 25 and 20 km s^{-1} in Hα and [O III]. Even though a certain contribution to the blue velocities could be attributed to Champagne effects near N595-1 and -2 (see Section 7.7.2.3, and Figures 7.16*c* and 7.17*c*), the kinematic behavior potentially indicates wind-blown bubbles characterized by slow-moving rear walls and fast-expanding front walls. This likely arises from dense, ionized material located behind the two shells and acting as a physical barrier, preventing the red component of Table 7.2 to reach velocities well-different from the actual molecular clouds' kinematics. This material probably has a molecular origin similar to the northern extension of the N595-1 cloud, referred as the inner ionized filament (see Section 7.7.2.4). Hence, while the rear walls are most likely slowed down, the front walls expand more freely and at greater velocities in a much more tenuous medium.

Table 7.9 provides a kinematic comparison between Shell-1 and -2. Both the blue and red components of the splitted lines are investigated separately. For each shell, we considered only the pixels circumscribed by the dashed and long-dashed circles of Figure 7.18. For each component, we provide the mean radial velocity (Column 4) and the mean line width (Column 6) in Hα and [O III]. The one-standard deviation (β_v, β_σ) for each distribution is also given in Columns 5 and 7. Comparing the velocity values provided in Column 4 leads to a general tendency linking the two shells : for a given ion and a given component, Shell-2 always appears slightly blueshifted with respect to Shell-1. The differences in velocities are between 3 and 4.5 km s^{-1} while a peak value of roughly 8 km s^{-1} is obtained for the blue component in Hα. This tendency clearly indicates that the two wind-blown bubbles are distinct, sepa-

Table 7.9: Kinematical comparison between Shell-1 and Shell-2.

Ion	Component	Shell	$\langle v \rangle$ (km s^{-1})	β_v (km s^{-1})	$\langle \sigma \rangle$ (km s^{-1})	β_σ (km s^{-1})
Hα	Blue	1	-212.24 ± 1.49	7.79 ± 1.08	14.78 ± 1.11	6.27 ± 0.80
		2	-220.55 ± 0.73	3.76 ± 0.53	6.68 ± 1.01	3.35 ± 0.75
	Red	1	-180.10 ± 1.42	8.28 ± 1.05	15.00 ± 1.12	5.94 ± 0.81
		2	-184.39 ± 0.61	3.11 ± 0.44	13.99 ± 0.52	2.66 ± 0.38
[O III]	Blue	1	-196.71 ± 2.19	11.60 ± 1.58	17.67 ± 1.58,	7.91 ± 1.14
		2	-199.78 ± 2.47	12.60 ± 1.78	14.13 ± 1.82	7.74 ± 1.33
	Red	1	-164.04 ± 1.92	11.19 ± 1.38	16.17 ± 1.93	10.00 ± 1.39
		2	-168.61 ± 1.17	5.95 ± 0.84	14.78 ± 1.69	6.56 ± 1.24

rate objects. Moreover, the velocity differences from Shell-1 to -2 follow [spatially] and are roughly of the same order of the velocity discrepancy observed between N595-1 and N595-2 (see Section 7.4). This could signify that each shell might be coupled to its own "molecular source" (Shell-1/N595-1, Shell-2/N595-2). The 3 km s^{-1} difference observed from one cloud to the other has been permeated in the shells' kinematics. This tends to favor the possibility that the two molecular clouds could be separate objects.

Table 7.2 seems to indicate that the red component will usually show larger line widths in Hα and [O III] than the blue component. This kinematic trend is barely observed in Table 7.9 for Shell-1 and -2. A larger mean line width is even obtained for the blue component in the [O III] Shell-1 when compared to the red component. In fact, the line-width behavior in both shells is best understood by considering the spatial variations rather than mean values. Panel (b) of Figures 7.10 and 7.12 shows that the red component in the southernmost portion of each shell presents particularly narrow line widths. This ionized material is likely associated to the rear walls of the expanding bubbles. We already demonstrated from our radial velocity investigation that the two bubbles are located in front of the molecular material in NGC 595. The lower half of the rear walls likely encloses ionized material in contact with the two large molecular clouds still observed in the nebula. The narrow line widths in Hα and [O III] are therefore easily explained by the low line-width molecular material (see Section 7.7.2.3). On the other hand, the upper half of the rear walls, slowly expanding in dense, now fully eroded molecular material, presents broader line widths. The slightly supersonic motions could result from deeper LOSs through the nebula since no molecular material blocks the ionized emission coming from the deepest parts of NGC 595. In particular, since we supposed that the material, in which the rear walls of Shell-1 and -2 expand, has a molecular origin, Champagne flows are expected to dominate the kinematics of the ionized gas located behind the two bubbles. The Champagne phase contributes for larger line widths (see Section 7.7.2.3).

Figures 7.10 and 7.12, however, indicate that the blue component is much narrower toward the upper half of both shells (a trend opposed to the behavior observed for the red component). In our previous argument, we supposed that NGC 595 is characterized by a "sea" of freshly eroded cloud material beyond the rear walls of Shell-1 and -2. If we suppose, on the other hand, that the front walls of both bubbles mark the front boundary of the nebula (i.e., the contribution to the observed spectra attributed to the NGC 595's ionized material located in front of the front walls is likely negligible), only the high-velocity material, found compressed by the outer shock waves, traces out the blue component's profiles. This sole contribution to the emission definitely favors narrow line widths. Toward the lower half of Shell-1 and -2, the blue component's line widths are slightly larger when compared to the line widths of the spatially coinciding red component. This could indicate that a certain distance now separates this emissive material and the molecular component (i.e., the argument, implying that ionized material still in contact with the molecular component should normally show narrow line widths, is no longer applicable). A few of the southernmost pixels, however, shows almost subsonic values which suggests a certain connection with the molecular material where the rear and front walls (of Shell-1 particularly) join. This contributes for $\langle\sigma_{b-c}\rangle$ values slightly smaller than $\langle\sigma_{r-c}\rangle$ in Table 7.2.

7.8 Conclusion

We provide results of a multi-ionic investigation of NGC 595, the second largest H II region in M33. An interferometric device system has allowed us to obtain velocity profiles of the Hα, [O III], and [S II] emissions with reliable S/Ns (Section 7.5). The ionized gas' kinematics is interpreted in conjunction with high-resolution 21 cm line observations of M33 (Section 7.5). An integrated intensity map of the CO (1-0) emission in the nebula was provided for this work.

The main results of our study of NGC 595 are :

I. The Hα and [O III] observations present two distinct kinematical regimes (Section 7.6.1). First, a large fraction of the nebula shows symmetric, usually supersonic, velocity profiles that were well-fitted using a single, Gaussian component (Section 7.7.2). On the other hand, a localized, circumscribed region, in the vicinity of the star cluster, presents evidence for line splitting (Section 7.7.3).

II. The [S II] observations reveal no evidence for line splitting (Section 7.7.2.1). The S^+ material does not seem to spatially coexist with the H^+ and O^{++} components (Sections 7.7.2.1, 7.7.2.3, and 7.7.2.5).

III. Mean velocities, in Hα, [O III] and [S II], are in agreement with the kinematics of the molecular material in NGC 595.

IV. Champagne flows are observed and regulate the photoerosion of the molecular clouds (Section 7.7.2.3). The accelerated, forward flows indicate ionizing sources located in front of the molecular features.

V. In areas not dominated by the photoerosion of the molecular gas, the spatially corresponding atomic and H^+ components show kinematical similitudes (Section 7.7.2.4). The latter is often redshifted by a few km s^{-1} with respect to the former near the eastern boundary of the nebula. This kinematics is expected from the photoionization of H I gas flowing toward the observer (Section 7.7.2).

VI. On a range of a few hundreds of parsecs at the periphery of the nebula, the atomic component shows important velocity variations. This particular behavior is likely related to the fact that two distinct H I clouds, showing slightly different kinematics, seem to be associated to NGC 595 (Section 7.7.2.4).

VII. Structure functions, over to full ionized extent of the O^{++} material, were computed in Hα, [O III] and [S II] (Section 7.7.2.5). A series of simulations were run in order to estimate the effect of large-scale radial velocity gradients on the observational structure functions (Section 7.7.2.5). With respect to the two other ions, the S^+ material seems to enclose a lower number of these contaminating gradients. Moreover, these gradients are likely weaker in "intensity", showing flatter slopes on the plane of the sky. This is in agreement with [S II] profiles being generally narrower than Hα and [O III] (Section 7.7.2.5).

VIII. The differences, noticed between the Hα and [O III] structures functions, could be attributed to the fact that the latter ion is more exposed to violent gas turbulence (Section 7.7.2.5). This is particularly expected since very supersonic non-thermal line widths emerge from the [O III] observations. The isotropic turbulence in NGC 595 remains to be properly investigated.

IX. We provide the first bidimensional electron density map of a giant extragalactic H II region (Section 7.6.5). The mean electron density in NGC 595 is estimated at roughly 160 cm^{-3}, in agreement with previous studies of similar GEHRs (Section 7.6.5). The electron density investigation was used to estimate the extent of the ionized supershell associated with the nebula (Section 7.7.2.1).

X. The partial supershell indicates that NGC 595 could be currently evolving into a dynamic chimney (Section 7.7.2.2). We have not been able to properly track the high-declination ionized material in order to clearly identify the kinematical signature attributed to shell's blowout (Section 7.7.2.2).

XI. Line splitting is directly attributed to the kinematical impact of strong stellar winds on the ionized material (Section 7.7.3). Two shells are identified and tested according to the theoretical model of wind-blown bubbles (Section 7.7.3.2). Both shells show a mitigated agreement with the theory. The sources of uncertainty are however numerous and a possible reconciliation with the model remains probable (Section 7.7.3.2).

XII. The wind-blown bubbles are characterized by asymmetric expansions ; while the front walls likely expand freely in an, apparently, tenuous medium, the rear walls seem to slow down in much denser material (Section 7.7.3.3). Combined with the large fraction of the nebula's surface dominated by Champagne effects (Section 7.7.2.4), this behavior indicates that the molecular complex of NGC 595, before being exposed to the photoerosion induced by numerous massive stars, was, a priori, very imposing in dimensions.

XIII. The velocity investigation of the blown bubbles also indicates that each of them is associated to its own molecular cloud (Section 7.7.3.3). This tends to favor the fact that the two identified clouds could be separate objects that happen to be seen side by side on the plane of the sky.

The apparently ovoid-shaped morphology of NGC 595 makes it a promising candidate of dynamic chimney. However, our optical observations have not allowed to track the very diffuse component located at high declinations and to kinematically identify the signature of hypothetical blowouts associated with the nebula. Similar measurements to the ones presented in this work, carried out however using a much better sensitivity and/or much greater acquisition times, might allow to investigate the kinematics of the tenuous ionized material in the northernmost portion of NGC 595 and to conclude on possible vented outflows.

A subsequent paper, in which we intend to subtract the large-scale gradients from the Hα, [O III] and [S II] velocity maps, will provide an exhaustive, quantitative investigation of the isotropic turbulence in NGC 595.

The authors would like to thank the Natural Sciences and Engineering Research Council of Canada and the Fonds Québécois de la Recherche sur la Nature et les Technologies who provided funds for this research project. This paper is based on observations obtained at the CFHT which is operated by the National Research Council of Canada, the Institut National des Sciences de l'Univers of the Centre National de la Recherche Scientifique of France and the University of Hawaii.

D. L. is grateful to M.-A. Miville-Deschênes and D. J. Marshall who provided useful IDL routines to carry out data reduction. D. L. thanks Leonardo Úbeda for convenient help regarding the use of the CHORIZOS procedure. D. L. would also like to thank B. Malenfant, G. Turcotte and P.-L. Lévesque for technical support during numerous observing nights at the Observatoire du mont Mégantic. Finally, D. L. and G. J. thank Pr. Christine Wilson (McMaster University, Canada) and Dr. David A. Thilker (Johns Hopkins University, USA) for providing useful data regarding the NGC 595 molecular and atomic components.

Troisième partie

III. Conclusion

“A conclusion is the place where you got tired of thinking.”
- Arthur Bloch, *Author of The Murphy’s law (1977)*

Chapitre 8

W4 et NGC 595 : deux régions H II évoluées

Sommaire

L'interférométrie Fabry-Pérot aura permis d'obtenir une image cinématique précise de deux régions H II géantes évoluées : W4 située dans le bras de Persée et NGC 595, dans M33. Pour notre étude, W4 fut observée exclusivement par l'entremise de la raie Hα. Ces observations optiques furent principalement combinées aux données H I et CO (1-0) obtenues à l'origine par le consortium du *Canadian Galactic Plane Survey.*

La région H II géante extragalactique NGC 595 fut observée en Hα, [O III] et [S II]. Les données H I et CO (1-0) furent fournies respectivement par le Dr. David A. Thilker (Université Johns Hopkins) et la Pr. Christine Wilson (Université McMaster). Les principaux résultats de notre étude se résument comme suit.

8.1 W4-sud : une structure complexe, dominée par la photoérosion de la composante neutre environnante

L'utilisation du système interférométrique FaNTOmM, spécialement conçue afin d'étudier les objets astronomiques étendus et de faible intensité, aura permis l'extraction de l'information cinématique associée à la composante ionisée confinée dans la portion sud de la superbulle/région H II galactique W4. Précédant notre investigation, la superbulle fut présentée comme une candidate prometteuse de cheminée dynamique en interaction énergétique avec la couronne galactique. À partir de vingt cubes en vitesse Hα, la photoionisation de nombreux agrégats moléculaires, situés à l'intérieur ou compressés en périphérie de la coquille externe, a mené à la détection d'au moins dix écoulements indépendants de matériel ionisé érodé en accord avec le modèle Champagne décrivant l'évolution dynamique des régions H II. Une série de gradients de vitesse, variant entre 0.31 et 2.60 km s^{-1} pc^{-1} (en valeur absolue), ont été détectés. La pente de chaque gradient indique approximativement l'angle de l'écoulement par rapport à la ligne de visée et, par le fait même, la position du matériel érodé par rapport aux sources ionisantes. Une reconstitution spatiale est proposée indiquant la distribution, le long de la ligne de visée, de chaque fragment moléculaire examiné dans W4-sud. Indubitablement, W4-sud montre le dernier stade de la photoérosion d'un nuage moléculaire géant. En périphérie de la superbulle en expansion, les fragments de nuage, situés au-dessus (sous) de l'amas stellaire, montrent des écoulements Champagne décalés sur le rouge (bleu) par rapport au matériel moléculaire. Nous avons démontré que ceci est en accord avec le fait que la superbulle W4 serait possiblement inclinée vers l'observateur.

Les gradients de vitesse ont tous montré des pentes inférieures au gradient maximal prédit par la phase Champagne (entre 3 et 5 km s^{-1} pc^{-1}). Des écoulements gazeux généralement perpendiculaires à la ligne de visée sont proposés afin d'expliquer le faible désordre cinématique observé sur le plan du ciel. Une contribution cinématique, aux gradients de vitesse, attribuée aux vents stellaires n'a pu être vérifiée en raison, possiblement, de cet effet géométrique. D'un autre côté, les vents stellaires pourraient avoir une contribution négligeable sur la cinématique du matériel ionisé confiné aux écoulements situés dans le voisinage de l'amas.

Le contraste en densité à la discontinuité en pression entre le matériel neutre, potentiellement érodable, et le MIS environnant a présenté des répercussions importantes sur la cinématique observée. En particulier, l'érosion par l'intérieur de la supercoquille W4, formée de fragments moléculaires partiellement compressés ou de gaz atomique, a révélé des mécanismes bien distincts. Dans le premier cas, les écoulements accélérés (vers le bleu ou le rouge), en accord avec le modèle Champagne, ont été observés tel que prévu. La photoérosion de la coquille atomique, caractérisée par une densité de trois à dix fois inférieure à la densité minimale anticipée sur l'enveloppe externe des nuages moléculaires, a mené à des écoulements décalés vers le rouge (par rapport à la coquille H I) se dirigeant vers le centre de la bulle. Plutôt que d'être interprétés comme des écoulements Champagne dirigés vers l'arrière, le matériel érodé pourrait être laissé derrière la supercoquille, cette dernière se déplaçant vers l'observateur. La cinématique de ces écoulements particuliers fut largement comparée au sillage de matériel laissé derrière un corps solide se mouvant dans un milieu visqueux. Ce matériel ralenti pourrait avoir un impact significatif sur certaines zones de notre relevé Hα de W4-sud désignées comme le milieu inter-écoulements.

Certains chocs Champagne ont montré des indices de dissipation. La transition du milieu intra-écoulement au milieu inter-écoulements indique une longueur de mélange à l'intérieur de laquelle le matériel ionisé accéléré s'échappe du choc compressif et graduellement évolue afin de retrouver l'état cinématique local du milieu inter-écoulements. Le milieu inter-écoulements explique partiellement que la vitesse radiale moyenne de notre relevé Hα soit décalée vers le rouge d'environ 5 km s^{-1} par rapport à la vitesse moyenne du matériel moléculaire détecté dans le voisinage de W4.

Une investigation du désordre cinématique le long de la ligne de visée a indiqué que W4 correspond à une phase transitoire entre régimes subsonique et supersonique, en accord avec les dimensions apparentes de l'objet. La largeur de raie Hα moyenne fut estimée à 9.213 ± 0.002 km s^{-1}. Les superbulles de type W4, caractérisées par des champs de vitesse complexes, pourraient représenter le chaînon manquant entre les régions H II galactiques de petite taille (< 30 pc) et les régions géantes extragalactiques (> 500 pc). Le comportement en largeur de raie Hα, au niveau des écoulements Champagne, fut particulièrement examiné. Une tendance à l'élargissement des raies, en accord avec la théorie, est expliquée par une série d'effets : l'augmentation constante du volume de matériel ionisé se retrouvant le long de la ligne de visée, une accumulation de gradients de vitesse au fur et à mesure que le matériel érodé s'éloigne de la discontinuité en pression, une dispersion localisée des sources ionisantes au voisinage du matériel érodable et porosité et imperfections en périphérie des agrégats neutres. Les gradients en largeur de raie sont estimés entre 0.16 et 3.62 km s^{-1} pc^{-1}. Par contre, une série de gradients montrant le rétrécissement des raies, au voisinage de l'amas stellaire, pourraient être attribués à l'absorption le long de la ligne de visée, de ce fait bloquant une fraction de l'information cinématique.

Le matériel ionisé confiné à W4-sud étant en partie dominé par une série d'écoulements Champagne à petite échelle ($\lesssim 10$ pc), aucune indication d'écoulement à grande échelle ne fut détectée. Ceci est contraire au modèle de cheminées dynamiques. Face à l'imposante distance (~ 180 pc), sur le plan du ciel, séparant la portion nord de la superbulle et W4-sud, nous avons supposé que les écoulements à grande échelle demeuraient non-détectés sous une certaine limite en latitude. Afin d'estimer l'implication de la superbulle W4 dans le soutien énergétique à la couronne galactique, une investigation similaire nous aura permis d'obtenir l'information cinématique et dynamique associée au matériel ionisé confiné à W4-nord. Les résultats de cette étude sont présentés à la section 8.2.

8.2 W4-nord : un scénario de raréfaction comme signature cinématique des cheminées dynamiques

L'utilisation du système interférométrique FaNTOmM, spécialement conçue afin d'étudier les objets astronomique étendus et de faible intensité, aura permis l'extraction de l'information cinématique associée à la composante ionisée confinée dans la portion nord de la superbulle/région H II galactique W4. Notre motivation fut basée sur la découverte potentielle de deux segments H I de très faible intensité au niveau de la coquille nord, un indice favorisant une possible fragmentation. Nous avons proposé une méthode quantitative permettant l'identification de failles à même la coquille. Notre modèle s'est appuyé sur la perturbation cinématique engendrée par la propagation interne d'ondes de raréfaction. Appliquant cette méthode, les résultats ont suggéré une situation similaire au modèle d'un contenant métallique percé.

Un total de sept champs Hα furent observés dans un intervalle en latitude entre 3° et 7°. Deux régimes cinématiques distincts auront été identifiés. Dans un premier temps, le matériel ionisé sous $b = 5°$ et retrouvé en périphérie de la région H II semble principalement dominé par l'érosion interne de la coquille H I, un comportement largement discuté au chapitre 5. Par contre, un écoulement sud-nord fut identifié sur un axe vertical de 125 pc entre $b = 3\overset{\circ}{.}5$ et $b = 6\overset{\circ}{.}5$ (approximativement centré sur $l = 134°$), en accord avec le passage d'une discontinuité associée à une onde de raréfaction. La discontinuité se propage en direction du plan galactique alors que l'onde de raréfaction elle-même résulte d'une faille au niveau de la calotte polaire de la coquille. Une seconde discontinuité (associée à la même onde) se dirige vers la couronne galactique. Notre investigation n'aura pas permis de conclure sur l'existence d'une faille au niveau de la section ouest de W4.

Une différence de 30 km s^{-1} en vitesse radiale fut observée entre le champ 25 (en apparence associé à la composante ionisée dite « au repos » à proximité de la discontinuité sud de l'onde) et le champ 22, renfermant le gaz Hα situé tout juste au-delà de la frontière nord de la région H II. Entre ces deux champs, une large cavité déficiente en Hα renferme le matériel raréfié et accéléré, en expansion (vers le nord) au-dessus de la discontinuité sud. Deux tendances en vitesse radiale auront été détectées : un gradient plutôt plat entre les champs 25 et 21 estimé à (-)0.17 km s^{-1} pc^{-1} et un gradient beaucoup plus abrupt de (-)3.13 km s^{-1} pc^{-1} entre les champs 21 et 22, les plus nordiques de notre étude. Le soudain changement de pente semble correspondre à l'augmentation brusque de la vitesse prédite par notre modèle de matériel hautement raréfié. Le comportement en vitesse radiale aura confirmé que W4 est inclinée en direction de l'observateur et démontre la formation d'une cheminée dynamique.

L'âge dynamique de la cheminée fut estimée à 4.1 Mans, supposant que les deux discontinuités associées à l'onde se déplacent avec des vitesses très similaires. Ceci implique que la faille serait apparue lorsque la calotte polaire était située environ 200 pc au-dessus du plan galactique. Dans ce cas, une série d'instabilités se seraient développées au niveau de la coquille à des altitudes bien en deçà du seuil d'éclatement de la bulle, estimé entre 280 et 420 pc au-dessus du plan à la distance de l'amas stellaire IC 1805. Des instabilités magnétohydrodynamiques, par exemple, pourraient donc s'être développées à un stade hâtif de l'expansion. Selon un modèle relativement simple d'expansion de bulles de vents stellaires, approximativement 10 Mans furent nécessaires afin d'atteindre 200 pc et d'ainsi initier la fragmentation de la coquille. Ajoutant l'âge de la cheminée, nous avons proposé un âge dynamique d'environ 14 Mans associé à la superbulle W4, une valeur supérieure aux estimations antérieures.

Les « murs » H I n'auraient en apparence aucun impact cinématique sur les écoulements de matériel ionisé éjecté. D'un autre côté, l'érosion interne de la coquille permet une augmentation considérable de la densité au niveau de certaines régions bien spécifiques. Selon notre modèle, ces champs auraient autrement été susceptibles de renfermer une composante ionisée excessivement raréfiée, potentiellement invisible à nos observations.

Notre modèle unidimensionnel n'aura fourni aucun indice sur le comportement en largeur de raie à l'intérieur de l'onde de raréfaction. Par contre, ce comportement a pu être expliqué suite à une série de suppositions visant l'hydrodynamique du matériel raréfié et la géométrie particulière de W4-nord. Une zone caractérisée par la dissipation de la turbulence est potentiellement située tout juste au-dessus de la discontinuité sud. Corrélé à la brusque accélération observée entre les champs 21 et 22, un gradient abrupt montrant le rétrécissement des largeurs de raie serait relié à la parallélisation des écoulements éjectés par la faille. Une collimation de ces écoulements pourrait éventuellement expliquer la cinématique particulière en vitesse et en largeur de raie rencontrée dans la portion nord du champ 22. Un autre scénario demanderait que la discontinuité nord de l'onde coïncide avec le champ 22 ; le matériel ionisé, s'écoulant par la faille et au-delà de la zone de raréfaction pourrait potentiellement évoluer sur une certaine distance afin d'atteindre la configuration cinématique du milieu ionisé diffus local situé au-dessus de la superbulle. Finalement, les valeurs particulièrement faibles de $\beta_{i,corr}$ au niveau du champ 22 auront indiqué une inclinaison relativement faible de W4 par rapport au plan du ciel. Utilisant de nouveau la condition que la discontinuité nord et le champ 22 coïncident en latitude, nous avons obtenu un angle d'inclinaison entre 9° et 27°.

Utilisant les observations présentées au chapitre 5, nous avons pu estimer la quantité de matériel photoérodé se déversant chaque année dans le milieu ionisé contenu par la coquille H I. Le taux auquel W4-nord semble perdre du matériel à travers la faille est légèrement inférieur à ce taux. Or, la présence de la cavité déficiente en Hα indique que le taux d'évacuation devrait normalement dominer. Les explications proposées auront surtout été liées à la géométrie de l'objet : une faille asymétrique potentiellement plus grande, un angle d'inclinaison de la superbulle (par rapport au plan du ciel) en deçà de la limite inférieure calculée ou une contribution non-négligeable à l'évacuation attribuée à la faille ouest (bien que cette dernière ne fut pas détectée en Hα).

La confirmation cinématique d'une faille au niveau de la calotte polaire de W4 signifie qu'une fraction non-négligeable du flux ionisant peut quitter la superbulle à travers le bris. La formation d'une cheminée dynamique à l'intérieur de la superbulle/région H II W4 représente le stade évolutif permettant d'établir une connexion énergétique entre l'amas stellaire IC 1805 et la structure de Reynolds située au niveau de la basse couronne galactique.

8.3 NGC 595 : photoérosion et vents stellaires associés à un amas massif

Nous avons présenté les résultats d'une étude multi-ionique de NGC 595, la seconde région H II géante extragalactique la plus imposante dans M33. L'utilisation du système interférométrique FaNTOmM aura permis d'obtenir une série de profils de vitesse en Hα et [S II]. Des observations similaires en [O III], obtenues au Télescope Canada-France-Hawaii grâce à un système d'acquisition semblable, furent également ajoutées à l'échantillon de données. Dans tous les cas, l'étendue en gaz ionisé, montrant des rapports signal-sur-bruit fiables, correspond à une fraction appréciable de la nébuleuse. La cinématique du gaz ionisé dans NGC 595 fut interprétée conjointement avec des observations à haute résolution de la raie à 21 cm de M33. Une carte d'intensité intégrée de l'émission CO (1-0) nous aura été fournie pour ce travail.

Les observations Hα et [O III] auront présenté deux régimes cinématiques distincts. Dans un premier temps, une fraction importante de la nébuleuse a montré des profils en vitesse symétriques, habituellement supersoniques, étant correctement ajustés par une seule composante gaussienne. À l'opposé, une région de relativement faible étendue, localisée au voisinage de l'amas stellaire, a montré des indices de dédoublement de raies. Ces profils particuliers furent ajustés par une double composante gaussienne. Les observations [S II] n'ont révélé aucune indication de dédoublement de raies. De ce fait, le matériel S^+ ne semble pas coexister spatialement avec les composantes H^+ et O^{++}.

L'investigation en vitesse radiale des profils à une composante aura montré des vitesses radiales moyennes Hα, [O III] et [S II] en accord avec la cinématique du matériel moléculaire présent dans NGC 595. Une série d'écoulements Champagne résultent de la photoérosion du matériel moléculaire. Les écoulements accélérés, décalés vers le bleu, indiquent vraissemblablement des sources ionisantes situées devant les nuages denses et neutres.

À une distance relativement appréciable du gaz moléculaire, certaines sections de la nébuleuse montrent un accord cinématique entre le matériel atomique et les composantes H^+ et S^+. En particulier, le gaz ionisé montre une cinématique légèrement décalée vers le rouge au niveau de la portion est de NGC 595. Ceci est en accord avec des écoulements en gaz atomique dirigés vers l'observateur. Sur une échelle de quelques centaines de parsecs sur le plan du ciel, la composante atomique montre d'importantes fluctuations en vitesses radiales. Ceci pourrait être relié au fait que deux nuages H I distincts semblent être associés à NGC 595.

Outil statistique visant à estimer la contribution turbulente à l'intérieur de la nébuleuse, la fonction de structure de second ordre fut calculée pour les trois ions de l'étude. À titre comparatif, une série de simulations furent également conduites afin d'estimer l'impact des gradients de vitesse à grande échelle sur les différentes fonctions de structure observationnelles. Il apparaît que le matériel S^+ semble renfermer un nombre inférieur de gradients de vitesse par rapport aux ions H^+ et O^{++}. Qui plus est, ces gradients pourraient être moins prononcés en « intensité », montrant des pentes plus aplaties sur le plan du ciel. Ceci est en accord avec les profils d'émission plus étroits observés en [S II]. Les différences observées, entre les fonctions de structure Hα et [O III], pourraient être attribuées au fait que ce dernier est en proie à une turbulence plus importante. Ceci est anticipé suite aux largeurs de raie particulièrement supersoniques émergeant des observations [O III].

Notre étude de NGC 595 aura permis de produire la première carte bidimensionnelle en densités électroniques d'une région H II géante extragalactique. La densité moyenne, à l'intérieur de la nébuleuse, est estimée approximativement à 160 cm^{-3}, en accord avec des études précédentes de régions H II similaires. L'investigation en densité électronique nous aura permis d'estimer la morphologie et les dimensions associées à la supercoquille de NGC 595. Cette coquille partielle indique que NGC 595 pourrait présentement évoluée en cheminée dynamique.

Le dédoublement de raies est directement attribué à l'interaction cinématique violente entre vents stellaires et gaz ionisé. Deux coquilles, confinées à la nébuleuse, sont identifiées et testées selon le modèle théorique de bulles de vents stellaires en expansion. L'accord avec la théorie n'est pas parfaitement concluant. Or, les sources d'incertitude sont relativement importantes et une réconciliation avec les observations demeure envisageable.

Les bulles semblent indiquer une expansion asymétrique ; alors que les parois « avants » sont apparemment en expansion dite « libre » dans une portion diffuse de la nébuleuse, les parois « arrières » semblent être ralenties par un milieu beaucoup plus dense. Combiné au fait que des écoulements Champagne sont observés sur une fraction non-négligeable de la surface de la région H II, ce comportement pourrait indiquer que le complexe moléculaire, associé à NGC 595, aurait été excessivement imposant en dimensions à un moment précédent la phase de photoérosion.

L'investigation en vitesses radiales des deux bulles hypothétiques montre que chacune d'elles semble associée à son propre nuage moléculaire. Ceci contribue à renforcer notre prise de position voulant que les fragments moléculaires, N595-1 et -2, soient deux objets distincts vus le long d'une ligne de visée similaire.

8.4 W4 vs NGC 595 : une comparaison des différentes propriétés globales

Les régions H II W4 et NGC 595 peuvent être qualifiées d'objets géants dû à leurs imposantes dimensions spatiales (>100 pc). Il advient, par contre, qu'une comparaison directe entre les deux nébuleuses est particulièrement boiteuse en raison, principalement, de stades évolutifs particulièrement différents. Si l'une est relativement jeune et imposante, l'autre, beaucoup plus âgée, montre des dimensions bien inférieures. Cette conclusion est plutôt contre-intuitive. Dans un cas contraire, il aurait été naturel de proposer que la région la plus imposante n'est que la contre-partie plus âgée de la nébuleuse plus petite. Les comparaisons n'auraient été que facilitées. Or, les différences spatio-temporelles, notées entre W4 et NGC 595, sont essentiellement liées à des amas d'étoiles bien distincts. Bien que notre étude confirme que W4 ne peut qu'avoir été formée suite à une succession d'amas stellaires, chacun de ces amas ne représente qu'une fraction infime de la « puissance » contenue dans l'amas de NGC 595. Le nombre important d'étoiles O et Wolf-Rayet, recensées dans la nébuleuse de M33, auront permis à cette dernière d'atteindre une taille phénoménale à l'intérieur d'un délai relativement restreint.

En plus de la contribution des sources ionisantes, les propriétés physiques du matériel neutre, à l'intérieur duquel croît une superbulle, sont directement liées aux dimensions que cette dernière atteindra en un temps donné. En particulier, une coquille de matériel atomique, potentiellement compressé, est détectée aux abords de NGC 595 montrant une densité de l'ordre de quelques dixièmes de particule par centimètre cube. D'autre part, la densité du gaz H I diffus (non-compressé), observé au niveau du plan galactique [dans le bras de Persée], est estimée à environ 5 cm^{-3} (Magdalen Normandeau, communication privée). La taille restreinte de W4, par comparaison à NGC 595, pourrait donc être partiellement associée à une composante neutre environnante plus dense, freinant de façon plus efficace la progression de la supercoquille en expansion.

Une connaissance accrue de la géométrie de l'objet examiné est critique afin d'interpréter correctement les mouvements du gaz ionisé. L'étude de W4 nous aura permis (1) de confirmer, par l'entremise de W4-sud, l'hypothèse selon laquelle la superbulle est inclinée en direction de l'observateur et (2) d'en estimer numériquement, par l'entremise de W4-nord, l'inclinaison par rapport au plan du ciel. La faible inclinaison de W4 aura servi comme argument afin d'expliquer le faible désordre cinématique recensé spatialement. Dans le cas de NGC 595, le désordre cinématique spatial semble légèrement plus important, laissant croire à une inclinaison de la nébuleuse favorable aux variations en vitesses radiales à l'intérieur des écoulements accélérés. Or, notre étude de NGC 595 n'aura pas permis d'en estimer l'importance, contrairement à W4. Bien que l'inclinaison de M33 soit relativement bien connue ($\sim 56°$, Stubbs & Garg 2005), relier cette valeur à l'inclinaison particulière des différentes régions H II s'étant formées au niveau de son disque représente une opération plus ou moins rigoureuse. Nous pouvons supposer, en première approximation, qu'une superbulle typique présentera des écoulements gazeux orientés selon la direction de moindre résistance, généralement dirigée vers la couronne galactique (i.e., d'où une certaine dépendance associée à l'inclinaison de la galaxie). En effet, un calcul très approximatif donnera donc une inclinaison, pour NGC 595, de 34° ($90° - 56°$) par rapport au plan du ciel. Cette valeur surpasse l'intervalle trouvé pour W4 (voir section 6.7.7), en accord avec le fait que les valeurs indiquées à la colonne 4 du Tableau 7.1 soient supérieures à celles listées à la colonne 4 du Tableau 5.1. Par contre, la proximité du milieu inter-bras complique le scénario pour le cas bien particulier de NGC 595. En fait, l'inclinaison d'une région H II est majoritairement dépendante de l'angle, par rapport à la ligne de visée, liant étoiles massives et matériel neutre susceptible d'être érodé. Bien que l'application du modèle Champagne à NGC 595 nous confirme que les étoiles sont situées devant les fragments moléculaires (i.e., favorisant une inclinaison « à la W4 », dirigée vers l'observateur), il nous est impossible d'en estimer précisément l'importance.

Il apparaît que W4 montre les derniers stades de photoérosion d'un ancien complexe moléculaire aux dimensions imposantes. L'inverse est déduit de NGC 595, renfermant toujours une quantité appréciable de gaz CO. Ceci découle essentiellement d'un âge plus jeune et, donc, d'un stade photoérosif moins avancé. Or, la photoérosion d'imposants agrégats de gaz moléculaire est à l'origine même d'une turbulence isotrope importante dans le plasma ionisé. Ceci explique en partie les largeurs de raie plus importantes observées au niveau de NGC 595. De plus, l'investigation en vitesses radiales montre que W4-sud et NGC 595 semblent chacune régies, de façon générale, par deux mécanismes dynamiques différents. Au niveau de W4, la faible abondance relative de fragments moléculaires laisse une place importante, comme mécanisme dominant, à la photoérosion de la coquille H I détectée en périphérie de l'objet. Statistiquement, ceci se traduit par une vitesse moyenne Hα décalée vers le rouge par rapport aux agrégats moléculaires résiduels. Alternativement, la taille importante des nuages N595-1 et N595-2 est à l'origine d'écoulements Champagne se propageant sur une fraction appréciable de la nébuleuse. Ceci résulte en des vitesses moyennes, en Hα et [S II] particulièrement, situées à l'extrémité bleue de l'intervalle en vitesse couvert par le gaz moléculaire associé à NGC 595.

Finalement, la notion de cheminée dynamique fut largement examinée pour les deux objets. À la lumière des résultats présentés au chapitre 6, il ne fait aucun doute que W4 évolue actuellement en phase « cheminée ». Approximativement 50% du volume de la nébuleuse renferme une composante ionisée, excessivement diffuse, dont la cinématique s'apparente à un scénario de raréfaction, une signature intimement liée à l'éjection de grandes quantités de matériel au-delà des limites de la région H II. La quête d'une telle signature dans NGC 595 ne s'est pas avérée concluante bien que nos observations nous permirent uniquement d'obtenir l'information cinématique des régions les plus émissives de la nébuleuse. De ce fait, la portion à haute déclinaison, susceptible de présenter une cinématique en accord avec le modèle de cheminée dynamique, ne fut pas cartographiée de façon appropriée pour cause de temps d'exposition limités. À ce stade, la possibilité d'une cheminée dynamique associée à NGC 595 doit demeurer envisageable.

À l'opposé des différences, les similitudes, entre W4 et NGC 595, sont peu nombreuses. Notons, en premier lieu, l'aspect morphologique, ovoïde et allongé, des deux nébuleuses. Cette forme particulière est attendue des régions H II relativement évoluées, caractérisées par des amas stellaires renfermant un nombre appréciable d'étoiles massives et entourées d'un milieu neutre, diffus, inhomogène et fortement anisotrope. De plus (et fort heureusement !), les mécanismes dynamiques (e.g., Champagne), permettant d'interpréter la cinématique du gaz ionisé résultant de l'érosion des agrégats neutres, sont les mêmes pour les deux objets étudiés.

Chapitre 9

Une fenêtre sur l'avenir

Notre étude aura certainement permis d'en apprendre davantage sur l'évolution cinématique des régions H II relativement âgées et de taille importante. Norman & Ikeuchi (1989) mentionnent qu'approximativement mille cheminées galactiques pourraient expliquer la présence du gaz chaud et diffus rencontré au niveau de la couronne galactique de la Voie lactée. Suite à nos travaux, la superbulle W4 montre une cinématique en accord avec le modèle d'interaction énergétique plan vs couronne. Or, nous demeurons très loin du compte initialement prévu. Les restes de supernova géants ont toujours la cote dans la littérature mais très peu de candidats restent connus. Pour la Voie lactée en particulier, nous pouvons supposer qu'une quantité appréciable de ces objets pourraient se retrouver au-delà du centre galactique, masqués par l'absorption le long de la ligne de visée.

Puisqu'aucune cause extérieure aux galaxies n'est susceptible d'expliquer les observations à haute altitude, seuls les disques peuvent alors agir comme source énergétique, par l'entremise des noyaux actifs et/ou des zones à haut taux de formation stellaire (Jiménez-Vicente & Battaner 2000). Dahlem (1997) indique clairement que les associations OB ne peuvent que partiellement expliquer le chauffage et l'alimentation de la couronne. Pour la Voie lactée, ceci contribue à expliquer l'important désaccord entre le nombre de cheminées prédit par les modèles et les candidates répertoriées à ce jour.

Certains questionnements et interrogations subsistent suite à notre investigation de W4 et de NGC 595. Par exemple, les modèles théoriques indiquent clairement une contribution non-négligeable des vents stellaires aux gradients de vitesse associés aux écoulements Champagne. Apparemment, cet effet dynamique n'a pu être détecté au niveau de W4-sud. Seule une explication, basée sur la géométrie de l'objet, a pu être proposée. De surcroît, les écoulements Champagne, associés à W4-sud, demeurent observables sur des distances de l'ordre de quelques parsecs tout au plus.

De son côté, NGC 595 renferment des écoulements se propageant sur plusieurs dizaines de parsecs. Considérant l'intervalle d'âge séparant les deux objets, comment peut-on imaginer que les fragments moléculaires, détectés dans W4-sud, puissent être à l'origine d'écoulements Champagne « faiblement » étendus alors que ces mêmes fragments sont exposés au flux UV d'étoiles massives depuis plus d'une dizaine de millions d'années ? Notez qu'en principe, chaque photon incident au globule neutre contribue, à sa façon, à alimenter l'écoulement accéléré tant et aussi longtemps que le matériel dense n'aura pas été complètement dispersé.

De façon hydrodynamique, peut-on expliquer que la composante atomique associée à la coquille brisée de W4-nord ne soit pas cinématiquement affectée, au même titre que le matériel ionisé, par le processus d'expulsion du gaz à haute vitesse ? Qui plus est, une quantité appréciable de travail demeure à être accomplie au niveau de W4-nord. Bien que la dégradation spatiale de nos observations optiques aura fortement réduit le nombre de spectres disponibles pour l'étude, un modèle tridimensionnel du scénario de raréfaction devra éventuellement être dérivé et appliqué aux données Hα. De surcroît, une investigation plus approfondie d'une possible faille ouest au niveau de la coquille de W4 est cruciale afin d'obtenir une image dynamique fiable de la formation de la cheminée et du taux d'évacuation de cette dernière.

Finalement, dans quelle mesure une connaissance accrue de l'historique de la formation stellaire dans NGC 595 nous permettrait de réconcilier théorie et observations suite à notre investigation des bulles de vents stellaires confinées à la nébuleuse ? Enfin, NGC 595, comme cheminée dynamique potentielle, demeure à être proprement examinée. Advenant que l'expulsion de matériel ionisé y soit détectée, pourrait-on estimer la direction de l'éjecta ? NGC 595 favoriserait-elle l'enrichissement du milieu inter-bras ou participerait-elle au maintien énergétique de la couronne de M33 ?

Nos études de W4 et de NGC 595 montrent une quantité phénoménale de données spectro-interférométriques optiques de haute qualité. Bien que nous ayons tenté d'en extraire toute l'information physique pertinente, ces données peuvent potentiellement servir à étendre la sphère de recherche. En particulier, les observations de NGC 595 pourraient servir à l'étude de la turbulence isotrope que l'on anticipe à l'intérieur des régions H II (Miville-Deschênes *et al.* 1995; Grosdidier *et al.* 2001). Entre autres, la loi de Kolmogorov stipule que le spectre en vitesse, résultant du processus de cascade turbulente des différents vortex, dépend de la taille de la région instable (Shu 1992, Chapitre 14). Afin de parvenir à réaliser une telle étude, les cartes de vitesse présentées aux chapitre 7 devront préalablement être filtrées dans le but d'en soustraire les gradients de vitesse à grande échelle. À la demande de l'arbitre anonyme, désigné comme responsable par *The Astrophysical Journal* pour l'évaluation du chapitre 7, une étude exhaustive de la turbulence isotrope dans NGC 595 est actuellement en cours (Lagrois & Joncas 2009d).

De plus, les données Hα, introduites aux chapitres 5 à 7, indiquent la présence de raies contaminantes de l'atmosphère terrestre. Ces raies d'émission ont montré d'importantes variations en intensité relative et en largeur de raie sur des distances angulaires de l'ordre de quelques minutes d'arc à l'intérieur du champ de vue. Une étude météorologique serait envisageable, pouvant combiner taille et turbulence des nuages d'hydroxyle au niveau de la mésosphère.

Finalement, les données interférométriques en Hα et [S II] présentées au chapitre 7 montrent une étendue spatiale bien supérieure au voisinage de NGC 595. Les observations couvrent une importante fraction de la portion nord de M33 jusqu'à proximité de la région H II supergéante NGC 604. Combinées à des observations similaires en Hα des portions centre et sud de la galaxie (Godbout 2003), nous avons récemment débuté une nouvelle étude statistique des régions H II dites normales (i.e., ne comportant aucune candidate Wolf-Rayet, aucun reste de supernova, possédant des profils en vitesse simples, non-dédoublés et relativement symétriques) de M33 (Lagrois *et al.* 2009). Une corrélation linéaire liant, pour une région donnée, l'écart-type de la distribution en vitesse radiale (« désordre » cinématique sur le plan du ciel) et la largeur de raie non-thermique moyenne (« désordre » cinématique le long de la ligne de visée) semble indubitable mais reste à être physiquement expliquée.

> "The fundamental point is that we ultimately are made of this stuff – stardust from the interstellar medium."
> - Andrew Westphal, *Astrophysicist*

Quatrième partie

IV. Annexe

"Hitherto shalt thou come, but no further."
- Job 38 :11, *The Holy Bible*

Chapitre 10

Une série d'écoulements en gaz ionisé dans W4-sud

Sommaire

10.1 Avant-propos : diagrammes du comportement cinématique spatial

Pour faire suite à la recommendation d'un des examinateurs, cet annexe présente une série de graphiques permettant un support visuel plus détaillé aux Figures 5.5 à 5.8. Tous les écoulements, A à X, du Tableau 5.4 y sont représentés d'une façon identique à la Figure 5.10. Les régions en « pointe-de-tarte », schématiquement identifiées aux Figures 5.5 à 5.8, sont composées d'une série d'arcs de cercle concentriques. Chaque arc croise et sélectionne un ensemble de points (pixels) sur les différentes cartes en vitesses radiales et en dispersions associées à W4-sud. Pour chaque arc, une moyenne est alors calculée parmi les pixels sélectionnés. Un point résulte alors sur le diagramme d vs v_{LSR} (ou d vs β_{corr} selon le cas) où d correspond ici à la distance spatiale (en unité de pc) sur le plan du ciel séparant l'arc de cercle en question et le centre de la région en « pointe-de-tarte ». Pour chaque point, l'incertitude (barre d'erreurs) est donnée par l'erreur cinématique moyenne de l'ensemble des pixels sélectionnés.

Afin d'éviter de masquer le gaz émissif des Figures 5.5 à 5.8, nous avons délibérément restreint le nombre d'arcs de cercle pour chaque écoulement examiné. Bien entendu, les régressions linéaires, présentées pour chaque figure de ce chapitre, supposent que les écoulement demeurent continus entre deux arcs de cercle adjacents. Tous les paramètres statistiques (pente, ordonnée à l'origine et coefficient de corrélation de Pearson), obtenus suite à ces régressions, sont indiqués au Tableau 5.4. Pour les panneaux (a) des Figures 10.1 à 10.24, associés à l'investigation en vitesses radiales, l'« astérisque » indique la vitesse radiale recensée du matériel neutre présenté comme étant à l'origine de l'écoulement ionisé. Pour les cas particuliers où deux « astérisques » se retrouvent sur un même diagramme, la droite les unissant indique l'intervalle en vitesses à l'intérieur duquel est susceptible de se retrouver la composante neutre. Pour chaque écoulement, la valeur du (ou des) symbole(s) « astérisque » est indiquée à la colonne 3 du Tableau 5.5.

10.2 Un apport visuel à la Figure 5.5

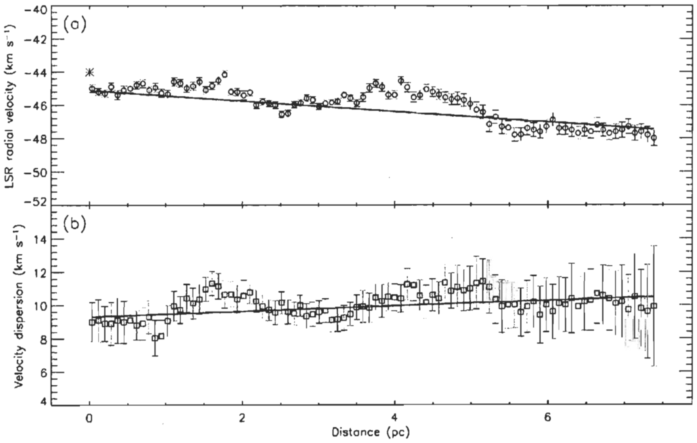

Figure 10.1: Comportement spatial de l'écoulement A.

Panneau (a) : en vitesses radiales, Panneau (b) : en largeurs de raie. Les cercles et carrés ouverts correspondent aux données observationnelles. Les traits solides représentent les régressions linéaires appliquées aux ensembles de points. Tous les paramètres statistiques de ces ajustements sont donnés au Tableau 5.4.

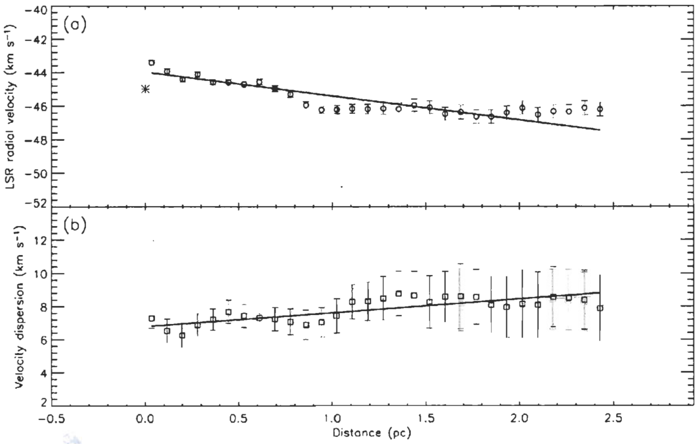

Figure 10.2: Comportement spatial de l'écoulement B.

Panneau (a) : en vitesses radiales, Panneau (b) : en largeurs de raie. Pour plus de détails, veuillez consulter la légende de la Figure 10.1.

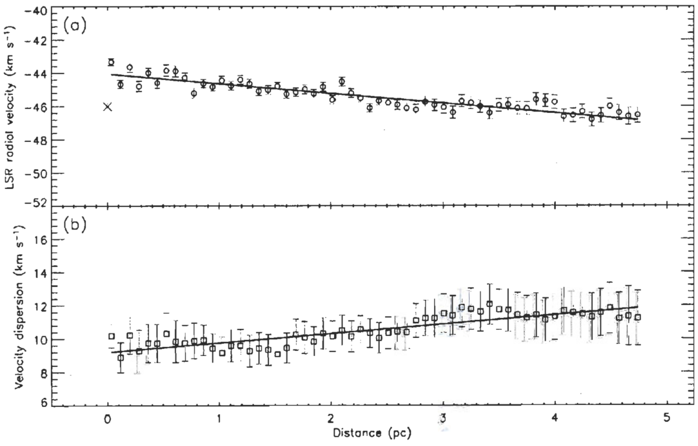

Figure 10.3: Comportement spatial de l'écoulement C.

Panneau (a) : en vitesses radiales, Panneau (b) : en largeurs de raie. Pour plus de détails, veuillez consulter la légende de la Figure 10.1.

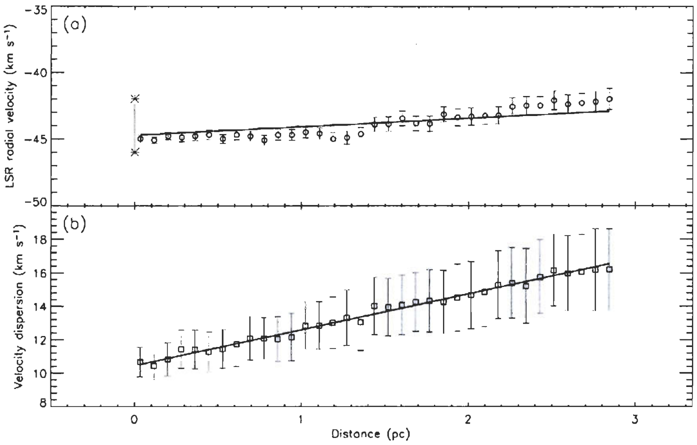

Figure 10.4: Comportement spatial de l'écoulement D.

Panneau (a) : en vitesses radiales, Panneau (b) : en largeurs de raie. Pour plus de détails, veuillez consulter la légende de la Figure 10.1.

10.3 Un apport visuel à la Figure 5.6

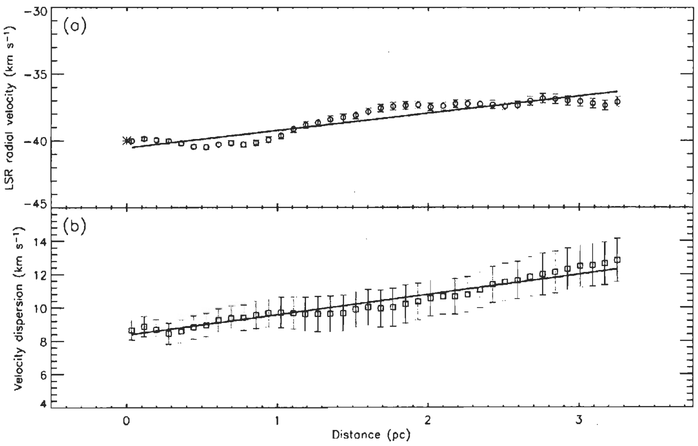

Figure 10.5: Comportement spatial de l'écoulement E.

Panneau (a) : en vitesses radiales, Panneau (b) : en largeurs de raie. Pour plus de détails, veuillez consulter la légende de la Figure 10.1.

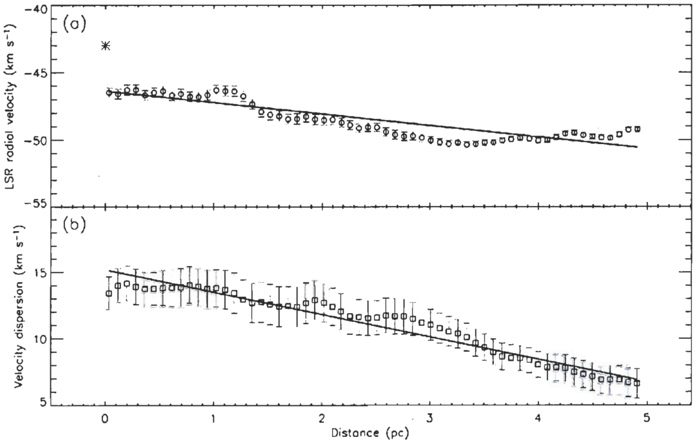

Figure 10.6: Comportement spatial de l'écoulement F.

Panneau (a) : en vitesses radiales, Panneau (b) : en largeurs de raie. Pour plus de détails, veuillez consulter la légende de la Figure 10.1.

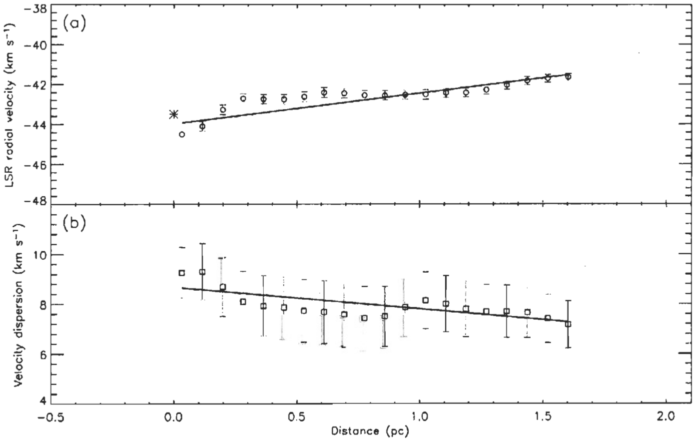

Figure 10.7: Comportement spatial de l'écoulement G.

Panneau (a) : en vitesses radiales, Panneau (b) : en largeurs de raie. Pour plus de détails, veuillez consulter la légende de la Figure 10.1.

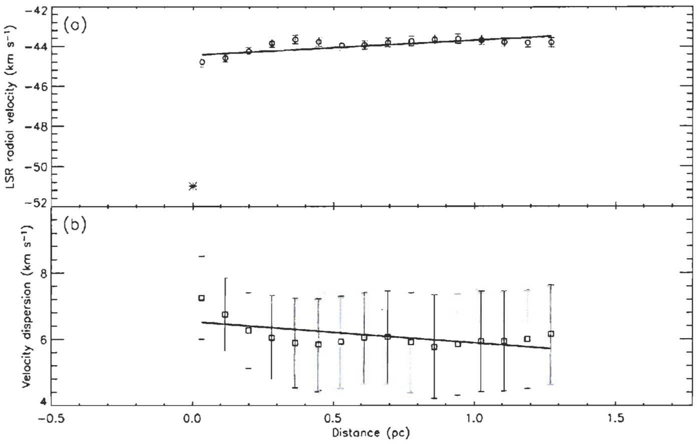

Figure 10.8: Comportement spatial de l'écoulement H.

Panneau (a) : en vitesses radiales, Panneau (b) : en largeurs de raie. Pour plus de détails, veuillez consulter la légende de la Figure 10.1.

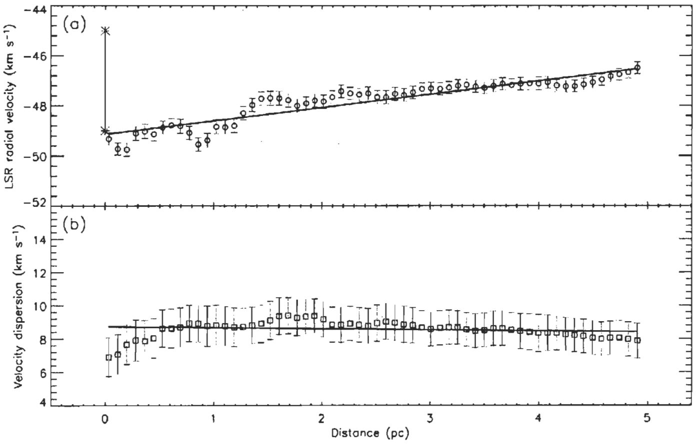

Figure 10.9: Comportement spatial de l'écoulement I.

Panneau (a) : en vitesses radiales, Panneau (b) : en largeurs de raie. Pour plus de détails, veuillez consulter la légende de la Figure 10.1.

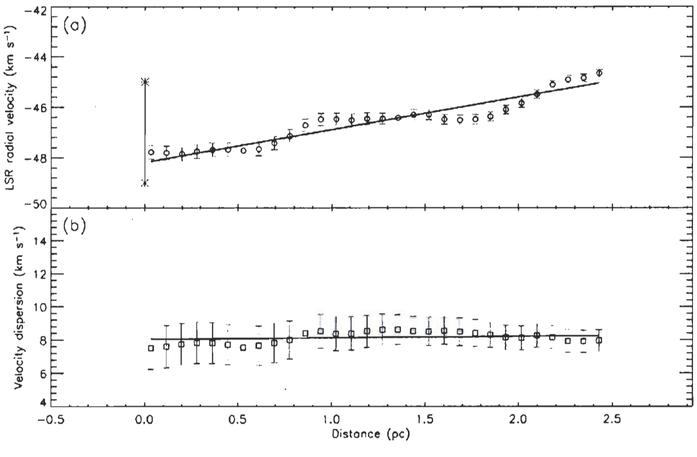

Figure 10.10: Comportement spatial de l'écoulement J.

Panneau (a) : en vitesses radiales, Panneau (b) : en largeurs de raie. Pour plus de détails, veuillez consulter la légende de la Figure 10.1.

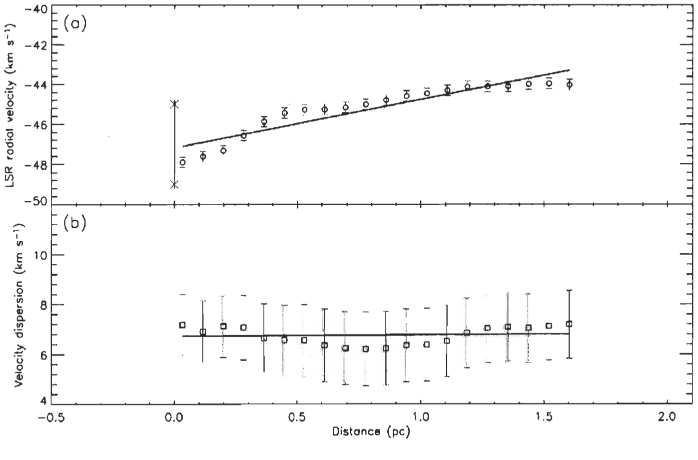

Figure 10.11: Comportement spatial de l'écoulement K.

Panneau (a) : en vitesses radiales, Panneau (b) : en largeurs de raie. Pour plus de détails, veuillez consulter la légende de la Figure 10.1.

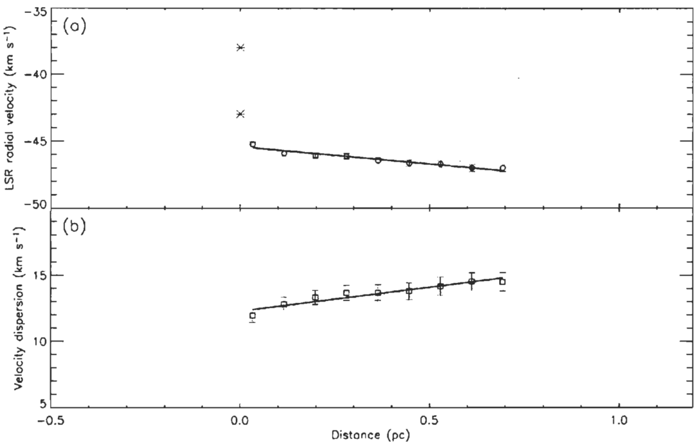

Figure 10.12: Comportement spatial de l'écoulement L.

Panneau (a) : en vitesses radiales, Panneau (b) : en largeurs de raie. Pour plus de détails, veuillez consulter la légende de la Figure 10.1.

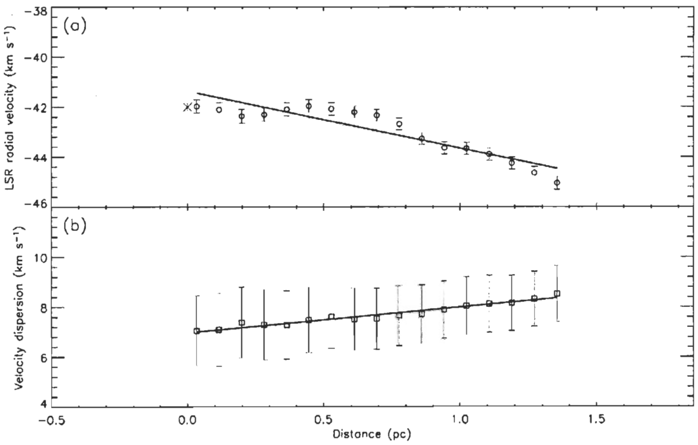

Figure 10.13: Comportement spatial de l'écoulement M.

Panneau (a) : en vitesses radiales, Panneau (b) : en largeurs de raie. Pour plus de détails, veuillez consulter la légende de la Figure 10.1.

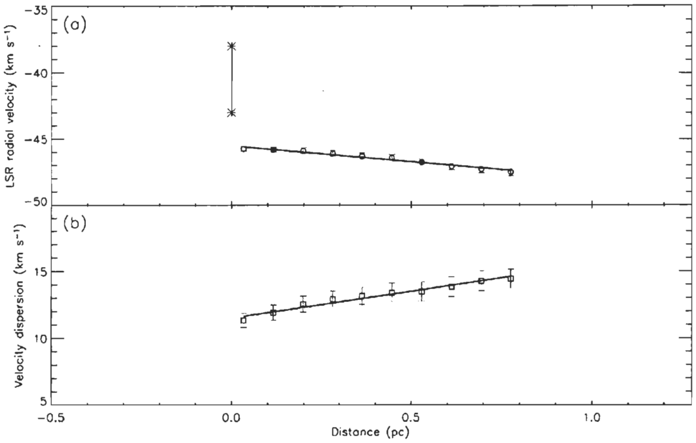

Figure 10.14: Comportement spatial de l'écoulement N.

Panneau (a) : en vitesses radiales, Panneau (b) : en largeurs de raie. Pour plus de détails, veuillez consulter la légende de la Figure 10.1.

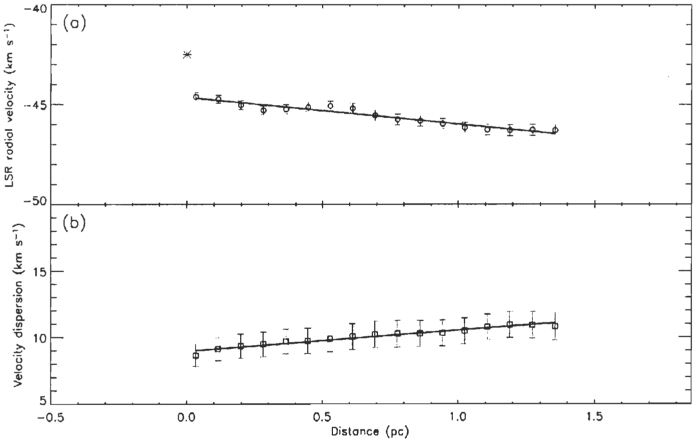

Figure 10.15: Comportement spatial de l'écoulement O.

Panneau (a) : en vitesses radiales, Panneau (b) : en largeurs de raie. Pour plus de détails, veuillez consulter la légende de la Figure 10.1.

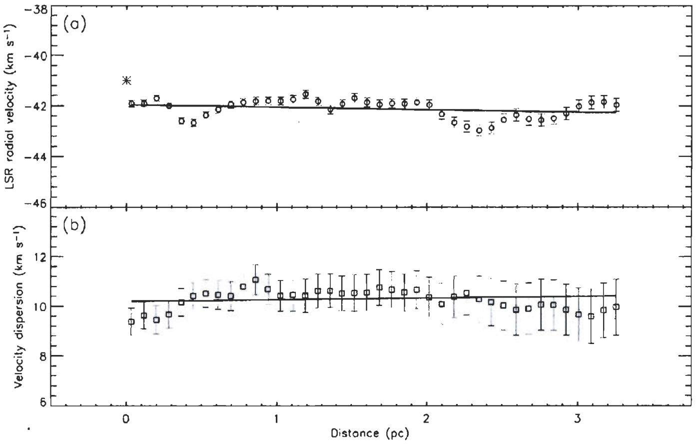

Figure 10.16: Comportement spatial de l'écoulement P.

Panneau (a) : en vitesses radiales, Panneau (b) : en largeurs de raie. Pour plus de détails, veuillez consulter la légende de la Figure 10.1.

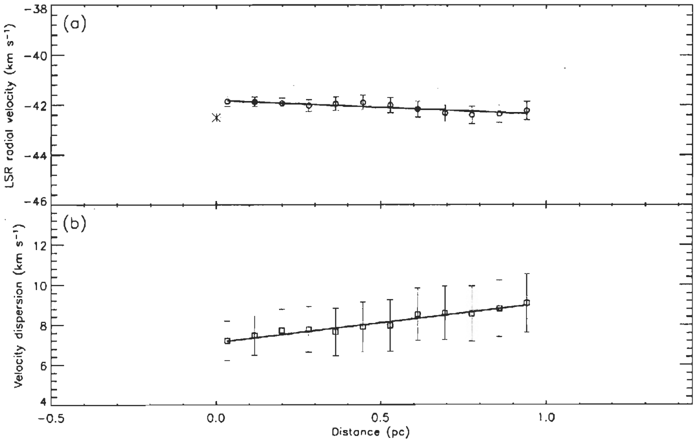

Figure 10.17: Comportement spatial de l'écoulement Q.

Panneau (a) : en vitesses radiales, Panneau (b) : en largeurs de raie. Pour plus de détails, veuillez consulter la légende de la Figure 10.1.

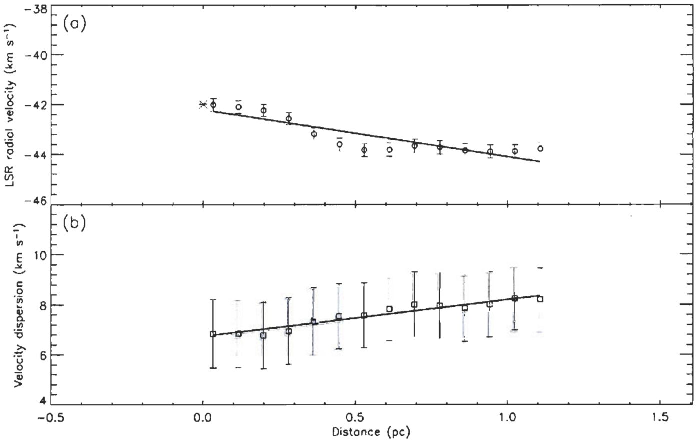

Figure 10.18: Comportement spatial de l'écoulement R.

Panneau (a) : en vitesses radiales, Panneau (b) : en largeurs de raie. Pour plus de détails, veuillez consulter la légende de la Figure 10.1.

10.4 Un apport visuel à la Figure 5.7

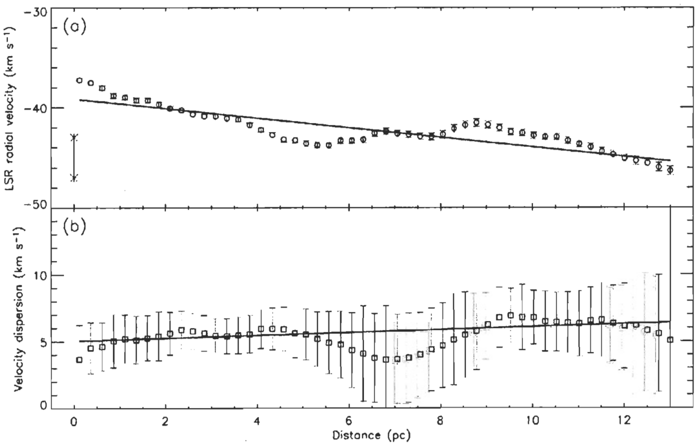

Figure 10.19: Comportement spatial de l'écoulement S.

Panneau (a) : en vitesses radiales, Panneau (b) : en largeurs de raie. Pour plus de détails, veuillez consulter la légende de la Figure 10.1.

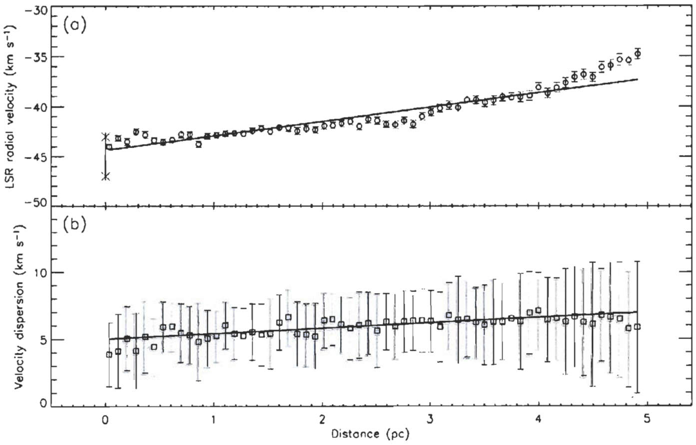

Figure 10.20: Comportement spatial de l'écoulement T.

Panneau (a) : en vitesses radiales, Panneau (b) : en largeurs de raie. Pour plus de détails, veuillez consulter la légende de la Figure 10.1.

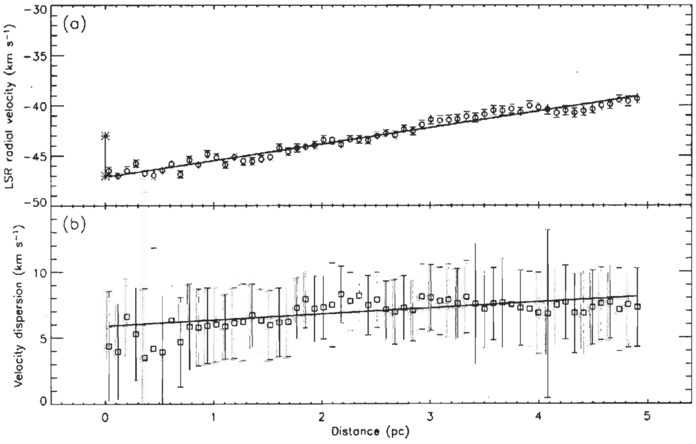

Figure 10.21: Comportement spatial de l'écoulement U.

Panneau (a) : en vitesses radiales, Panneau (b) : en largeurs de raie. Pour plus de détails, veuillez consulter la légende de la Figure 10.1.

10.5 Un apport visuel à la Figure 5.8

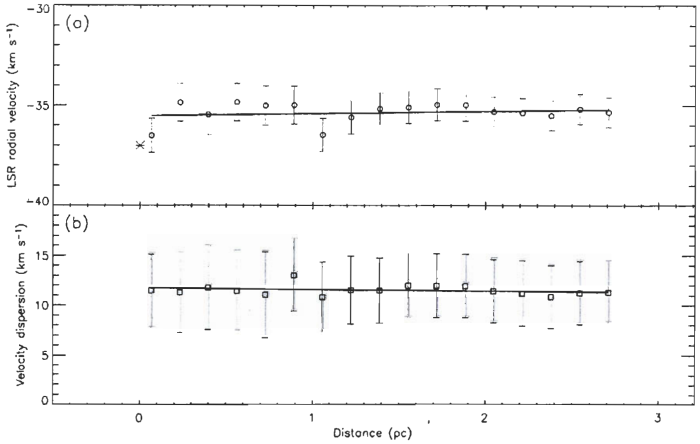

Figure 10.22: Comportement spatial de l'écoulement V.
Panneau (a) : en vitesses radiales, Panneau (b) : en largeurs de raie. Pour plus de détails, veuillez consulter la légende de la Figure 10.1.

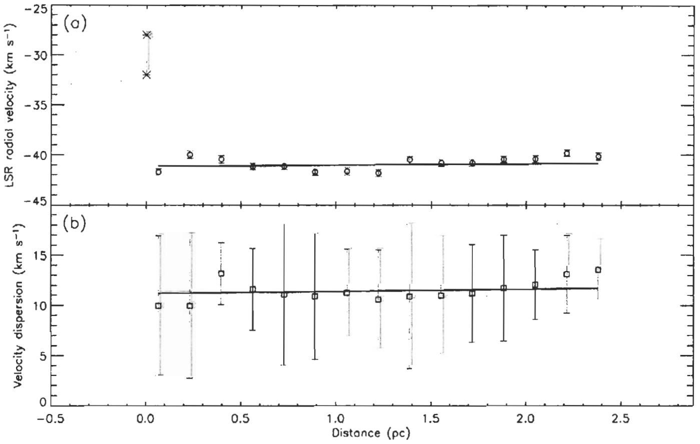

Figure 10.23: Comportement spatial de l'écoulement W.
Panneau (a) : en vitesses radiales, Panneau (b) : en largeurs de raie. Pour plus de détails, veuillez consulter la légende de la Figure 10.1.

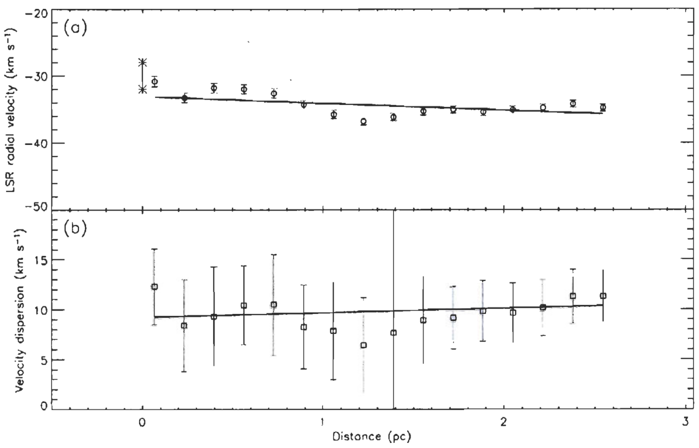

Figure 10.24: Comportement spatial de l'écoulement X.

Panneau (a) : en vitesses radiales, Panneau (b) : en largeurs de raie. Pour plus de détails, veuillez consulter la légende de la Figure 10.1.

Bibliographie

Abbot, D. C. 1982, *ApJ*, 263, 723

Amram, P. 1991, Thèse de doctorat, Université de Provence, France

Arsenault, R., & Roy, J.-R. 1988, *A&A*, 201, 199

Atherton, P. D., Taylor, K., Pike, C. D., Harmer, C. F. W., Parker, N. M., & Hook, R. N. 1982, *MNRAS*, 201, 661

Barriault, L., & Joncas, G. 2007, *ApJ*, 667, 257

Basu, S., Johnstone, D., & Martin, P. G. 1999, *ApJ*, 516, 843

Bekki, K., Tsujimoto, T., & Chiba, M. 2009, *ApJ*, 692, L24

Bevington, P. R. 1969, Data Reduction and Error Analysis for the Physical Sciences (New York : McGraw-Hill)

Bland, J., & Tully, B. 1989, *AJ*, 98, 723

Blitz, L., Fich, M., & Stark, A. A. 1982, *ApJS*, 49, 183

Bodenheimer, P., Tenorio-Tagle, G., & Yorke, H. W. 1979, *ApJ*, 233, 85

Bosch, G., Terlevich, E., & Terlevich, R. 2009, *AJ*, 137, 3437

Callaway, M. B., Savage, B. D., Benjamin, R. A., Haffner, L. M., & Tufte, S. L. 2000, *ApJ*, 532, 943

Capriotti, E. R., & Kozminski, J. F. 2001, *PASP*, 113, 677

Cardelli, J. A., Clayton, G. C., & Mathis, J. S. 1989, *ApJ*, 345, 245

Castañeda, H. O., Vílchez, J. M., & Copetti, M. V. F. 1992, *A&A*, 260, 370

Castañeda, H. O. 1994, *Ap&SS*, 216, 285

Castellanos, M., Díaz, Á. I., & Tenorio-Tagle, G. 2002, *ApJ*, 565, L79

Castor, J., McCray, R., & Weaver, R. 1975, *ApJ*, 200, L107

Chevalier, R. A., & Gardner, J. 1974, *ApJ*, 192, 457

Chiosi, C., & Maeder, A. 1986, *ARA&A*, 24, 329

Chu, Y.-H., & Kennicutt, R. C. 1994, *ApJ*, 425, 720

Comerón, F. 1997, *A&A*, 326, 1195

Comte, G., & Monnet, G. 1974, *A&A*, 33, 161

Corbelli, E., & Salucci, P. 2000, *MNRAS*, 311, 441

Courtès, G., Petit, H., Sivan, J.-P., Dodonov, S., & Petit, M. 1987, *A&A*, 174, 28

Cox, J. P., & Giuli, R. T. 1968, Principles of Stellar Structure (Gordon and Breach : New York)

Crowther, P. A. 2007, *ARA&A*, 45, 177

Cyganowski, C. J., Reid, M. J., Fish, V. L., & Ho, P. T. P. 2003, *ApJ*, 596, 344

Dahlem, M. 1997, *PASP*, 109, 1298

Daigle, O., Carignan, C., Hernandez, O., Chemin, L., & Amram, P. 2006, *MNRAS*, 368, 1016

Daigle, O., Gach, J.-L., Guillaume, C., Lessard, S., Carignan, C., & Blais-Ouellette, S. 2008, *Proc. SPIE*, 7014, 219

de Avillez, M. A., & Berry, D. L. 2001, *MNRAS*, 328, 708

de Avillez, M. A., & Breitschwerdt, D. 2005, *A&A*, 436, 585

De Robertis, M. M., Dufour, R. J., & Hunt, R. W. 1987, JRASC, 81, 195

Dennison, B., Topasna, G. A., & Simonetti, J. H. 1997, *ApJ*, 474, 31

Deul, E. R., & van der Hulst, J. M. 1987, *A&AS*, 67, 509

Deul, E. R., & den Hartog, R. H. 1990, *A&A*, 229, 362

Dickey, J. M., & Lockman, F. J. 1990, *ARA&A*, 28, 215

Digel, S. W., Lyder, D. A., Philbrick, A. J., Puche, D., & Thaddeus, P. 1996, *ApJ*, 458, 561

Dove, J. B., Shull, J. M., & Ferrara, A. 2000, *ApJ*, 531, 846

Drissen, L., Moffat, A. F. J., & Shara, M. M. 1990, *ApJ*, 364, 496

Drissen, L., Moffat, A. F. J., & Shara, M. M. 1993, *ApJ*, 105, 1400

Drissen, L., Crowther, P. A., Úbeda, L., & Martin, P. 2008, *MNRAS*, 389, 1033

Dyson, J. E. 1979, *A&A*, 73, 132

Dyson, J. E., & Meaburn, J. 1971, *A&A*, 12, 219

Dyson, J. E., & Williams, D. A. 1980, The Physics of the Interstellar Medium (Manchester : MUP)

Felli, M., Habing, H. J., & Israël, F. P. 1977, *A&A*, 59, 43

Field, G. B., Goldsmith, D. W., & Habing, H. J. 1969, *ApJ*, 155, 149

Firpo, V., Bosch, G., & Morrell, N. 2005, *MNRAS*, 356, 1357

Franco, J., Tenorio-Tagle, G., & Bodenheimer, P. 1990, *ApJ*, 349, 126

Gach, J.-L., Hernandez, O., Boulesteix, J., Amram, P., Boissin, O., Carignan, C., Garrido, O., Marcelin, M., Östlin, G., Plana, H., & Rampazzo, R. 2002, *PASP*, 114, 1043

Galleti, S., Bellazzini, M., & Ferraro, F. R. 2004, *A&A*, 423, 925

García-Segura, G., Mac Low, M.-M., & Langer, N. 1996, *A&A*, 305, 229

Gill, T. P. 1965, The Doopler Effect - An Introduction to the Theory of the Effect (London : Logos Press)

Godbout, S., Joncas, G., Durand, D., & Arsenault, R. 1997, *ApJ*, 478, 271

Godbout, S., Joncas, G., & Drissen, L. 1998, PASA, 15, 60

Godbout, S. 2003, Thèse de doctorat, Université Laval, Canada

Gol'dfel'd, M. A., Zinov'ev, V. N., & Lebiga, V. A. 1987, Fluid Dynamics, 22, 40

Grosdidier, Y., Moffat, A. F. J., Blais-Ouellette, S., Joncas, G., & Acker, A. 2001, *ApJ*, 562, 753

Heiles, C. 1991, IAUS, 147, 43

Henney, W. J., Arthur, S. J., & Garciá-Díaz, Ma. T. 2005, *ApJ*, 627, 813

Henny, J. G., Lamers, L. M., & Cassinelli, J. P. 1999, Introduction to stellar winds (Cambridge : CUP)

Hernandez, O., Gach, J.-L., Carignan, C., & Boulesteix, J. 2003, *Proc. SPIE*, 4841, 1472

Hester, J. J., *et al.* 1996, *AJ*, 111, 2349

Heyer, M. H., Brunt, C., Snell, R. L., Howe, J. E., & Schloerb, F. P. 1998, *ApJS*, 115, 241

Hippelein, H., & Fried, J. W. 1984, *A&A*, 141, 49

Hoopes, C. G., & Walterbos, R. A. M. 2000, *ApJ*, 541, 597

Hunter, D. A., Shaya, E. J., Scowen, P., Hester, J. J., Groth, E. J., Lynds, R., & O'Neil, E. J. Jr. 1995, *ApJ*, 444, 758

Jiménez-Vicente, J., & Battaner, E. 2000, *A&A*, 358, 812

Jenkins, E. B., & Meloy, D. A. 1974, *ApJ*, 193, 121

Joncas, G., & Roy, J.-R., 1984, *ApJ*, 283, 640

Joncas, G., & Roy, J.-R., 1986, *ApJ*, 307, 649

Kennicutt, R. C. 1984, *ApJ*, 287, 116

Kleiner, S. C., & Dickman, R. L. 1985, *ApJ*, 295, 466

Kolmogorov, A. N. 1941, Dokl. Akad. Nauk. SSSR, 30, 301

Kudritzki, R.-P., & Puls, J. 2000, *ARA&A*, 38, 613

Kutner, M. L. 1984, Fundam. Cosm. Phys., 9, 233

Lagrois, D., & Joncas, G. 2009a, *ApJ*, 691, 1109 (Paper I)

Lagrois, D., & Joncas, G. 2009b, *ApJ*, 693, 186 (Paper II)

Lagrois, D., & Joncas, G. 2009c, *ApJ*, sous presse

Lagrois, D., & Joncas, G. 2009d, *ApJ*, en préparation

Lagrois, D., Joncas, G., & Godbout, S. 2009, *ApJ*, en préparation

Landau, L. D., & Lifshitz, E. M. 1987, Fluid Mechanics 2nd edition (Toronto : Permagon Press)

Laval, A., Boulesteix, J., Georgelin, Y. P., Georgelin, Y. M., & Marcelin, M. 1987, *A&A*, 175, 199

Lee, Y., Jung, J. H., Chung, H. S., Kim, H.-G., Park, Y.-S., Kim, H. R., Kim, B.-G., Kim, J., & Han, S.-T. 1999, *ApJS*, 138, 187

Leitherer, C. 1988, *ApJ*, 334, 626

Leitherer, C., Robert, C., & Drissen, L. 1992, *ApJ*, 401, 596

Lenz, D. D., & Ayres, T. R. 1992, *PASP*, 104, 1104

Lequeux, J. 2005, The Interstellar Medium (Berlin : Springer)

Llorente de Andrés, F., Burki, G., & Ruiz del Arbol, J. A. 1982, *A&A*, 107, 43

Lozinskaya, T. A. 1992, Supernovae and Stellar Wind in the Interstellar Medium (New York : AIP)

Mac Low, M.-M., & McCray, R. 1988, *ApJ*, 324, 776

Mac Low, M.-M., McCray, R., & Norman, M. L. 1989, *ApJ*, 337, 141

Magrini, L., Vílchez, J. M., Mampaso, A., Corradi, R. L. M., & Leisy, P. 2007, *A&A*, 470, 865

Maíz-Apellániz, J. 2004, *PASP*, 116, 859

Malmann, J. A. H., Copetti, M. V. F., dos Santos, I. C. F, Castañeda, H. O., & Vílchez, J. M. 2002, dans Revista Mexicana de Astronomía y Astrofísica (Paris : IAU), eds. Clariá, J. J., Lambas, D. G., & Levato, H., 14, 57

Malumuth, E. M., Waller, W. H., & Parker, J. WM. 1996, *AJ*, 111, 1128

Massey, P., Johnson, K. E., & DeGioia-Eastwood, K. 1995, *ApJ*, 454, 151

Mathis, J. S. 1986, *ApJ*, 301, 423

McClure-Griffiths, N. M., Dickey, J. M., Gaensler, B. M., Green, A. J., Haynes, R. F., & Wieringa, M. H. 2000, *AJ*, 119, 2828

McClure-Griffiths, N. M., Green, A. J., Dickey, J. M., Gaensler, B. M., & Wieringa, M. H. 2001, *ApJ*, 551, 394

McClure-Griffiths, N. M., Ford, A., Pisano, D. J., Gibson, B. K., Staveley-Smith, L., Calabretta, M. R., Dedes, L., & Kalberla, P. M. W. 2006, *ApJ*, 638, 196

McKee, C. F., & Ostriker, J. P. 1977, *ApJ*, 218, 148

Medina-Tanco, G. A., Sabalisck, N., Jatenco-Pereira, V., & Opher, R. 1997, *ApJ*, 487, 163

Melnick, J. 1977, *ApJ*, 213, 15

Melnick, J., Tenorio-Tagle, G., & Terlevich, R. 1999, *MNRAS*, 302, 677

Meynet, G., & Maeder, A. 2005, *A&A*, 429, 581

Miesch, M. S., & Bally, J. 1994, *ApJ*, 429, 645

Miville-Deschênes, M.-A., Joncas, G., & Durand, D. 1995, *ApJ*, 454, 316

Miville-Deschênes, M.-A., Levrier, F., & Falgarone, E. 2003, *ApJ*, 593, 831

Mizuta, A., Kane, J. O., Pound, M. W., Remington, B. A., Ryutov, D. D., & Takabe, H. 2005, *AJ*, 621, 803

Mokiem, M. R., de Koter, A., Evans, C. J., Puls, J., Smartt, S. J., Crowther, P. A., Herrero, A., Langer, N., Lennon, D. J., Najarro, F., Villamariz, M. R., & Vink, J. S. 2007, *A&A*, 465, 1003

Müller, P., Reif, K., & Reich, W. 1987, *A&A*, 183, 327

Muñoz-Tuñón, C., Tenorio-Tagle, G., Castañeda, H. O., & Terlevich, R. 1996, *AJ*, 112, 1636

Niedzielski, A., & Skórzyński, W. 2002, AcA, 52, 81

Norman, C. A., & Ikeuchi, S. 1989, *ApJ*, 345, 372

Normandeau, M., Taylor, A. R., & Dewdney, P. E. 1996, *Nature*, 380, 687

Normandeau, M., Taylor, A. R., & Dewdney, P. E. 1997, *ApJS*, 108, 279

Normandeau, M. 2000, dans ASP Conference Series, Stars, Gas and Dust in Galaxies : Exploring the Links, eds. Alloin, D., Galaz, G., & Olsen, K., 221, 41

O'Dell, C. R., & Townsley, L. K. 1988, *A&A*, 198, 283

Osterbrock, D. E. 1989, Astrophysics of Gaseous Nebulae and Active Galactic Nuclei (Mill Valey : University Science Books)

Osterbrock, D. E., Fulbright, J. P., Martel, A. R., Keane, M. J., Trager, S. C., & Basri, G. 1996, *PASP*, 108, 277

Paladini, R., Davies, R. D., & DeZotti, G. 2004, *MNRAS*, 347, 237

Pellerin, A. 2006, *AJ*, 131, 849

Prinja, R. K., Barlow, M. J., & Howarth, I. D. 1990, *ApJ*, 361, 607

Rathborne, J. M., Johnson, A. M., Jackson, J. M., Shah, R. Y., & Simon, R. 2009, *ApJS*, 182, 131

Rees, M. H. 1989, Physics and Chemistry of the Upper Atmosphere (Cambridge : CUP)

Relaño, M., & Beckman, J. E. 2005, *A&A*, 430, 911

Reynolds, R. J. 1989a, *ApJ*, 339, L29

Reynolds, R. J. 1989b, *ApJ*, 345, 811

Reynolds, R. J., Sterling, N. C., & Haffner, L. M. 2001, *ApJ*, 558, 101

Reynolds, R. J. 2004, AdSpR, 34, 27

Roger, R. S., & Dewdney, P. E. 1992, *ApJ*, 385, 536

Rola, C., & Pelat, D. 1994, *A&A*, 287, 676

Rosa, M. 1983, Highlights of Astronomy, 6, 625

Rosa, M., & Solf, J. 1984, *A&A*, 130, 29

Rosa, M. 1993, dans Lecture Notes in Physics, New Aspects of Magellanic Cloud Research (Berlin : Springer)

Rosolowsky, E., Keto, E., Matsushita, S., & Willner, S. P. 2007, *ApJ*, 661, 830

Roy, J.-R., Arsenault, R., & Joncas, G. 1986, *ApJ*, 300, 624

Roy, J.-R., Aubé, M., McCall, M. L., & Dufour, R. J. 1992, *ApJ*, 386, 498

Rozas, M., Richer, G., López, J. A., Relaño, M., & Beckman, J. E. 2006a, *A&A*, 455, 539

Rozas, M., Richer, G., López, J. A., Relaño, M., & Beckman, J. E. 2006b, *A&A*, 455, 549

Rozas, M., Richer, G., Steffen, W., García-Segura, G., & López, J. A. 2007, *A&A*, 467, 603

Rubin, R. H. 1983, *ApJ*, 274, 671

Sáinz, A., García, M. C., & Calzada, M. D. 2005, dans 32nd EPS Conference on Plasma Physics 29C, ed. C. Hidalgo & B. Ph. van Milligen (Bristol : IOP Publishing), 4.132

Scalo, J. M. 1984, *ApJ*, 277, 556

Shapiro, P. R., & Field, G. B. 1976, *ApJ*, 205, 762

Sharpless, S. 1959, *ApJS*, 4, 257

Shi, H. M., & Hu, J. Y. 1999, *A&AS*, 136, 313

Shu, F. H. 1992, Gas Dynamics Vol. II (Mill Valley : University Science Books)

Shu, F. H., Lizano, S., Galli, D., Cantó, J., & Laughlin, G. 2002, *ApJ*, 580, 969

Shields, G. A. 1990, *ARA&A*, 28, 525

Skillman, E. D, & Balick, B. 1984, *ApJ*, 280, 580

Skinner, W. R., Yee, J.-H., Hays, P. B., & Burrage, M. D. 1998, AdSpR, 21, 835

Smith, M. G., & Weedman, D. 1970, *ApJ*, 161, 33

Spitoni, E., Recchi, S., & Matteucci, F. 2008, *A&A*, 484, 743

Spitzer, L. Jr. 1956, *ApJ*, 124, 20

Strömgren, B. 1939, *ApJ*, 89, 526

Stubbs, C. W., & Garg, A. 2005, astro-ph/0512067v1

Taylor, A. R., Irwin, J. A., Matthews, H. E., & Heyer, M. H. 1999, *ApJ*, 513, 339

Tenorio-Tagle, G., 1979, *A&A*, 71, 59

Tenorio-Tagle, G., & Bedjin, J. P. 1981, *A&A*, 99, 305

Tenorio-Tagle, G., Beltrametti, M., Bodenheimer, P., & Yorke, H. W. 1982, *A&A*, 112, 104

Tenorio-Tagle, G., Muñoz-Tuñón, C., & Cox, D. P. 1993, *ApJ*, 418, 767

Tenorio-Tagle, G., Muñoz-Tuñón, C., Pérez, E., Maíz-Apellániz, J., & Medina-Tanco, G. 2000, *ApJ*, 541, 720

Terlevich, R., & Melnick, J. 1981, *MNRAS*, 195, 839

Terebey, S., Fich, M., Taylor, R., Cao, Y., & Hancock, T. 2003, *ApJ*, 590, 906

Thilker, D. A., Braun, R., & Walterbos, R. A. M. 2002, dans ASP Conference Series, Seeing Through the Dust (San Francisco : ASP), eds. Taylor, A. R., Landecker, T. L., & Willis, A. G., 276, 370

Thilker, D. A., Braun, R., Walterbos, R. A. M., Corbelli, E., Lockman, F. J., Murphy, E., & Maddalena, R. 2004, *ApJ*, 601, 39

Thilker, D. A., Braun, R., & Walterbos, R. A. M. 2009, *ApJ*, en préparation

Thorne, A. P. 1974, Spectrophysics (London : Chapman and Hall)

Vainio, R., & Laitinen, T. 2007, *ApJ*, 658, 622

Viallefond, F., Donas, J., & Goss, W. N. 1983, *A&A*, 119, 185

Viallefond, F., & Goss, W. N. 1983, *A&A*, 154, 357

Viironen, K., Delgado-Inglada, G., Mampaso, A., Magrini, L., & Corradi, R. L. M. 2007, *MNRAS*, 381, 1719

Vishniac, E. T. 1994, *ApJ*, 428, 186

Wakker, B. P. 2001, *ApJS*, 136, 463

Wang, X., & Dalton, C. 1991, International journal for numerical methods in fluids, 12, 383

Wang, J. & Heckman, T. M. 1997, *ApJ*, 491, 114

Watson, C., Zweibel, E. G., Heitsch, F., & Churchwell, E. 2004, *ApJ*, 608, 274

Weaver, R., McCray, R., Castor, J., Shapiro, P., & Moore, R. 1977, *ApJ*, 218, 377

West, J. L. 2003, Thèse de maîtrise, Université du Manitoba, Canada

West, J. L., English, J., Normandeau, M., & Landecker, T. L. 2007, *ApJ*, 656, 914

Westerhout, G. 1958, Bull. Astron. Inst. Neth., 14, 215

Wilson, C. D., & Scoville, N. 1992, *ApJ*, 385, 512

Wilson, C. D., Scoville, N., Madden, S. C., & Charmandaris, V. 2003, *ApJ*, 599, 1049

Yang, H., Chu, Y.-H., Skillman, E. D., & Terlevich, R. 1996, *AJ*, 112, 146

Yariv, A. 1997, Optical Electronics in Modern Communications (New York : OUP)

Yentis, D. J., Novick, R., & vanden Bout, P. 1972, *ApJ*, 177, 375

Yorke, H. W., Tenorio-Tagle, G., & Bodenheimer, P. 1984, *A&A*, 138, 325

Zurflueh, E. G. 1967, *J. Geophys. Res.*, 32(6), 1015